FLOW STRUCTURES AND HEAT TRANSFER ENHANCEMENT IN THE WAKES OF SLIDING BUBBLES

RUDI O'REILLY MEEHAN

Department of Mechanical & Manufacturing Engineering

Parsons Building

University of Dublin, Trinity College

Dublin 2

Ireland

March 2016

A thesis submitted to the University of Dublin in partial fulfillment of the requirements for the degree of Ph.D.

b

Declaration

I declare that this thesis has not been submitted as an exercise for a degree at this or any other university and is entirely my own work.

I agree to deposit this thesis in the University's open access institutional repository or allow the library to do so on my behalf, subject to Irish Copyright Legislation and Trinity College Library conditions of use and acknowledgement.

Rudi O'Reilly Meehan, March 2016

Abstract

The motion of a bubble through a fluid has attracted considerable scientific attention for many years due to the complex, interesting fluid dynamics in their wakes, coupled to a rich and varied interface motion. Additionally, vapour and gas bubbles have been found to significantly increase convective heat transfer rates between a heated surface and the surrounding fluid. Bubbles play a key role within two phase heat exchangers, in addition to applications in chemical engineering, water treatment and medicine. Of particular interest are two-phase cooling systems, which can achieve heat transfer coefficients considerably larger than their single-phase counterparts. However, a widespread implementation of these systems has yet to occur. This is due to their considerable size and to reliability issues resulting from the complexity of the flow, since the mechanisms involved in this bubble motion are dynamic and are often poorly understood. Although numerous studies exist for bubbles rising in an unbounded medium, that of bubbles rising in constricted geometries has received less attention. The particular case of a gas bubble sliding underneath an inclined surface in a quiescent medium is of key importance in the above applications. In particular, the wake of a sliding bubble and how it influences bubble interactions has received little to no attention in the literature.

This study experimentally investigates air bubbles sliding under an inclined surface in quiescent water in terms of the bubble mechanics, fluid motion and resulting heat transfer. Time-resolved particle image velocimetry (PIV) is utilised in three measurement planes to study the flow features in the wakes of sliding bubbles for a range of bubble diameters and surface inclination angles. High speed imaging and advanced analytical techniques are used to capture the dynamics of the bubble and the motion of its interface. High speed, high resolution infrared thermography is used to measure the two dimensional transient convective

surface heat transfer. An experimental setup has been designed and built to facilitate these measurements, while purpose specific code has been developed to analyse the experimental data in detail. These measurements are performed both for single bubbles and an in-line bubble pair.

Analysis of the measured velocity and vorticity fields reveals a wake structure consisting of a near wake that moves in close proximity to the bubble, shedding vorticity at the extrema of the bubble path. Downstream of the bubble in the far wake, these structures evolve into asymmetrical, oppositely-oriented hairpin vortices that are generated in the near wake. These hairpin vortices bear similarities to those observed behind freely rising bubbles and near-wall bluff bodies and are found to cause significant motion of the bulk fluid. This fluid motion is key to the convective heat transfer enhancement associated with a sliding bubble. Sliding bubbles were also found to provide local heat transfer enhancement of up to 6 times natural convection levels, which evolves dynamically as the bubble traverses the surface, spreading over a large area and affecting heat transfer rates. The current work links the bubble wake to the centroidal and interfacial dynamics of the bubble, in addition to quantifying the bubble-wake interactions in terms of fluid flow, bubble dynamics and surface heat transfer. This in-depth description of complex flow phenomena will be key in the future optimisation of multiphase convective heat transfer.

Acknowledgements

This work has been a collective effort and would not have been possible without the support of the following people. First, I would like to thank my family, especially my parents, for their unwavering support. I would like to thank my supervisor, Prof. Darina Murray, for her guidance, advice and willingness to make time available for me. I am also extremely thankful to Dr. Tim Persoons for his assistance and incredible mind and Mr. Gerry Byrne for his input, common sense and bad jokes.

One can count themselves fortunate to work in an exciting, dynamic group: I was even luckier in that I got to work in two. In Bell Labs Ireland, I owe much to my co-supervisor Dr. Brian Donnelly, who provided excellent advice and was great fun to work with. I am also very grateful to Dr. Domhnaill Hernon, who made this collaboration possible. I would like to thank the whole Bell Labs Ireland thermal management research group for being so welcoming. Special thanks to Mr. Ollie Burns, Dr. Rayhaan Farrelly and Dr. Kevin Nolan, who went out of their way to provide help.

In the thermal research group in TCD, I would like to thank Seamus, Diarmuid, Michael, Stephen, Richard, Kate, David, Cian, Eoin, Maurice and Sajad: it has been a blast working, collaborating and travelling with you. Our office that we shared with the Bio team of Matt, Ger, Michael, Guibing, Greg and Melika has been unbelievable fun. Work has rarely seemed like work, and I can think of a few coffee shops (and pubs) in Dublin that will be devastated to lose our business. Finally, I would like to thank all of my friends, particularly Ronan, Andy and Aisling, who somehow put up with me when I came home babbling about wake structures and surfactants.

Contents

List of Figures

List of Tables

Nomenclature

a	Minor axis of ellipsoidal bubble	$[m]$
a	Radius of spherical bubble	$[m]$
A_T	Transverse surface area	$[m^2]$
b	Breadth of bubble	$[m]$
C	Cross correlation	[-]
C_D	Drag coefficient	[-]
C_L	Lift coefficient	[-]
C_p	Specific heat capacity	$[J/kgK]$
C_{AM}	Added mass coefficient	[-]
D	Displacement	$[m]$
d_e	Equivalent diameter	$[m]$
D_I	Interrogation window size	$[px]$
d_p	Particle image diameter	$[m]$
E	Energy	$[J]$
F	Force	$[N]$
f	Frequency	$[Hz]$
g	Gravitational acceleration	$[m/s^2]$
h	Heat transfer coefficient	$[W/m^2K]$
I	Current	$[A]$
k	Thermal conductivity	$[W/mK]$
L_c	Characteristic length	$[m]$

M	Image magnification	[-]
N_I	Particle image density	[-]
q''	Heat flux	$[W/m^2]$
R	Electrical resistance	$[ohm]$
R	Radius of curvature	$[m]$
R_D	Correlation peak	[-]
s	Displacement	$[m]$
T	Temperature	[K]
t	Time	$[m]$
U	Bubble velocity	$[m/s]$
U_T	Terminal rise velocity	$[m/s]$
V	Bubble volume	$[m^3]$
V	Voltage	$[V]$
w	Width	[m]

Dimensionless Numbers

Bi	Biot number, $Bi = hL_c/k$	[-]
Eo	Eötvös number, $Eo = \Delta\rho g d_e^2/\sigma$	[-]
Fr	Froude number, $Fr = U_T/(gd_e \sin\theta)^{1/2}$	[-]
Mo	Morton number, $Mo = g\mu^4/\rho\sigma^3$	[-]
Nu	Nusselt number, $Nu = hL/k$	[-]
Ra	Rayleigh number, $Ra = GrPr$	[-]
Re	Reynolds number, $Re = \rho U_T d_e/\mu$	[-]
Sr	Strouhal number, $Sr = fd_e/U_T$	[-]
We	Weber number, $We = \rho U_T^2 d_e/\sigma$	[-]

Greek Symbols

α	Surface inclination angle	$[^\circ]$
α	Thermal diffusivity	$[m^2/s]$
β	Volumetric thermal expansion coefficient	$[1/K]$

χ	Aspect Ratio	[-]
Δz_0	Light-sheet thickness	$[m]$
δ	Thickness	$[m]$
ε	Bubble eccentricity	[-]
ε	Emissivity	[-]
ε	Flow enstrophy	$[s^2/m^2]$
λ	Light wavelength	[m]
μ	Fluid viscosity	$[kg/ms]$
ν	Kinematic viscosity	$[m^2/s]$
Ω	Vorticity	[1/s]
ϕ	Phase angle	$[^\circ]$
ρ	Fluid density	$[kg/m^3]$
ρ_{elec}	Resistivity	$[ohm.m]$
ρ_{x_1,x_2}	Pearson coefficient	[-]
σ	Stefan-Boltzman constant	$[W/m^2K^4]$
σ	Surface tension	$[N/m]$
τ	Shear stress	$[N/m^2]$
θ	Bubble separation angle	$[^\circ]$

Subscripts

∞	Bulk or infinity
0	Initial
cap	Storage
cond	Conductive
conv	Convective
f	Fluid
gen	Generated
g	Gas
lc	Lateral conduction

l	Liquid
p	Particle
rad	Radiative
RTD	RTD probe
surr	Surrounding walls
s	Surface
w	Water

Publications

- R. O'Reilly Meehan, B. Donnelly, K. Nolan, T. Persoons and D. B. Murray. Flow structures and dynamics in the wakes of sliding bubbles, *International Journal of Multiphase Flow*, Available online 30 April 2016, ISSN 0301-9322, 2016

- B. Donnelly, R. O'Reilly Meehan, K. Nolan and D. B. Murray. The dynamics of sliding air bubbles and the effects on surface heat transfer. *International Journal of Heat and Mass Transfer*, 91, 532-542, 2015.

- R. O'Reilly Meehan, B. Donnelly, T. Persoons and D. B. Murray. Dynamic flow structures in the wakes of sliding bubbles for convective heat transfer enhancment. In *IHTC-15: 15th International Heat Transfer Conference, Kyoto, Japan, 2014.*

- T. Persoons, R. O'Reilly Meehan and D. B. Murray. Time resolved high dynamic range PIV using local uncertainty estimation methods. In *17th International Symposium on Applications of Laser Techniques to Fluid Mechanics, Lisbon, Portugal, 2014.*

- R. O'Reilly Meehan. Enhancing heat transfer by the examination of flow structures in the wakes of sliding bubbles. 1st place in the *17th Annual Sir Bernard Crossland Symposium*, Galway, Ireland, 2014.

- R. O'Reilly Meehan, B. Donnelly, T. Persoons and D. B. Murray. Flow visualisation and wake characterisation of a sliding bubble using Particle Image Velocimetry. In *ExHFT 8: World Congress of Experimental Heat Transfer, Fluid Mechanics and Thermodynamics, Lisbon, Portugal, 2013.*

Chapter 1

Introduction

1.1 Background

By the year 2060, the amount of energy used worldwide in cooling will overtake that used in heating [1]. Traditionally, thermal management meant dissipating heat from a device by the use of simple heat sinks. However, as designers pack more devices and components into shrinking spaces, the thermal densities grow substantially. The thermal challenges thus grow with increasing levels of integration. As such, in recent years there has been a great demand for efficient, high-performance thermal management technologies. This also has implications on how we use energy: for instance, the 2014 IPCC report placed a heavy emphasis not only on renewable energy, but also on cutting waste energy through the development of novel technologies [2].

Two phase flows occur widely in both nature and industrial applications, including chemical engineering (bubble columns), water treatment (oxygenation and purification), energy production (stream generators in nuclear power plants) and even medicine (bursting of micro-bubbles). Two phase flows offer extremely high heat transfer coefficients, temperature homogenisation and passive or low power consumptions, all of which are extremely desirable from a cooling perspective [3]. However, despite extensive recent research, the widespread implementation of two phase technologies has yet to occur. This is in part due to the complex nature of the flows, which leads to significant uncertainty regarding the reliability of new two phase technologies. This complexity arises from the coupling between the motion of the

gas and liquid phases. Bubbles are compressible and deformable, meaning their mechanics are rich and complex. Furthermore, the behaviour of bubbly flows is highly dependent on a range of interdependent parameters, with changes in fluid properties and temperature leading to fundamentally altered system behaviour. When combined with phase change and associated heat transfer processes, the scale of the challenges faced in reliably predicting the performance of two phase systems is obvious.

Two-phase flow is known to significantly enhance heat transfer from a range of geometries. Current research on two phase flow has focused on the effect of bubbles moving against horizontal, vertical or inclined surfaces [4–8]. A key configuration of this flow is the motion of a bubble underneath a heated, inclined surface, which is relevant for two-phase shell and tube heat exchangers. Both vapour and gas bubbles have been found to significantly increase the convective heat transfer rate between a heated surface and the surrounding fluid. This has been attributed to the interaction between the bubble and the thermal boundary layer at the surface [8]. Bubble-based cooling could offer significant advantages over traditional single-phase liquid cooling systems. For vapour bubbles, a boiling phase change provides heat transfer coefficients that can be an order of magnitude greater than single-phase systems. Even without phase change, high heat transfer coefficients can be obtained using gas bubbles [6]. These bubbles could be generated either passively, or actively at very low power inputs. For instance, Wan et al. [9] used carbon nanocoils to achieve micro-bubble generation at $< 70\ \mu W$.

By de-coupling the interdependent parameters that make up two phase flows, the current work seeks a better understanding of the underlying behaviour from a fundamental point of view. This is achieved by studying air bubbles sliding under an inclined surface in quiescent water with no phase change, and initially no heat transfer. Although previous work has quantified the surface heat transfer enhancement offered by sliding air bubbles, limited research exists on the fluid behaviour that is responsible for this enhancement. Thus, a more complete knowledge of the sliding bubble wake will lead to improved modelling of two-phase phenomena and can provide insight into the wake-driven convective heat transfer involved. Finally, the base case of a single sliding bubble can be expanded to study the effects of the interactions between multiple bubbles, which are ubiquitous to two-phase systems. The influence of these interactions will be discussed with respect to the bubble dynamics, wake

structure and bubble-induced heat transfer enhancement. The overall goal of this work is to provide this fundamental platform and use it as a foundation for optimising two-phase convective heat transfer.

1.2 Dimensionless Numbers

A physical understanding of dimensionless numbers is important when interpreting the results observed in the literature on two-phase flow. These are a useful tool when looking at multiple data sets, as they allow for comparison between different experiments. In effect, by removing the dimensions, knowledge can be extended beyond the specific data set. For the current study, several key parameters can describe the transition between different modes of bubble behaviour. The dimensionless numbers used in this work are as follows:

Reynolds number:

$$Re = \frac{\rho U L}{\mu} = \frac{\rho U_T d_e}{\mu} \tag{1.1}$$

Weber number:

$$We = \frac{\rho U^2 L}{\sigma} = \frac{\rho U_T^2 d_e}{\sigma} \tag{1.2}$$

Morton number:

$$Mo = \frac{g\mu^4 \Delta\rho}{\rho^2 \sigma^3} \tag{1.3}$$

Eötvös number:

$$Eo = \frac{\Delta\rho g L^2}{\sigma} = \frac{\Delta\rho g d_e^2}{\sigma} \tag{1.4}$$

Froude number:

$$Fr = \frac{U}{\sqrt{g d_e}} \tag{1.5}$$

Capillary number:

$$Ca = \frac{\mu U}{\sigma} \tag{1.6}$$

Strouhal number:

$$Sr = \frac{fL}{U} = \frac{f d_e}{U_T} \tag{1.7}$$

Nusselt number:

$$Nu = \frac{hL}{k} \tag{1.8}$$

Rayleigh number:

$$Ra = \frac{g\beta\rho\Delta TL^3}{\mu\alpha} \tag{1.9}$$

The most often-used dimensionless parameter in fluid mechanics is the Reynolds number *Re*, which is the ratio of inertial to viscous forces. Depending on its magnitude, either the inertial forces dominate ($Re \gg 1$), the viscous forces dominate ($Re \ll 1$) or there is an approximate balance between the two ($Re \approx 1$). The Reynolds number is frequently used to determine the onset of turbulence or vortex shedding. In the general case in equation 1.1, ρ and μ are the fluid density and viscosity respectively, U is the velocity and L is a characteristic length. In the study of rising bubbles, the characteristic velocity is the relative velocity between the bubble and the fluid and is often expressed as the terminal rise velocity, U_T, while characteristic length is usually chosen to be the diameter of a sphere with the same volume as the bubble, i.e. the equivalent spherical diameter, d_e. For larger bubbles (volume > 3 cm^3), the base width, b, is generally used as the characteristic length, resulting in $Re = \rho U_T b/\mu$.

In two phase systems, it is common to use the Reynolds number in conjunction with the Morton and Eötvös numbers, to predict bubble shapes, terminal velocity and the onset of wake instability. The Morton number describes the physical properties of the surrounding medium and the pressure field. The value of Morton number, *Mo*, which is a fluid property and as such is not affected by bubble size or velocity, is highly dependent on the viscosity of the system: that is, its resistance to deformation by shear stress. There is an extremely wide range of possible Morton numbers, with low viscosity fluids such as water having values as low as $Mo = 2.5 \times 10^{-11}$, while high viscosity fluids such as corn syrup can have *Mo* of the order of 10^8. The Eötvös number, *Eo*, (often referred to as the Bond number outside of Europe) is a ratio of the buoyancy forces to the surface tension forces. High Eötvös number flows ($Eo \gg 1$) indicate the system is generally unaffected by surface tension forces, while low Eötvös number flows ($Eo < 1$) indicate the system is affected. The bubbles in the current study have a moderate Eötvös number.

Equally important for two-phase systems is the Weber number, *We*, which measures

the relative contributions of the dynamic pressure (ρU^2) and the surface tension pressure (σ/L). This balance between pressure and surface tension characterises the deformation of the bubble. For a Weber number that is < 3, the bubble deformation and motion are dominated by surface tension forces, while bubble behaviour for $We > 3$ is dominated by inertia. The surface tension, σ, is sensitive to the fluid temperature and purity: this will be explored in further detail in chapter 2. Some studies also use the Froude number (equation 1.5), which is the ratio of flow inertia to the external field (typically gravity).

It will become apparent in chapter 2 that the literature on bubbly flows does not use a common framework: instead, a bewildering amount of various dimensionless groups are presented. Where possible, the bubble regime in the current study will be characterised in terms of the Reynolds, Eötvös and Morton numbers. However, this range of dimensionless numbers fails to capture the influence of the liquid film that exists between the surface and the bubble. This is characterised by the capillary number in equation 1.6, which represents the ratio of the viscous drag forces (μU) to the surface tension forces across a liquid-gas interface.

For oscillating fluid systems, the Strouhal number is a useful dimensionless parameter. It can be used to characterise the vortex shedding behind a body, relating the frequency of vortex shedding, f, to the bubble or flow velocity with a characteristic length scale. For a cylinder in cross flow, the Strouhal number is approximately 0.2 over a large Reynolds number range [10]. There are also dimensionless parameters relating to heat transfer that are often used in empirical correlations to find heat transfer coefficients. In the current study, a relevant parameter is the Nusselt number, which represents the dimensionless temperature gradient at a heated or cooled surface. In equation 1.8, h is the heat transfer coefficient, L is the characteristic length and k is the thermal conductivity of the fluid medium. Finally, a useful parameter in free convection systems is the Rayleigh number, given by equation 1.9, where ΔT is the difference between the surface and fluid temperatures, β is the thermal expansion coefficient, v is the kinematic viscosity and α is the thermal diffusivity. The Rayleigh number can be thought of as the ratio between conductive and convective heat transfer for free convection flows. When necessary, other dimensionless numbers will be defined when encountered in the text.

Chapter 2

Literature Review

The inherent complexities of bubble shape, motion, path and wakes are well known, and have been recognised as a barrier to optimisation of bubbly flows in practical applications. The specific properties of bubbles make their dynamics rich and varied; the purpose of this section, therefore, is to provide an overview of bubble behaviour before narrowing the focus to determine the existing gaps in the literature. This chapter will first examine the many experimental and numerical studies on the mechanics of single and interacting freely rising bubbles, paying particular attention to the wake structures observed. The literature associated with the mechanics and heat transfer enhancement of sliding bubbles will also be reviewed. It will become apparent that the literature on sliding bubble wake structures is very limited: thus, to better understand the wake mechanics of sliding bubbles, the review will look into pertinent numerical and experimental studies of near-wall turbulence and of the wakes of near-wall bluff objects for greater insight.

2.1 Freely Rising Bubbles

Freely rising bubbles have been studied extensively in the literature, and have much in common with sliding bubbles. As such, any study on sliding bubbles requires a knowledge of rising bubble behaviour. This review intends to discuss rising bubbles in terms of the bubble and wake mechanics, but a complete overview of rising bubble behaviour is not the goal. Instead, information about rising bubbles that is pertinent to understanding sliding bubbles is discussed.

2.1.1 Single Bubble Mechanics

The interaction between a gas bubble and the surrounding medium determines its shape, and the associated disruption of the surrounding flow field. Bubbles experience a dynamic pressure as they move. At the front of the bubble, there is a stagnation point that results in a pressure acting inwards towards the bubble surface. At the sides of the bubble, the liquid must accelerate around the bubble to maintain its flow, meaning the pressure decreases from the front stagnation point to the sides. This causes the bubble surface at the sides to move outwards and increase its local curvature. At the back, the presence of the wake (this will be discussed in section 2.1.2) means that the pressure does not recover to the ambient value.

Bubbles rising in a quiescent medium can be broadly grouped into three shapes, in order of increasing Reynolds number: spherical, ellipsoidal and spherical-cap shape. The shape of a bubble depends upon the relative magnitudes of the relevant forces acting on the bubble. These are determined by a range of physical variables, with some simplifying assumptions. Haberman & Morton [11] proposed that the bubble shape was a function of 8 parameters, namely acceleration due to gravity, g, the terminal rise velocity, U_b, the equivalent spherical diameter d_e, viscosity of the liquid, μ_l, and gas, μ_g, the density of the liquid ρ_l and gas, ρ_g, and the surface tension of the liquid, σ. For gas bubbles rising in water, the viscosity and density of the gas are significantly lower than that of the fluid and can be ignored. These parameters can then be grouped together in terms of dimensionless numbers, although, as stated in section 1.3, the choice of dimensionless numbers is something of a dark art in two-phase fluid mechanics. For the current study, bubbles will be represented in terms of the Reynolds number, Weber number and Morton number.

The plot in figure 2.1 (a) shows the bubble shape regime in terms of the Eötvös, Morton and Reynolds numbers, based on the experiments of Bhaga & Weber [12], who studied bubbles rising in aqueous water/glucose solutions. The shapes were classified as spherical, oblate ellipsoidal, oblate ellipsoidal cap, spherical cap with an open or closed wake, and skirted bubbles with open or closed wakes. The various regimes observed were sketched by Fan and Tsuchiya [13] in their seminal work on rising bubble wake dynamics, and are shown in figure 2.1 (b). Note that while this shape regime map has been heavily cited in the literature, it has some drawbacks. To explain why this is the case requires a more in-depth

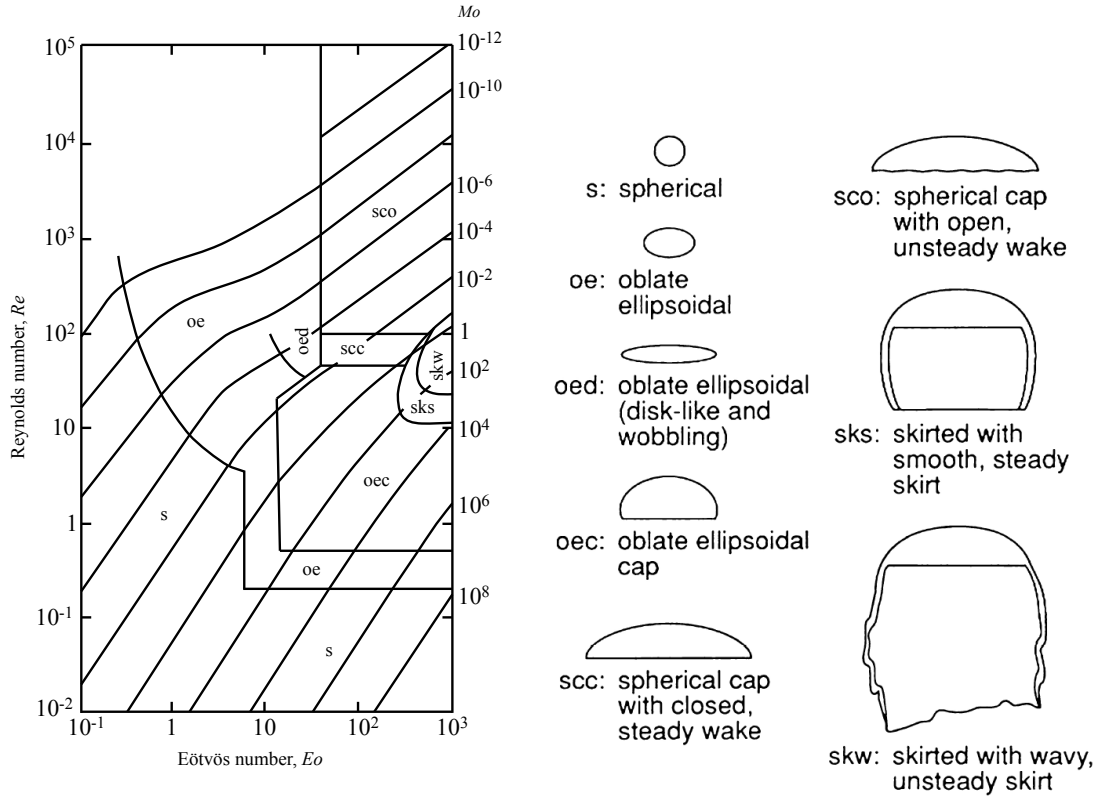

Figure 2.1: (a) The bubble shape regime map, characterised by the Reynolds, Eötvös & Morton numbers, Bhaga & Weber [12]. The individual shapes corresponding to each regime are described in (b) by Fan & Tsuchiya [13].

knowledge of the bubble dynamics. For now, we will continue to reference the Bhaga & Weber [12] shape regime map, but will return later to discuss its limitations.

At low bubble diameters ($d_e < 1\ mm$), the surface tension forces are dominant and the shapes approximate spheres.The flow around the bubble is dictated by viscosity, and if the Reynolds number $Re << 1$, it can be described by creeping flow. For bubbles of intermediate size, the effects of surface tension and inertia, which is due almost entirely to the fluid surrounding the bubble decelerating or accelerating, are both important. In this regime, the bubbles are also strongly influenced by the liquid viscosity and impurities in the fluid. In liquids with low viscosity and Morton number (e.g. water), these bubbles, which can be broadly classed as ellipsoidal, experience complex motion in terms of shape and path. These bubbles often lack fore-and-aft symmetry, and have a complicated wake structure to the rear. It transpires that these complex bubbles are used in the current study.

As a bubble rises through a fluid, work is done on the fluid by the bubble. This occurs

at a rate equal to the rise velocity times the buoyancy force. At low Reynolds numbers, the energy associated with this work is dissipated through viscosity, and results in rectilinear bubble motion. However, in a low viscosity fluid, the energy generated by the rising bubble is not entirely consumed by viscous dissipation, with some energy released through turbulent dissipation in the wake. This wake instability induces a secondary motion on the bubble, causing oscillations in bubble path and shape. As the Reynolds number increases, the path changes first from rectilinear to zigzag, and finally to spiral. This was studied for bubbles rising in pure water by Saffman [14], who found that bubbles rose with a rectilinear path when the bubble diameter, d_e, was less then 1.4 *mm*. Between d_e of 1.4 – 2 *mm*, the bubble appeared to zigzag within a fixed plane throughout its rise, although the orientation of this plane seemed to be random. Bubbles with d_e in the range of 2 – 4.6 *mm* could experience either zigzag or spiral motion. At about 4.6 *mm* the degree of path oscillations began to reduce in magnitude, and was fully dissipated for diameters above 6 *mm*. Saffman [14] attributed this zigzag behaviour to the vortex shedding in the wake initiating an instability in the bubble motion. This is not dissimilar to the situation with solid spheres, but occurs at higher Reynolds numbers for bubbles due to the different surface boundary conditions (zero-slip for a sphere, zero-stress for a bubble).

An important parameter in the field of rising bubbles is the terminal rise velocity U_T. There is extensive work in the literature on defining this in terms of the other five parameters previously mentioned, that is, $U_T = f(\mu_l, \rho_l, d_b, \sigma, g)$. However, in the current study, the bubble's rise height is short (< 30 mm), preventing the bubble from reaching its terminal rise velocity. Instead, it is the sliding terminal velocity that is of interest here; this will be discussed in section 2.1.2. As such, the various governing equations for terminal rise velocity are not provided. At extremely low Reynolds numbers, Hadamard [15] and Rybczynski [16], independently solved for the terminal rise velocity in 1911. The assumptions in the analysis were those of creeping flow and no contaminants, resulting in a constant surface tension boundary condition. This model predicted that bubbles remain spherical until the inertial forces become significant (this transition number corresponds to the $(s-oe)$ curve in figure 2.1). In reality, the Hadamard-Rybczynski formula acts as a limiting case for the terminal rise velocity, as it is virtually impossible to remove all impurities from a fluid system. For an entirely contaminated surface, the velocity can be expressed in terms of Stokes formula

for flow past rigid spheres.

It transpires that these contaminants in the liquid phase, often called surfactants, are crucial to two-phase systems, and can fundamentally alter the bubble mechanics. Surfactants can gather on the surface of the bubble, reducing its mobility and dramatically reducing the surface tension. As the bubble rises through the contaminated medium, these impurities are pushed from the front stagnation point to the rear, which causes a no-slip boundary condition at the rear of the bubble and a tangential surface tension gradient. This gradient causes a tangential stress, referred to as a Marangoni stress, which acts to oppose the flow shear stress. This is often referred to as the "stagnant cap" hypothesis, as the rear of the bubble is immobile [17–19]. This has the result that the drag coefficient of the bubble approaches that of a sphere, which can be calculated easily from Stokes drag model. Savic [20] assumed a surface tension gradient over the bubble, which transitioned from surfactant-free at the front to zero surface tension at the rear, whereas Griffith [18] performed experiments with excessive fluid contaminants. The results obtained by both of these studies are shown in figure 2.2 (a). As a general rule, Griffith's curve is used when the contaminant is both known and plentiful, while Savic's curve should be used when the type or amount of contaminant is unknown. As the bubble shape changes from spherical to ellipsoidal, the experimental data become more scattered. Clift et al. [21] combined the terminal velocities measured by various authors into figure 2.2 (b), combining tests in pure water (upper curve) and contaminated water (lower curve). As can be observed in figure 2.2 (b), the upper and lower bounds of the data converge at smaller and larger bubble diameters, but for ellipsoidal bubbles, the water purity has a significant effect on the terminal velocity. For instance, Duineveld [22] showed the velocity for 1.6 *mm* bubbles rising in tap water was half that of pure water.

So far, it has been observed that bubbles in the ellipsoidal regime experience large distortions in bubble shape, which are also time-dependent. The precise mechanics of this motion remains difficult to quantify, with many studies obtaining different terminal velocity results for the same dimensionless parameters [23–26]. This difference is often attributed to differences in surfactant concentration. Tomiyama et al. [27] make the point that few studies have actually quantified this change in concentration as being the key reason behind this scatter, referring to the experiments of Zhang and Finch [28], who found U_T to be independent of surfactant concentration for $d_e = 1.3$ *mm*. Instead, the authors claimed that

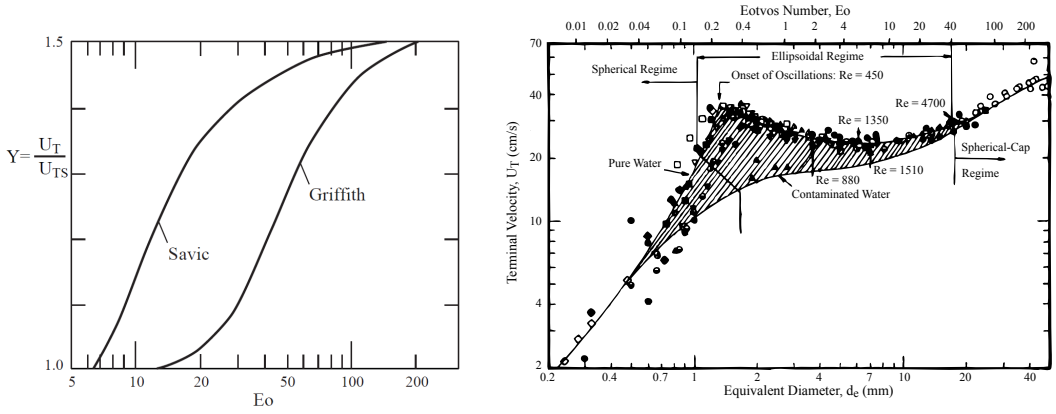

Figure 2.2: (a) Ratio of rising bubble terminal velocity to Stokes terminal velocity versus Eötvös number, (b) Terminal velocity of air bubbles versus the equivalent diameter, d_e, in water at 20°C, with the upper curve corresponding to pure systems, the lower curve to fully contaminated systems, Clift et al. [21].

the considerable scatter in U_T in the surface tension force dominant regime was caused not by differences in surfactant concentration but by the initial displacement experienced by the bubble. Additionally, Ellingsen and Risso [26] showed that if a strong initial perturbation is applied to the bubble surface, it is possible to observe helical motion without any preceding zigzag motion.

Figure 2.3 shows the results of Tomiyama et al. [27], showing the bubble shapes and trajectories in pure and impure systems, for small and large initial deformations. Deformations were caused based on the static pressure difference between the injector nozzle and the elevation of a small container. In pure water, the 3 *mm* diameter bubbles released with a small initial shape deformation experienced a low terminal rise velocity and a zigzag path. When released with a large initial deformation, however, the terminal velocity was higher, with a more helical bubble motion. For the same bubble diameter and large deformation, but in water containing 0.0075% liquid soap, the motion became similar to the pure system with small initial shape deformation. This coincidence was explained by considering that the damping coefficient of a surface tension wave or capillary wave is known to become much larger when surfactants are accumulated on the gas-liquid interface. Thus, for the ellipsoidal regime, the influence of surfactants is to damp the initial displacement, and as such, the oscillations of the bubble. This also has the result of reducing the degree of scatter in the system. The effect of surfactants is more pronounced for larger ellipsoidal bubbles, with the motion in contaminated

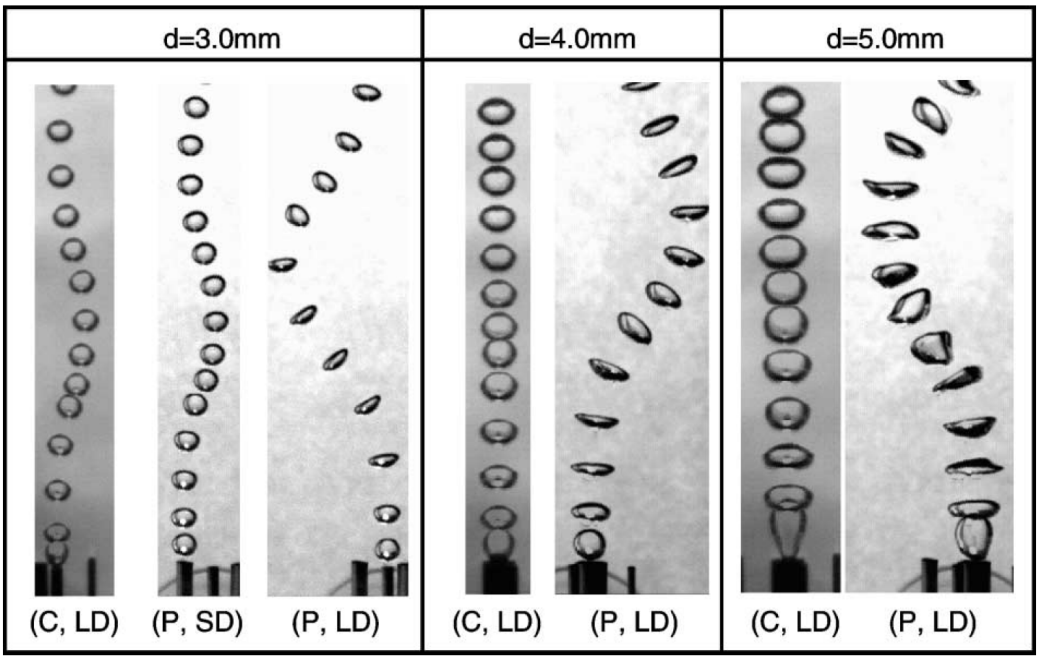

Figure 2.3: Shapes and trajectories of single bubbles in pure (P) and contaminated (C) systems, subject to large initial shape deformations (LD) and small initial shape deformations (SD). The influence of surfactants in the contaminated system is to damp the initial shape deformation, leading to a more rectilinear bubble rise, Tomiyama [27].

water exhibiting almost rectilinear motion and significant shape oscillations. The findings of this work show that, contrary to the opinion of much of the literature, it is not possible to predict a motion type with the only information available being the equivalent diameter and fluid properties; instead, the release mechanism must also be known. In reality, there are few engineering applications that are completely surfactant-free. Practically, problems most often arise when comparing results from the same experimental setup, particularly if the impurities are a direct consequence of the flow measurement technique. The issue of surfactants and the effect on flow measurement will be addressed later in this work.

With this knowledge, it is now worth making an amendment to our initial discussion regarding the comparison of the various correlations derived by different authors. Wallis [29] expressed concern regarding these comparisons, since the initial conditions and the method of presentation can vary. To this extent, the author presented a regime map of dimensionless speed, v^* versus radius, r^* for a single bubble rising in an infinite medium, as shown in figure 2.4. This work showed results for a large variety of systems on a common scale, as opposed to Bhaga and Weber [12], who used aqueous water/glucose solutions. In this

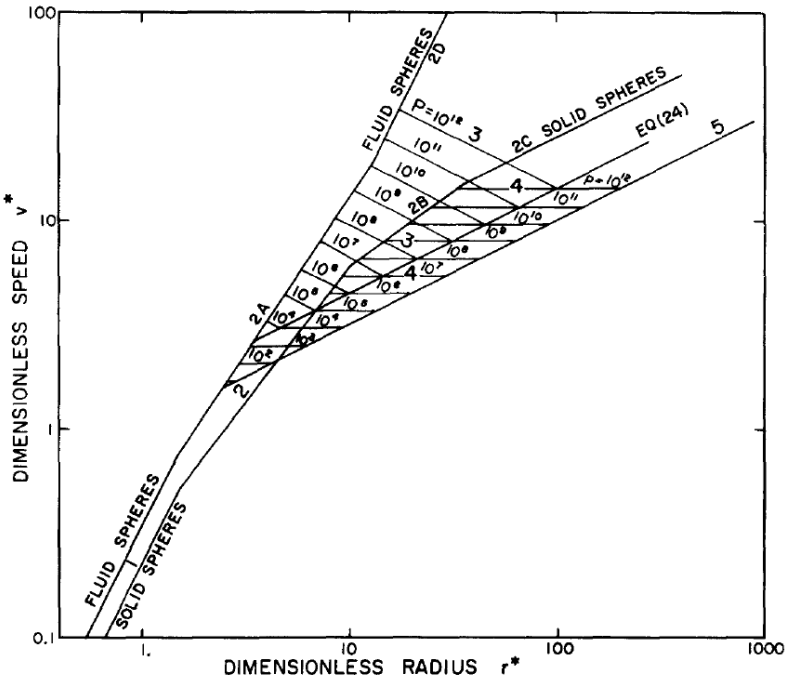

Figure 2.4: Dimensionless velocity, $v^* = v_\infty \left(\frac{\rho_c^2}{\mu_c g \Delta\rho}\right)^{\frac{1}{3}}$ versus dimensionless radius $r^* = r\left(\frac{\rho_c g \Delta\rho}{\mu_c^2}\right)^{\frac{1}{3}}$. The parameter P is the reciprocal of the Morton number. Wallis [29]

map, Willis defined five distinct regimes of bubble behaviour. Note that the parameter P is the reciprocal of the Morton number. Region 1 is creeping flow, where the viscous forces dominate and the bubble interface is spherical. In region 2, the bubbles remain spherical with increasing radius, provided the surface tension is sufficiently large. Eventually, the bubbles are too large to remain spherical (region 3), which is characterised by ellipsoidal bubble shapes, helical bubble paths and an increase in drag. As the bubble radius increases further (region 4), the velocity becomes independent of the bubble size or the fluid viscosity. Finally the largest bubbles (region 5) form spherical cap shapes with a flat base. The rise velocity in this case can be provided by a force balance between the form drag and buoyancy. The author also stressed that bubble motion in regimes 1-3 is heavily influenced by the fluid purity. However, this work provides useful bounds for the terminal bubble velocity, and is a more general case of bubble behaviour to serve a starting point in our later discussion of sliding bubbles.

2.1.2 Wake Structures and Instability

Returning to the Hadamard-Rybczynski formula for a bubble with $Re << 1$, in which the relative motion between the bubble and the surrounding fluid is very small. As such, the fluid flow around the bubble will follow the bubble interface very closely, i.e. the contour of the bubble forms part of a streamline. Now let us increase the Reynolds number. At some critical value, the flow will start to separate from the bubble surface, with the separated streamlines branching off and re-joining some distance downstream of the body, forming a closed region. This closed region is known as the wake, and can also be defined as the region of non-zero vorticity downstream of the body. Strictly, vorticity is a pseudo-vector field Ω, defined as the rotational curl of the flow velocity vector $\overrightarrow{U}$. More practically, the vorticity describes the changes of a local velocity vector when one moves by an infinitesimal distance in a direction perpendicular to it. At this critical value, the wake region consists of a symmetric pair of stationary vortices, often referred to as the recirculation zone. As the Reynolds number increases further, past $Re = 100$, the free shear layers become unstable, leading to the formation of complex flow structures. The following section will look at research on the nature of these structures for a range of rising bubble parameters. To aid in this analysis, wake structures are generally defined in terms of the primary, or near wake, which moves in close association with the bubble, and the secondary, or far wake, which extends downstream. The latter has an open structure and is far less defined, with the possibility of free shear layers and shed vortices from the primary wake being present in this region [13]. It is also difficult to identify the exact boundary between the primary and secondary wake in a quantitative manner.

Consider a bubble injected into a quiescent medium. Shortly after injection, the bubble wake consists of a symmetrical closed laminar region of a toroidal vortex ring, followed by a short tail. As the bubble accelerates, the wake grows in size. At some stage, the symmetry in the wake is broken and some wake material is discharged. As the bubble accelerates, the shape deforms, and vorticity is generated around the bubble edges at the highest rate. High vorticity generation implies a high velocity gradient near the bubble edges, meaning the flow becomes more prone to separation. Additionally, the pressure downstream of a rising bubble cannot be recovered completely, as the pressure defect to the rear of the bubble induces a flow

towards the bubble base, which in turn promotes the tendency for external flow to separate over either side of the bubble. The formation of the bubble wake and the separation from the bubble surface, thus, have a symbiotic relationship. Once flow separation occurs, there must exist a pair of vortical flows to the rear of the bubble (i.e. a recirculation region). Fan and Tsuchiya [13] provided sketches of the different possible types of wakes, which are shown for a spherical cap shaped bubble in figure 2.5 in terms of the two extremes: a closed laminar wake with a stable tail and an open turbulent wake.

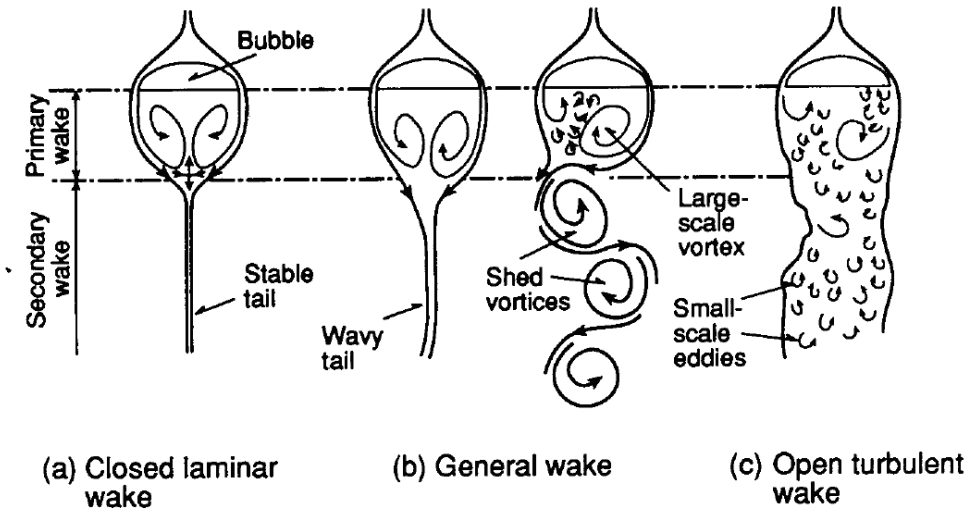

Figure 2.5: Schematic representation of the general wake structure behind a spherical-cap bubble between a closed laminar wake with a stable tail and an open turbulent wake. The primary and secondary wake structures are also provided, Fan & Tsuchiya [13].

Vortex shedding can be either symmetric or asymmetric with respect to the wake central axis, although the latter mode often dominates. For a bubble rising in two-dimensional space, the asymmetry arises mainly from the non-linear interaction between the two vorticity layers emanating from each side and from a disturbance or bias triggered by the external flow. This is analogous to the asymmetry behind a cylinder in cross flow [30]. Fan and Tsuchiya [13] describe this shedding in two dimensions. During the cyclic shedding period, the formation of large scale vortices originates from the separation of the external flow at the bubble edges. This forms a free shear layer, along which the vorticity travels. This vortex sheet tends to roll up into a spiral form due to the pressure defect in the wake region and due to the velocity differences between the outer and inner boundaries of this shear layer. Eventually, the shear layer forms a vortex with a circular cross section. The vortex grows as vorticity continues

to be supplied from the shear layer, and finally becomes strong enough to draw over the opposite shear flow across the wake, thereby removing any further supply of vorticity. The vortex subsequently sheds from the rear of the bubble.

Up to this point, the structures have been considered in two dimensions. Upon expanding into three dimensions, a similarly detailed description of the wake is very difficult, with different ranges of instability occurring over a wide range of Reynolds numbers. These large scale vortical structures have several forms. For ellipsoidal and spherical-cap bubbles, Lindt [31] argued that the periodic change in bubble orientation, and corresponding rotational drag component, meant that the wake configuration should consist of a helical vortex in the near wake. This helical vortex is a three-dimensional extension of the stable two-dimensional von Kárman vortex-street wake, which is the ubiquitous repeating pattern of swirling vortices caused by unsteady separation of flow around a bluff body. Although such a structure is unstable in three dimensions, the helical vortex wake has been experimentally found to persist for some time before dissipating. Understanding the flow structures of bluff bodies in three dimensions is of key to this study; as such, section 2.3 is devoted to it. For now, let us make a brief detour into bluff body flow behind a solid sphere in cross flow, as studied by Achenbach [32], who used visualisation experiments at $Re = 400 - 3000$. These revealed an apparently helical discharge of vorticity from one direction, with a discharge of vortex loops perpendicular to this. This is shown schematically in figure 2.6 for two mutually perpendicular planes, with the direction of vorticity indicated by the arrows. This series of interconnected loops is commonly referred to as a *hairpin*, or horseshoe vortex. Fan and Tsuchiya [13] claimed that for ellipsoidal bubbles, the three-dimensional wake structure is likely some form of helical vortex in the near wake, with the possibility of shed loops further downstream of the bubble.

Experimental studies on bubble wakes typically use either visualisation techniques or flow measurement techniques. Fan and Tsuchiya [13] used the former, basing their observations on flows seeded with minute hydrogen bubbles, which provided the basis for their deductions. Lunde and Perkins [24; 33] used photochromic dye to investigate the shape oscillations and motion of rising bubbles. Digital image analysis of bubbles rising in unfiltered water was undertaken with a Reynolds number range of $700 - 1300$. The results revealed a regular oscillation in the bubble shape. The authors were able to identify three frequencies of

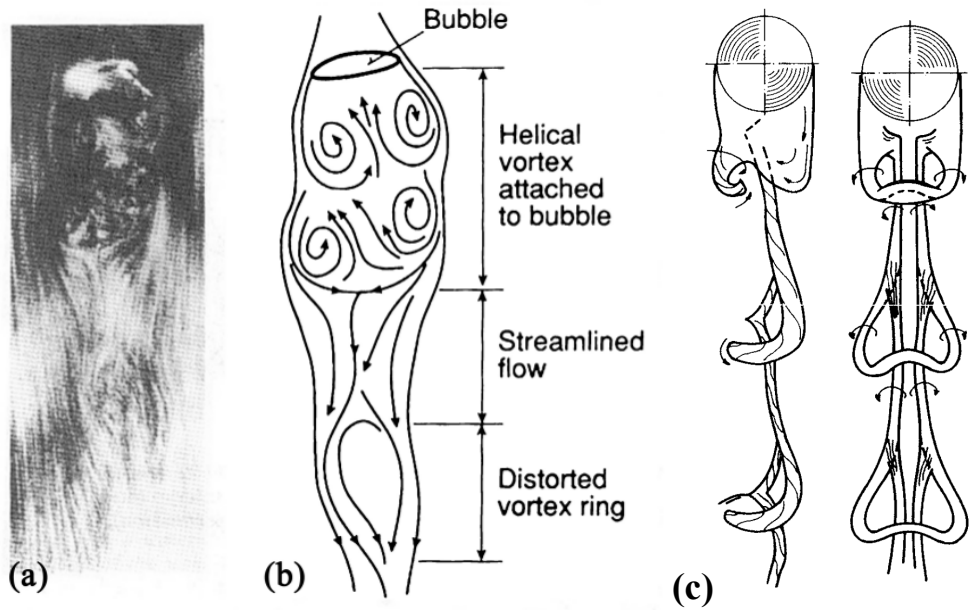

Figure 2.6: (a) Photograph and (b) description of helical vortex attached to a spherical cap bubble in two dimensions, (c) sketches of a proposed “hairpin” three dimensional structure of the wake of a solid sphere at Re = 1000 in two perpendicular planes, adapted from the work of Achenbach [32]. All images taken from Fan & Tsuchiya [13].

oscillation, corresponding to vortex shedding from the bubble and two modes of ellipsoidal harmonics. These harmonics were identified as mode 2,0 (oscillation between oblate (aspect ratio $\chi > 1$) and prolate ($\chi < 1$) shapes) and mode 2,2 (waves travelling around the equator of the bubbles). By analysis of the bubble shape time series, it was discovered that there was a strong interaction between the shape oscillations of mode 2,0 and the bubble path. These low mode shape oscillations can account for both the "wobbling" of oblate spheroids and the "rocking" of spiralling or zigzag bubbles. As the Reynolds number increased, the frequency of both harmonic modes approached that of the vortex shedding of approximately 12 Hz. Using data from Lindt [31], it was found that the vortex shedding became fixed on mode 2,0 for bubbles larger than 4.4 mm in diameter. Sanada et al. [34] used photochromic dye as in Lunde and Perkins, but in this case investigated the wake structures of a single rising nitrogen gas bubble rising in silicone oil solution, in which case the effect of contaminants was negligible. This study was the first to provide experimental support for the existence of a standing eddy behind a clean bubble, which had been predicted previously in the numerical study by Ryskin and Leal [35]. This only occurred in the case of smaller (d_e =2 mm), spherical bubbles. Figure 2.7 shows the elevation and side view of a single rising bubble. It

was found that for a bubble rising in axi-asymmetric motion, a pair of vortex filaments, also referred to as a double-threaded wake, was observed. When the bubble changed direction, a pair of streamwise vortices rotated and changed places with each other. Also observed was the complex formation of multiple hairpin vortices, caused by the instability within the double-threaded vortices. The authors made a point of contention with Lunde & Perkins [33], who had previously stated that a hairpin vortex was formed every time the bubble changed its direction, (i.e. twice in one period of a zigzag motion). Figure 2.7 suggests, however, that vortices were formed not twice but multiple times in one period.

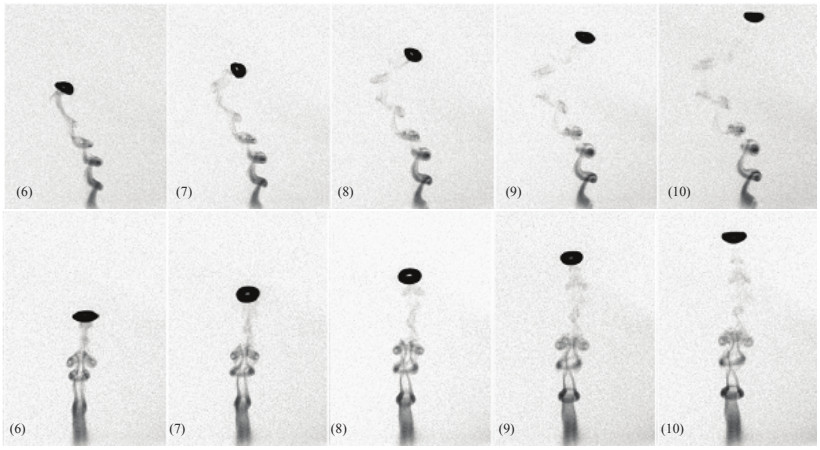

Figure 2.7: Side view of the photochromatic dye observation of multiple hairpin vortices shedding behind a rising bubble, $Re = 330, We = 3$. Each image is separated by 10 ms. Sanada et al. [34].

Schlieren photography is a non-intrusive technique that makes use of the variations in refractive index caused by density gradients of the fluids to create a spatial variation in light intensity [36]. Experiments using Schlieren photography do not suffer from the possibility of tracer particles altering flow behaviour, and as such can use highly purified systems. De Vries et al. [37] used this method to visualise the wake of rising bubbles in ultra-purified water. A density gradient in this case was achieved by heating the upper parts of the tank. As the bubble rose, it entrained cold water in its wake, dragging it into the measurement region. A double-threaded wake consisting of a pair of counter-rotating vortex filaments was found to be present whenever the curvature of the bubble path was non-zero. The near wake was found to consist of hairpin-type loops, which were formed and closed each time the bubble passed through the axis of symmetry of the zigzag. The vortex loops were formed and closed when the bubble is at maximum amplitude, i.e. the point furthest away from the centre-line

of the zigzag. As the bubble continues to rise, new components of the wake emerged that caused the bubble to follow a curved path. These results were later built upon by Veldhuis [38], who used stereoscopic Schleiren measurements, provided here in figure 2.8. The bubble wake started as axisymmetric but broke into a double-threaded wake after the initialisation of a path instability. In this case, the bubble shape was found not to be influenced by these initial wake instabilities. This lead the author to propose that the presence of wake oscillations without shape oscillations means the former triggered the latter. Figure 2.8 (b) shows the occurrence of shape oscillations, which creates discrete zones of high vorticity. As with the results of Sanada et al. [34], the wake appeared to consist of multiple hairpin vortices in each period.

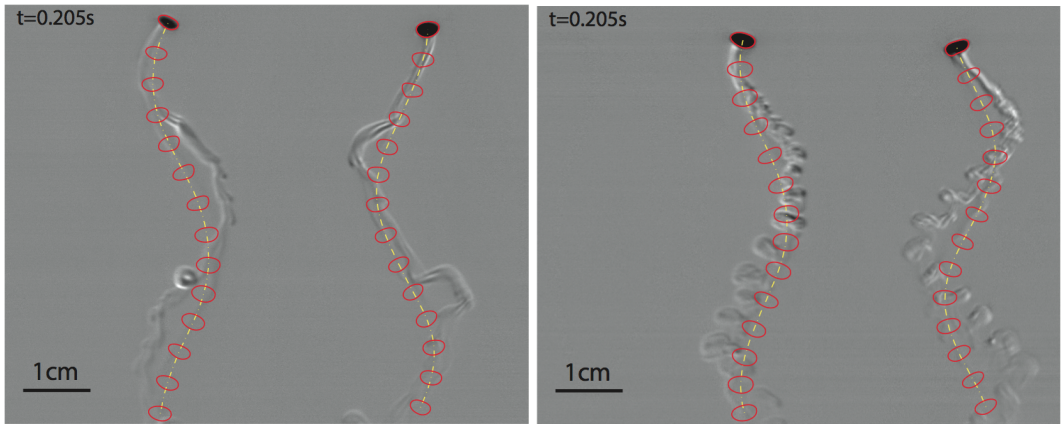

Figure 2.8: Stereoscopic Schlieren images of rising bubbles. The yellow line denotes the path, the red circles the shape every 0.64s. The elapsed time between first and last bubble shape is 0.205s. The equivalent diameters are (a) 2.5 and (b) 2.8 mm. Veldhuis et al. [38].

Brücker [39] performed Particle Image Velocimetry (PIV) on the wakes of freely rising bubbles. The experiments were performed in counterflow conditions, which kept the bubble stationary in the y-direction and hence within the interrogation window. Bubble diameters ranging from 4-8 mm were investigated, and a 200 Hz frame rate was deemed sufficient to capture the full wake structures. Measurements of the rise velocity of the bubbles revealed that they behaved as in a contaminated system, with slightly lower velocity magnitudes. Fluid flow velocity was measured in planes parallel and perpendicular to the bubble flow direction. The latter is shown in figure 2.9 (a), acquired in a plane 10 mm downstream of the bubble. The flow field in this cross section showed the alternate generation of a pair of counter-rotating vortices close to the bubble base. For the parallel plane, shown in figure 2.9

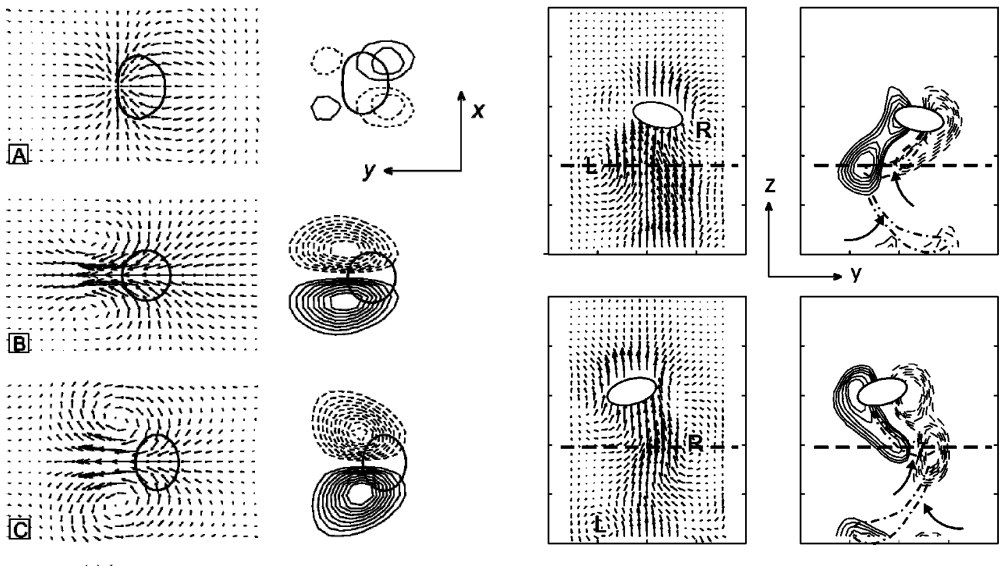

Figure 2.9: (a) Evolution of the velocity field and streamwise vorticity distribution in a horizontal plane 1 cm downstream of the bubble, (b) flow field in a vertical plane through the wake of a rocking bubble, with the counterflow subtracted from the vector field. In both cases, the vector plots are the fluid velocity, while the contour plots are vorticity, Brücker [39].

(b), regions of concentrated vorticity were observed at the locations of maximum surface curvature of the bubble, i.e. at the major axis edges. The region denoted as “L” on this figure indicated a cross section of a head of a shed hairpin vortex pointing to the left.

By combining information acquired in two 2-D planes, the author deduced the structures in three dimensions, with the accompanying sketches shown in figure 2.10 (a). Brücker [39] claimed that the wake of bubbles within this Reynolds number range consisted of a chain of vortex loops of alternate circulation and orientation. These hairpin vortices composed of two streamwise vortex filaments or "legs", connected at the upper end by a vortex “head” and at the bottom by a vortex “tail” to form a closed contour. From this model, the zigzagging motion can be explained by the shedding of the hairpin vortex head, with the interaction between the circulation around the bubble periphery and the free stream velocity generating a transversal lift. The zigzagging bubble motion was coupled to a regular generation and discharge of alternate, oppositely oriented hairpin vortices. Associated with this wake oscillation was a strong asymmetric deformation in the equatorial plane of the bubble, which occurred at the inversion points of the zigzag path. The author claimed that azimuthal deformation along the bubble equator was caused by an uneven pressure distribution at the inversion points,

which in turn was caused by the shedding of vortices from the bubble base. Two frequency modes were identified: the aforementioned vortex shedding mode, and a secondary, "weak" wake oscillation. It was hypothesised that this weak mode may have been by capillary waves travelling from the front stagnation point to the rear stagnation point of the bubble. Delauré et al. [40] performed a qualitative analysis of the work of Brücker [39], explaining that the self-induction of the opposite circulating vortices on either side ideally led to a wake pattern that extended downwards, with successive hairpin vortices forming a vortex chain, as visible in the sketch in figure 2.10 (a). However, by considering the work of Lunde & Perkins [33], the authors suggested that rather than forming a long chain, vortices quickly evolved to generate a complex flow structure. This could have resulted from the non-uniform self-induction effects distorting the hairpin vortex unevenly.

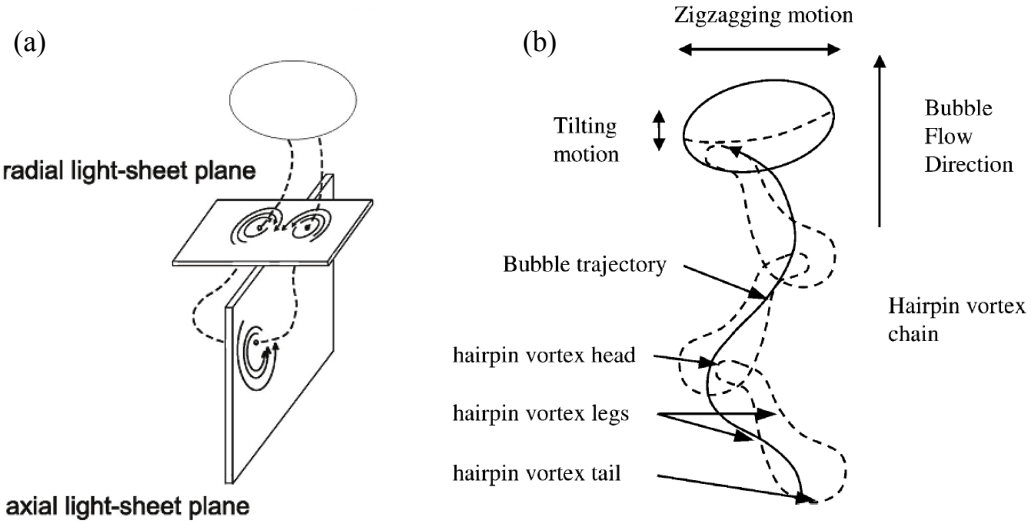

Figure 2.10: (a) Schematic showing projection of flow structures onto the PIV planes tested from Brücker [39], (b) schematic diagram of the interconnected vortex chain formed by the shedding of hairpin vortices from a freely rising ellipsoidal bubble, interpreted from (a) by Delauré et al. [40].

The work of Zenit & Magnaudet [41] is key to the PIV approach adopted in the current study. For their experiments, the authors looked at a perpendicular plane downstream of a rising oscillating bubble in silicon oil, with the bubble velocity and shape found to be virtually unaffected by the presence of tracer particles. The authors noted the appearance of two swirling regions of vorticity in this plane downstream of the bubble, which in time moved, reducing in strength. The authors were able to reconstruct the 3-D structure of the wake to the rear of the bubble by converting the vorticity a different time instances into

the flow at different streamwise distances z, given by $z = U_b N_i f$, where N_i and f were the image number and frame-rate respectively. Although this Lagrangian approach was only an approximation, it provided extremely useful visualisation data. These are shown in figure 2.11 for two isosurfaces of vorticity at two different views of the same flow. Immediately apparent from this figure should be the strength of PIV at providing flow information, in this case relating to two counter-rotating tubes of streamwise vorticity that stretched up to 7 diameters downstream of the bubble. The authors were also able to calculate the lift and drag forces from the bubble wake itself, based on the circulation theory developed by De Vries [37] and adopted by Veldhuis [42].

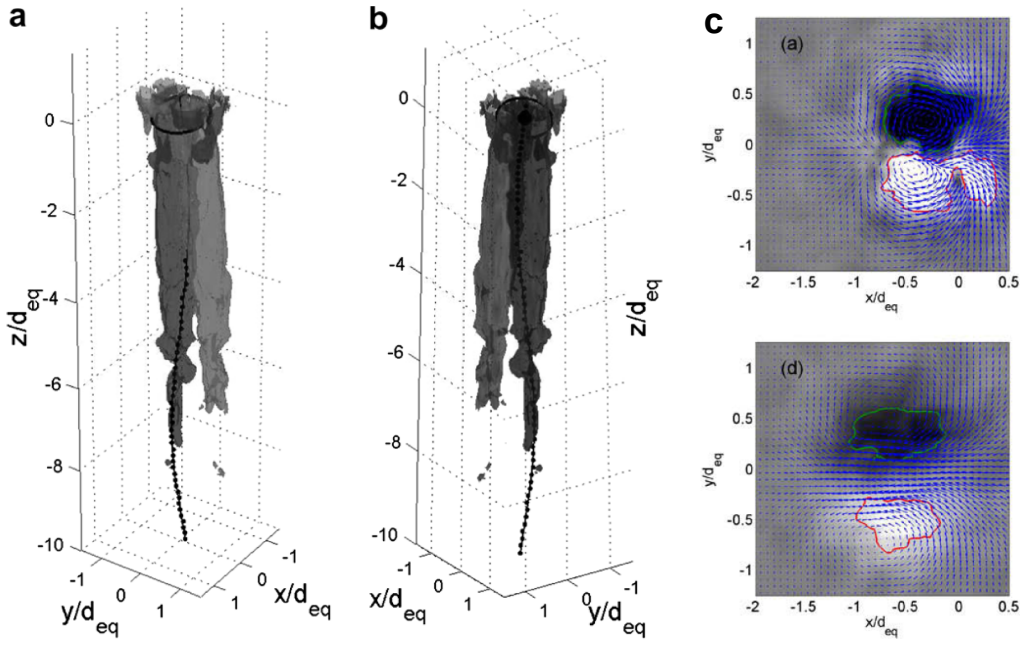

Figure 2.11: (a,b) Reconstructed isovorticity surfaces showing double counter-rotating tubes of vorticity, (c) velocity vectors (arrows) and vorticity fields (gray level), at dimensionless times $t^* = \frac{t}{U_b/d_e} = 1$ and 4. Zenit & Magnaudet [41].

When examining numerical studies on bubble wake structures, it is important to consider the model being applied. Mougin & Magnaudet [43] investigated wake instability by taking a numerical approach, first considering the bubble as a spheroidal body of fixed shape, and subsequently solving the coupled fluid-body problem. The 3-D Navier-Stokes equations were solved for a large domain of fluid surrounding a spherical bubble and were coupled with the force and torque balances that determine the motion of the bubble. The spiral path discussed in section 2.1 consequently emerged as the most stable configuration, as it allowed vorticity

to be shed with the greatest efficiency. Mougin & Magnaudet [44] later expanded this study, showing that the bubble transitioning from a straight to a planar zigzag path corresponded to the first bifurcation of the system, which broke the axial symmetry of the initial wake. The subsequent transition from a zigzag to spiral path corresponded to a second bifurcation, which resulted in the planar symmetry being broken. This was also reported by Jenny et al. [45] for a bluff sphere. It was found that as soon as the wake transitioned to a three-dimensional structure, a lateral lift force of magnitude similar to that of the buoyancy force was observed perpendicular to the rise direction. Cano-Lozano et al. [46] found the real bubble shapes from axisymmetric numerical simulations and imported these into a full 3-D flow simulation. The onset of instability was in agreement with the simulations of Magnaudet & Eames [25] and the experimental results of Zenit & Magnaudet [41]. The authors found that the net effect of instability was to induce the development of a counter rotating vortex pair in the recirculation region, which triggered the zigzag behaviour. The degree of fore and aft asymmetry of the bubble and the corresponding increase in maximum curvature were identified as the crucial parameters in the production of vorticity.

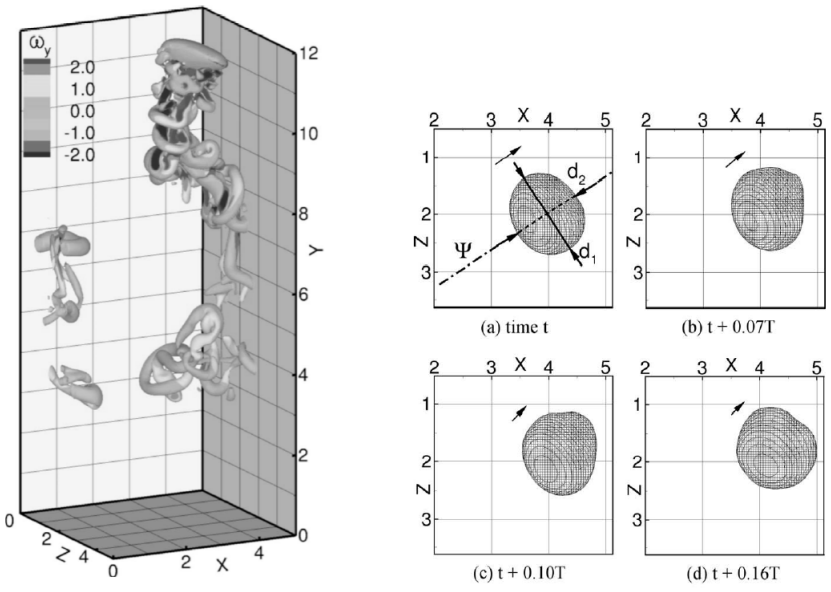

Figure 2.12: (a) Wake of a zigzagging bubble at time t, with vortex structures shown as an isosurface ∇_2, shaded by vertical vorticity, (b) top views of a zigzagging bubble, starting at the same time t as in (a). Note that the bubble is asymmetric about its major axis. Gaudlitz & Adams [47].

Gaudlitz and Adams [47] performed a numerical study on the unsteady wake of a zigzagging bubble of $d_e = 5.2\ mm$ using the hybrid particle-level-set (HPLS) method proposed by

Enright et al. [48]. The choice of parameters chosen to facilitate comparison with the work of Brücker [39]. The numerical simulation showed the presence of periodically shed hairpin vortices in the bubble wake, with a chain of up to four connected vortices observed, as shown in figure 2.12 (a). Interestingly, this is in agreement with Veldhuis et al. [38] but not with Brücker [39], who found only a single hairpin vortex at the base of the bubble. Differences between the results of the simulation and that of Brücker [39] and Lunde & Perkins [33] were attributed to the influence of surfactants in such experiments, with the authors noting that agreement was achieved with the work of Veldhuis et al. [38], who used highly purified water in their experiments. In the simulations, the vortex chains became twisted, possibly indicating the transition from a zigzag to a spiralling rise path. The ellipsoidal bubble shape was found to experience 2,2-mode shape oscillations. The results indicated the formation of a new hairpin vortex caused a local bulging of the bubble, which in turn was reduced by surface tension and formed two surface waves. These were found to travel circumferentially in opposite directions around the bubble, interfering with each other. The authors claimed this superposition of waves could be what was causing the periodically asymmetric bubble shape seen both in experiments and in figure 2.12 (b).

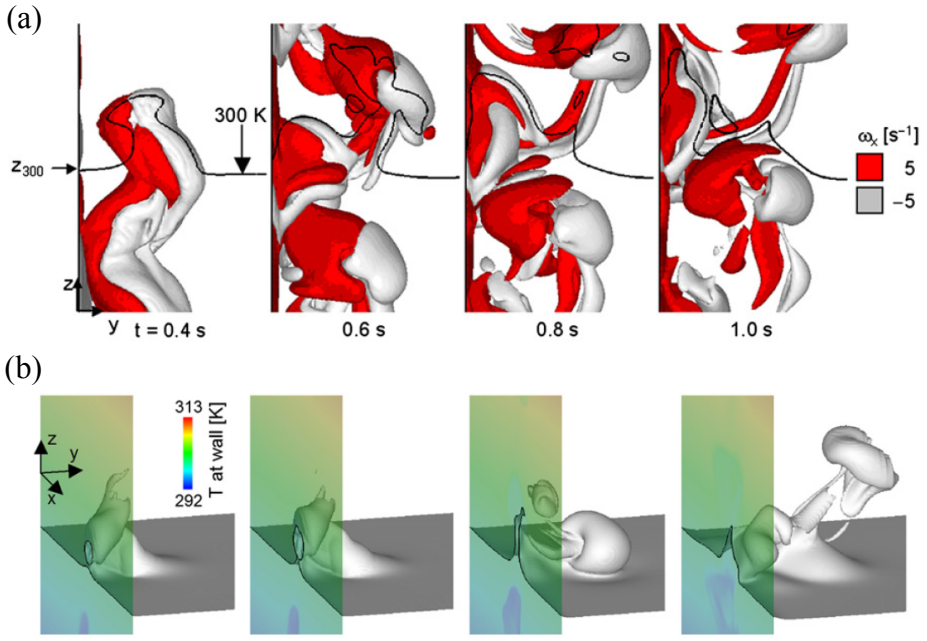

Figure 2.13: (a) Wake of a 6 *mm* bubble impacting a wall, with vortex structures shown as isosurfaces of vorticity, (b) predicted iso-temperature surfaces for a typical interaction process. Zun et al. [49]

Zun et al. [49] studied the bubble-induced liquid motion of a thermally stratified water

layer. The bubble wake structures were studied numerically using a 3D interface tracking simulation. The results indicated a long, open wake region formed along the fluctuating bubble path. A set of vortex rings were observed, which the authors referred to as "Omega"-shaped but which are consistent with hairpin vortex loops. These vortex rings were linked together in the near wake. The coherent self-induction of these vortex rings was found to lead to more complex patterns in the far wake, with a loss in the coherence of the vortex chain downstream. Significant fluid mixing was observed in both the longitudinal and transverse directions, which led to alterations in the wall temperature. Figure 2.13 shows the process of a collision between these hairpin vortices and a wall. Furthermore, the wall temperature corresponding to a typical wake impact is also shown. The time scale of this mixing was found to be large due to the long lifetime of the bubble wake. The wake impact on the wall was found to vary temporally, since the wake structures evolved in time. The characteristic time scale of heat transfer enhancement of approximately 8 seconds was considerably greater than that of the bubble passage. This is shown in figure 2.14 (b) for different average bubble centre distances from the wall.

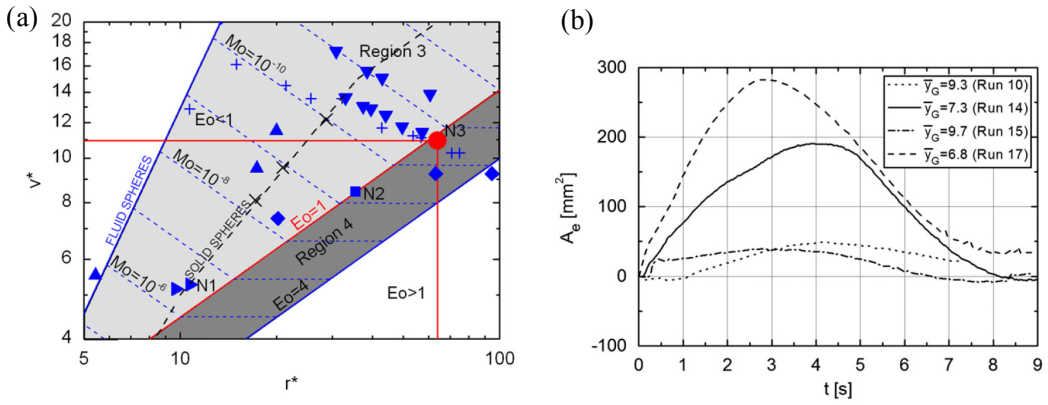

Figure 2.14: (a) Expansion of map in figure 2.4 showing simulations of Zun et al. [49] (N1,N2,N3), where the experiments of Brücker [39] ■ and Veldhuis et al. [50]. ▼ are also shown. (b) Measured evolution of the entrainment capacity A_e, which is the deflection of an isotherm caused by bubble agitation. Zun et al. [49]

In the same work, Zun et al. [49] also updated the terminal velocity plot of Wallis [29] with more recent experimental data. The regions 1-4 from figure 2.4 are visible on this plot. The authors claimed fluid structures observed in their simulations (marked N2 and N3 on figure 2.14 (a)) corresponded to the onset of region 4 motion, for which the terminal velocity was independent of the bubble volume. This was support by the Schlieren experiments of

Veldhuis et al. [50].

2.1.3 Interacting Bubbles

In reality, many bubbly flows will involve more than a single bubble, wherein the wake plays a key role. In such systems, understanding the fundamental mechanisms of these interactions is of great importance to determine process efficiency and optimisation. Extensive numerical and experimental work has focused on interacting rising bubbles, from a single bubble pair to large swarms. This section will draw from both of these to provide insight into the physics of these interactions and the effect of the wake on a trailing bubble.

As was the case for single bubbles, the key reference for interacting bubbles is that of Fan & Tsuchiya [13]. Based on experimental observations, bubbles were found to interact through the following steps: (1) vertical alignment of both bubbles along the same axis; (2) acceleration and elongation of the trailing bubble; (3) the trailing bubble overtaking the leading one; and (4) either a collision of both bubbles, or coalescence due to the draining of the liquid film between the bubbles. Thus, the wake is responsible for the bubble-bubble interactions (1-3). Tsuchiya et al. [51] visually studied in-line bubble-bubble interactions in two-dimensional liquid-solid fluidised beds, determining that coalescence could be due to suction of the trailing bubble into the primary wake of the leading bubble, with this driven by the pressure defect in the primary wake. This means that the initial interaction between bubble and wake is of importance, as it determines the future bubble behaviour. Additionally, at any one time in a bubble swarm it is likely that many the bubbles are interacting with the wake of another. Figure 2.15 shows the results of Tsuchiya et al. [51], with the bubble paths highlighted for clarity. In this case, the bubble shed a series of vortices in an alternating manner, creating a snake-like liquid flow pattern downstream of the leading bubble. This liquid enhanced the zigzag motion of the trailing bubble. When the distance between these bubbles relative to the breadth of the first bubble, i.e. (L_b/b), was small, the trailing bubble accelerated and became profoundly elongated, before colliding with the leading bubble. For bubbles with unsteady wakes, the extent of this interaction depended on (L_b/b), with bubbles within a critical distance of $(L_b/b) = 5-7$ being affected by the leading bubble wake. At this critical distance, a gradual acceleration started beneath the bubble base, with a rapid

acceleration and large shape elongation when the bubble entered the leading bubble primary wake. When the trailing bubble entered the primary wake of the leading bubble, the structure of the primary wake was disturbed, although its size did not change significantly. For a side-by-side bubble pair, the free shear layers interfered with each other, and rolled up to form a large-scale vortical structure. The structure of a side-by-side bubble pair bore similarity to the wake behind a single plate, as studied by Hayashi et al. [52], amongst others.

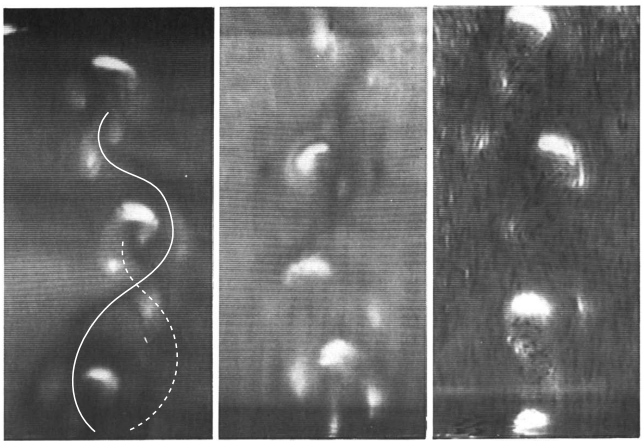

Figure 2.15: Interacting rising bubbles in a two-dimensional liquid-solid fluidised bed with glass beads of 460 and 774 μm and 1.5 mm acetate particles, with the first image modified to show the leading and trailing bubble paths, Tsuchiya et al. [51].

Brücker [39] also performed experiments with interacting rising bubbles in cross flow. In all experiments, the trailing bubble was first captured in the wake of the leading bubble, and thereafter accelerated until it collided with the leading bubble. The position of both bubbles with respect to time is shown in figure 2.16. By comparing the regions marked as A, A^* etc. with the corresponding locations of the trailing bubble wake structure in figure 2.16, along with the flow field induced by the leading hairpin vortex at this point shown by the arrows, it was possible to correlate the bubble wake with the bubble interaction. For instance, in the first capture cycle denoted as A, the bubble was captured from the side and was accelerated, but was then decelerated after the release of the head of the next hairpin vortex from the leading bubble (A^*). Hence, the acceleration and deceleration phase of the trailing bubble was coupled in time to the passing of the head of a shed hairpin vortex from the leading bubble, with the flow being accelerated in front of the approaching vortex ring and decelerated behind it. The trailing bubble essentially followed a series of "jumps" from one hairpin vortex to the

next, until the final wake capture wherein it was continuously accelerated. Bubble collision resulted in a considerable enlargement of the wake region for a short time period, which indicated the amplification of turbulent energy production by the collision process. In three dimensions, the wake capture process depended on the location at which the trailing bubble laterally approached the wake of the leading bubble, as well as to whether the bubble was to be captured or decelerated.

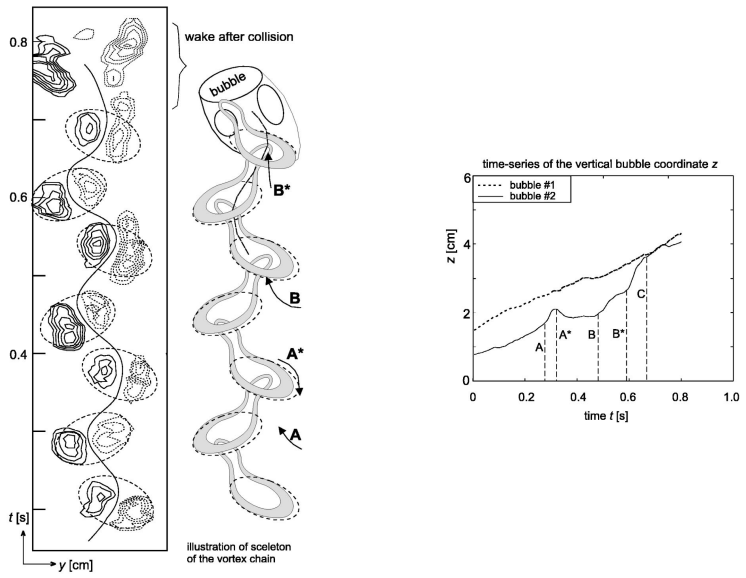

Figure 2.16: Illustration of hairpin vortex chain shed by a trailing bubble in counterflow, with the direction at A and B corresponding to the induced flow by the leading bubble hairpin vortex (left), corresponding time-series of the vertical bubble co-ordinate, z, with the times A, B etc. marked (right). Brücker [39].

Stewart [53] carried out an experimental study on the interaction between freely rising ellipsoidal bubbles in low viscosity aqueous sugar solutions. Pulsed swarms of $10-20$ bubbles of diameters ranging from $6.5-12.8$ *mm* were released simultaneously from a circular plate and recorded with a high-speed camera. The author found that the leading bubble wake was the sole mechanism for bubble interaction, with all coalescence or breakup events occurring after an initial wake capture. The first indication that a trailing bubble entered the leader's wake was a disturbance in the trailing bubble wobble pattern, which took place approximately 6 equivalent diameters behind the leader, consistent with the previous findings of Tsuchiya [51]. Once captured in the wake, the trailing bubble was accelerated, and subsequently overtook the leader bubble in a series of jumps, as in Brücker [39]. The initial

collision, where the trailing bubble pushed past the leader and slightly ahead of it, lasted only a fraction of a wobble period, approximately 0.1 s. After collision, the bubbles could take two different configurations depending on their paths and velocity: either separating with no further interaction or "dancing" together for a short period, wherein the leading and trailing bubbles swapped positions several times. After this, the bubbles were found to either drift apart, coalesce or break up. The wake capture process transferred mechanical energy from the bubble to the liquid more rapidly than with independent rising bubbles, again implying a large amplification of turbulent energy production. For the range of dimensionless parameters tested, Stewart noted that the two bubbles never coalesce during the initial collision. When several bubbles were captured in the wake of another, they formed clusters, which were found to trade places in a "leapfrog" manner. There exists a large body of work for these bubble clusters, in which fluid properties and surfactants play a key role in determining the system behaviour.

The factors influencing bubble coalescence were discussed by Horn et al. [54]. The authors explained that the reason bubbles coalesce is a natural tendency to reduce their combined interfacial area against the continuous phase; however, this is resisted by both the finite time it takes to remove the liquid between two bubbles as they approach and the repulsive forces acting between the two bubble surfaces. Thus, the probability of whether coalescence occurs is a function of the time taken for the film to drain and the time the bubbles are in close proximity, with slow drainage leading to bubbles bouncing apart. Additionally, the difference between the aforementioned repulsive forces and the attractive Van der Waals' forces determines whether the bubbles coalesce. The authors found that when the bubbles were very close, they could become dimpled by hydrodynamic forces. A simplified model for coalescence was developed by Chesters & Hofman [55], who considered coalescence for inviscid liquids. With no viscosity, collisions were elastic, and a recovery of kinetic energy before coalescence caused bubbles to bounce apart. It follows that this was more likely to occur at high approach speeds. Chesters and Hofman [55] estimated that bubbles should bounce apart if the approach speed exceeded $\sqrt{\sigma/2\rho R}$, where σ is the surface tension of the liquid, ρ the liquid density and R the radius of curvature. Although this model is simplified, it is in fact consistent with many experimental measurements, particularly at high Reynolds number. Bubble interactions and coalescence were also studied by Broder & Sommerfield

[56], who performed experiments on turbulent bubbly flow in a double loop reactor. It was found that the coalescence rate was an order of magnitude less than the overall collision rate. Bubble coalescence is also a key aspect to nucleate boiling, where a moderate coalescence rate is believed to improve heat transfer. Bonjour et al. [57] characterised the thermal effect of bubble coalescence on nucleate pool boiling from artificial nucleation sites, showing that at moderate heat fluxes, coalescence led to a decrease in bubble frequency. Although coalescence was found to improve the heat transfer coefficient, the highest heat transfer coefficient was observed at an optimal spacing between nucleation sites at which coalescence did not occur.

There exists extensive numerical work on interacting bubbles. Hallez & Legendre [58] performed a numerical study on the interaction between two freely rising bubbles in quiescent fluid for ($50 < Re < 500$). Potential flow was assumed everywhere except at the bubble surface, at which the zero shear stress assumption resulted in an interfacial distribution of vorticity. The relative position between the bubbles was described using both the separating distance and the angle formed between the centreline of the two bubbles and the x-axis. The interaction was found to be the combination of three effects: the potential effect, a viscous correction (also known as Moore's correction) and a wake effect that was observed on both the drag and the transverse forces of the second bubble when located in the wake of the leader. The maximum drag reduction was observed for the in-line configuration, although the stable final position for two rising bubbles was the side-by-side configuration. For the latter, this is not always the case in reality, such as the small bubbles that rise in an-line formation in a glass of champagne. The authors attributed this difference to surfactant contamination. Bunner & Tryggvason [59] performed direct numerical simulation (DNS) on the motion of 27 three-dimensional deformable rising bubbles at low Reynolds numbers ($17 < Re < 26$). This work solved the Navier-Stokes equations using a parallel finite-difference/front-tracking method, which took into account the effects of interface deformation and surface tension. Three different void fractions were used to describe the space occupied by the bubbles relative to the total volume: 2%, 6% and 12%. At 6% void fraction, the bubbles, which were initially homogeneously distributed, formed large-scale wake structures, where bubbles gathered into vertical columns, or streams. This occurred only after the bubbles had risen by approximately 90 bubble diameters. As in Brücker [39], the dynamic interaction process

for any two bubbles was dominated by wake effects. An important observation was that the bubble distribution revealed a preference for pairs of spherical bubbles to be aligned horizontally, while deformed (i.e. ellipsoidal) bubbles tended to become aligned vertically. Deformable bubbles experienced much stronger interactions than spherical bubbles, and thus induced larger velocity fluctuations in the liquid. These fluctuations were much larger in the vertical than in the horizontal direction. Within these stream macrostructures, there was a marked increase in bubble velocity, which was explained by analysing the lift force on the bubbles. For spherical bubbles, the lift force acted perpendicular to the bubbles. However, for deformable bubbles, the generated lift force pointed towards the wake, acting to reinforce the bubble stream. A typical interaction event between two bubbles is shown in figure 2.17.

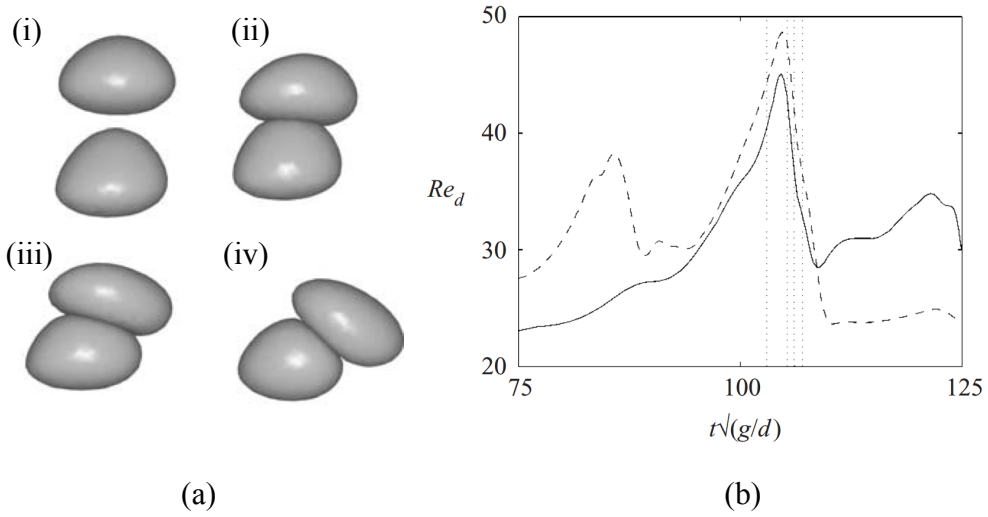

Figure 2.17: (a) Interaction event from two bubbles, of $Eo = 5$, $\alpha = 2\%$ simulation, at times 103, 105.3, 106.1 and 107 seconds from (i) to (iv) respectively, (b) Reynolds number vs time for the leading bubble (solid line) and trailing bubble (dashed line) in the same simulation, in which the above times are shown as the dotted vertical line. Bunner & Tryggvason [59].

For the particular collision shown in figure 2.17, the trailing bubble was accelerated in the wake of a leading bubble until collision, after which it can be seen to push the leading bubble aside. This is what the authors somewhat poetically referred to as the "drafting, kissing and tumbling" process. When the bubbles were close to each other, their rise velocities increased. Upon touching, their rise velocity started to decrease, with the deformation of the leading bubble increasing by approximately 50% as the kinetic energy of the fluid was transformed into surface energy at the bubble interface. The trailing bubble also experienced a minor deformation. After separation, the deformations experienced small under-relaxations,

but no shape oscillations as in Lunde & Perkins [33], as the Reynolds numbers used by Bunner & Tryggvason [59] were far lower. The collision in figure 2.17 is nearly on-axis, and as a result experiences relatively large increases in deformation and rise velocity. Bubbles frequently experience slightly off-axis collisions, which are characterized by smaller increases in deformation and rise velocity. The description of the collision process differed from that of Stewart [53] and Brücker [39] in that the trailing bubble did not experience the observed jumps. This was attributed to the more complex wake structures in the latter cases due to high Reynolds numbers.

2.2 Sliding Bubbles

Up to this point, the bubbles have been rising freely in an unbounded medium. There are many practical applications, however, where the confines of the geometry restrict the motion of the bubble. The first research into these geometries began with tubes in the 1960s. This was motivated in part by physical observations of two phase tube arrays. It was noticed that bubbles generated from the upstream tubes impacted and slid along the downstream tubes, increasing the local heat transfer coefficients. These sliding bubbles maintained the surface temperature below that required for phase change, suppressing boiling [60]. Since then, the field of sliding bubbles has expanded to include other geometries, such as bubble rise under inclined plates. Studies on sliding bubbles typically focus on either the sliding bubble mechanics or the heat transfer enhancement offered, which provides a suitable structure for this section. To date, there has been no study characterising the wake in the same fashion as Brücker [39] did for rising bubbles. It is useful to keep in mind the wake structures discussed in section 2.1.2 when approaching this section, as there are many ways in which sliding and rising bubbles are similar. An important distinction to make at this point is that although sliding bubbles will be discussed in terms of the same dimensionless numbers as were freely rising bubbles, a direct comparison with the regime map of Bhaga and Weber [12] or even that of Wallis [29] is not possible. This is due to two factors. Firstly, the sliding surface itself changes the boundary conditions, with a liquid film also existing between the bubble and surface. Secondly, the initial conditions also change: in almost all cases, bubbles will impact the surface before subsequently sliding.

2.2.1 Sliding Bubble Mechanics

Consider a two-phase flow in a tube, where the gas phase exists as large, bullet-shaped bubbles separated by liquid. "Large" in this case means the bubble volume is such as to fill the diameter of the tube entirely. If the ratio of bubble length to diameter is greater than 1.5, the velocity is independent of bubble length [21]. These bubbles are referred to as slugs, or Taylor bubbles, and have been studied in detail for tubes of circular and square cross-section. In the 1960s, these were expanded to include tubes inclined away from the vertical configuration. For inclined tubes, the bubbles tended to cling to the upper wall, and reached a maximum velocity at an inclination angle of approximately 45°. This was observed for circular tubes by Zukoski [61], who also found that once the Reynolds number exceeded a critical value of $Re = 200$, the propagation rates became largely independent of the viscous forces. The results also showed that as the Eötvös number increased, the Froude number for a vertical tube rapidly approached a limiting value, whereas at inclination it continued to increase. This indicates that bubbles within tubes can reach higher terminal velocity when inclined than when vertical. Maneri & Zuber [62] focused on bubbles in inclined ducts of square cross section, characterising the motion of inclined bubbles into one of three regimes. The first of these was the properties dependent regime, which extended from $\alpha = 0°$ to 60° from the horizontal. In this regime, the bubble velocity was influenced by the duct geometry and the fluid properties, with a rise velocity that was twice that of the vertical case. As α increased up to 80°, there was a transition corresponding to a sharp decrease in rise velocity. Finally, the bubbles reached the inertial dominant regime, ranging from $\alpha = 80°$ to 90° from the horizontal, with a rise velocity similar to the vertical case and independent of the fluid properties.

By the 1990s, bubbles in constricted geometries had been studied for a number of configurations. However, one case that was missing was that of bubble rise under an inclined plate in a large container, which was resolved by Maxworthy [63]. For this configuration, the effects of all of the walls apart from the inclined one could be ignored. Maxworthy [63] used large air bubbles (5 *ml* to 60 *ml*) sliding under an inclined plate in water, obtaining plan and side view images for a large range of inclination angles. Figure 2.18 shows sketches of a plan and side view for a large bubble at $\alpha = 25°$, and a photograph of a 60 *ml* bubble,

also at $\alpha = 25°$, modified to show the radius of curvature. Indeed, the side view photographs showed that large bubbles had a leading edge of essentially constant radius of curvature, for all angles tested.

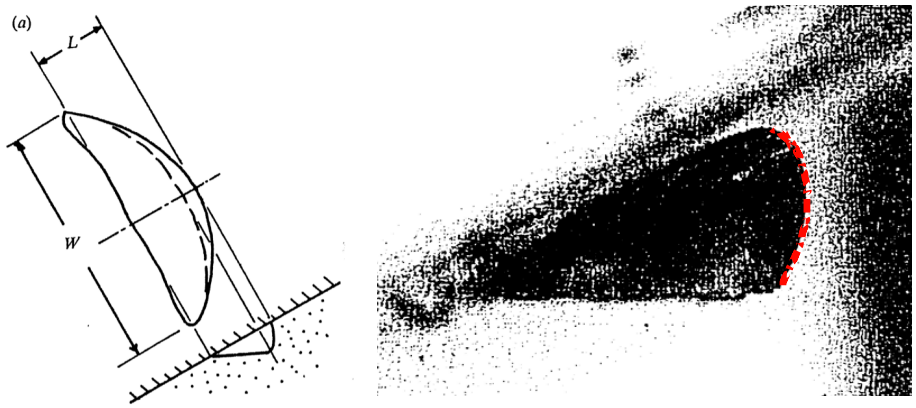

Figure 2.18: (a) Plan and side view sketches of a large sliding bubble at $\alpha = 30°$, (b) side view photograph for $V = 60\ ml$, $\alpha = 25°$, edited to show the leading radius of curvature, Maxworthy [63].

Experimental results were represented in terms of the Froude number, $1 = \frac{U_T}{(gV^{1/3})^{1/2}}$ and the modified Froude number $Fr_2 = \frac{U_T}{(gV^{1/3}sin\alpha)^{1/2}}$, which took into account the surface inclination angle. The drag coefficient was found by equating the buoyancy force and the drag force felt by the bubble, which for a spherical cap bubble is $C_D = 1.65/Fr_1^2$. These parameters are all shown on figure 2.19 (a) for a single bubble volume, although the modified Froude number was shown to remain reasonably constant with increasing volume. A Froude number was constructed using the radius of curvature of the bubble as a length scale, and is shown in figure 2.19 (b). Maxworthy [63] also performed a numerical analysis based on the methods of Davies & Taylor [64], who assumed that the flow over the bubble leading edge was equivalent to that over an oblate spheroid, moving parallel to its circular cross-section. The relation between the ellipticity of this spheroid and the surface inclination angle assumed inviscid, irrotational flow, and constant pressure along the surface of the ellipsoid, meaning that the decrease in static pressure had to be balanced by the increase in hydrostatic pressure. The Davies-Taylor method is only valid when $\alpha = \pi/2$, but the author was able to expand this such that the surface pressure is zero in an integral sense over the whole surface. The ellipticity and resultant Froude number based on this method are also shown in figure 2.19 (b). There was a reasonable agreement between these values and numerical results, suggesting

that the inviscid assumption used was valid. The numerical results matched the experimental values more closely at relatively larger inclination angles, which was attributed to the greater relative effect of surface tension and contact angle effects at low Reynolds numbers.

$$\frac{c^2}{R^2} = \frac{1}{4}\frac{\alpha - \frac{1}{2}sin2\alpha}{(\alpha - sin\alpha) + cot\alpha(1 - cos\alpha)}$$

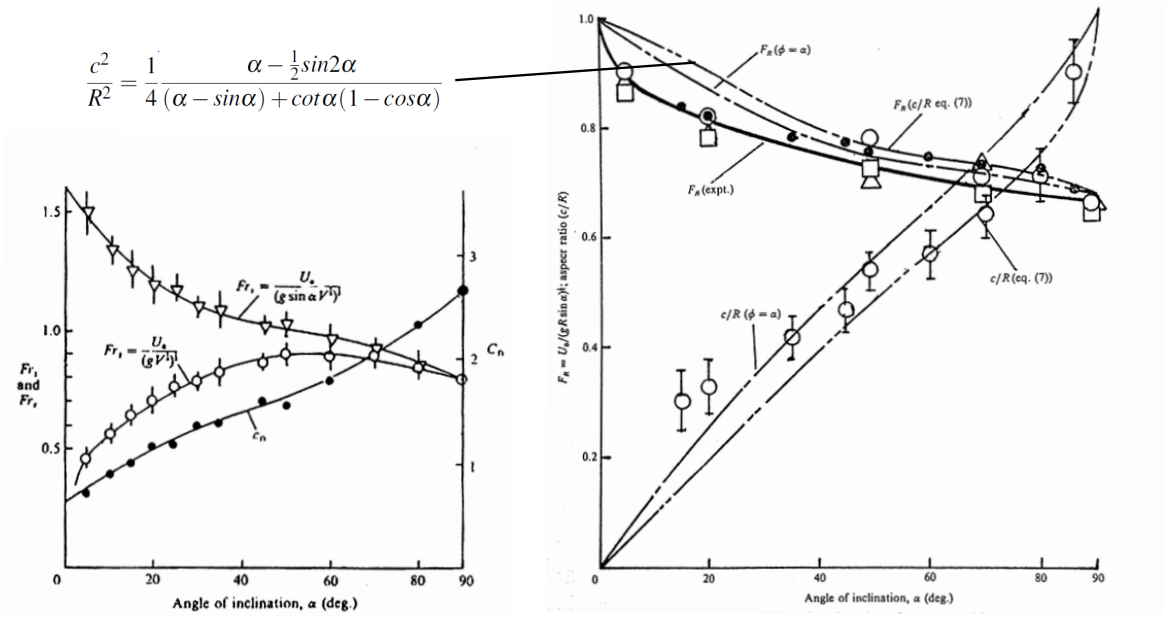

Figure 2.19: (a) Froude number and drag coefficient versus surface inclination angle, α. Fr_1 is the modified Froude number, and takes into account the surface inclination angle. Fr_2 does not. The drag coefficient is calculated from $C_D = \frac{1.65}{Fr_1{}^2}$. (b) Open shapes: Froude number based on radius of curvature. Double-dashed curve: the derived equation for ellipticity. Straight line: experimental results for Froude number. Maxworthy [63].

Tsao and Koch [65] performed experiments on smaller, spherical bubbles of d_e = 1-1.4 *mm* impacting a slanted surface that was oriented at angles between 10° and 85° to the horizontal. After impact, bubbles acted in one of two ways. When the inclination angle α was less than 55°, the bubble slid steadily along the wall, with a shape that was almost spherical but will some deformation against the wall. At these inclination angles and corresponding Reynolds and Weber numbers (45-200 and 0.03-0.4, respectively), it was found empirically that the drag coefficient, C_d could be fit with the curve $100/Re$, in contrast with $C_d = 48/Re$ for a spherical bubble rising in the absence of a wall. The inertial lift force was also calculated, and found to be insufficient to balance the buoyancy force. Instead, the lift force was attributed to the liquid film layer between the bubble and the wall, within which the viscous forces dominate. The authors claimed that viscous lift is capable of balancing the buoyancy force. The authors used a scaling analysis to predicted the thickness of the liquid

film between the bubble and the surface, which was found to be of the order of 10 μm. This was sufficiently thick to dominate the Van der Waals' forces that exist between the bubble and wall; however, it was observed qualitatively that very small inclination angles or bubble volumes lead to the bubbles sticking to the surface rather than sliding. At angles greater than 55°, the bubble bounced repeatedly along the wall, with no observable loss in amplitude after 30 bounces. This would be in contrast with an elastic particle, which with a coefficient of 0.95 would bounce to only 5% of its initial height after 30 bounces. The authors concluded that rather than the energy dissipation being immeasurably small, the bouncing was instead maintained through an energy balance between translational, rotational and deformation modes of bubble motion.

A more recent study by Perron et al. [66] used a plexiglass surface with α between 2° and 10° to the horizontal and bubble volumes varying from 3 to 90 *ml* to quantify the sliding bubble shape regime. The authors showed that the terminal velocity does not increase linearly with volume, instead having distinct regimes, each corresponding to a different shape. These regimes are identified in figure 2.20, and in order of increasing volume are defined as immobile, crawling, semi-rigid, oval oscillating, deformed and bulged. At the lowest Reynolds number for $\alpha = 4°$, the bubbles are immobile, with the in-plane component of the buoyancy force balanced by the difference in contact angles between the upper and lower ends of the bubble. This regime results from the surface inhomogeneities of the sliding surface and possible Van der Waals' forces: that is, if the surface was perfectly smooth, this regime would not exist due to the non-zero component of the buoyancy force acting on the bubble. When the bubble volume was increased, the bubbles were found to move slowly, with strongly attenuated motion. Bubbles in this regime were referred to as crawling bubbles. With a further increase in volume, the wetting film at the bubble nose was penetrated, and the bubbles transitioned to semi-rigid bubbles. These were almost circular in shape, except that the radius of curvature was slightly larger at the nose than the rear. These bubbles experienced minor sinusoidal path oscillations. As the volume was increased, the bubbles became elongated in the direction perpendicular to motion and the periodic shape oscillations became more pronounced. These bubbles are defined as oval oscillating. With further volume increases, the bubbles became deformed, which the authors claimed was caused by the release of asymmetric three-dimensional trailing vortices. At the largest volume, the bubbles formed

two distinct tails on either side, experiencing a near-constant drag coefficient. These were referred to as bulged bubbles. Figure 2.20 shows the latter four regimes (the first two are spherical like the semi-rigid bubbles but smaller), as well as the relationship between both aspect ratio and terminal velocity with bubble volume. Perron et al. [66] also compared the terminal velocity to the experimental data of Chen et al. [67], finding that although the terminal velocity increased with inclination angle, it did not do so linearly. This is because the inclination angle influenced the magnitude of the buoyancy force, which in turn deformed the bubble shape. As before, viscosity and surface tension determined the shape for smaller bubbles, while larger bubbles were dominated by inertial effects.

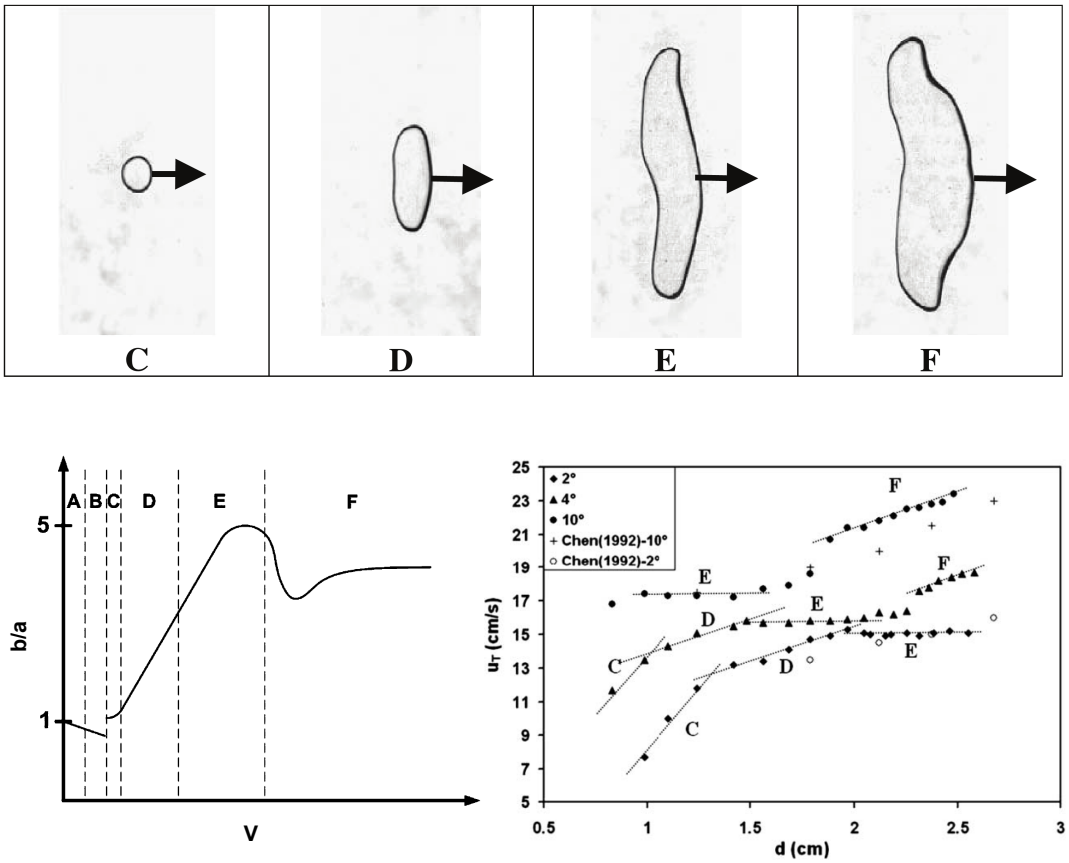

Figure 2.20: Shapes of bubbles moving under an inclined surface with increased volume from left to right. The regions are characterised as (A) - Static, (B) - Crawling, (C) - Semi-regid, (D) - Oval oscillating, (E) - Deformable, (F) - Bulged. (b) Variation of the aspect ratio as a function of the bubble volume at low inclination angle ($\alpha < 10°$). The letters (A) through (F) correspond to the outlined bubble shapes. (c) Bubble terminal velocity versus diameter at low surface inclination angles, with data of Chen et al. [67] provided for comparison, Perron et al. [66].

Perron et al. [66] also performed a force balance on the bubbles, solving for the bubble

drag coefficient by means of a kinematic approach. The authors considered a bubble at terminal velocity and equated the buoyancy and drag forces. These were given by the following expressions:

$$F_b = \Delta\rho V g \sin\alpha \tag{2.1}$$

$$F_d = C_D A_T \frac{\rho_L U_T^2}{2} \tag{2.2}$$

where $\Delta\rho$ is the difference in density between the fluid and bubble, which for air bubbles is $\approx \rho_L$, V is the bubble volume and α the surface inclination angle. The authors considered the frontal area, A_T, through which the bubble contacts the surface, to be circular. While this method allows for the calculation of C_D for comparison between different studies, such an analysis can be problematic from a physical standpoint. This will be discussed in more detail in chapter 5.

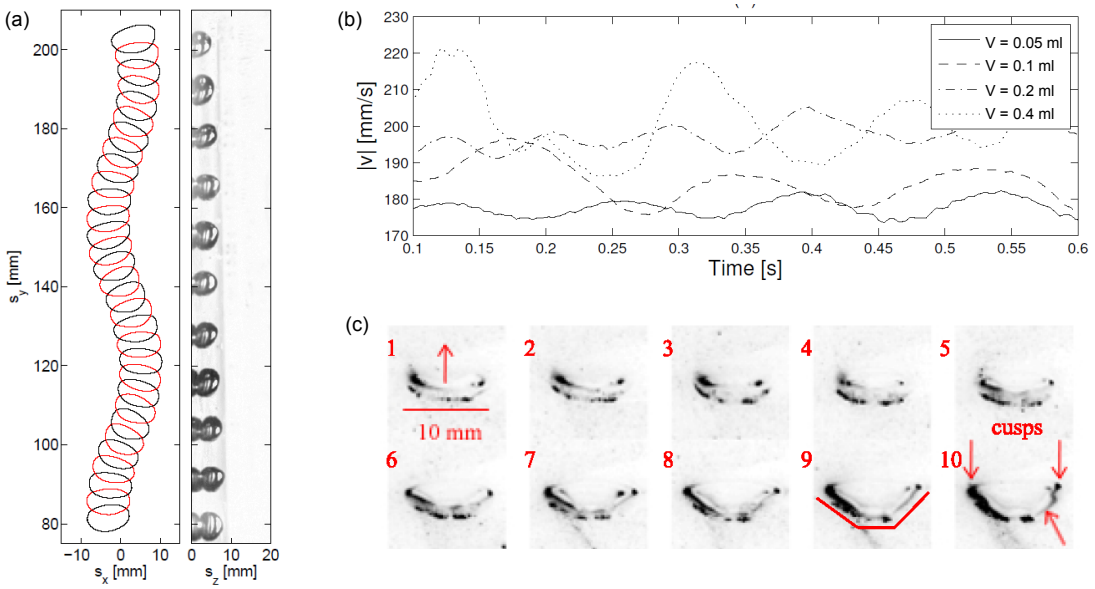

Figure 2.21: Bubble shape and path variations for a heated surface (plan and side view) inclined at 30° to the horizontal for a 7.23 *mm* bubble, (b) bubble velocity versus time for different volumes, (c) sequential images showing large shape oscillations upon the introduction of tracer particles, Donnelly et al. [68].

The current study builds on the work of Donnelly et al. [4; 68; 69], who performed an investigation into the effect of a single air bubble sliding under a heated inclined surface. The experimental rig used was a tilting glass tank, inclined at 30° to the horizontal. Bubbles of

approximately 5-9 *mm* equivalent diameter slid under a thin aluminium foil heated to 32°C, obtaining simultaneous measurements of bubble motion and heat transfer from the surface. It was found that bubbles, which were in the ellipsoidal regime, exhibited sinusoidal path oscillations. The authors attributed this motion to the asymmetrical generation and shedding of vortices, with one vortex shed for each half period of path oscillation, as was found for rising bubbles by Brücker [39]. The bubble shape fluctuations were closely linked to the path oscillations. At larger bubble volumes, there was a loss in planar symmetry along the major axis of the bubble, with a subtle periodic shape oscillation. The bubble interface was also found to recoil sharply back towards the bubble after the bubble reached its maximum x-displacement from the mean, likely due to shedding a vortex. This caused the bubble to change direction. There was found to be little difference in bubble motion for a heated and unheated foil at lower bubble volumes, although the presence of a natural convection thermal boundary layer caused the heated tests to exhibit a greater mean velocity. At higher volumes, a thinning of the bubble tips was observed along with a rougher interface, both of which were attributed to the thermal boundary layer at the surface. The authors also measured parameters such as bubble velocity, ellipticity and force. Interestingly, bubbles were found to occasionally exhibit markedly different behaviour, characterised by the bubble initially rising rectilinearly before experiencing an onset of strong x-velocity fluctuations. This was referred to as the "transitional" mode, and was attributed to the shedding of a large quantity of material from the bubble wake. Another key finding of this study was that the addition of the glass tracer particles required to perform PIV altered the bubble behaviour dramatically. Rather than the sinusoidal path expected, all bubble volumes tested took a rectilinear path, with the bubble shape experiencing dramatic oscillations from oblate to prolate. The bubble velocity was also significantly larger in this case than before. This was attributed to the tracer particles acting as surfactants: however, this contradicted much of the work on freely rising bubbles discussed in section 2.1, which explained the effect of surfactants was to *reduce* the bubble velocity. Additionally, other work in the literature did not face the same problem when performing PIV measurements. Without doubt, the possibility of the flow measurement system fundamentally altering the flow behaviour is a serious issue, and will be addressed in the current study. The key bubble mechanics results from Donnelly et al. [68] are provided in figure 2.21, showing the bubble motion in the plan and side view, the bubble velocity as a

function of time and images of the bubble shape upon the addition of tracer particles.

Debisshop et al. [70] numerically modelled bubbles rising in an inclined channel in two dimensions using a boundary integral method, with and without insoluble surfactant. For the surfactant case, linear and non-linear relationships between surface tension and surfactant concentration were both considered. For a sliding bubble, the surfactants were found to accumulate at the rear of the bubble due to convection along the interface. Thus, the surface tension was less at the rear of the bubble, allowing for a greater deformation of the interface. With increasing surfactant concentration, the bubbles became more elongated and slender. Crucially, for sliding bubbles, the addition of the surfactant was found to *increase* the bubble velocity. This is in agreement with the experiments of Donnelly [68], and is the opposite to the situation for freely rising bubbles. For sliding bubbles, surfactants could also be used to cause otherwise static bubbles to detach from the surface by altering the adhesion or drag forces, which could have applications in dislodging gas microbubbles in cardiac surgery [71].

Delauré et al. [40] extended their qualitative analysis of Brücker's [39] model to include the influence of an inclined surface on the bubble path and dynamics. The authors claimed that for both inclined and vertical walls, the bubble passage was followed by its wake, shedding vortices that were convected upwards. With this shedding, the flow at the surface should experience strong variations both in magnitude and direction. The authors considered the scenario of an ideal hairpin vortex impacting on an inclined surface with its plane of symmetry perpendicular to the surface. In this case, the flow at the surface should be influenced by both streamwise and transversal vortices, i.e. the head and tail of the hairpin vortex should induce vertical flow components of opposite signs. As the hairpin is convected upwards from its head to tail, the induced flow components could tilt successively towards and away from the horizontal direction. The authors admitted that this analysis was idealised, since in reality the shape and strength of the legs of the vortex hairpin are unsteady, and evolve following complex and largely unpredictable patterns as in Lunde and Perkins [24].

Masliyah et al. [72] experimentally measured drag coefficients for freely rising and sliding air bubbles ($d_e = 1.7 - 2.9\ mm$) at small Weber numbers. For rising bubbles, the buoyancy and drag forces were equated to find the general drag coefficient, as shown in figure 2.22 (a). Due to the deformation of the bubble at the wall, the drag coefficient for a sliding bubble could not be characterised in terms of the Reynolds number alone; instead,

the experimental data was collapsed by the Reynolds and Eötvös numbers. This provided an empirical fit for the drag coefficient, given as:

$$C_D = \left(\frac{16}{Re_b}\right)\left[\left(1+0.007Re_b^{0.65}\right)\left(1+1.31\left(Eo\cos\alpha\right)^{0.51}\right)\right] \tag{2.3}$$

which is valid for $Re_b = 0-130$, $Eo = 0.4-1.7$ and $\alpha = 35^\circ - 90^\circ$. Figure 2.22 (b) compares this equation and experimental data to the $16/Re$ relation for creeping flow obtained by boundary layer theory. The authors also found a fore and aft asymmetry of the sliding bubbles; a situation that was not present for a bubble resting on a horizontal surface nor a rigid sphere rising along an inclined surface. As the parameters tested in the current study are outside this defined range, it is not possible to apply this correlation to the current study.

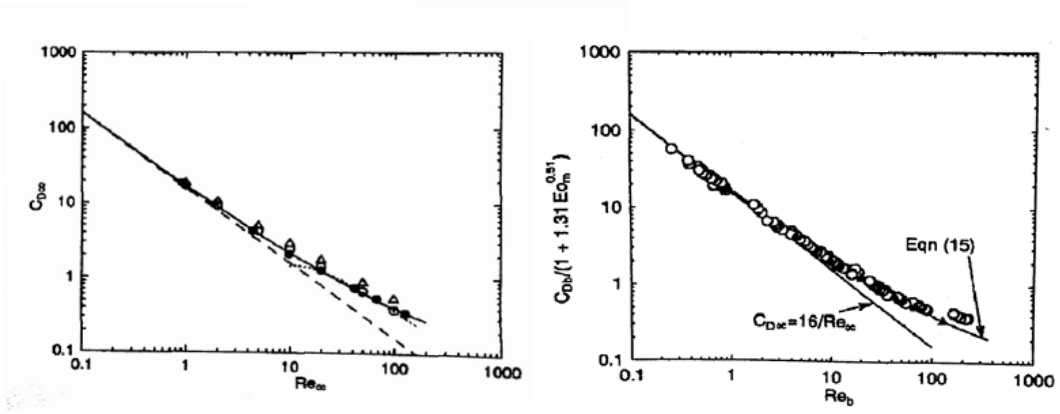

Figure 2.22: (a) Drag coefficient as a function of Reynolds number for freely rising bubbles, (b) drag coefficient as a function of Reynolds number for sliding bubbles, given by equation 2.3, Masliyah et al. [72].

The existence of a liquid film between the bubble and the surface, predicted by boundary layer theory, is well known, and forms an important part of the sliding bubble behaviour. Inside the liquid film, there are two additional types of force that act on the bubble. Del Castillo et al. [73] explained that the first of these are the Van Der Waals' forces that act between the bubble and the surface, causing bubbles to stick at low angles. The second force is the electrical double layer, described by Grahame [74] and Guldbrand et al. [75]. The double layer refers to two parallel layers of charge around the sliding surface. The first layer was found to be the surface charge, consisting of ions adsorbed onto the surface chemically, while the second layer comprised ions attracted to the surface via the Coulomb force. Del Castillo et al. [73] looked at the microscopic Van Der Waals' forces and the electrical double

layer acting in the liquid film by changing the salt concentration of water and aqueous KCl solutions. It was found that there was an electrical double layer repulsion that occurred since both the surface and the air-water interface were negatively charged, which dominated over the Van Der Waals' forces, acting as an additional, disjoining pressure in the liquid film. These forces played a key role at very low inclination angles ($\alpha = 1^\circ - 5^\circ$). Addlesee & Kew [76], [77] predicted the liquid film thickness by assuming a velocity profile polynomial that satisfied the conditions of no slip at the wall, no shear at the free surface and a flow per unit width of the boundary layer at the nose of the bubble. A first estimate of this film thickness is:

$$\delta_f = \sqrt{\frac{vD}{U}} \tag{2.4}$$

The resultant equation for the film thickness required the bubble velocity; for this, the authors used a semi-analytic solution based on the experiments of Maxworthy [63] that also took into account the inclination angle. The authors found that the liquid film thickness was in the range of 200-400 μm for $\alpha < 15^\circ$, with a substantial rise at larger inclination angles. This was close to the empirical findings of Kenning [78]. The results were typically in the range of 200 to 400 μm, although beyond angles of 15° a substantial rise in the thickness was found. This lead the authors to claim that the liquid film thickness was determined by flow phenomena, rather than by heat transfer.

Podvin et al. [79] derived a model based on lubrication theory to describe the interaction of a bubble with an inclined wall. Bubble sizes of $1-2$ mm were studied. The model used was two-dimensional, focusing on the forces in the tangential and transverse directions (i.e. lateral oscillations were ignored). The equations of motion for the bubble centroid were obtained from applying the following force balance:

$$\rho_b V \frac{dU}{dt} = F_{buoyancy} + F_{drag} + F_{addedmass} + F_{history} + F_{wall} \tag{2.5}$$

Some of these terms will come into the force balances being used in chapter 5. Note the use of the history force, also known as the Basset force. Notoriously difficult to implement (i.e. ignored by many models), the Basset term describes the force due to the lagging boundary layer development as the bodies moving through the fluid are accelerated. There is

also an additional wall force, F_{wall}, which the authors claimed acted via an excess pressure exerted on the top of the bubble, which corresponded to a deformation of the interface. The flow between the bubble and the wall is a film, which the authors subsequently solved using lubrication theory, assuming the pressure and velocity were uniform in the liquid film between bubble and surface. This model was then compared to experiments where bubbles of 1.2 - 1.8 *mm* diameter were allowed to reach terminal rising velocity before impacting an inclined surface. As in the case of Tsao and Koch [65], there were three regimes of behaviour. At low angles $(0^\circ - 10^\circ)$, the bubbles bounced 2-3 times before stopping moving, as has been shown by Donoghue et al. [80] for a bubble impacting a horizontal surface. For moderate wall inclinations up to a critical angle $(10^\circ - 55^\circ)$, the bubble slid under the wall at a constant speed. Occasionally in this regime, there was an occurrence of transient bouncing, where the bubbles bounced several times with decreasing amplitude before sliding motion began. Finally, for large wall inclinations > 55°, the bubble experienced steady bouncing of constant amplitude. The model was able to predict the rebound amplitude well, although the drag in the tangential direction was likely under-predicted when the bubble was close to the wall. Figure 2.23 shows the force balance in the normal and tangential directions for a 1.02 *mm* diameter bubble impacting a surface at 45°. Note that in the normal direction, the buoyancy is balanced by the wall force, whereas in the tangential direction, the buoyancy is balanced by drag. In both cases, the added mass force is only significant at the moment of bubble impact. In the tangential direction, the wall force is equal to zero and is hence omitted from the force balance in the current study.

Legendre et al. [81] performed a numerical analysis on a bubble sliding at some initial velocity U_b along a horizontal wall in a liquid at rest to find the lift, drag and added mass coefficients. This involved solving the full Navier-Stokes equations in a boundary-fitted domain, with a no-slip boundary condition at the wall and zero normal velocity and stress on the bubble interface. The authors found the lift coefficient to be inversely proportional to $Re^{0.5}$, which they attributed to the shear generated on the wall by flow moving around the bubble. The drag coefficient in this case was slightly larger than for a freely rising bubble, attributed to the additional dissipation induced by the rigid wall. For Reynolds numbers above 50, the drag for this configuration was found to be controlled by viscous effects. To find the added mass coefficient, the bubble was modelled as having a time-dependent radius

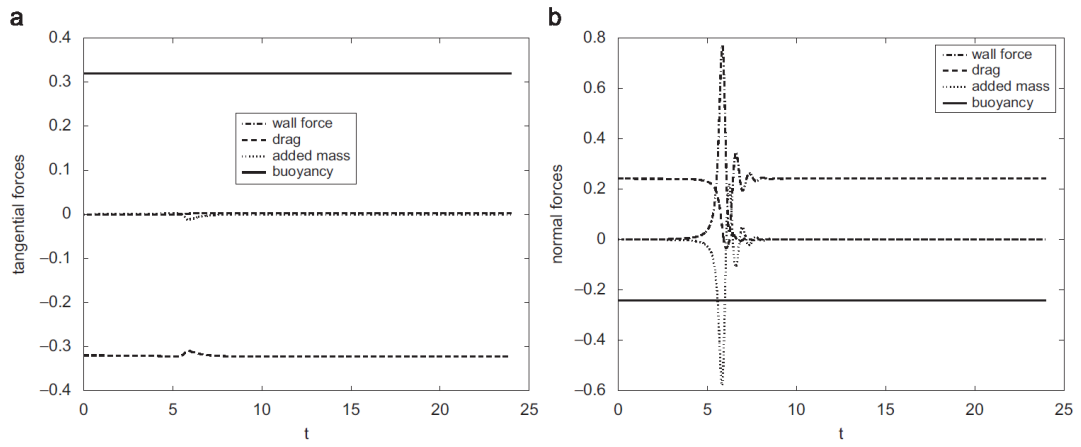

Figure 2.23: Force balance in (a) the tangential direction and (b) the normal direction for a 1.02 *mm* diameter bubble impacting and sliding under a wall inclined at $\alpha = 45°$, Podvin et al. [79].

$r(t)$. It was found that the added mass effect had contributions normal and tangential to the wall, and could be given by potential theory for viscous solutions.

2.2.2 Sliding Bubbles and Heat Transfer

Boiling heat transfer is ubiquitous to many applications, including heat exchangers, manufacturing processes and advanced cooling applications. Boiling is characterised by the formation of vapour bubbles that grow and subsequently detach from the surface, the dynamics of which are complex, depending on parameters such as the excess wall temperature, nature of the surface and the properties of the fluid. If we consider applications such as bubble nucleation on the surface of a horizontal tube (i.e. within a shell-and-tube heat exchanger) or nucleation on a downward-facing surface (as occurs in the production of aluminium), it is clear that the motion of a bubble, be it vapour or gas, disrupts the liquid in the system. This fluid mixing is known to substantially increase local heat transfer coefficients. The precise heat transfer contribution of sliding vapour bubbles is a function of bubble nucleation, detachment from the surface and sliding along or under the surface.

Cornwell [8] studied the influence of bubbly flow on boiling from a tube, with the author splitting the heat transfer coefficient into constituent parts in order to quantify the influence of bubbly flow on heat transfer. That is:

$$h = h_{fc} + h_{sb} + h_{nb} \tag{2.6}$$

where the notional parts are the contribution of forced liquid convection at the local fluid velocity, h_{fc}, the contribution of bubbles that slide along the surface h_{sb} and that of bubbles which nucleate as in pool boiling h_{nb}. The sliding bubble term consisted of two parts: that due to turbulence in the liquid boundary layer and that due to the evaporation of the micro-layer under the bubble. Experiments were performed in a tube bundle heated to provide a mean bundle heat flux, with a test tube that had its own heating setup. To study the constituent parts individually, initial experiments were performed on the test tube at a low heating level, insufficient to generate nucleation. By heating the tube further, the commencement of nucleation could be defined. Separate experiments in single phase liquid conditions allowed for measurement of the forced convective heat transfer coefficient, meaning h_{sb} could be found by subtraction. Cornwell [8] found that the presence of bubbles caused a many-fold increase in heat transfer from the tubes to the liquid. This was found to occur even at low wall superheat, where no nucleation was occurring, with the author postulating that this was due to the bubbles in the flow sliding around the tube. Additionally, even when boiling did occur at higher ΔT values, the heat transfer due to forced convection and sliding bubbles fully accounted for that on the upper tubes, with nucleation suppressed at these locations. This work was extended by Houston & Cornwell [6] to include non-evaporating air bubbles. The same experimental setup as before was used with R113, with air bubbles injected below the tubes. The authors found that bubbly flow turbulence was a prominent mechanism in heat transfer enhancement, and although the evaporation of the bubbles was a major factor in heat transfer enhancement, at low heat fluxes it is not significantly larger than the bubbly flow turbulence. This led the authors to conclude that the heat transfer due to translating bubbles was at least as important as the mechanism within the thermal boundary layer under the bubble. Indeed, the disturbance effects alone accounted for a third of the heat transfer.

Yan et al. [7], and subsequently Kenning & Yan [82], used liquid crystal thermography to investigate the contribution of sliding vapour bubbles to heat transfer, calculating the heat flux and associated heat transfer coefficient by performing an energy balance on a heated wall. Due to the heat input from the surface, the vapour bubble grew in time. By relating this growth to the rate of heat flow into the bubble, the authors found that the heat flux from the wall was insufficient to explain the growth; instead, there had to be some heat flow to the bubble from the surrounding superheated fluid. There was no hot spot observed under the

bubble, which led the authors to assume there existed a continuous layer of liquid beneath the bubble, which is referred to as the liquid micro-layer. The authors analytically estimated the thickness of this layer to be of the order $100 - 200$ microns. The measurements of Kenning & Yan [82] confirmed that the evaporation of this micro-layer was consistent with the cooling of the wall during bubble growth.

In a follow-up study, Yan et al. [83] looked at steam bubbles sliding under an inclined plate at low superheats, using the experimental techniques outlined above. The authors confirmed the existence of a cooled wake region approximately the width of the bubble, with a local heat transfer coefficient of three to five times the undisturbed value. Immediately behind the leading edge, a rapid reduction in wall temperature was observed; however, there remained a region of slightly elevated temperature near the rear edge of the bubble. Temperature distribution plots showed that at moderate surface inclination angles (30°-50°), the cooling effects persisted long after bubble passage, spreading into the bulk fluid and affecting a region 50% wider than the bubble. These effects lasted even after the bubble left the plate. Some occurrences of bubble sticking were observed at the lower surface inclination angle of 15°. For the thin walls required for liquid crystal thermography, the evaporative pre-cooling of the wall beneath the bubble reduced the amount of available ΔT to drive convective heat transfer. This meant that there would be little heat transfer in spite of a large heat transfer coefficient, although this effect is dependent on wall properties, such as thickness (it would be reduced for thicker walls). Experiments with curved surfaces showed that bubbles approaching from below tended to stick to the surface, causing a hot spot by drying out the liquid micro-layer, inducing elevated temperatures. The bubble subsequently grew in size to some critical diameter, at which point it began to slide. In doing so, the bubble took the dry spot with it, which occasionally acted to create unstable nucleation sites across the plate.

Bayazit et al. [84] performed experiments to quantify the heat transfer enhancement offered by a sliding vapour bubble sliding at 12° to the horizontal in FC-87, a dielectric perfluorocarbon fluid. The results showed that the bubble grew rapidly due to evaporation, with the bubble shape changing from hemispherical to a cap shape. Figure 2.24 shows the contour plot of the change in wall temperature, measured using liquid crystal thermography, at two instances after the bubble passing. In these figures, the bubble is moving from left

to right, with the initial wall temperature subtracted. Analysis of these images revealed a triangular thermal wake growing behind the bubble with sharp lateral edges, with the wall temperature not recovering quickly from this thermal depression. At the sharp edges, thin shear layers were observed shedding. The authors claimed these were possibly small-scale vortices shedding from the bubble extrema. As the bubble grew, the size of the wake similarly rescaled. The effect of the sliding bubble was substantial, accounting for a third of the total temperature change between the wall and bulk fluid. The authors also measured the terminal velocity of the bubble, somewhat surprisingly achieving strong agreement with the adiabatic gas bubble results of Maxworthy [63]. Hollingsworth et al. [85] also used liquid crystal thermography measurements of sliding vapour spherical cap bubbles in FC-87, finding the maximum heat transfer coefficients to be of the order of 2.5 kW/m^2K. Such values were found to occur in very sharply peaked curves that moved with the bubble.

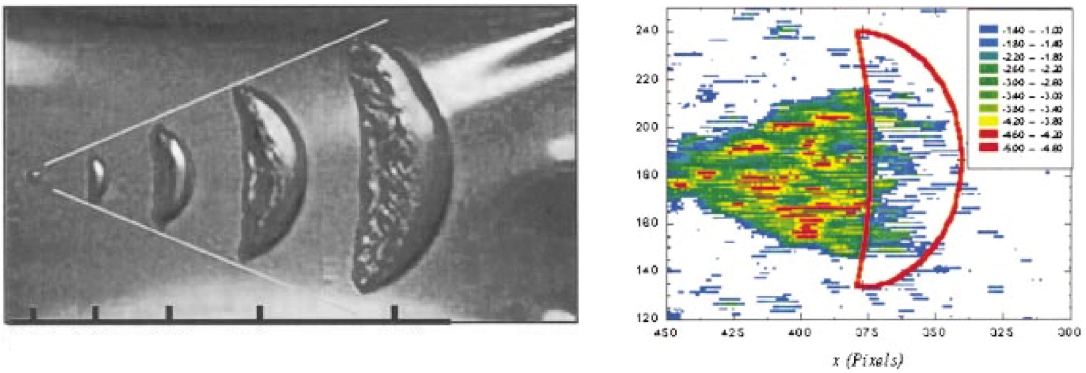

Figure 2.24: (a) Evolution of vapour bubble shape at $\alpha = 12°$, (b) contour plot of the change in wall temperature at 280 ms after the passage of a vapour bubble. The solid red line represents the bubble outline. The original surface temperature is shown in white, blue represents a drop of 1°C, and red a drop of 4°C, Bayazit et al. [84].

Sateesh et al. [86] performed an analysis of pool boiling on non-horizontal surfaces. The authors created a model incorporating different contributions to heat transfer, including microlayer evaporation, transient conduction and natural convection, placing a particular emphasis on sliding bubbles. The authors found that the contributions of the various mechanisms changed over the range of control parameters, which were governed by different fluids, pressures and wall superheats. This model agreed well with experimental results obtained by Wang and Dhir [87] for $\alpha = 90°$ and Barthau and Hahne [88] for a horizontal cylinder. For the surface inclined at 90° in water, it was found that for a low superheat of $5K$, the heat

transfer due to sliding bubbles accounted for half the total heat transfer.

Qiu and Dhir [89] performed an experimental study to find the flow pattern and heat transfer associated with a vapour bubble sliding under a downward facing, heated silicon wafer immersed in working fluid PF-5060. In this work, key to the current study, the authors sought to explain some of the conflicting studies in the literature regarding dry-out, micro-layer thickness and the relative contributions of various mechanisms to heat transfer. To achieve this, the authors used holographic interferometry and PIV to measure the fluid temperature and velocity, respectively, with the polished silicon wafer chosen to remove possible nucleation sites. Meanwhile, separate element heaters along the surface allowed the wall superheat to be maintained at a near-uniform level. At $\alpha < 60^\circ$, the bubble volume increased as the bubble traversed the surface, with the shape changing from spherical to an elongated spheroid. At $\alpha > 60^\circ$, the sliding bubbles reverted to being spherical and initially slid along the surface, before lifting off and striking the surface, subsequently experiencing a "hopping" motion. This lift off meant that the forces that acted to push the bubble towards the wall could not balance the forces lifting it away. As with Maxworthy [63], increasing the inclination angle led to a large sliding velocity. Also observed was a wedge-like liquid gap between bubble and surface for plate angles between 15° and 60°, which seemed to penetrate into the bubble base. The angle of this apparent wedge decreases with increasing bubble volume. At low inclinations ($\alpha < 15^\circ$), the bubble was found to be elongated significantly along its major axis, with the bubble covering the entire width of the baseplate (49 *mm*) at the lowest angles. Values for the film thickness varied from 160 to 64 μm from the front to the back of the bubble, in broad agreement with Kenning et al. [82]. This changing film thickness indicated an increasing temperature gradient across the bubble, with the authors observing new, "fresh" fluid entering the liquid layer as the bubble slid under the surface. This is in contradiction with the findings of Kenning et al. [82], who modelled the conduction as inviscid flow diverting around the bubble base.

The associated flow patterns of the sliding vapour bubble were reported for a near-horizontal and near-vertical case, corresponding to $\alpha = 15^\circ$ and 75°. Measurements were taken at a point 11.5 *mm* downstream of the bubble, at which stage the bubbles were generally large. Holographic interferometry provided visualisation as a series of fringe patterns, shown in figure 2.25 (a) for a bubble at $\alpha = 15^\circ$ with a low wall superheat and low liquid subcooling.

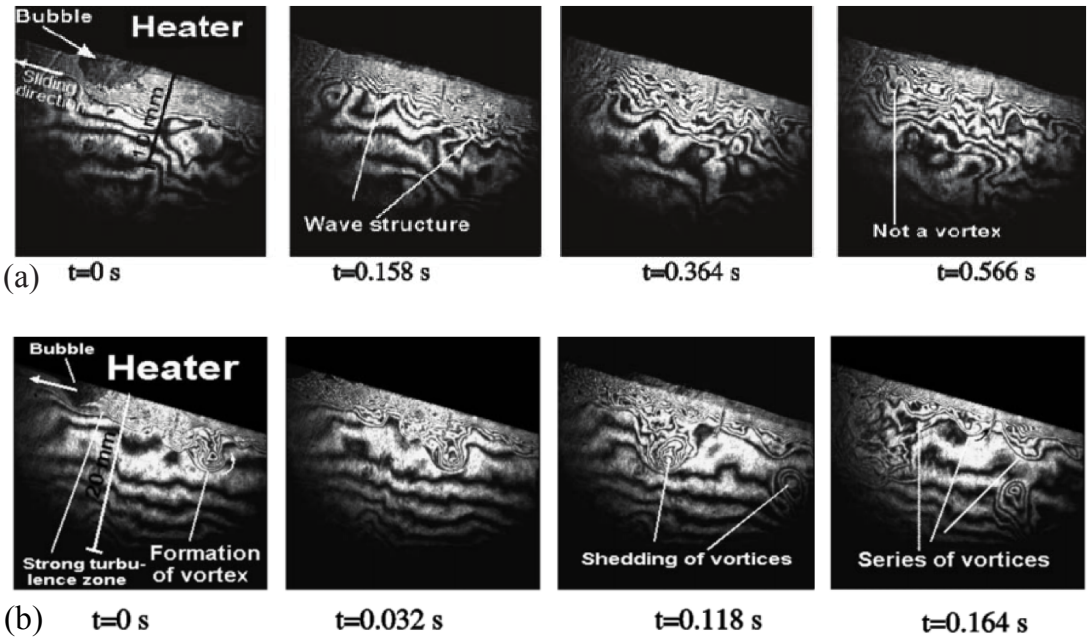

Figure 2.25: (a) Fringe pattern of a sliding bubble with small superheat and subcooling ($\theta = 15°$, $T_w - T_{sat} = 0.8°$C, $\Delta T_{sub} = 0.4°C, Ra = 1.0$ x 10^9). (b) Fringe pattern of a sliding bubble with small superheat but large subcooling ($\theta = 15°$, $T_w - T_{sat} = 0.4°$C, $\Delta T_{sub} = 2.7°C, Ra = 2.4$ x 10^9), Qiu & Dhir [89].

In this range, large, wave-like motion was observed in the liquid to the rear of the bubble. At the frontal top of the bubble, the fringes of fluid turned towards and around the spherical cap, indicating that hot liquid originally in the thermal boundary layer was diverted to the top of the bubble as a result of sliding motion. In the far wake to the rear of the bubble, it can be observed that the effects of the bubble lasted a relatively long time, with outer fringes spreading into the liquid bulk. Increasing the liquid subcooling caused a different pattern in the wake, shown in figure 2.25 (b). In this case, large vortices were formed downstream of the bubble at $t = 0.032$ and $0.118s$, detaching from the disturbed thermal boundary layer and moving outwards to the thermal bulk, rotating in an anticlockwise direction before being dissipated. The denser fringes in these vortices indicated that an eddy of hot fluid was being removed from the surface. Smaller vortices were also formed between the bulk fluid and the thermal boundary layer. Some of these were found to increase in size, while others dissipated while still inside the thermal boundary layer. The authors also found that the period of efficient heat removal from the surface was followed by a *degradation* in heat removal, caused by a reduction in temperature difference between the surface and the bulk liquid. The heat transfer at the farthest location from the bubble release was increased by 10%.

Although this improvement is tiny, bubbles were only present on the surface of the heater for less than 1% of the measurement time. PIV measurements at $\alpha = 30^\circ$ were consistent with the visualisation, revealing that fluid was pushed outwards away from the wall at the front of the bubble. Meanwhile, to the rear of the bubble, liquid was pulled inwards, with a vortical structure observed. Li al. [90] performed a three dimensional numerical simulation of a single vapour bubble sliding on a downward facing heated surface. This involved solving the continuity, momentum and energy equations using a finite-difference method, with the level-set method used to find the bubble shape. The numerical findings matched the experiments of Qiu et al. [89] well, with the bubble growing in size as it slid along the heated surface, changing in shape from spherical to ellipsoid, and finally to a spherical cap. The wall heat flux downstream of the bubble was significantly greater than that upstream, with the flow pattern obtained showing the bubble pushing the liquid away from the wall in front and a vortex to the rear. The numerical model for the bubble shape deviated slightly from the experimental work Qiu et al. [89] in that it did not show the sharp thinning of the bubble at the tips visible at larger bubble volumes.

Donnelly et al. [69] also performed heat transfer measurements using liquid crystals to quantify the heat transfer coefficient for air bubbles of ≈ 6 *mm* equivalent diameter sliding under a heated inclined surface in water, defining the enhancement factor h^* as the ratio of forced convective heat transfer to natural convection and revealing a maximum enhancement of 1.8 for $\alpha = 30^\circ$. However, the method of liquid crystals has its limitations for highly transient flows, for which the liquid crystal layer may not respond sufficiently to rapid fluctuations in temperature. As such, infrared thermography seems a logical alternative to this method. By using a high-speed thermal camera and at thin heated foil, it should be possible to resolve the surface temperature more accurately. This was confirmed by Donnelly et al. [68], who later performed heat transfer measurements on a heated foil to determine the dimensionless temperature difference $T^* = \frac{T_s - T_\infty}{T_0 - T_\infty}$ and h^* at the surface, using the energy balance developed by Stafford et al. [91]. Figure 2.26 shows measurements of these two values for $d_e = 5.8$ *mm*, $\alpha = 30^\circ$ with the bubble shape and path overlaid. In the wake of the bubble was an extended region of reduced surface temperature and increased heat transfer coefficient due to forced convection, approximately $3-4$ times that of natural convection levels. This zone was approximately the width of the bubble base immediately

behind the bubble and widened to approximately 1.5 times the bubble diameter at the base of the interrogation window. The authors claimed that these regions of cooling were related to both the displacement of fluid in the thermal boundary layer via bluff body convection and secondary mixing caused by vortex shedding in the bubble wake. To the immediate rear of the bubble (up to one diameter downstream of the bubble) was a region of significantly increased heat transfer, although the surface temperature in this zone was not significantly lower than the rest of the region. The authors claimed this region was conceivably the recirculation region to the rear of the bubble, which was found to travel with the bubble as it traversed the surface, with very little cool fluid allowed to enter the recirculating zone. Further downstream of the bubble, in images taken 1 *s* later, the surface temperature plots revealed regions of ellipsoidal cooling separated by regions of less intense cooling. At this point, the structures had reduced in strength but spread out, with the affected area approaching twice the bubble diameter at the base of the interrogation window.

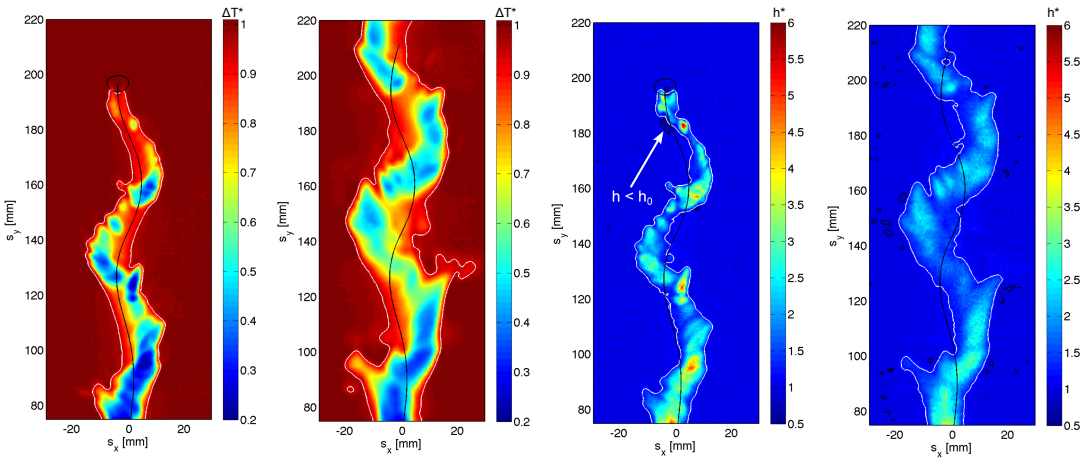

Figure 2.26: Heat transfer results for the 5.76 *mm* diameter bubble sliding under a heated surface at $\alpha = 30^c irc$ at two instances 1 second apart. The first two images show the non-dimensionalised temperature difference, T^*, the following two the non-dimensionalised convective heat transfer coefficient, h^*. The bubble shape and path are also shown overlaid on these plots. Donnelly et al. [68].

Donnelly et al. [68] also noted that the cooled regions on the heated surface tended to overshoot the bubble path, as the cooled region was advected upwards and outwards due to the associated movement of the bubble and upwards due to the moving thermal boundary layer. Although transient, the heat transfer enhancement was found to last a significant time: between 30 and 60 seconds depending on the bubble volume. Also found in figure 2.26 was that the heat transfer in the near bubble wake was greater when the bubble was nearer the

bottom of the interrogation window than when it was near the top. This was explained by considering that the thermal boundary layer grew in thickness as it moved up the surface, with reduced scope for drawing cooler fluid towards the surface. Finally, the observation was made that parts of the surface in the near wake of the bubble experienced a heat transfer coefficient *below* that of natural convection levels, as shown by the white arrow on figure 2.26. These occurred immediately across from the advancing regions of cooling, on the inside of the bubble path. These regions of suppressed heat transfer were in agreement with the work of Delauré et al. [40], who noticed small regions of suppressed heat transfer upon interaction between a single rising bubble and free convection flow from an inclined heated copper block.

There are other possible modes of interaction between bubble and surface that can occur in the industrial applications previously mentioned: for instance, impingement and subsequent bouncing against a wall. Donoghue et al. [80] considered the convective heat transfer and bubble motion due to a single air bubble impacting and bouncing on a heated horizontal foil, also measured using the heated-thin-foil technique. The effect that a single bouncing bubble had on the surface temperature was found to be significant, with its effect lasting as long as 8 *s* due to the wake of the bubble following its initial impact. Upon the bubble impacting the surface, a substantial, spatially symmetric variation in convective heat transfer was observed. Within an area the approximate size of the bubble, large, rapid fluctuations in convective heat flux were observed. Rather than just solely the degradation in heat transfer observed in Donnelly et al. [68], on some occasions a negative heat flux was observed, indicating that warm liquid was momentarily in contact with the previously cooled surface. Upon striking the surface, the bubble bounced, with the wake found to spread significantly in the opposite direction to the bubble's motion. Once the bubble had returned to the surface, the film separating the bubble and surface ruptured, which resulted in an immediate rise in the surface temperature in this region. Figure 2.27 (a) shows the instantaneous heat flux 10 *ms* after the impact of a 2.8 *mm* bubble released at a height of 30 *mm*. The heat flux along the black line is plotted in figure 2.27 (b) as a function of time, with each line spaced 2*ms* apart. For this particular test, this showed the left side of the bubble to impact before the right hand side. The bubble then bounced, leaving the surface after 8 ms, which resulted in a drop in heat flux, although the surface temperature continued to drop. The convective heat transfer

due to a single bouncing bubble was found to be significant, and appropriate models will need to take this into account. However, in the current study, surface inclination angles below the onset of bouncing are used.

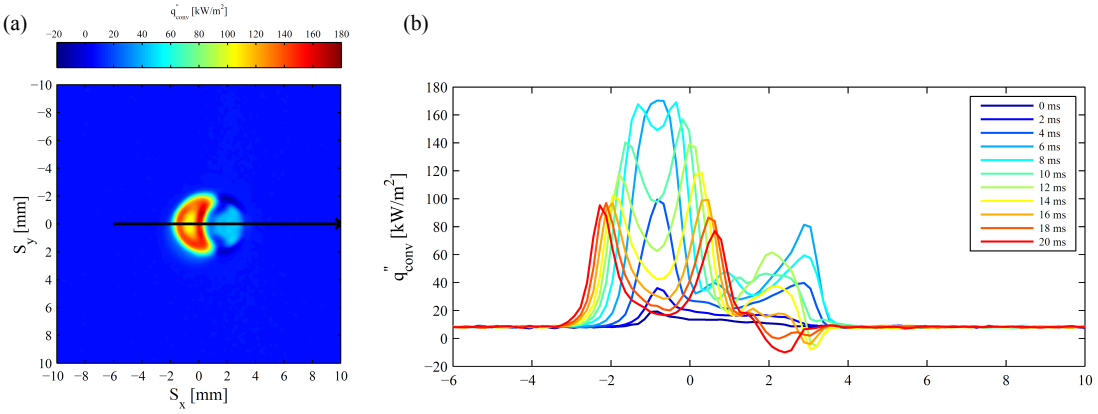

Figure 2.27: (a) Convective heat flux for a 2.8 *mm* diameter bubble 10 *ms* after impacting a horizontal heated surface, with the flux along the black line shown as a function of time in (b), where each line is 2*ms* apart. Donoghue et al. [80].

2.3 Bluff Body Flows

Up to this point, relevant numerical and experimental studies regarding bubble mechanics have been discussed. The discussion of wake structures has been limited to that of rising bubbles, with no study to date quantifying the sliding bubble wake in a rigorous manner. To aid in this quantification process, let us take a step back from bubbles and take a more broad view of vortex structures in the field of fluid mechanics. This section will start by examining the structures formed next to a wall in turbulent flow, before moving onto flow past bluff bodies next to a wall. Understanding wall turbulence and structures shed behind bluff bodies will aid considerably in interpreting the wake structures later observed.

2.3.1 Turbulent Wall Flow

Turbulent flow is ubiquitous in the world around us, and much of the driving force behind understanding vortex structures in fluid mechanics comes from the field of turbulence. In his seminal paper describing turbulent flow, Adrian [92] claimed that key to the study of turbulence is the breaking down of the multi-scaled, complex types of turbulent motion

into more elementary organised motions, discretising turbulent motion into smaller scale eddies. How does one define such an eddy? The author explained that by continuity, all fluid motions possess spatial coherence. For an eddy, the motion must have some form of *temporal* coherence. Theodorsen [93] proposed a model of a near-wall eddy in the late 1950s by using a conceptual approach. The author considered a flow travelling with a velocity U past a wall, and a vortex filament oriented spanwise to the mean flow, perturbed by some small upward motion. The further away part, or "head", of the vortex should experience a greater mean flow velocity, and as such would be convected downstream faster than the lower-lying part. Theodorsen [93] claimed it logically followed that the sections connecting these two parts should be stretched, causing the structure to lift away from the wall into still higher mean velocity, resulting in more stretching of these two "legs". This was named the horseshoe vortex, and is depicted in figure 2.28 (a) . These structures were also known as horseshoe eddies or hairpin vortices, with the latter term being used in the current study. Theodorsen [93] supported this with a sketch based on the smoke visualisations that have since been attributed to Weske, which was reproduced in Adrian et al. [92] and is provided in figure 2.28 (b). At the time, it was not possible to measure vorticity; if it were, it likely would have been established that the loops of smoke were in fact vortices.

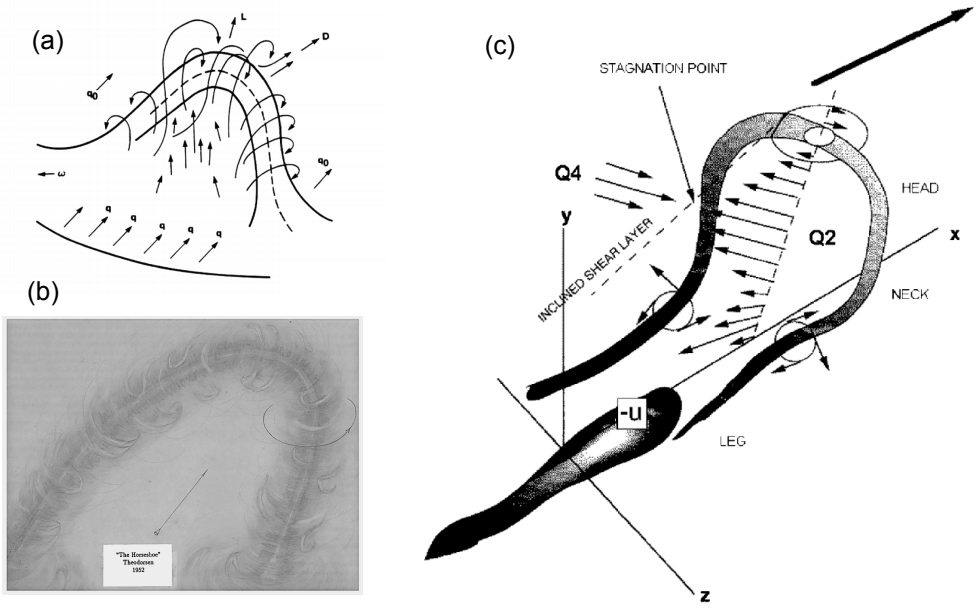

Figure 2.28: (a) Depiction of a horseshoe vortex from, (b) sketch entitled "The Horseshoe" by Theordsen [93] (c) schematic of a hairpin eddy attached to the wall defined by $y = 0$, with the inclined shear layer also shown. Provided by Adrian [92].

Unfortunately, this work met with some resistance, as in the field of fluid mechanics at the time, there was a divergence of opinions on how vorticity operated [92]. As such, the hairpin vortex structure went years without any significant breakthroughs. The advent of techniques such as large eddy simulation (LES), direct numerical simulation (DNS) and PIV proved to be a catalyst for studies on coherent structures. These powerful numerical and experimental techniques cab provide full fields of velocity, vorticity and pressure for visualisation, and as such offered the means to unify previously conceptual models. This resulted in a revival in the study of near-wall turbulent vortices in the 1980's and 1990's. An updated version of the horseshoe structure was provided by Adrian [92], and is shown in figure 2.28 (c). For this structure, the hairpin head was combined with two short, counter-rotating quasi-streamwise vortex legs. The head, neck and legs are labelled on the diagram. The author claimed that inside the structure, the flow was swept up from around the eddy and thrust upwards, with vortex induction from the vorticity elements in each leg and in the head creating a concentrated flow. In outward regions, the fluid flowed downwards and was weaker than the ejection, as the induction from the vortex elements was not as focused. Due to this induction, the eddy propagated in the direction Q2 in figure 2.28 (c). In a Lagrangian frame moving with the eddy, the surrounding flow appeared to follow the motion of Q4. These opposing points created a stagnation point where they cancelled, along with an inclined shear layer consistent with experimental observations.

A major conclusion of DNS and PIV was that the hairpin vortex structures occurred most often in packets; namely groups of hairpin vortices travelling with nearly equal velocities.This minimal dispersion in velocity propagation is also necessary for the structures to have temporal coherence, rather than descending into random turbulence. An example of a vortex packet is provided in figure 2.29 (a), which shows the DNS of Zhou et al. [94]. The flow configuration in this case consisted of an initial eddy and a turbulent mean flow. A hairpin vortex was found to occur at the wall, and grow in all directions. Of interest is that as well as this primary hairpin vortex (denoted on the diagram as PHV), a downstream hairpin vortex (DHV) and a secondary hairpin vortex (SHV) also formed. The downstream vortex was created by protrusions on the downstream face of the conditional eddy being pulled out into a pair of streamwise vortices, acting in the same way as the wall-attached legs. The secondary vortex was created by the interaction of the low-speed fluid that moved upwards due to

induction from the legs with the high-speed fluid above the legs, which led to an arch-shaped vortex roll-up. This formation of new hairpin vortices is referred to as auto-generation [94].

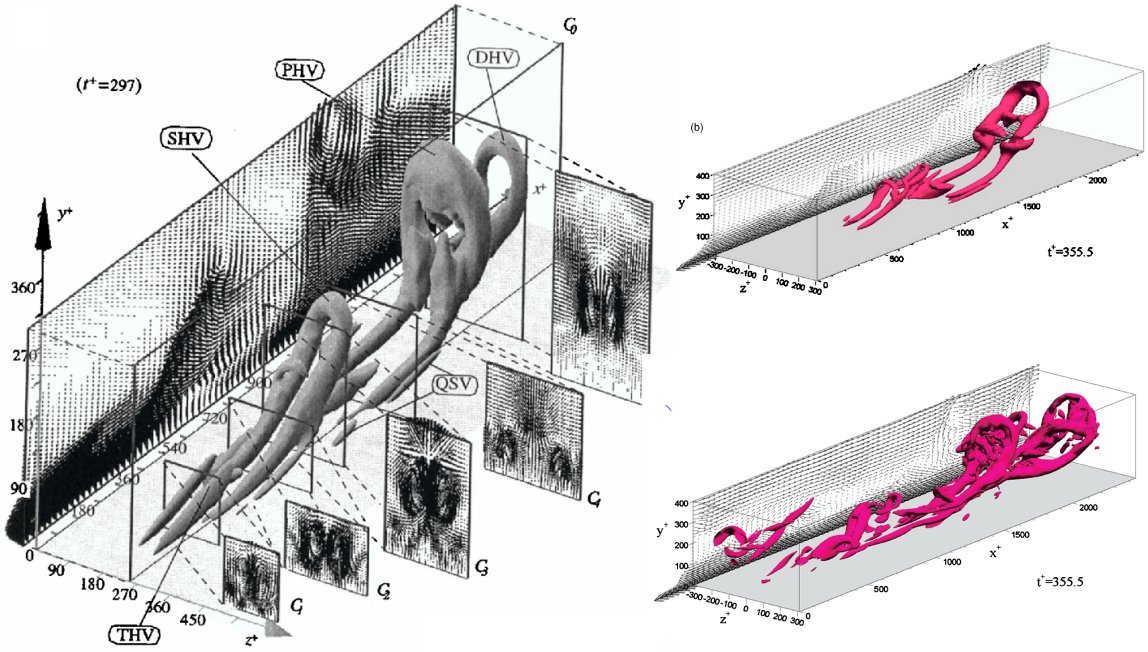

Figure 2.29: (a) DNS simulation of a packet of hairpins that evolves from an initial conditional eddy in a turbulent mean flow at $Re = 180$. The shaded regions are isosurfaces of the vorticity. Also marked are the primary hairpin vortex (PHV), secondary hairpin vortex (SHV) and downstream hairpin vortex (DHV), taken from Zhou et al. [94], (b) evolution of a hairpin packet at $Re = 180$, (c) evolution of a similar packet with 5% noise added to simulate growth in a turbulent environment provided by Kim for [92].

Figure 2.29 (b) is taken from the video accompanying the paper of Adrian [92], provided by Kim for Adrian [92]. It shows the Large Eddy Simulation (LES) for the growth of a packet out of a symmetric eddy, which displayed a similar form to figure 2.29 (a). The authors also added a small amount of noise (5%) to the formation of the same hairpin, as in figure 2.29 (c). Interestingly, although it developed chaotically, the hairpin packet retained the same general properties of the clean packet, with the distances between successive vortices approximately the same. Further evidence was provided in the literature that these hairpin vortices occur in streamwise succession, with the size of the vortices increasing downstream. The growth of hairpin vortex packets, therefore, provides a mechanism to transport vorticity from the wall in turbulence, although it does not do so exclusively, as turbulence is also produced away from the wall. Nonetheless, the components of the hairpin vortex discussed will be useful for the next section, when the flow will be considered on a macro-scale in the wake of bluff

bodies.

2.3.2 Bluff Body Flow

Hairpin vortices have now been identified as a prevalent, coherent structure in wall turbulence. However, it will become apparent that they are not limited to such small scales, and exist in the wakes of solid objects. The purpose of this section is to investigate studies on bluff bodies that show similar boundary conditions to a sliding bubble. In the 1950s, Rosenhead [95] speculated that the only possible 3-D configuration of the flow field behind a sphere was a set of asymmetrical vortex loops, based on the experimental work of Marshall & Stanton [96]. Achenbach [32] built on this by experimentally visualising the vortex structures behind spheres, obtaining the schematic shown back in figure 2.6 (c). Metzler [97] made observations on the separated laminar wake behind a hemisphere, noting that under certain conditions symmetric, controlled hairpin vortices were generated. These findings were the basis for one of the key works in hairpin vortices. Thus, upon noting the observations of Metzler [97], Acarlar and Smith [98] performed an in-depth study of the vortex structures generated by the interaction of a hemispherical protuberance on a flat plate in cross-flow within a developing laminar boundary layer. This configuration and the range of Reynolds numbers tested are similar to that used in the current study. Their experimental work used flow visualisation and hot-film anemometry techniques to investigate the vortex structures. With a hemispherical protrusion, a stationary standing vortex was generated at the leading edge of the hemisphere. Tests were also performed with a teardrop-shaped protrusion, which did not have a standing vortex, but had a largely similar hairpin structure. This meant that the standing vortex had little effect on the production of hairpin vortices, at least for the Reynolds number range tested (340 - 3000). The standing vortex varied from the hairpin vortices in the sense that it was not shed periodically. Figure 2.30 shows a schematic of the interactions between the sequential hairpin vortices generated. Such sketches were interpretations of dual-view picture sequences of flow patterns created using hydrogen bubble visualisation. The authors, using the directions denoted on the diagram, proposed that low-speed fluid within the legs would be advected away from the surface by the legs, with fluid just outside the legs moving towards the surface.

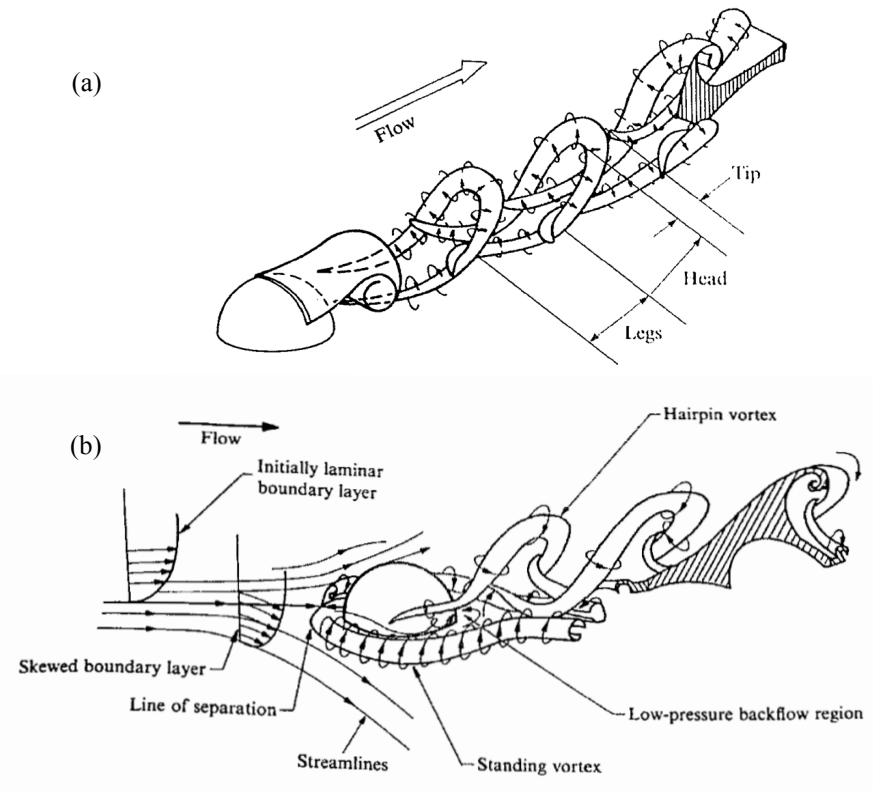

Figure 2.30: Schematics of the near-wake structures in the wake of a hemisphere on a flat plate, where arrows indicate both flow and rotation. Shown in (a) are the vortex legs, head and tip, and shown in (b) is the low-pressure backflow region, referred to as the base pressure. Acarlar & Smith [98].

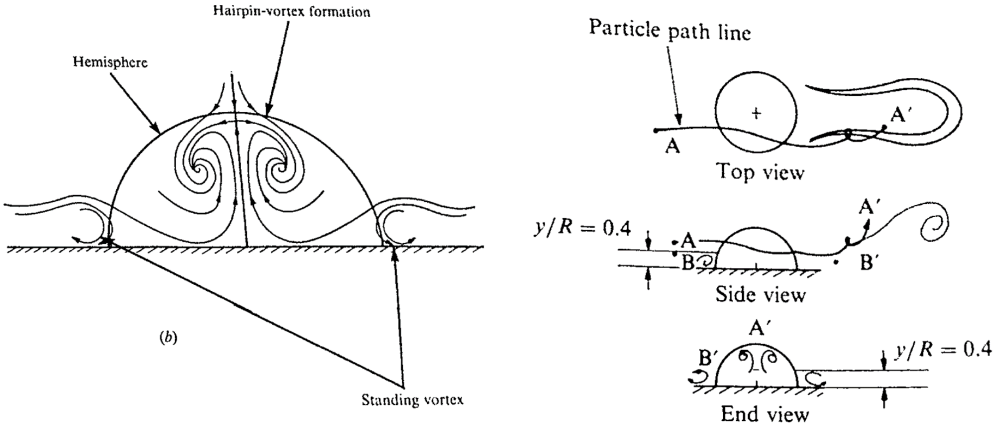

Figure 2.31: (a) End view of the hemisphere, showing the standing vortex formed on either side and the hairpin vortex moving away from the surface, (b) top, side and end view showing the motion of fluid particles at A and B to A' and B', Acarlar & Smith [98].

The authors indicated that hairpin vortex formation took place in the near wake (0 - 3 radii downstream), with the structures evolving and growing immediately afterwards (3-15 radii downstream). In the far wake (15-80 R), secondary structures were generated due to

the interactions between sequential vortices, which initiated chaotic behaviour. To explain the mechanism of hairpin vortex formation, the authors hypothesised that it was the process of build-up and release of concentrated vorticity, in which the base pressure (a low pressure region downstream of the hemisphere) was crucial. They claimed that once the boundary layer separated from the body, it dragged fluid downstream with it, with the outer flow field acting to narrow the region between the separated boundary layer and the wall, which in turn caused the fluid streamlines to curve inwards. In order to balance the pressure across the curved streamlines, a centrifugal force field should be developed, as explained by Willie et al. [99]. The proposed mechanism for vortex formation therefore was the interaction of the potential flow with this base pressure, which would cause the vortex lines to spiral inwards, concentrating to form a vortex tube. After this concentration, vorticity was said to be discharged as discrete hairpin vortices, with a subsequent vortex appearing directly after the previous hairpin was discharged. This low-pressure region is identified in figure 2.30 (b), which shows the near wake of the protrusion. Figure 2.31 (a) shows the streamlines some distance downstream of the hemisphere. Taking a cross section of the hairpin vortex in this plane revealed a counter-rotating vortex pair, which pushed fluid away from the surface, drawing in fluid laterally from approximately $y/R = 0.4$ (any fluid approaching the surface at a lower height than this was discharged through the downstream extensions of the standing vortex). A schematic illustrating the motion of fluid particles for the top, side and rear views is provided in figure 2.31 (b). The authors found that upstream fluid that approached the hemisphere at a height greater than $y/R = 0.4$, denoted as A, passed into the hairpin formation zone (i.e. the near wake), orbiting the core of the counter-rotating legs before being carried away by the vortex to the location A', while fluid at less than $y/R = 0.4$ was transported to the location B'. Finally, the experiments also revealed secondary vortical structures in multiple planes. A weak counter-rotating pair of vortices was generated to the sides of the original hairpin vortex, while a second set was generated at 90° to these, on the plane of symmetry. The authors claimed that all secondary vortices were generated by the rolling up of the three-dimensional shear layer, which itself was created by the interaction of higher-speed outer boundary layer flow with the low-momentum fluid lifted up from the wall by the counter-rotating "legs" of the original hairpin vortex. These secondary vortices increased the complexity of the flow structure to the point that the flow could be construed

as turbulent. The striking comparison observed between these hairpin vortices and those in turbulent boundary layers led the authors to strongly suggest that hairpin vortices were a basic flow structure of the latter.

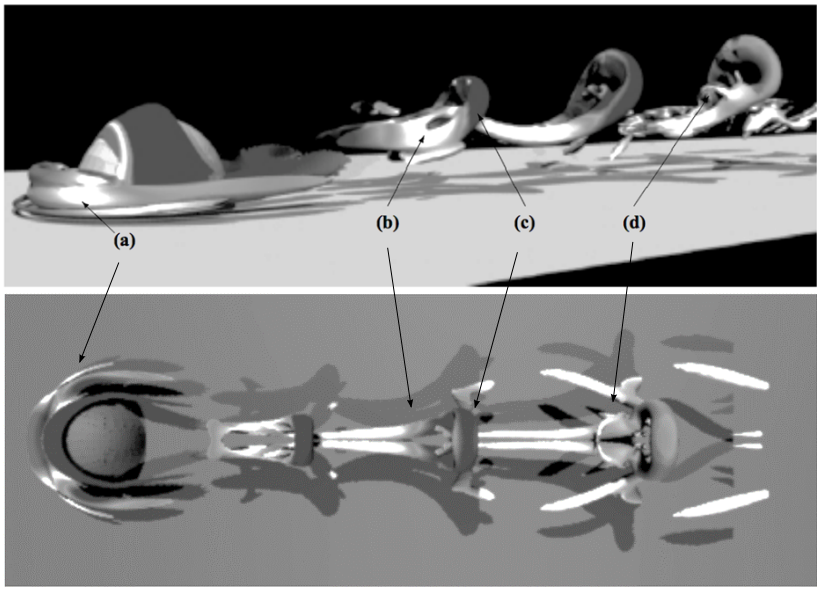

Figure 2.32: Plan and side views of numerically modelled flow over a hemisphere at $Re = 700$: standing vortex (a), interlaced tails (b), hairpin head (c), and bridge (d). Contours mapped onto $\lambda_2 = 1$ surface represent pressure (light: high, dark: low). Tufo et al. [100].

Tufo et al. [100] performed a numerical simulation on a hemispherical protrusion in a flat-plate boundary layer, intended to follow closely the experiments of Acarlar & Smith [98]. This model numerically integrated the unsteady incompressible Navier-Stokes equations, with discretisation based on the spectral element method (SEM). Two dimension simulations along the plane of symmetry found that the flow downstream of the hemisphere experienced very little unsteadiness, although near-wall flow activity was found to grow downstream of the protrusion. As before, hairpin vortex heads and tips moved away from the flat plate, while the hairpin tails stretched and moved towards the wall. The 3-D simulations, with side and top views for $Re = 700$ displayed in figure 2.32, showed excellent agreement with the aforementioned experiments. Identified on this figure were the standing vortex upstream of the protrusion (a), the interlacing vortex tails (b), the hairpin head (c) and a vortex bridge (d). The vortex bridge, which is a common form of vortex reconnection in viscous flows, was observed by Acarlar & Smith [98] to separate from the hairpin and lift off as a separate vortex ring. In the numerical simulations, the ring was dissipated by viscosity so quickly that

the liftoff was not observed. The numerical results also showed evidence of interlacing of successive vortex tails, along with the aforementioned secondary structures. These became more pronounced at higher Reynolds numbers.

The work of Stewart et al. [101] combined numerical and experimental methods to investigate the wake behind a solid sphere rolling at a wall over a range of Reynolds numbers and sphere rotation rates. The experimental setup consisted of a sphere, fixed in a position $< 1\%$ of its 9 *mm* diameter away from a moving wall in cross flow, while the numerical method solved the viscous, incompressible Navier-Stokes equations using SEM, as in Tufo [100]. For both methods, four distinct wake modes were identified: two steady and two unsteady. At low Reynolds numbers, the steady modes maintained a planar symmetry about the centre of the sphere, with the particular modes found to be highly dependent on the Reynolds number and sphere rotation rate. For the case of forward rolling, the steady wake consisted of a compact recirculation zone behind the sphere. With increasing Reynolds number, this recirculation zone developed into two streamwise vortices a short distance downstream of the sphere, with the recirculation region growing in strength. With further increases, the wake was found to undergo a smooth transition to unsteady flow, with vorticity being rolled up and shed over the top of the sphere surface; this resulted in the formation of hairpin vortices that were subsequently transported downstream. This was referred to as the symmetric mode. For a sphere that was in reversed rolling, the steady wake was found to take the form of a streamwise vortex pair that originated at the sides of the sphere. As the Reynolds number increased, this wake took the form of a counter-rotating spiral vortex pair that was half a wavelength out of phase, with a slight divergence of the wake downstream. An excellent qualitative agreement was observed between the numerical and experimental results. The forward rotation case bore the most similarity to a sphere or hemisphere in a free stream. Figure 2.33 and 2.34 show examples of some of these modes. The authors also calculated the wake-induced drag force on the sphere. A plot of drag coefficient is provided in Figure 2.34 for the forward rotating sphere, with the fluctuations in C_D corresponding to the shedding of hairpin vortices. Indeed, the variations in the value of the local maximum drag indicated that hairpin vortices of different strengths were being shed by the sphere, despite the fact that it was laterally constrained.

Unfortunately, it is not possible to directly extrapolate the results from this section to

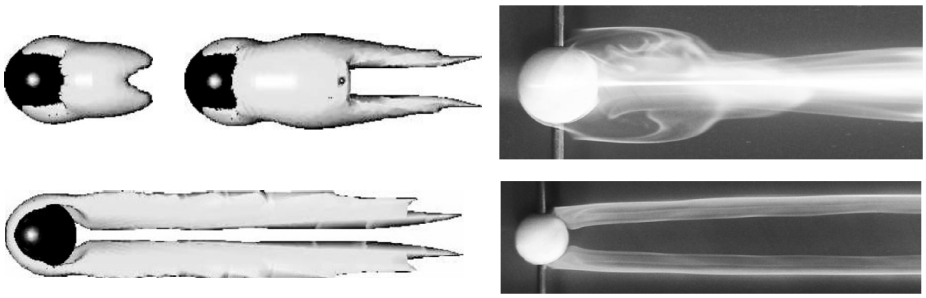

Figure 2.33: Numerical (left) and experimental (right) results for the steady sphere wake under forward rotation (top), with numerical results at $Re = 50$ and 100, experimental results at $Re = 100$, and reverse rotation (bottom) at $Re = 100$, Stewart et al. [101].

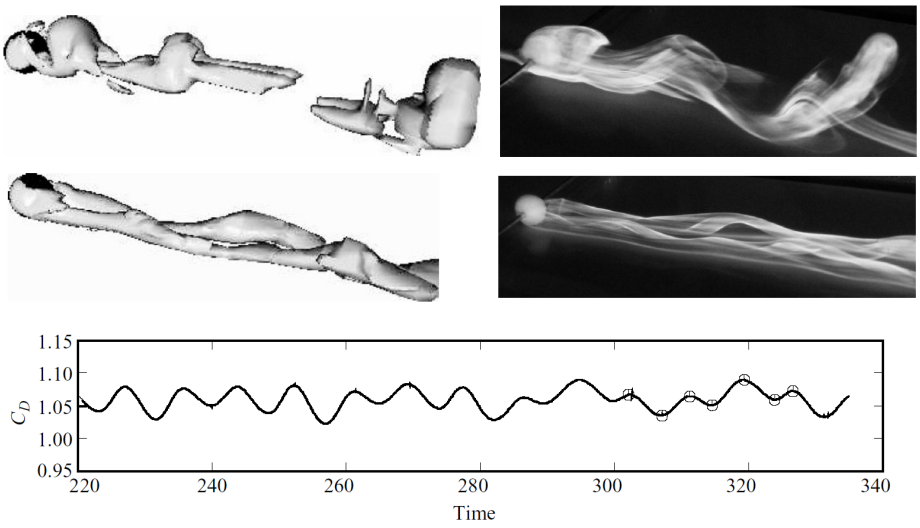

Figure 2.34: Numerical (left) and experimental (right) results for the unsteady sphere wake under forward rotation (top), both at $Re = 200$, and reverse rotation (bottom) with numerical results at $Re = 300$, experimental at $Re = 200$. Below this is a plot of the fluctuating drag coefficient as a function of time, Stewart et al. [101].

the wake of a sliding bubble. This is in part due to the different boundary conditions at the surface (no-slip for a bluff body versus zero stress for a bubble). Additionally, the solid bodies examined were laterally constrained. As the bubbles being studied here are in the ellipsoidal regime, they experience path oscillations, adding another layer of complexity to the wake structures. Veldhuis et al. [102] also performed Schlierein visualisation on hollow plastic spheres rising in water, with a density of $4-5\%$ lower than water. At Reynolds numbers of 500, as was observed for De Vries et al. [37] behind zigzagging bubbles, two counter-rotating threads in the wake were formed, crossing at the centreline of the zigzag path, with the force directed towards the centre-line. Close to the sphere, each of the vortices developed a

"kink", As these kinks developed downstream of the sphere, they came together, combining into a hairpin vortex. Unlike Lunde and Perkins [24], who interpreted the flow pattern as a series of hairpin vortices of alternating signs, Veldhuis et al. [102] instead suggested that the streamwise vorticity at the surface of the sphere did not change sign, with the legs of similarly signed hairpin vortices crossing at the path centreline. Increasing the Reynolds number caused a more irregular wake structure, with a clearly defined near wake structure and a double-threaded wake containing hairpin loops and secondary structures.

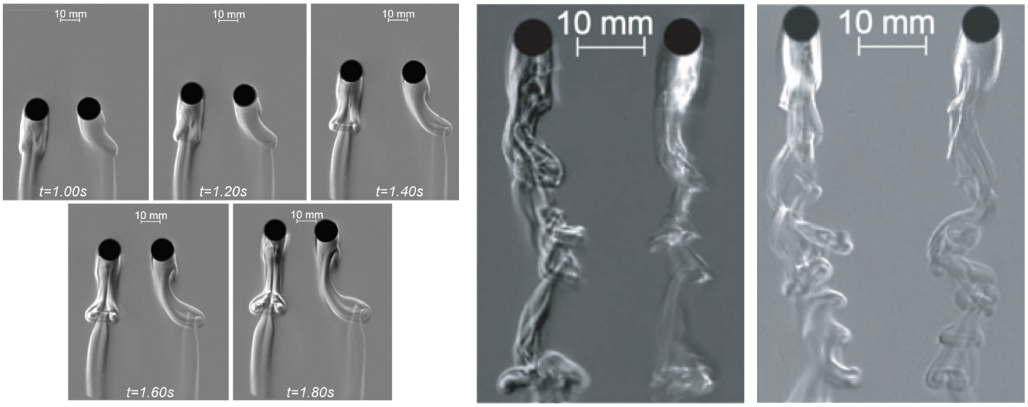

Figure 2.35: (left) Sequence of stereoscopic views showing process of hairpin vortex formation around a rising sphere at $Re = 576$, (right) the more chaotic wake structures observed at larger Reynolds numbers of 920 and 1350, respectively, Veldhuis et al. [102].

2.4 Summary

An extensive review of the literature surrounding bubbly flow and solid body wake mechanics has been provided. It is clear that extensive work exists for bubbles rising in an unbounded medium, in terms of their dynamics, wake mechanics and interactions. However, those rising in constricted geometries have received far less attention: to the knowledge of the author, no study has experimentally or numerically quantified the wake to the rear of a bubble sliding under a heated surface. As such, a study of near wall bluff bodies proves useful in understanding what possible forms the structures to the rear of a sliding bubble could take. Furthermore, the interactions of multiple sliding bubbles have not been studied in any great detail, despite their prevalence in two-phase tube bundles and other applications. The gaps in literature identified will aid in deciding the scope of the current study, which will be

discussed in the following chapter.

Chapter 3

Research Motivation & Objectives

A review of the literature surrounding bubbly flow and solid body wake mechanics has been provided. This chapter uses the findings of the review to highlight the limitations in these fields, identifying the gaps in the literature that will provide the motivations for this work. The objectives and scope of this study are also defined.

3.1 Motivation for this Research

Two-phase flow is a thriving field, with much research ongoing in liquid-liquid and liquid-gas systems. A comprehensive review of the literature has been provided for rising and sliding gas and vapour bubbles. Rising bubbles have been studied in terms of their shape, velocity, path and wake behaviour, with particular attention being paid to the latter. The review has also highlighted the complexity associated with the interaction between multiple rising bubbles. These interactions are highly complex and dependent on the system properties; however, they can largely be split into bubble-bubble and bubble-wake interactions, with both interactions found to create an increase in turbulent mixing in the liquid phase. Rising bubbles, at least those in Newtonian fluids, have been studied in the literature in great detail. However, although bubbles sliding in constricted geometries have many applications, particularly with regards to two-phase cooling, their associated body of work is far smaller. A fundamental knowledge of the physics of sliding bubbles is necessary for a more complete understanding of two-phase flows and optimisation of two-phase convective heat transfer. Studies to date on sliding bubbles have examined the bubble mechanics and the convective heat transfer

enhancement offered. The review on rising bubbles showed the wake to be integral to bubble path instabilities and motion, while prior research on sliding bubbles indicated the importance of the wake for convective heat transfer. For gas bubbles, this is particularly relevant in situations with low wall superheats. To de-couple the interdependent parameters that impact convective heat transfer, an air-water system is used. This means that phase change, and initially heat transfer, will be ignored. For a greater insight into the possible nature of the wake, a discussion of the fields of near-wall turbulence and bluff body flows was provided. To the knowledge of the author, no study to date has quantified the wake structures of sliding bubbles in the same way as Brücker [39] or Zenit & Magnaudet [41] did for rising bubbles or Acarlar and Smith [98] did for a hemispherical protrusion on a flat plate. Understanding the wake structures of sliding bubbles will not only address this gap but will provide an explanation as to *why* the bubbles are so effective at enhancing heat transfer and promoting turbulent mixing in the wake. The current study will build substantially on the body of work in the literature by quantifying the sliding bubble wake, by performing PIV measurements in multiple 2-D, 2-C planes to build up a three-dimensional construction of the flow field. The influences of this wake on bubble motion and heat transfer will also be explored.

Although understanding the structure and dynamics of the sliding bubble wake is necessary for the optimisation of two-phase convective heat transfer, it is unlikely that real engineering systems will involve a single sliding bubble. The current study intends to address this shortcoming by expanding the body of knowledge on sliding bubbles to include that of an in-line bubble pair. The literature review on freely rising interacting bubbles showed that the effect of bubble interactions is to increase the degree of mixing in the bulk fluid, causing an amplification of turbulence in the wake. There are many types of bubble interaction, e.g. dancing, drafting, coalescence, and breakup. What these phenomena all have in common is that they are all triggered by a trailing bubble entering the wake of a leading bubble. As such, it is the *bubble-wake* interactions that are of most importance, as this initial capture leads to all subsequent bubble motion. From a fluid mechanics perspective, the greater turbulent mixing of a bubble pair should result in an increase in convective heat transfer. However, due to the complex interactions that occur between the bubbles and the thermal boundary layer, this is not a trivial problem. Again, to the author's knowledge, there exists no study involving characterising the wake-driven motion of a sliding bubble pair. In order to achieve

this understanding, it will be necessary to first examine the shape, path and wake of a single sliding bubble in detail, for a range of bubble volumes and inclination angles. Next, it will be observed which of these parameters *change* when observing a bubble-wake interaction. Finally, the flow structures and heat transfer enhancement offered by multiple sliding bubbles can be studied. The current study intends to achieve this understanding through experimental measurement, analysis and interpretation.

3.2 Problem Description

The flow under consideration is shown in figure 3.1 for a side view. An air bubble of either 5.8 *mm* or 7.2 *mm* equivalent spherical diameter d_e is injected into an tank of water inclined at some angle α to the horizontal. At the top of this tank is a sliding surface, 50 *mm* above the injection site. Due to the difference in density between the air inside the bubble and the surrounding fluid, the bubble feels a buoyancy force, F_b, which acts in the opposite direction to gravity. The bubble will thus rise a vertical distance $s_z = \frac{50}{cos\alpha}$ *mm* before impacting the surface. This dynamic impact creates a new initial condition for the bubble, which will also change as a function of the surface inclination angle. This process is not under consideration in the current study, although it is certainly an area that requires future work. Additionally, between the surface and the bubble is a liquid film, within which the viscous forces dominate. This alters the boundary condition at the surface and deforms the bubble shape. At moderate inclination angles, the bubble will slide along the underside of the inclined surface at some velocity U_b. Knowing this velocity, a rough estimate of the film thickness can be made using equation 2.4, which works out to be of the order of 20 μm, a physically reasonable value. Addlesee & Kew [77], however, showed that this film thickness changes from the front to the rear of the bubble, adding further complexity to its dynamics. For this experiment, the bubble and its surrounding flow will be measured on a larger scale, meaning it is not possible to measure the film thickness directly. This is simply due to the choice of scale, since a phenomenological study of all scales is beyond the scope of most experimental studies.

The presence of the inclined surface means that the bubble only experiences the component of the buoyancy force parallel to the surface, i.e. $F_b \sin\alpha$. The component of this force normal to the surface pushes the bubble against the liquid film. At low inclination angles,

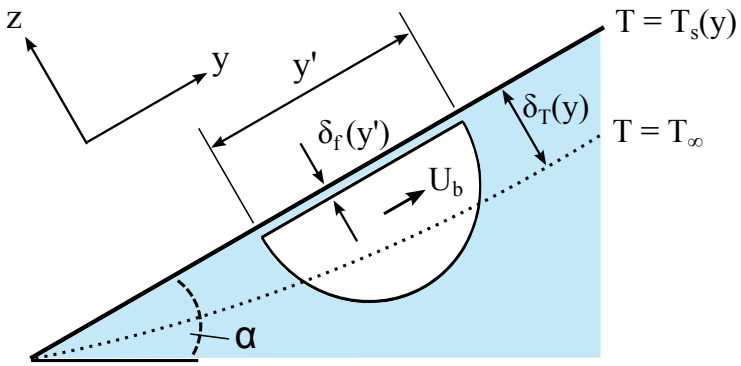

Figure 3.1: Schematic of an air bubble sliding underneath a heated, inclined surface

surface forces such as Van Der Waals' effects and electro double-layer repulsion can cause the bubble to stick to the surface; however, these low inclination angles are not considered in the current study. Within the bubble, the pressure of the gas acts outwards, and is sufficient to oppose the atmospheric and hydrostatic pressure acting on the bubble. Additionally, the surface tension force acts to oppose the formation of new liquid surface area, resulting in a no-stress boundary condition along the bubble interface. The surface tension also influences the contact angle, defined as the angle formed between the air-water interface and the solid boundary. This depends on the properties of the liquid, gas and surface, with many numerical models adopting a constant contact angle boundary condition. The bubble is deformable and inertialess; however, it must displace the liquid in order to travel. This displaced fluid, which is known as added mass, certainly has inertia! Thus, the "momentum" of the bubble is really the momentum of the bubble and the fluid it displaces.

For the case of the current study, the bubble is intended to have reached its terminal velocity by the time it is observed. When the surface is heated, a thermal boundary layer exists on the underside of the surface, transferring heat to the water via natural convection. In a natural convection boundary layer, the surface temperature T_s changes as a function of the vertical displacement. When the bubble slides under the surface, it will disrupt this thermal boundary layer, changing the mechanism of heat transfer from free to forced convection. This will move fluid from the cooler bulk (T_∞) to the surface, improving heat transfer rates.

There are some aspects of bubble motion not captured by the schematic in figure 3.1. For instance, the bubbles in the current study undergo undulating path oscillations and complex shape fluctuations triggered by the initial conditions of the bubble impact, the liquid film and

by instability. This means that the bubble velocity will not be constant, instead fluctuating about a mean value. Thus, the measurements of the bubble path, shape, wake and heat transfer enhancement will be taken in a parallel plane. In the parallel plane, the fluctuating bubble shape is found to be elliptical. However, the shape oscillations are far smoother and less chaotic than the freely rising ellipsoidal bubbles defined by the Bhaga and Weber regime map [12]. As such, we will define the bubbles in the current study as *stable ellipsoids*. Using the experimental techniques outlined in the next chapter, measurements will be taken of the dynamics of the bubble and its wake for the case of a single bubble and an in-line bubble pair.

3.3 Research Objectives

Having identified the relevant gaps in the literature, the key objectives of this study are as follows:

- To experimentally quantify the flow structures in the wake of a sliding air bubble by performing particle image velocimetry (PIV) in multiple 2-D planes to deduce a three-dimensional wake structure.
- To study the path, shape and dynamics of a single sliding bubble and use this information to understand what changes during a bubble-wake interaction occurring between an in-line bubble pair.
- To link the wake mechanics to bubble shape, path, and heat transfer measurements for both single bubble and in-line bubble pairs, thereby providing a foundation for future optimisation of convective heat transfer enhancement.

Chapter 4

Experimental Apparatus

This chapter describes the experimental apparatus used to achieve the outlined objectives, namely the measurement of the motion, wake structures and heat transfer associated with single and multiple sliding bubbles. For this, two configurations are necessary: one to explore the bubble and fluid motion and one for the heat transfer enhancement.

4.1 Case 1: Bubble and Fluid Motion

The structure for measuring bubble and fluid motion consists of an inclined glass tank mounted in an aluminium support structure and a PMMA surface under which the bubble slides. The tank is an open top box of internal dimensions $300 \times 108 \times 200$ mm^3 with a bubble injection system mounted in the base. Two stainless steel wheels, brackets and a steel rod are used to secure the tank in place at inclination angles, α, of 20°, 30° and 40° to the horizontal. Angles are measured using an inclinometer accurate to within 0.1°. The tank is filled with deionised water or a mixture of deionised water and 10 μm diameter hollow glass spheres (Dantec Dynamics *80A6011*) as tracer particles for PIV measurements. Deionised water is used rather than distilled water due to its uniformity between batches, meaning more consistent fluid properties between tests. The base support structure is comparatively large in comparison to the tank as the camera is mounted to the tank in one of two possible locations, meaning that there must be space for the tank to rotate for all camera positions and inclination angles.

The surface under which the bubbles slide is a 6 *mm* thick, 290×105 mm^2 PMMA sheet

that forms the underside of a box mounted into the support structure. A hole drilled near the top of this box prevents the air pressure in the tank increasing upon bubble injection. PMMA was chosen as a sliding surface because of its transparency for surface lighting. The sliding surface is hydrophilic, meaning its contact angle is less than 90 degrees, while the contact angles change between the front and the back of the bubble. The surface is maintained clean and free from aberrations. When tracking the bubble's motion, backlighting is achieved by mounting a 40 W LED light above the tank. LEDs provide white light with very little change in temperature, meaning there is no discernible change in liquid properties with respect to time. In order to diffuse the light, a sheet of high quality tracing paper is mounted to the top of the tank. This provides sharp, clear high speed images, with the bubble forming a dark outline on a light background. An exposure time of 30 μs ensures no saturation in these images. The bubble dynamics are discussed in terms of a single plane parallel to the surface.

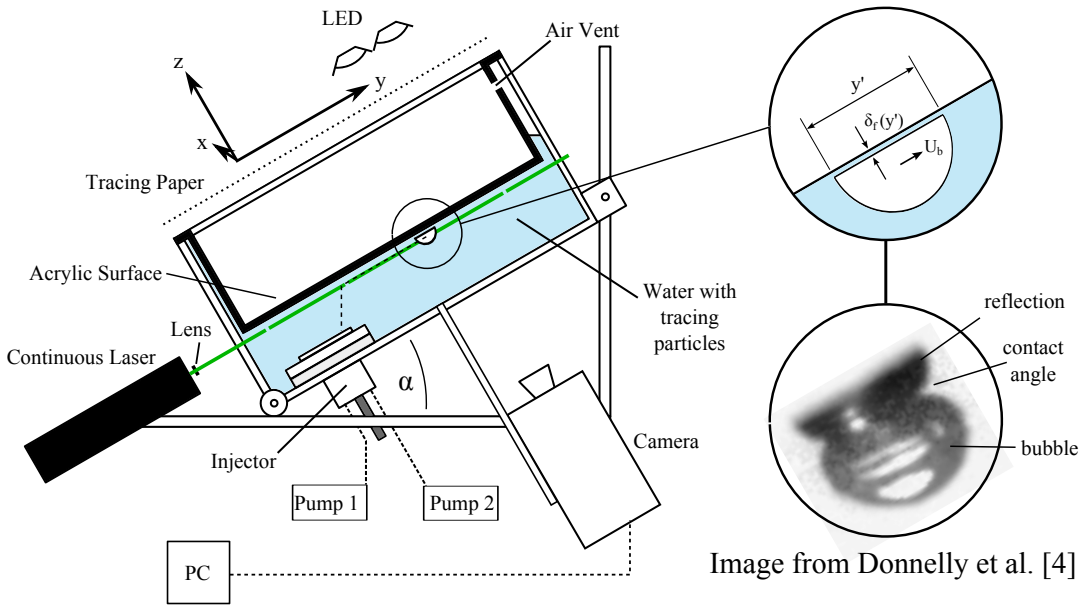

Figure 4.1: Schematic of the experimental apparatus used for the parallel plane configuration and the $x-y-z$ notation adopted. For the bubble motion setup, illumination is provided by the LED light, while for the fluid motion setup, it is provided by the laser sheet. A reference side image from Donnelly et al. [4] is provided for reference.

To track the bubble and fluid motion, a Phantom $v311$ high speed camera is used. This camera has a 12-bit widescreen 1280×800 CMOS sensor and 1 μs minimum exposure time, 20 μm pixel size and 8 GB internal storage. This allows for a maximum frame-rate of 3250 Hz at maximum resolution up to 500,000 Hz at reduced resolutions. The camera is controlled

by a dedicated computer using the Phantom Camera Control 1.3 (*PCC*) software package. For these experiments, a framerate of 1000 Hz is more than sufficient to capture the full spatial and temporal bubble and fluid behaviour, while the exposure time varies between 20-60 μs. The camera is fitted with a Nikon AF Nikkor 50 mm $f/1.4$ D lens, commonly used in high-speed measurements. These lenses offer very low radial image distortion as well as letting in large amounts of light. A lens aperture setting of $f/2.8$ ensures a sufficient depth of focus for the current study. The tank support structure includes two mounts for the high speed camera, meaning the camera is in the same position relative to the surface regardless of inclination angle. Figure 4.1 shows a reference side image of the bubble taken from Donnelly et al. [4]. Such measurements are not provided in the current study since the oscillations of the bubble would be out of plane, meaning the bubble would move in and out of focus, meaning high-fidelity image tracking is not possible. The current study seeks instead to link the parallel plane motion to the fluid motion and surface heat transfer. Although the fluid motion and surface heat transfer are 3-d flow phenomena, the surface itself (i.e. what is being cooled) is two-dimensional. Thus, using solely a parallel plane to resolve the bubble motion is not a major disadvantage of this work.

Particle image velocimetry (PIV) is based on the principle of illuminating small, neutrally buoyant seeding particles in the working fluid, using a high intensity stroboscopic light sheet, and tracking the displacement of these particles. The current study uses an Optotronics *VA-II-2000-532* continuous wave laser (2 W maximum power, beam divergence 3 ± 0.2 *mrad*), a 3.9 *mm* focal length plano-concave cylindrical lens and an adjustable lens mount to provide a 1.2 *mm* thick green plane of 532 *nm* wavelength. For better z-axis control, the laser is mounted on a separate tripod rather than to the tank itself, and is aligned using a laser alignment sheet before every test.

Measurements are performed in three planes in two mutually perpendicular directions. These are highlighted in figure 4.2. There are two measurement planes parallel to the surface at heights of $s_z = 3$ *mm* and 9 *mm* and one perpendicular plane at $s_y = 60$ *mm* that looks at the streamwise flow structures after the bubble has passed through the plane. The selection of the parallel planes was based on a heuristic approach. Reflections from the bubble interface are a significant issue for two-phase PIV, and can restrict the efficacy of the measurement. To overcome this, many studies use fluorescent particles and a suitable optical bandstop

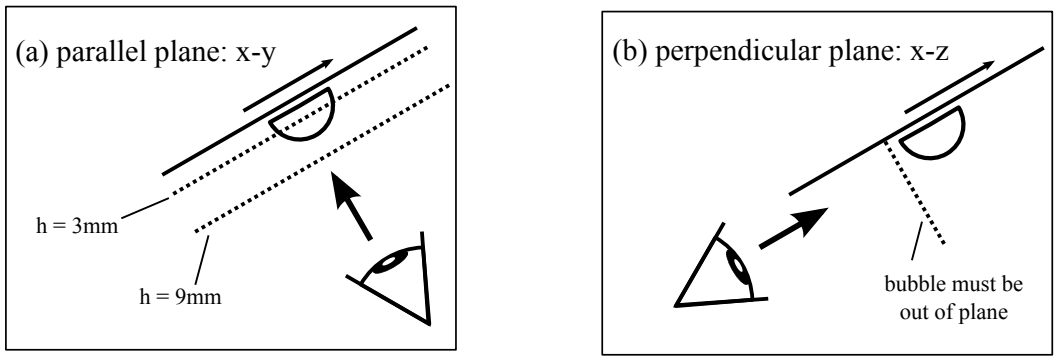

Figure 4.2: Schematic of the (a) parallel and (b) perpendicular PIV measurement planes. Note that the thickness of the liquid film has been exaggerated.

filter to remove the laser excitation wavelength. In the current study, a different approach is adopted. Thus, the bubbles are fixed in the z-direction by the surface and have a height in the z-direction of approximately 5 *mm*. It transpires that the majority of the reflections occur when the bubble-liquid interface at its outermost point intersects the laser sheet. However, if the plane *bisects* the bubble, the reflections are reduced significantly. This motivates the selection of the 3 *mm* parallel plane height to examine the structures in the near wake of the bubble and the 9 *mm* height, below the maximum extent of the bubble, to study fluid motion away from the bubble. The PIV evaluation process will be discussed in greater detail in section 4.2. A full rendering of the experimental apparatus for the fluid motion testing is provided in figure 4.3.

4.1.1 Bubble Injection

The method of introducing bubbles to the surface is key to this study. A solution is required that delivers bubbles of repeatable volumes to the surface in a controlled manner, for both a single bubble and an in-line bubble pair. Furthermore, the injection system cannot block the view of the high speed camera or laser plane when performing bubble and fluid motion measurements. The solution developed for the current study is shown in figure 4.4. Bubbles are introduced to the surface by an injector system comprising of an acetal copolymer box, gas-tight syringes (model Hamilton 1000 series GASTIGHT, 5 ml), silicone rubber tubing, a syringe needle, a pair of syringe pumps (NE-1000 from New Era Pump Systems, Inc.) and a rotating plate. The acetal box is mounted on a polycarbonate flange bonded to the base of the tank using UV-cured glue. When performing a test, a series of small bubbles are introduced

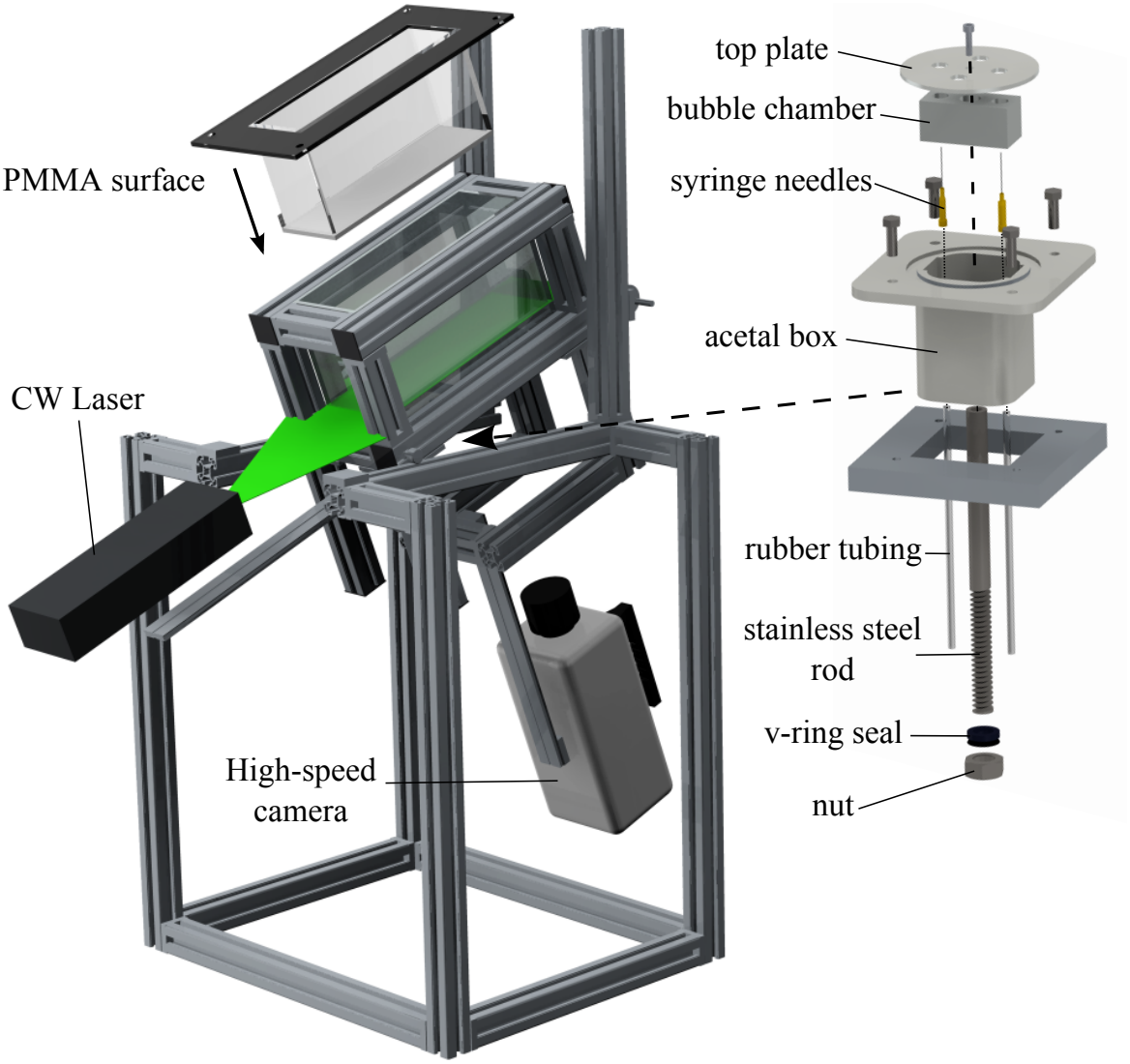

Figure 4.3: Rendering of experimental apparatus for fluid motion testing with part of the top bars removed, with an exploded view of the injection system at the base of the tank.

into the cylindrical bubble chamber via the syringe pump/s and the 5 *mm* diameter tubing, coalescing inside the chamber to form either one or two bubbles of known size.

On top of this chamber sits a 2 *mm* thick circular acetal top plate, which contains 5 *mm* diameter holes corresponding to the chamber locations. Upon turning a stainless steel rod, the holes in the chamber are aligned with the holes in the top plate. This causes the bubble or bubbles to rise, impact the surface and slide up into the measurement region. Upon reaching the measurement region, the bubbles are at their terminal velocity and exhibit no bouncing behaviour. There is some variation in the initial rise cycle of the bubbles, which is the case since the injector must be sufficiently far from the surface to not block the view of the camera

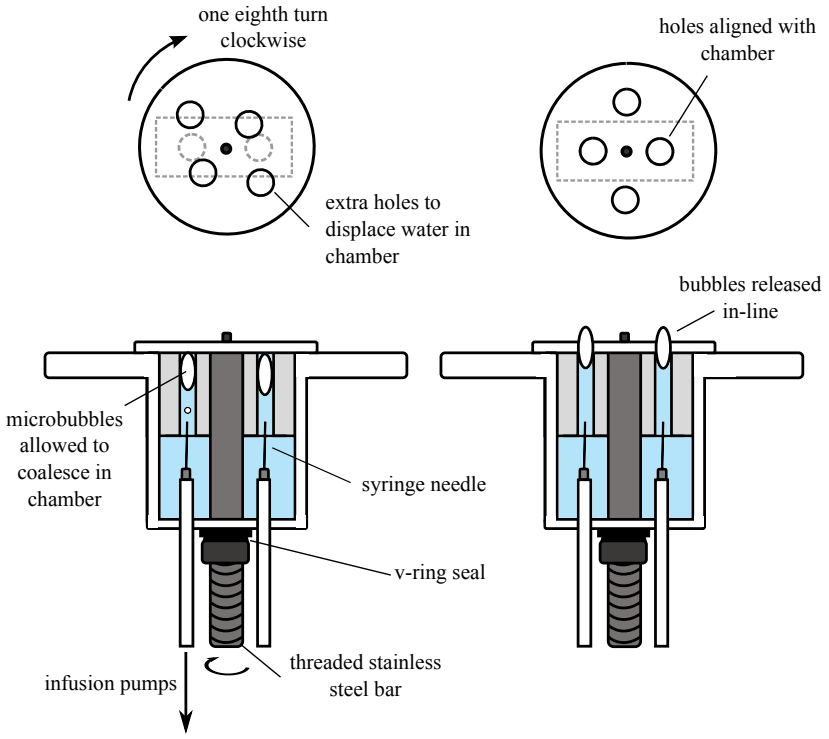

Figure 4.4: Plan and elevation view of bubble injection system.

in the perpendicular plane. Additionally, numerous tests have been performed to show that the direction of plate rotation does not alter the initial displacement of the bubble, with successive tests having opposite spanwise displacements despite the same plate rotation.

4.2 Case 2: Heat Transfer

The review of literature on sliding bubble heat transfer has revealed that the cooling patterns observed are dynamic and have short temporal scales. To resolve the convective heat transfer at such scales, an electrically heated, thin, metal foil and high-speed infrared thermography are utilised. Heated foils have been used extensively for heat transfer measurements in the literature due to their ease of implementation and to the high spatial and temporal resolution that can be achieved. For this experiment, the foil must be allowed reach a steady state temperature, T_s, before the introduction of the bubble, while maintaining a temperature gradient, ΔT, between itself and the bulk fluid. One option to maintain this temperature difference could be a flow loop/heat exchanger combination, although this fluid motion would alter the thermal boundary layer that exists on the surface. Instead, an experimental structure

is utilised that is geometrically similar to that in section 4.1 but has with dimensions of 400 $\times$ 400 $\times$ 300 mm^3, allowing for a greater volume of bulk fluid. Again, the tank contains the sliding surface and a mount for the bubble injection system. The sliding surface in this case is the heated foil section; this forms the base of a PMMA piece which is mounted into the top of the tank. A schematic of this apparatus is shown in figure 4.5.

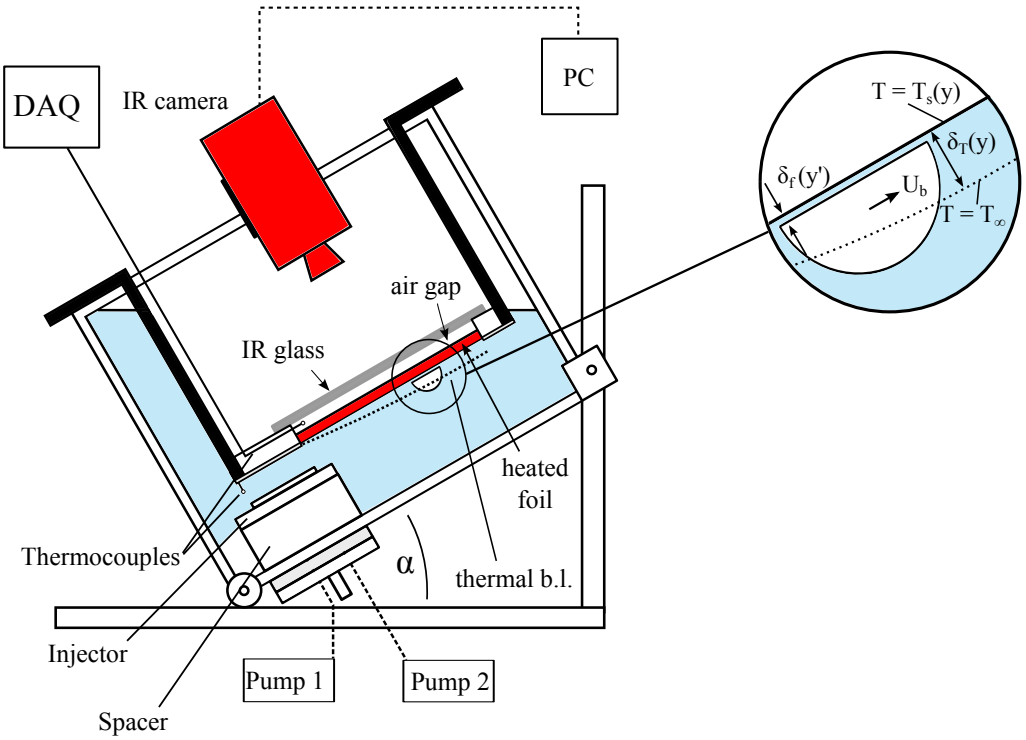

Figure 4.5: Schematic of the experimental apparatus used for heated tests, which uses a stainless steel foil and infrared camera.

4.2.1 Heated Foil

The foil in this case is a 25 μm thick, 130 $\times$ 250 mm^2 AISI 316 stainless steel foil manufactured by Goodfellow. The foil is bonded to a pair of copper busbars using thermally conductive epoxy to ensure good electrical contact and uniform heat generation. Each copper bar has two connections on each end, which receive power via 5 mm diameter copper cables from a Lambda GENESYS GEN6-200 DC power supply. This power supply is able to provide 6 volts and 200 amps in either constant voltage or constant current modes. The latter is used in the current study, as it allows the foil to be heated to a desired temperature.

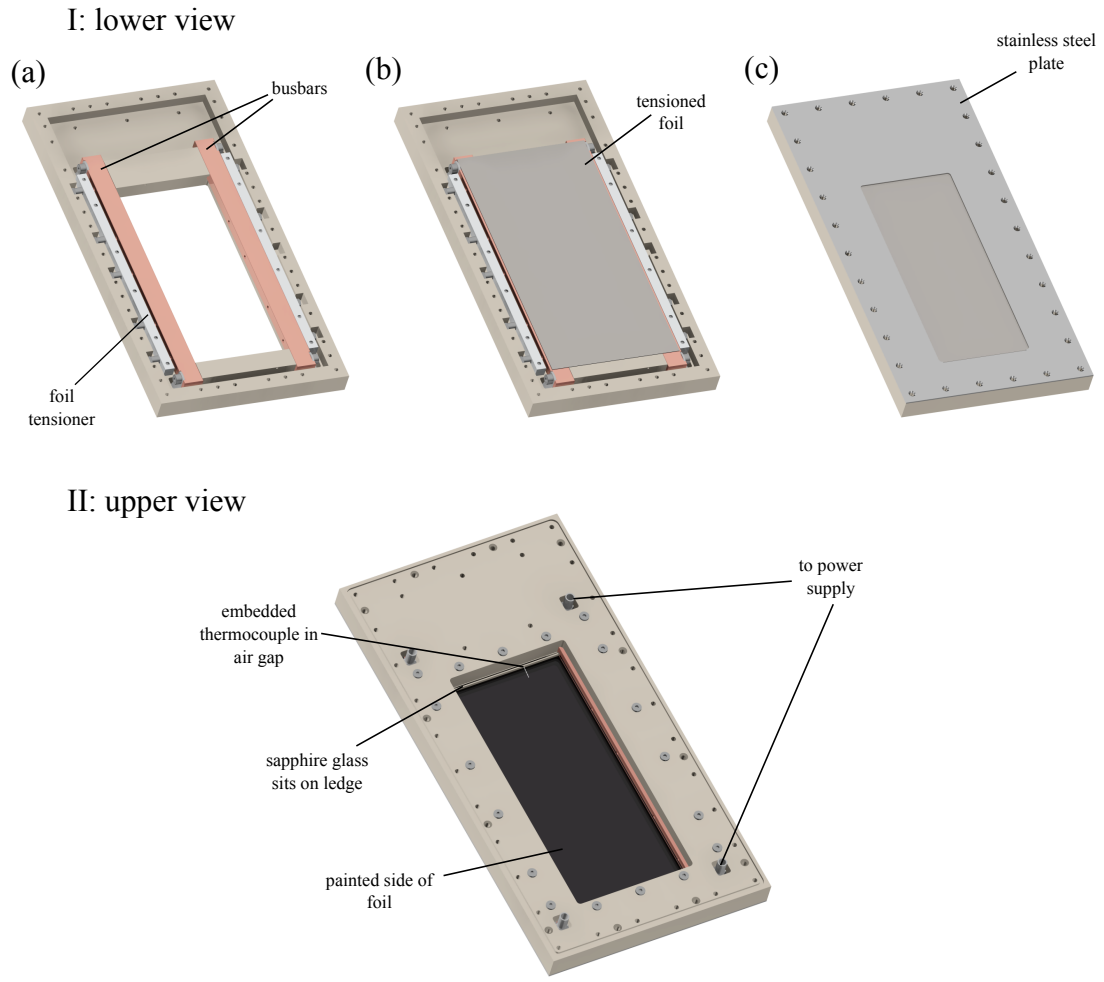

Figure 4.6: Rendering of heated foil and surrounding PEEK 1000 structure, with a lower view (I) showing the busbars and tensioning brass bars (a), the tensioned foil (b) , the stainless steel plate (c) and an upper view (II) showing the ledge for the sapphire glass and embedded thermocouple (d).

When the foil is heated, thermal expansion, and thereby warping, can occur. To reduce this problem and to ensure the surface is sufficiently smooth, the foil is tensioned by a pair of brass tensioners mounted in a support structure made from Polyether ether ketone (PEEK) 1000 plastic. One of these brass bars is fixed in place in the support structure, while the other can be adjusted by four screws that pass through the brass and the copper. By adjusting these screws, the foil tension can be controlled. The busbars, tensioner and foil are shown in figure 4.6 (a) and (b). PEEK 1000 plastic is utilised in the foil support due to its high temperature rigidity at temperatures in excess of 200 $^{\circ}C$. On the water side of the foil is a stainless steel plate that prevents water from coming in contact with the electrical contacts. A rectangular section machined into this plate forms the foil surface under which the bubbles slide, while a 3 mm chamfer on the upper edge of this section prevents bubbles from gathering

at the lip between the foil and plate. The stainless steel plate, which is shown in figure 4.6 (c), is sealed to the PEEK plastic by means of 32 screws ($M5 \times 60$ *mm*), two neoprene gaskets and an O-ring.

On the observation side of the foil, a lip is machined into the PEEK support structure, 3 *mm* above the foil. A piece of infrared transparent sapphire glass sits on this ledge, creating an insulating air gap between itself and the foil. This air acts as a thermally insulating barrier, ensuring that the majority of heat generated in the foil is convected to the water below rather than through the air above. Additionally, if this gap is sufficiently small, the heat transfer on the air side can be modelled as one-dimensional conduction. This will be quantified in section 5.3. This requires a second temperature measurement, achieved by inserting a thermocouple through a 1.5 *mm* hole drilled halfway up the 3 *mm* ledge. The observation side of the foil is shown in figure 4.6 (d). Finally, the observation side of the foil is painted to reduce the reflectivity of the foil and provide a known emissivity value for the thermal camera. This is performed using black paint and a spray gun, and its thickness measured by use of a micrometer. This value, among others, will be discussed in section 5.3.

4.2.2 Infrared Camera

To capture high speed IR images, a FLIR SC6000 camera is used in conjunction with the FLIR ExaminIR software package and a high speed data recorder (HSDR). This camera features an Indium Antimonide (InSb) focal plane array (FPA) measuring 640×512 pixels, which is sensitive to light in the 3-5 μm range, otherwise known as the mid-wavelength infrared (MWIR) range. This sensor is cooled by an internal Stirling engine, which reduces its temperature to approximately 78 *K* to prevent the sensor being flooded by the camera's own infrared light. The camera is mounted directly to the top of the tilting tank, observing the foil through a 25 *mm* lens. To reduce external reflections, the test surface and camera are surrounded by a black card enclosure.

At 640×512 pixels, the maximum framerate is 126 Hz. For high quality thermal measurements of transient phenomena, it is necessary to balance spatial and temporal accuracy. Thus, a smaller window size is adopted, measuring 320×256 pixels, which allows for a maximum framerate of 400 Hz. As the image is no longer full frame, an offset value is also

selected. In order to reduce reflections from the IR glass, the camera is mounted at a slight angle (5°), with the centre of the area of interest offset from the centre of the focal array. This prevents the camera from observing its own sensor due to internal lens reflections, also known as the Narcissus effect [103]. Offsets of 112 and 100 pixels were chosen in the x and y directions, respectively. The IR camera has a 14 bit range sensor, corresponding to 16383 possible measurement levels, otherwise known as counts. An integration time of 1.4 seconds at 400 Hz ensured the highest calibrated temperature (not exceeding 50°C) corresponds to a count value of approximately 14000, preventing saturation of the sensor. A rendering of the experimental apparatus including the IR camera is provided in figure 4.7.

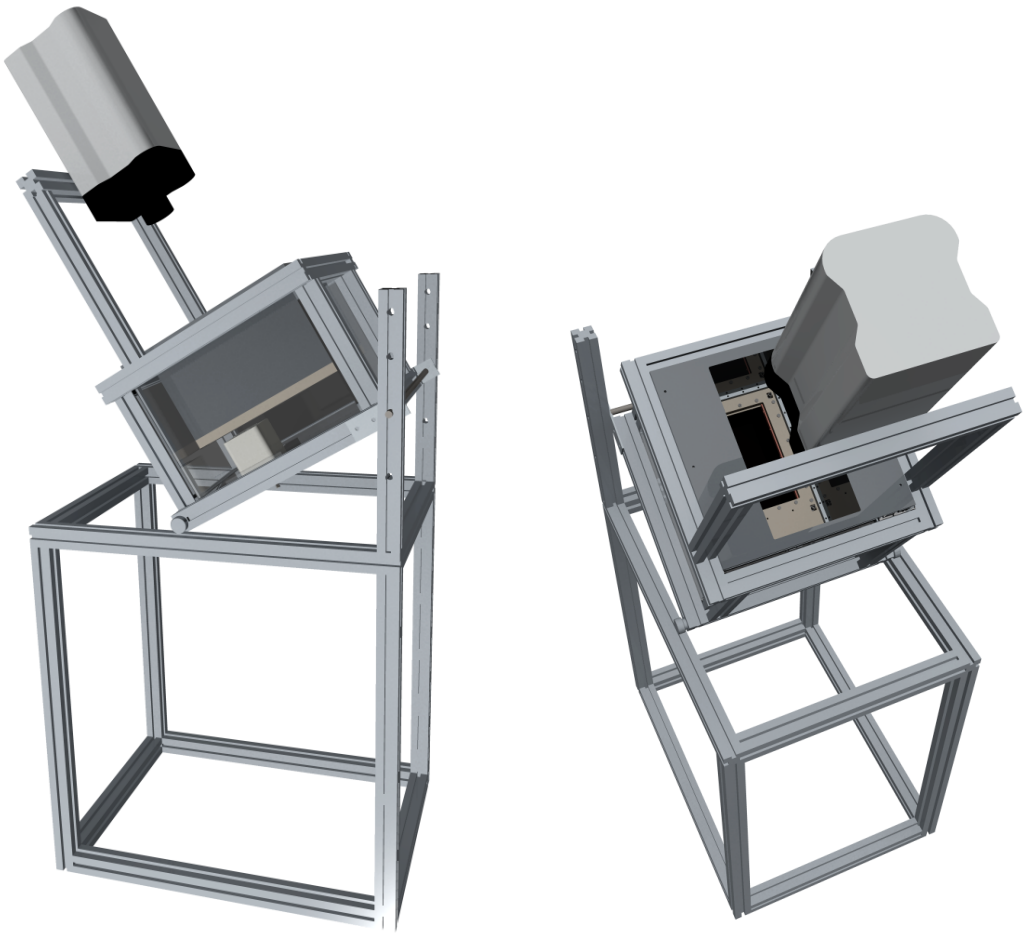

Figure 4.7: Rendering of experimental apparatus from two views, showing the IR camera and its view of the heated foil.

4.2.3 Calibration

The detector of the IR camera requires a temperature calibration and a non-uniformity correction (NUC) in order to convert from counts to temperature and ensure every pixel of the FPA exhibits the same behaviour. The NUC is required since the optics introduce inhomogeneities to the FPA due to the lens and IR window, which results in the camera reading a uniform temperature source as non-uniform. To perform a NUC, a flatfield black body is heated to a high and then a low temperature, in this case: $40°C$ (corresponding to 0.8 times the maximum calibrated temperature) and $21°C$ (room temperature). At each temperature, the black body is placed such that it fully occupies the interrogation window of the thermal camera, and 16 images are recorded and averaged. At each temperature, the ExaminIR software corrects the raw signals of the pixels by individual gains and offsets to the respective mean values.

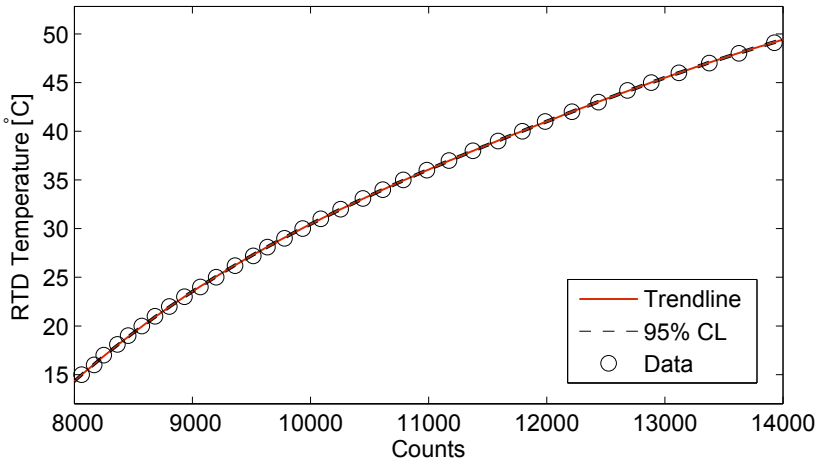

Figure 4.8: Calibration curve for infra-red camera, including 95% confidence limits and a 4th order polynomial fit given by equation 4.1.

The calibration of the thermal camera is performed *in-situ*, with the sapphire window in place. This ensures that the effects of paint emissivity and the sapphire window, which in practice transmits $\approx 90-95\%$ of the infra-red light, are taken into account. The camera is set to the same settings as during testing and the tank is filled with tap water at room temperature. To change the water temperature, an open flow loop is formed between the tilting test tank, a chiller (Grant RC 1400G) and an external reservoir. By adjusting the flow rate through this loop using a ball valve, a steady flow of 3 L/min is achieved. The chiller ensures accurate

temperature control in slowly increasing the water temperature from $15°C$ to $50°C$. A certified RTD (resistance temperature detector) master probe is used as a temperature reference. Thus, the foil temperature can be calibrated off this probe at a range of temperatures. This is based on the assumption that the foil surface reaches the same temperature as the adjacent water, which is anticipated to be the case due to the small thickness of the foil and the insulating effect of the air gap above it. Count values are recorded every $1°C$, with the water being left to settle for several seconds before taking each measurement to reduce the effects of larger-scale fluid motion. Count values are also averaged over a 100 px $\times$ 50 px region of the foil to reduce the effect of noise. This allows for direct conversion from measured counts to temperature values. A plot of RTD temperature versus counts is shown in figure 4.8. Applying a 4th order fit to these data yields the equation:

$$T_s = -1.5839 \times 10^{-14} c^4 + 7.6832 \times 10^{-10} c^3 - 1.4181 \times 10^{-5} c^2 + 0.1226c - 387.5179 \tag{4.1}$$

The uncertainty of this measured fit at a count level of 10,000 is 0.45% at a confidence level of 95% . This corresponds to $\pm$ $0.14°C$ at approximately $30°C$, which is not visible on figure 4.8 but will be discussed further in section 5.3.

A pair of T-type thermocouples are used to measure the temperature of the bulk water and the insulating air gap. These are calibrated simultaneously against the master RTD probe by immersing all three probes in a constant temperature water bath and varying its temperature from $10°C$ to $60°C$ over increments of $5°C$. The calibration curves for these two thermocouples are shown in figure 4.9. The equations of the 1st-order line fits to this data are:

$$T_{RTD} = 0.9968 T_{air} - 0.0008 \tag{4.2}$$

$$T_{RTD} = 0.9968 T_{water} + 0.0247 \tag{4.3}$$

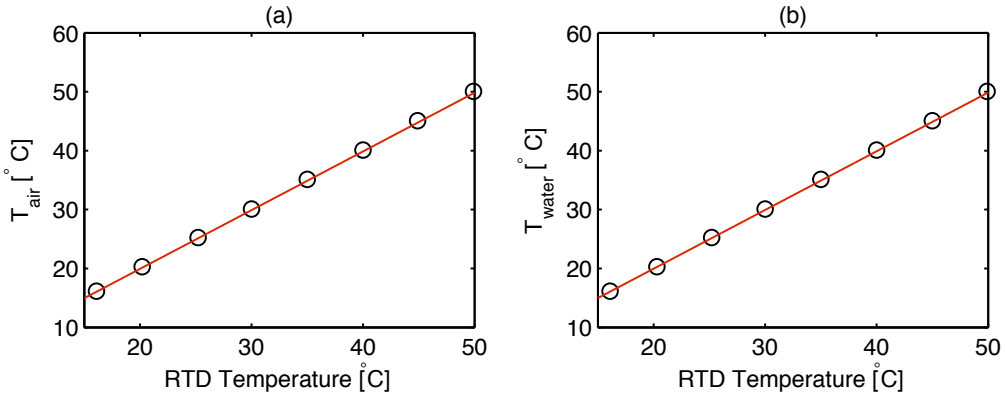

Figure 4.9: Calibration curves for the (a) air and (b) water thermocouples, including the linear fits of equations 4.2 and 4.3.

4.3 Experimental Procedure

There are some minor differences in the experimental procedure depending on the experimental apparatus being used. One key difference is the use of distilled water in the heated foil tests. This is necessary since the deionised water used for the bubble/fluid motion experiments contains dissolved oxygen, which when heated would result in microbubbles forming on the surface and suppressing heat transfer between foil and water. However, for the adiabatic tests it is advantageous to use deionised water due to its homogeneity and known surface tension. This is particularly pertinent to the fluid motion tests with seeded water, which are more sensitive to the purity of the fluid.

4.3.1 Bubble and Fluid Motion

The inclined tank is first set to the desired inclination angle (20°, 30° or 40° to the horizontal) and filled with deionised water. For the case of the fluid motion tests, 20 ml of $1\%w/v$ tracer particle solution is added. These particles have been stored overnight in deionised water and are siphoned from the centre of the beaker, thereby removing particles of densities greater or less than that of the water. Next, the surface is bolted into the top of the tank and the infusion pumps are primed. The high speed camera is mounted to the tank and is set to record for up to 4 seconds at 1000 Hz. Either the LED back light (bubble motion) or the continuous wave laser (fluid motion) is turned on, depending on the measurement setup. Next, the desired volume of air (0.1 or 0.2 ml) is specified on one or both of the infusion pumps, which is

introduced via the syringe(s) to the injector at a rate of 1 *ml*/*min*. The user triggers the camera and turns the baseplate 1/4 turn clockwise, thereby releasing either one or two bubbles to the surface. The recorded images are exported as a multi-frame `.tif` file. For the bubble motion setup, these are imported directly into MATLAB. For the fluid motion case, the files are first renamed and then imported into the TSI Insight 4G package for PIV vector processing. The system is allowed to settle for 10 minutes between tests.

4.3.2 Heat Transfer

The inclined tank is at an inclination angle of 30°, with the heated foil assembly and IR camera mounted to the tank. The high speed camera is set to record for up to 5 seconds at 400 Hz, writing files to the HSDR. The power supply is set to 63.9 A constant current, and the foil is allowed to reach an approximately uniform temperature by allowing surface heating for 10 minutes. The bubbles are injected in the same manner as for the bubble motion case and the temperature readings of the air and water thermocouples are also recorded. After each test, the power supply is powered off to prevent excessive heating of the bulk fluid between tests. The recorded images are saved as a FLIR `.sfmov` movie file, which purpose-written code converts into a three dimensional array of x, y temperatures and time in MATLAB. The system is allowed to settle for 10 minutes before the foil is switched back on for the next test.

Chapter 5

Experimental Analysis & Uncertainty

This chapter explains the techniques applied in the analysis, post-processing and interpretation of the data obtained using the experimental methods outlined in chapter 4. The three key areas in this study, namely bubble motion, fluid motion and heat transfer, will be discussed individually. The uncertainty associated with each of these measurements will also be quantified.

5.1 High Speed Image Processing

The raw images from the high speed camera are processed in MATLAB in order to obtain information about the sliding bubble mechanics. This requires high speed tracking of the bubble centroid and boundary. This study takes a novel approach to bubble tracking, using a combination of object-based tracking methods. The various steps of this tracking process are shown in figure 5.1 for the case of a streamwise in-line sliding bubble pair.

First, the images acquired from the high speed camera at 1000 Hz are exported as an uncompressed multi-page `.tif` file. This file is read into MATLAB as an image stack of grayscale images, each of resolution 800×1280 pixels. The mean of the first 10 images in the stack is assigned as the background image, without any bubble in-frame. For each frame in the stack containing a bubble, as in figure 5.1 (a), the generated background image is first subtracted. The resultant image is median filtered and converted to a binary image using Otsu's method [104]. This method selects a threshold value, th, to minimise the intra-class variance of a distribution of grayscale pixels by maximising the inter-class variance, i.e.

finding the optimal separation of a bimodal distribution. The thresholding algorithm uses this value to convert to binary with the equation:

$$g(x,y) = \begin{cases} 1 & if \quad f(x,y) > th \\ 0 & if \quad f(x,y) \leq th \end{cases} \tag{5.1}$$

The resulting binary image, shown in figure 5.1 (b), provides the bubble shape to single pixel precision. Occasionally, other regions on the image are also detected by the algorithm. These are typically several pixels in size, and can be removed by sorting the tracked regions in ascending size using the MATLAB function `regionprops`, which finds the properties of non-zero regions in a binary image. In addition to the area, this function can also be used to track the bubble centroid, bounding box (the smallest rectangle containing the full bubble) and convex hull (a per-pixel boundary of the object). When there are two large objects in frame (i.e. an in-line bubble pair), they are sorted based on the y-position of the centroid. This is provided the trailing bubble does not interact with or overtake the leading bubble, which is the case for the current study.

Traditional object tracking methods, also known as "blob analysis", often use this centroid value to define the mechanics of the bubble, including the velocity and acceleration. However, the accuracy of these measurements is limited by aliasing, as the bubble boundary is based off a per-pixel value. This results in a non-physical "jagged" bubble shape being tracked. More importantly, calculation of the centroid based on the average of these aliased edge points adds a bias error to the centroid calculation. This error is small in magnitude, with the centroids tracked in figure 5.1 (c) appearing accurate. However, significant issues arise when calculating the velocity and acceleration of the centroid based off this values, as this systemic error is multiplied by $2\pi \times 10^3$ and $(2\pi \times 10^3)^2$, respectively. Smoothing methods can be employed to reduce this noise; however, the current study takes a different approach. The methods outlined previously are employed, but are only used to find the bounding boxes around each bubble rather than the centroids. The bounding boxes are padded by 20 pixels in the x and y directions (figure 5.1 (c)), and are applied to the original background-subtracted grayscale bubble image. The image inside each box is subsequently sensitised and interpolated in order to increase the edge resolution. Sensitisation is achieved by converting to floating-point representation and performing median filtering and morphological closing. Morphological

closing probes the image with a structuring element, which in this case is a disk shape. Such operations do not rely on numerical values, but only on the relative ordering of the image, which makes this a useful method of detecting the approximately disk-shaped bubble and removing non-disk shaped noise. Interpolation using a spline method is subsequently used to increase the resolution by a factor of 4. This sensitised background-subtracted image is shown in figure 5.1 (d). A low-level contour function is applied to this image using the threshold value, th. This results in a reasonable sub-pixel representation of the bubble perimeter, shown in figure 5.1 (e). This can be performed to track both the leading and trailing bubbles to sub-pixel representation, as in figure 5.1 (f).

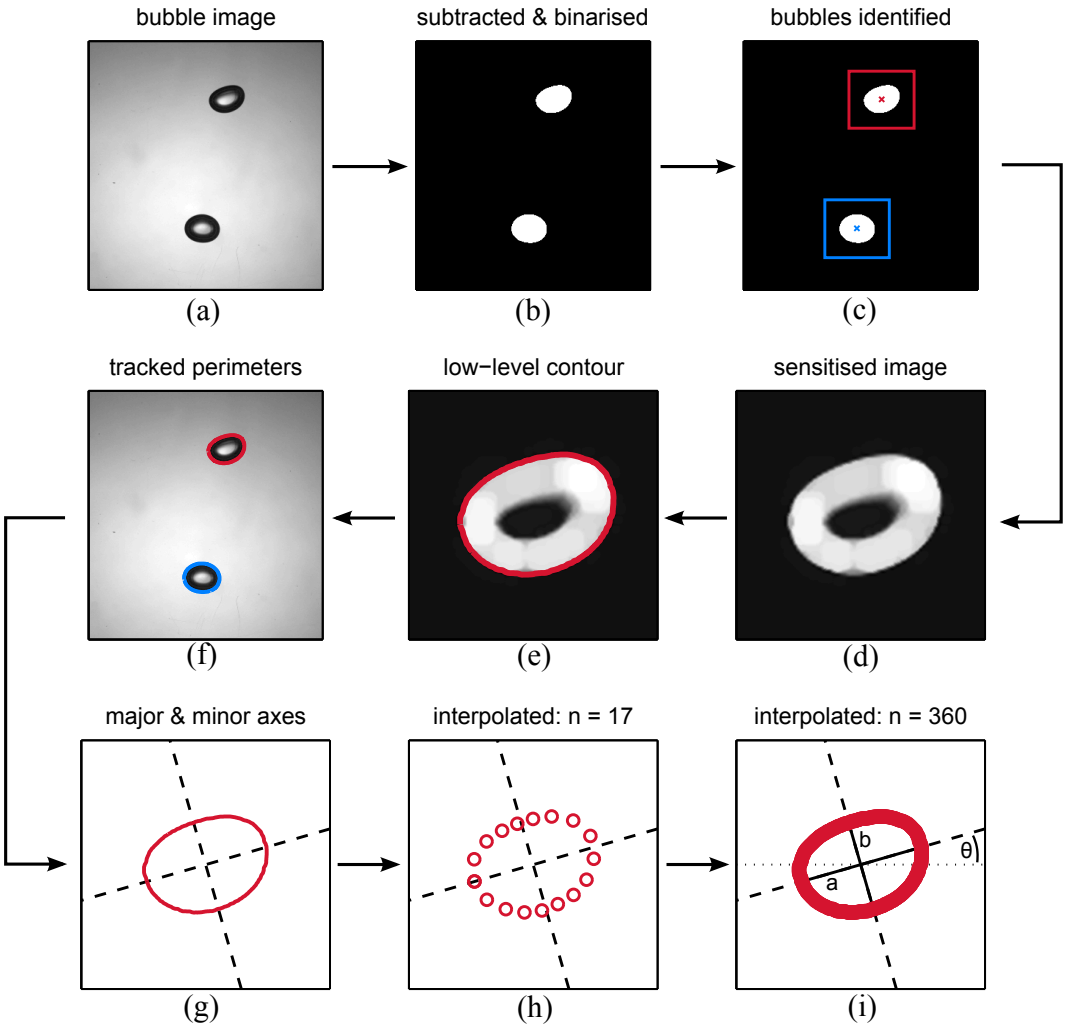

Figure 5.1: The image processing operations applied to each frame containing a bubble.

From this enhanced image, a more accurate description of the bubble centroid can be obtained. Traditional object tracking methods base the dynamics of the tracked body on the displacement of its centroid. Although this approach is physically sensible, its application to two-phase phenomena results in a loss in the rich dynamics of the bubble. This arises from the deformable bubble interface, experiencing complex changes in shape, particularly when captured in the wake of a leading bubble. To capture a more complete picture of the bubble dynamics, it would be advantageous to track the bubble interface, in addition to the centroid. This is not achievable with the bubble perimeter plots obtained thus far, as the number of points in the perimeter varies as a function of bubble shape, meaning that it would not be possible to track the evolution of a particular point on the bubble's edge. A method is therefore necessary to discern and track key edge points.

To interpolate the edge data to n points, some reference points on the bubble interface are necessary. In this study, the major and minor axes are used for this. These can be found based on the central moment of the edge data, which in two dimensions is the covariance matrix of the edge data. This involves applying a multivariate normal distribution to the perimeter data, with the contour lines of this distribution forming ellipses (i.e. the shape of the bubble). The directions and length of the ellipse's axes are given by the eigenvectors and eigenvalues of the covariance matrix of the edge data. The first eigenvector, which describes the bubble major axis, is the direction along the bubble in which the edge data experiences the greatest variance, while the second eigenvector (the minor axis) is the direction of greatest variance orthogonal to the first eigenvector. These form the known reference points on the bubble perimeter, and are shown in figure 5.1 (g). With these reference points found, the edge data is converted into polar coordinates and interpolated onto n points from $-\pi$ to π about the major and minor axes. This is shown in figure 5.1 (h) for $n = 17$. This results in the same number of tracked locations in each frame, meaning the behaviour at each of these points can be tracked spatio-temporally. In reality, the arbitrarily chosen $n = 17$ is too small to fully resolve this behaviour; 360 points around the bubble perimeter are used instead. Other useful data can also be derived from this representation of the bubble, such as the major and minor axis length (denoted by a and b respectively) and the bubble's orientation, θ, which is the inverse tangent of the major axis. In the current study, the shape of the bubble is considered in terms of its eccentricity, defined as the ratio of the distance between the two foci and the

major axis length. Eccentricity can be thought of as the extent of elongation of an ellipse, where 0 in this case is a perfect circle and 1 is a flat line, although these do not scale linearly. It is given by:

$$\varepsilon = \sqrt{1 - \left(\frac{b}{a}\right)^2} \tag{5.2}$$

This description has described a single iteration of the tracking algorithm. The algorithm performs the above steps for all images in the stack, finding the edge and centroid data in the manner outlined above. Finally, the image is calibrated by finding the length in pixels of a known length on the image (for all tests, this is the width of the PMMA surface). The mean of the bubble x-position is also subtracted such that the bubble fluctuates about a mean of $s_x = 0$.

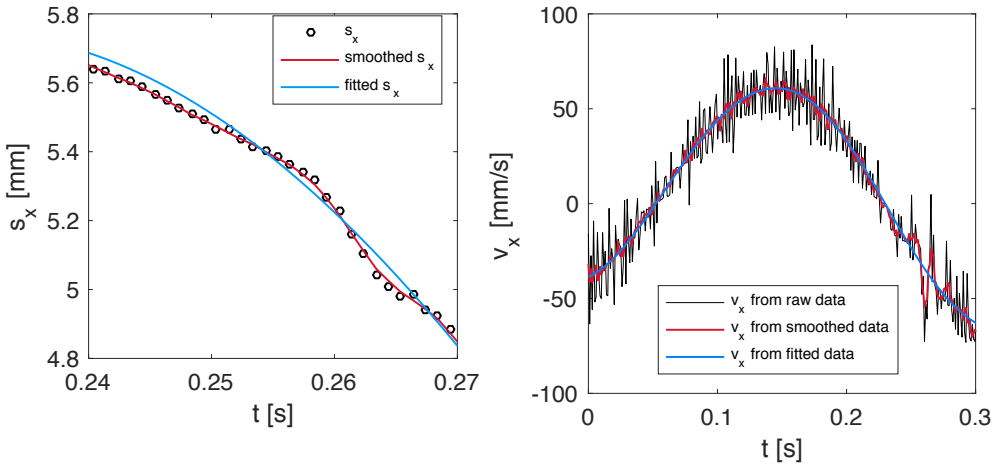

Figure 5.2: (a) zooming in on a section of the bubble x-position versus time graph for the raw s_x data, the same data smoothed with a low-pass filter and finally the same data fitted with a 6th order sum of sines fit. (b) propagation of these displacement fluctuations when calculating v_x for each of these three cases.

Even with this enhanced tracking capability, there are still issues when calculating derivatives. Figure 5.2 (a) shows that although the x-displacement versus time curve appears smooth, zooming in on a small region of the bubble path reveals minute fluctuations in the centroidal position. These are propagated if the bubble velocity and acceleration are calculated directly, resulting in the noisy data in figure 5.2 (b). A logical approach would be to apply a smoothing spline to the displacement data before taking its derivative. However, a basic low pass filter does not remove all of these fluctuations, as shown by the red line

in figure 5.2 (b). The smoothing in this figure remains too "faithful" to the errors in the centroidal tracking algorithm. However, smoothing further can run the risk of excessive smoothing, which can mean losing the real dynamics. This smoothing would also have to be optimised for each individual test, as the errors in centroidal calculation are different for each case (due to changes in lighting, reflections, bubble interface rebounds, etc.) This problem is solved by considering that the bubbles in the current study have an undulating, approximately sinusoidal path. Thus, by expressing the displacement in the x-direction as a sum of sinusoids, it is possible to both dramatically reduce the residual errors and be physically appropriate (blue lines on figure 5.2). Similarly, the y-displacement can be expressed as the superposition of the best-fit first-order polynomial (describing the mean vertical displacement due to buoyancy) and a sum-of-sines fit on the residuals of this polynomial.

These curve fits are applied to the displacement data using the in-built MATLAB curve-fitting toolbox. This fits a periodic function given by:

$$y = \sum_{i=1}^{n} a_i \sin(b_i x + c_i) \tag{5.3}$$

where a is the amplitude, b is the frequency and c is the phase content for each sine series. This equation bears similarity to a Fourier series, although it includes the phase constant c instead of an intercept term. The toolbox calculates optimised start points for the fit based on the data set. The calculation of the velocity and acceleration is simply the case of finding the first and second derivatives of these curves. The advantage of this approach is that it is a general case, which means that it can be applied to all tests without the need for further tuning. Furthermore, it is not limited to the centroid, and can be applied to any of the approximately sinusoidal curves traced by each point along the bubble interface.

Thus far, the bubble centroid, velocity and acceleration can be calculated directly from the edge data. Let us return to the 1-d force balance of Perron et al. [66] introduced in section 2.2. Using the same rationale, it is possible to calculate the forces in the x and y directions of the bubble by using Newton's second law $\Sigma F = ma$. This mass term takes into account both the mass of the air inside the bubble and the added mass of the fluid accelerated and displaced by the bubble. The symmetric added-mass tensor $\mathbf{C_M}$ depends only on the geometry of the body and confinement effects of the tank. This is characterised by the dimensionless

added mass coefficient, C_{AM}, which is the added mass divided by the displaced fluid mass. For small, spherical bubbles, Magnaudet & Eames [25] showed that $C_{AM} = 0.5$. For larger, deformable bubbles, the relationship is more complex, given by Klaseboer et al. [105] as $C_{AM} = 0.62\chi - 0.12$, where χ is the aspect ratio of the bubble.

Using a 1-d kinematics approach, this net force must be balanced by the buoyancy and drag forces. The equation of motion for the bubble in the streamwise direction can be written as:

$$C_{AM}V\frac{d^2s_y}{dt^2} = Vg\sin\alpha - \frac{\pi}{8}C_D\left(D\frac{ds_y}{dt}\right)^2 \tag{5.4}$$

Thus, given the dimensions and displacement of the bubble, it is possible to calculate the forces acting on the bubble in the spanwise and length directions, along with the fluctuating drag coefficient, C_D. This allows for comparisons with values obtained in the literature, which use a similar approach. However, it is important to note that this simplified analysis is fundamentally flawed and provides indicative values only for drag coefficient. This all stems from the limiting the bubble motion to a single degree of freedom to assess the force system results. In reality, the forces experienced by the bubble are complex and three-dimensional. For instance, this approach ignores the interaction between the bubble interface and the fluid or wall. The surface tension force, surface drag force, and Basset force will all be neglected by the model. Additionally, the added mass term is based only on the parallel projection of the bubble shape.

Therefore, the approach taken is as follows. The forces and drag coefficients calculated by this method will be presented and discussed briefly, since this was an approach that has been used in the literature. Furthermore, the force plots are simply the acceleration data scaled by the added mass term that changes only slightly with the bubble shape, meaning a discussion of the force analysis in this case is analogous to that of the accelerations experienced by the bubble.

5.2 Particle Image Velocimetry

In this section, the concepts behind the particle image velocimetry (PIV) measurement technique will be described. The key work describing PIV is the exemplary "Particle Image Velocimetry, A Practical Guide" by Raffel et al. [106]. PIV offers many advantages as a flow measurement technique as it is non-intrusive and offers whole-field measurements. The robust nature of PIV is due to its simplicity. It is based on the principle of illuminating small, neutrally buoyant seeding particles in the working fluid using a high intensity stroboscopic light sheet, and tracking the displacement of these particles in time. Tracer particles are assumed ideal if they follow the motion of the fluid exactly and do not alter the flow. The velocity is measured indirectly as a displacement $D(\mathbf{X};t',t'')$ of the tracer particles in a time interval $\Delta t = t'' - t'$. This is an integral approach [107], given by:

$$D\left(\mathbf{X};t',t''\right) = \int_{t'}^{t''} v\left[\mathbf{X}(t),t\right] dt \tag{5.5}$$

where $v\left[\mathbf{X}(t),t\right]$ is the velocity of the tracer particle. For ideal particles, the particle velocity v is exactly equal to the local fluid velocity, $u\left[\mathbf{X}(t),t\right]$. In reality, the particle velocity is an approximation of the local fluid velocity to within a finite error ε, that is:

$$\|D - u \,.\, \Delta t\| < \varepsilon \tag{5.6}$$

The error, ε, can be negligible in cases where the spatial and temporal scales of the flow are considerably larger than the spatial resolution and the particle lag.

Consider next the illumination of these particles. For spherical particles with a diameter d_P, the incident light experiences Mie scattering, proportional to the square of the particle diameter. The amount of light scattered by a particle due to Mie scattering is dependent on the angle between light sheet and camera, with the ideal case being a camera that is placed perpendicular to the light sheet. Ideally, the light sheet should be thin, of high intensity and have accurate timing control. For this reason, lasers are synonymous with PIV. Generally, the greater the sheet intensity is, the larger the signal-to-noise (SNR) ratio. Double-pulsed Nd:YAG lasers, which are based on neodymium-doped yttrium aluminium garnet, are commonly used in high speed PIV. A series of cylindrical concave lenses expand

the beam into a thin plane. These lasers allow a very short time delay between laser pulses, which is necessary for high speed flows.

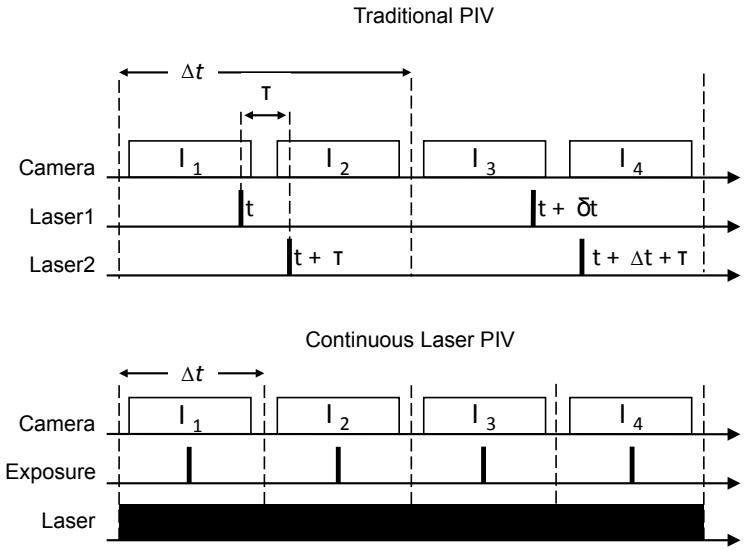

Figure 5.3: Laser and camera timings for (top) double-pulsed and (bottom) continuous PIV.

In the current study, the flow fields instead are evaluated frame-by-frame using a continuous wave laser, as opposed to the double-pulsed systems more common to stroboscopic PIV measurement. This is because temporal resolution of the time scales of the flow requires a very short repetition rate between successive image pairs: while double pulsed lasers can offer unbounded timing between each pulse (Δt), the time between successive image pairs does not usually permit time-resolved measurements, with most commercial PIV systems limited to just 15 Hz repetition rate. In this study, the relatively low flow velocity and the high frame-rate of the camera (and consequently short reciprocal exposure time) allows good stroboscopic imaging of the tracer particles, without streaking, in lieu of a high frequency double-pulsed laser. The difference between the two methods is highlighted in figure 5.3. Although the double-pulsed laser offers a very short time delay, τ, between the laser pulses, the time Δt is large, of the order of 15 Hz. Additionally, PIV can only be performed at every second set of frames I_{1-2}, I_{3-4}, etc. The timings for the continuous wave laser are shown in figure 5.3. In this case, the particles are illuminated with a continuous wave laser and are recorded using a high-speed camera. The "pulse" is now the camera exposure, and the Δt is the camera frame-rate. Using a continuous wave laser can therefore in many cases provide

extremely high temporal resolution at a fraction of the cost and complexity of double-pulsed systems. This comes with the caveat that the exposure time, in this case 30 μs, is much longer than the 5 *ns* for a pulsed Nd:YAG laser and the 100 *ns* of a pulsed Nd:YLF laser, meaning high-speed particle images are prone to streaking.

Once the particle images have been obtained, they are processed using the *TSI Insight 4G* software package. At its core, the PIV algorithm involves locating each tracer particle and measuring its distance travelled in the time Δt. Particles are tracked using correlation, which measures the similarity in intensity between two images. For instance, auto-correlation, or the similarity between an image matrix I_1 and itself, reaches its maximum value at $dx = 0$, $dy = 0$, or when the two images are perfectly aligned on top of one other. In three dimensions, the correlation at this point forms a positive peak. Mathematically, this can be expressed as:

$$C_{I_1,I_1}(s_x, s_y) = \int_A I_1(x,y) I_1(x+dx, y+dy) dxdy \tag{5.7}$$

In order to track the particles in time, cross correlation is used, correlating two successive images against each other. When performed between two image matrices I_1, I_2 that are Δt apart, the cross correlation has its maximum value when the two images are as similar as possible. This can be expressed as:

$$C_{I_1,I_2}(s_x, s_y) = \int_A I_1(x,y) I_2(x+dx, y+dy) dxdy \tag{5.8}$$

If the flow velocity is non-zero, the maximum correlation will no longer be at $[dx = 0, dy = 0]$, and instead will be at some finite integer value. This process would be trivial if the image contained just a single particle, but PIV requires a high particle density to resolve the full spatial and temporal scales of the flow, meaning the identification of individual particles can prove challenging. To achieve this, the PIV image is split into sub-windows called interrogation regions. Each of these regions is cross-correlated to the nearest pixel, with the strength of correlation determining the quality of the PIV. To move to sub-pixel accuracy, a 3-point Gaussian fit is performed in the horizontal and vertical direction on the cross-correlation map, with the peak position adjusted to the maximum of this fit. The correlation strength of PIV, denoted as R_D, is the value of the resultant peak. The cross correlation $C(s)$ can be expressed as:

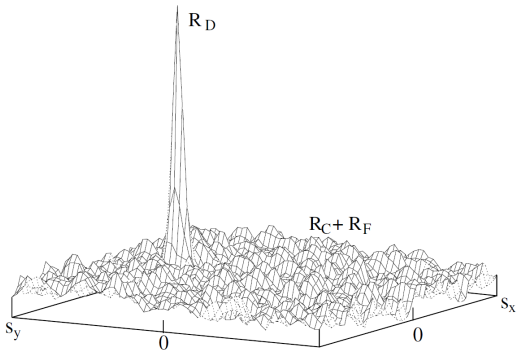

Figure 5.4: PIV correlation peak, taken from Raffel et al. [106]

$$C(s) = R_C + R_F + R_D \tag{5.9}$$

where R_C is the convolution of the mean intensities of the image (essentially the constant background level) and R_F is the correlation between the mean and fluctuating image intensities. These can be reduced by subtracting the mean image intensity from images I_1 and I_2, thereby increasing the signal-to-noise ratio. Figure 5.4 shows the contribution of the terms in equation 5.9 to a cross correlation.

The noise level of the correlation due to in-plane, out-of-window particle displacement cannot be solved by decreasing Δt. Instead, the interrogation windows are shifted by a distance dr. To determine this distance, multigrid analysis is used. First, the displacement calculation is performed based on a relatively large sub-window (in this case, 64×64 pixels). The displacement of this large sub-window, dr_1 is found, and the window shifted by this amount. Next, the displacement is calculated in a smaller sub-window of 32×32 pixels. The window is then shifted again based on this new displacement dr_2. This can be performed multiple times, with the total movement given as the sum of each displacement $dr = dr_1 + dr_2 + ...$ etc. Modern PIV algorithms can increase accuracy further by using window deformation, where images are deformed based on the surrounding predictors by a spline function, providing a greater amount of particles per interrogation window.

5.2.1 Vector Field Processing

An example of a typical parallel plane PIV image is provided in figure 5.5, showing that high quality particle images can be obtained without the use of a double-pulsed laser or fluorescent

tracer particles. Also visible is the saturation image at the bubble boundary due to minor reflections from the laser.

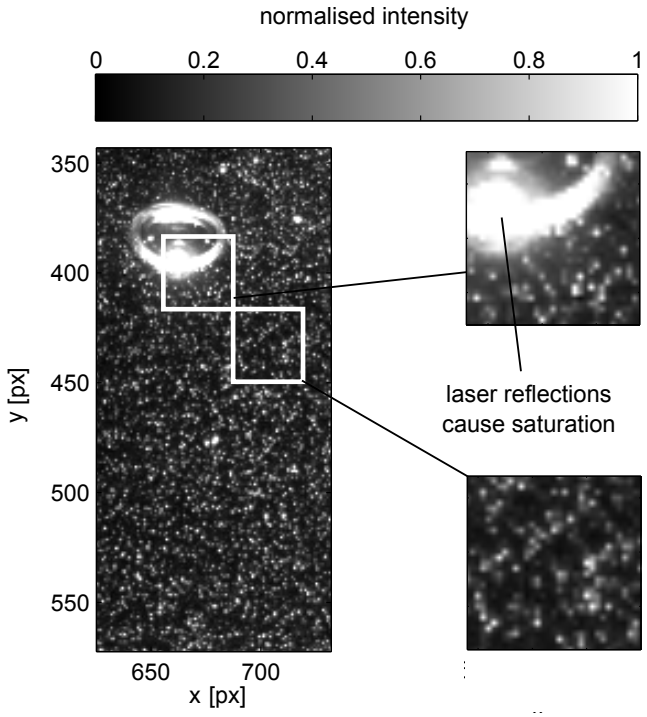

Figure 5.5: Raw PIV image showing bubble and minor reflections (left), zooming in on the two highlighted regions to show the particles per interrogation window and the saturation of near-bubble PIV (right).

All PIV vectors for the current study are evaluated using the Insight *4G V3V* package provided by TSI and are post-processed in MATLAB in order to present instantaneous velocity and vorticity plots. In the parallel plane tests, the PIV algorithm in Insight applies a multi-pass, multi-grid correlation with image deformation [108] and Gaussian sub-pixel fitting that decreases in size from 64 $\times$ 64 to 32 $\times$ 32 pixels, in 3 passes, applying a 50% window overlap for the first pass and a 75% overlap in the subsequent two passes. Figure 5.5 shows that there are significantly more than the minimum recommended 10 particles in each initial interrogation window contributing to the correlation.

To improve accuracy, the vectors are post-processed. Modern PIV algorithms possess options such as filling regions where the PIV algorithm has failed to identify a correlation peak by interpolating the local vectors, which is often used for time-averaged flows. However, the spatial and temporal scales of time-resolved flows make recursive hole filling a dangerous "black box" approach, returning data that at best are over-averaged and at worst are entirely

false. Thus, the current study places an emphasis on obtaining high-quality images rather than applying extensive post-processing techniques, with the only post-processing step applied being that of bad vector replacement. Occasionally, the primary correlation peak identified in correlation is an outlier, with a significantly higher RMS velocity than its neighbours. To correct for this, the algorithm also exports the second and third highest peaks from each correlation plane. If one of these two peaks are within the designated velocity range (i.e. < 1.5 times the RMS velocity of the neighbouring vectors), the bad vector is replaced with this new result. In the perpendicular plane, the same techniques are applied but with a smaller window size of 32 $\times$ 32 to 16 $\times$ 16 pixels.

The Insight software exports displacement and velocity data as `.txt` files. A purpose-written MATLAB algorithm reads in these files and performs a calibration based on a known distance on images taken in each plane. PIV yields the velocity gradient tensor, which the algorithm converts into a series of instantaneous 2-D representations of the velocity and vorticity fields. Vorticity describes the changes in the velocity vector in an infinitesimal distance perpendicular to the vector. Strictly, the vorticity, $\overrightarrow{\Omega}$, is a pseudovector field defined as the curl of the velocity vector $\mathbf{U}$. In a two dimensional field (x, y), the vorticity is parallel to the z axis. The vorticity, Ω_z, can thus be expressed as:

$$\Omega_z = \nabla \times \mathbf{U} = \left(\frac{dV}{dx} - \frac{dU}{du} \right) \overrightarrow{z} \tag{5.10}$$

Traditionally, PIV struggles to resolve vectors near solid boundaries, both fixed (i.e. near wall PIV) and moving (i.e. the bubble). In the current study, the PIV algorithm identifies the bubble as a collection of particles moving at the bubble velocity U_T. This makes it challenging to distinguish between the bubble and the near wake, which is in close association with the bubble at a velocity close to U_T. To amend this, the position of the bubble in the raw PIV images is also tracked in MATLAB. It is not possible to use the algorithm described in section 5.1, which requires a well-defined, sharp bubble boundary. Instead, the bubble is tracked using Otsu's method [104] from the median filtered raw PIV image for each frame containing a bubble. This returns the approximate bubble shape and path, allowing for a distinction between the bubble and the near wake.

The perpendicular measurement plane is fixed in space at $s_y = 60\ mm$ from the base of the

parallel plane interrogation window. This provides a view of the time-varying cross section of the fluid mixing in both the streamwise and normal directions. For these measurements, the phase angle, ϕ, is defined as the location along the bubble's undulating path at which it passes through the laser plane. The dependency of PIV measurements in this configuration on the phase angle will be explored in chapter 7. In this configuration, coherent regions of in-plane streamwise vorticity are identified at different instances in time. Thus, the methods of Zenit & Magnaudet [41] discussed in section 2.1.2 can be employed to reconstruct the streamwise wake structures to the rear of the bubble. This is achieved by converting the vorticity at different instances in time into a cross section of a vortex element, with the distance between adjacent cross sections Δs_y given by $\Delta s_y = U_b t$. Strictly, this method represents the Lagrangian vorticity at a short time (or short distances) behind the bubble. This can also be considered as an implementation of Taylor's frozen turbulence, which claims that if the turbulence intensity is sufficiently small, the advection contributed by turbulent circulations is small and the advection of the turbulence field can be attributed to the mean flow. This method cannot be used to show a complete three-dimensional wake structure, as it will become apparent that the flow structures downstream of the near wake are advected through the plane at a velocity considerably less than U_b. Indeed, it is not possible to solve this method from an Eulerian reference plane. Instead, the third dimension of the plots is the distance Δs_y, which describes the distance the fixed measurement plane is behind the bubble if it were to continue sliding indefinitely. Despite these limitations, this approach provides useful visualisations of the flow structures in a time/space plot, particularly in terms of the downstream mixing offered by the bubble.

5.2.2 PIV Effectiveness

Successful PIV measurements require the identification of the displacement correlation peak R_D, implying that it is advantageous to maximise its amplitude. Keane and Adrian [109] have studied this process in great detail, and have specified the following two "design rules" for PIV, which form a guide for determining PIV effectiveness. The first of these is:

$$N_I F_I F_O > 7 \tag{5.11}$$

In this equation, the term N_I refers to the number of particles per interrogation window, of which should be at least 10. The size of the particles in the PIV images is also an issue in determining PIV effectiveness, where optimal particle images are approximately 2 pixels in size. Above this value, random errors will spread the maximum cross-correlation over more than one pixel, while at low particle image sizes a phenomenon known as pixel locking (or peak locking) occurs. This effect is caused by the tendency of the sub-pixel Gaussian estimator to bias displacement values towards integer values. In figure 5.5, the average particle size is 2-3 pixels, while N_I is ≈ 35 in an interrogation window with no bubble but reduces in windows that are partially obscured by the bubble boundary. The influence of in-plane displacement on the loss of correlation, F_I, is given by:

$$F_I(\Delta x, \Delta y) = \left(1 - \frac{|\Delta x|}{D_I}\right)\left(1 - \frac{|\Delta y|}{D_I}\right) \tag{5.12}$$

where $\Delta x, \Delta_y$ are the particle displacements and D_I is the interrogation window size. To minimise this loss, the particle displacement $|\Delta x|$ should be less than $0.25D_I$, which is otherwise known as the quarter-window rule. However, a displacement of greater than 1 pixel is necessary due to bias errors. Typically, bias errors in PIV are reduced by optimising the pulse spacing Δt. For flows with a high dynamic range, defined as the ratio of the maximum to minimum resolvable displacement, or $DR_v = \Delta s_{max}/\Delta s_{min}$, very low displacements will be biased between 0 and Δs_{min}, creating low-level noise in low velocity regions. To increase the dynamic range, low velocity images (i.e. in the far wake of the bubble), are processed at larger separations Δt, to ensure a sufficiently large particle displacement, while a small amount of low-level noise due to bias errors in zero-velocity regions is tolerated in images with a high dynamic range (i.e. images of the near wake).

The quality of PIV is also linked to the out-of-plane loss of correlation F_O. Particular attention should be paid to this for the current study, where the flow structures are evolving in three dimensions. The loss in correlation F_O is given by:

$$F_O(\Delta z) = \left(1 - \frac{|\Delta z|}{\Delta z_0}\right) \tag{5.13}$$

The allowable out-of-plane displacement Δz is $|\Delta z| < 0.25\Delta z_0$, where Δz_0 is the light sheet thickness of 1.5 *mm*. Chapter 7 will show that in the current study the majority of the

fluid motion is parallel to the surface. This means that F_O is small for the parallel plane measurements. However, this creates some issues in the perpendicular plane, where the in-plane displacement is small. As a result, a compromise is required between processing at a larger Δt to allow for sufficient in-plane pixel displacement and preventing the Δz term exceeding the maximum allowable value. This means that effective PIV in the perpendicular measurement plane is not possible in the high-velocity regions in the near wake. At these instances in time, flow visualisation will be provided to deduce the fluid motion rather than PIV.

The second design equation developed by Keane and Adrian [109] describes the loss of correlation by spatial gradients and is given as:

$$M|\Delta U|\Delta t < d_\tau \tag{5.14}$$

where M is the magnification and $|\Delta U|$ is change in flow velocity. If the spatial gradients due to large shearing components or high acceleration are too large, the correlation strength decreases. Thus, the design rule of Keane & Adrian [109] recommends spatial gradients within the particle image diameter, or $\Delta(\Delta(x)) < d_\tau$, meaning that these gradients should be less than 2 pixels. Keane & Adrian [109] showed that if $N_I F_I F_O > 5$, the probability of a valid R_D peak being detected is greater than 90%. By obeying these design rules, high quality velocity data are obtained without interpolative filling or smoothing. For each test presented in this study, the in-built vector validation method of Insight 4G has been found to detect a valid R_D peak in every interrogation window.

5.3 Thermal Image Processing

This section details the techniques used to convert the temperature plots obtained from the thermal camera to the convective heat flux associated with the sliding bubble, q''_{conv}. For this energy balance, the relevant properties of the foil and paint layers are provided in table 5.1. Values for the paint density, thermal conductivity and heat capacity are taken from the work of Raghu & Phillip [110], who measured the thermal properties of paint samples using the PA scanning technique. The foil properties are provided by the manufacturers, Goodfellow,

while the foil and paint thickness are measured using a micrometer.

Table 5.1: [1] Foil properties for SS-316, provided by Goodfellow. [2] Thermal properties of paint samples, Raghu & Phillip [110].

	Thickness, δ $\times 10^{-6} m$	Density, ρ kg/m^3	Thermal conductivity, k W/mK	Heat capacity, C_p J/kgK
Foil	25 ± 1	7960 [1]	16.3 [1]	502 [1]
Paint	28 ± 3	1295 [2]	0.57 [2]	2835 [2]

As a first step in the thermal analysis, it is necessary to establish whether the temperature at the observation side of the foil can provide quantitative information on the convective heat transfer on the water side. This is achieved by performing a lumped thermal capacitance analysis on the system, which describes the temperature of a solid as spatially uniform at any instant in time during a transient process. To validate this method, the Biot number, Bi, is used. This is a dimensionless quantity that provides a measure of the temperature gradient in the solid relative to the temperature difference between the surface and the fluid. Incorpera et al. [111] stated if the Biot number is significantly less than unity, it can be assumed that the temperature is uniform within the solid at any time during the transient process, that is:

$$Bi = \frac{h_{max} L_c}{k} < 0.1 \tag{5.15}$$

where h_{max} is the highest heat transfer coefficient observed and k is the thermal conductivity of the material. L_c is the characteristic length of the surface, which reduces to a half-thickness, L, for a plane wall of thickness δ cooled from both sides (that is: $2L = \delta$). The maximum heat transfer coefficient observed during the tests is found to be $h_{max} = 1600\, W/m^2K$. Using this and the constants from table 5.1 results in a Biot number of 1.2×10^{-3} for the foil and 39.3×10^{-3} for the paint layer. This means that the lumped capacitance approach is valid for the current configuration and it is possible to proceed to the energy balance.

5.3.1 Element Energy Balance

Within the foil, heat generated by the Joule effect is dissipated by convection and other secondary heat transfer modes. The desired quantity is the convective heat flux, which can be found by performing an energy balance on a section of the foil. Consider a differential

control volume consisting of both the foil and paint layer, forming a cuboid of dimensions $dx \times dy \times (\delta_p + \delta_f)$. This is illustrated in Figure 5.6. Performing a conservation of energy balance on this volume yields:

$$\dot{E}_{in} + \dot{E}_{gen} - \dot{E}_{out} = \dot{E}_{st} \tag{5.16}$$

where $\dot{E}_{in}$ and $\dot{E}_{out}$ describe the energy transport across the surfaces of the control volume, $\dot{E}_{gen}$ is the thermal energy generated within the control volume and $\dot{E}_{st}$ is the thermal energy stored within the control volume. Note that heat is transferred through adjacent foil elements by lateral conduction, and from the air and water sides by a combination of conduction, radiation and convection. By taking the approach outlined in Incropera et al. [111] and Stafford et al. [91] to find the constituent terms in figure 5.6 and grouping like terms together, the following expression is obtained:

$$\begin{aligned} q_{x,f} + q_{y,f} + q_{x,p} + q_{y,p} + \dot{q}_{gen} dx dy \delta_f - \\ q_{x+dx,f} - q_{y+dy,f} - q_{x+dx,p} - q_{y+dy,p} - \\ q_{conv} - q_{cd} - q_{rad} - q_{cap} = 0 \end{aligned} \tag{5.17}$$

where the q terms are in Watts. The subscripts f and p denote heat transfer through the foil and paint layer, respectively, $\dot{q}_{gen}$ is the heat generated by Joule heating, q_{rad} is the rate of radiative exchange from the foil to the surroundings, q_{cd} is the heat loss on the air side of the foil and q_{conv} is the convective heat loss from the foil; this is the desired parameter. Additionally, as the experiment is not steady state, the energy stored within the foil is non-zero, meaning the term q_{cap} must be added to describe the changes in internal energy within the control volume in response to temporal fluctuations in surface temperature. By representing the conduction heat flux perpendicular to the control volume edges at x and y using Fourier's law, equation 5.17 can be rewritten as:

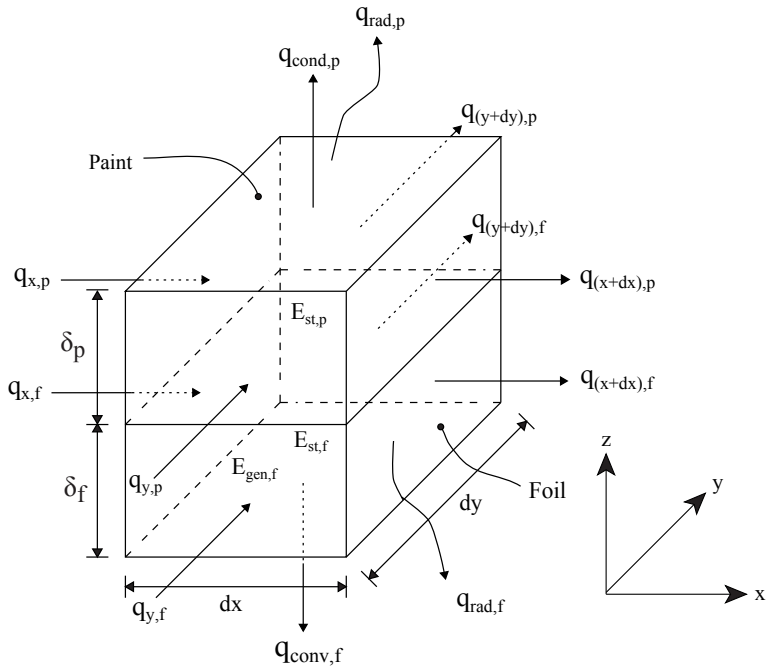

Figure 5.6: Illustration of heat transfer through a single element with a surface area of $dx \times dy$ with thickness of, δ_{foil}, δ_{paint} for the foil and paint layer respectively.

$$\left(k_f\delta_f + k_p\delta_p\right)\left(\frac{\partial^2 T}{\partial x^2} + \frac{\partial^2 T}{\partial y^2}\right)dxdy + \dot{q}_{gen}\delta_f dxdy - q''_{conv}dxdy - q''_{cd}dxdy - q''_{rad}dxdy - q''_{cap}dxdy = 0 \quad (5.18)$$

It is assumed that the electrical energy generation is distributed evenly through out all the elements within the foil, meaning the Joule heating can be calculated on an element by element basis. This energy balance is thus applied to every pixel of the thermal image, therefore $dx = dy$. Dividing by dx^2 we can arrange the energy balance in terms of q''_{conv} as:

$$q''_{conv} = q''_{gen} - q''_{cond} - q''_{rad} - q''_{cap} - \left(k_f\delta_f + k_p\delta_p\right)\left(\frac{\partial^2 T}{\partial x^2} + \frac{\partial^2 T}{\partial y^2}\right) \quad (5.19)$$

Each constituent term in equation 5.19 will now be examined. For each of the fluctuating terms, a figure showing the surface temperature distribution and heat flux at the bubble will be provided. The heat generated within each element by the Joule effect is:

$$q''_{gen} = \frac{I^2_{elec}R_{elec}}{dx^2} \quad (5.20)$$

where I_{elec} is the current through one foil element of resistance R_{elec}. This resistance of the foil can be found using:

$$R_{elec} = \rho_{elec} \frac{w}{A_{cs}} \tag{5.21}$$

where ρ_{elec} is the electrical resistivity of the foil, w is the length of foil parallel to the current flow (i.e. the width of the foil) and A_{cs} is the cross-sectional area, i.e $\delta_f \times l$. The power generated by one volumetric element of size $\delta_f \times dx^2$, is calculated by splitting the foil into elements of size dx^2. To verify this calculation, the voltage drop across the foil was measured using a voltmeter, providing a value for q''_{gen} within 2% of that determined from equation 5.20.

On the observation side, the mode of heat transfer is natural convection. However, the majority of the natural convection correlations provided in the literature are for the mean Nusselt number, which is not applicable to time-variant systems. The purpose of the sapphire glass is to create a stagnant air gap above the foil that limits the heat lost to the air to one-dimensional conduction. This is only the case if there is no recirculation in the air gap. For a rectangular cavity, Ostrach [112] showed that for any inclination angle α, there is no flow within the gap if the Rayleigh number is less than a critical value. That is:

$$Ra_{L,c} = \frac{1708}{\cos \alpha} \tag{5.22}$$

Although this critical Rayleigh number initially appears very small, its associated characteristic length is the thickness of the cavity, z, which in this case is only 3 mm. Although the temperature at inside of the sapphire glass layer is not known, an unrealistic worst-case scenario of $T_s - T_{glass} = 25°C$ is still two orders of magnitude less than the critical value for flow to occur. Thus, in the air gap, Fourier's law can be applied, yielding:

$$q''_{cd} = k_{air} \frac{dT}{dz} \tag{5.23}$$

where k_{air} is the thermal conductivity of air and dT/dz is the temperature gradient across the air gap to the glass. This temperature gradient is measured using the embedded thermocouple and assumes a uniform gradient across the entire gap, i.e. $d^2T/dz^2 = 0$. This calculated

conductive heat flux is shown for typical temperature distribution in figure 5.7, alongside the surface temperature, with positive heat transfer indicating heat transfer from the air gap into the foil.

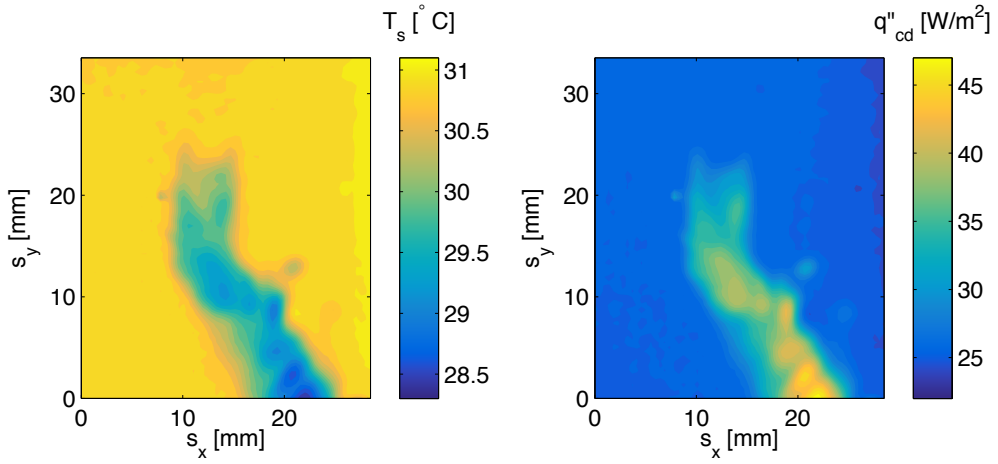

Figure 5.7: (a) Instantaneous surface temperature and (b) instantaneous conduction within the 3 *mm* air gap, q''_{cd} for $d_e = 5.7$ *mm*, $\alpha = 30°$ and a mean superheat $\Delta T = 10°C$. Positive values indicate heat flow into a foil element.

Note the conduction levels in figure 5.7 indicate that heat is in fact flowing from the air gap into the foil. It has been established that this is due to the copper busbars, which form the sides of the air gap, being at a temperature of $50°C$ and thereby heating the air to above the foil temperature. However, since the Rayleigh number remains sufficiently low to prevent recirculation within the air gap, the sole mode of heat transfer remains 1-D conduction into the foil. As such, the temperature gradient, be it positive or negative, can be inferred by the thermocouple. This term contributes under 1% to the overall convective heat flux, as will become apparent presently.

Heat is also transferred from the foil to the surroundings via radiation, although this term is small due to the comparatively low wall superheats under investigation. The radiative heat loss is negligible on the water side due to the low emissivity of stainless steel and the fact that the adjacent water is opaque. On the observation side, the heat lost from radiation can be estimated by:

$$q''_{rad} = \varepsilon\sigma\left(T_s^4 - T_{surr}^4\right) \tag{5.24}$$

where ε is the surface emissivity, σ is the Stefan-Boltzman constant, T_s is the surface temperature and T_{surr} assumes the surrounding walls are at the ambient air temperature. The instantaneous heat flux due to radiation, q''_{rad}, is illustrated in figure 5.8 for the same case as figure 5.7.

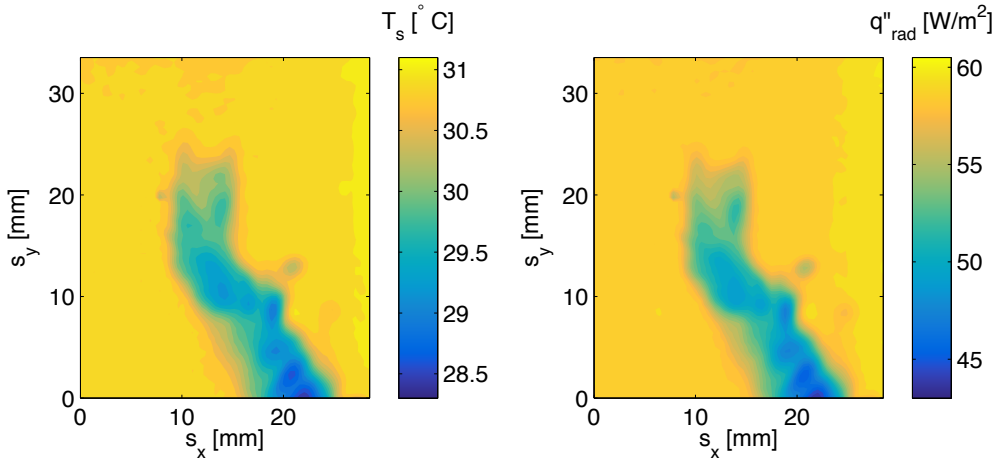

Figure 5.8: (a) Instantaneous surface temperature and (b) instantaneous heat transfer by radiation, q''_{rad}, from the foil to the surroundings.

The heat transfer through lateral conduction within the foil, q''_{lc}, requires calculation of the Laplacian, $\nabla^2 T$, of the surface temperature field. It is given by:

$$q''_{lc} = \left(k_f \delta_f + k_p \delta_p\right)\left(\frac{\partial^2 T}{\partial x^2} + \frac{\partial^2 T}{\partial y^2}\right) \tag{5.25}$$

where δ and k are the thickness and thermal conductivity of the foil or paint from table 5.1. The Laplacian is solved by the MATLAB function `grad`, which implements the central-difference method to solve the spatial derivatives in the main field and automatically switches to first order differences near the edges of the field. Additionally, a median filter is applied to the temperature data before the derivatives are taken, as applying a second order partial derivative to noisy data acts to amplify the noise. Figure 5.9 shows that this term is larger than either the conduction or the radiation.

Finally, the unsteady term that accounts for the storage effects within the foil, q''_{cap}, can be quantified using the relation:

$$q''_{cap} = \left(\rho_f C p_f \delta_f + \rho_p C p_p \delta_p\right)\frac{\partial T}{\partial t} \tag{5.26}$$

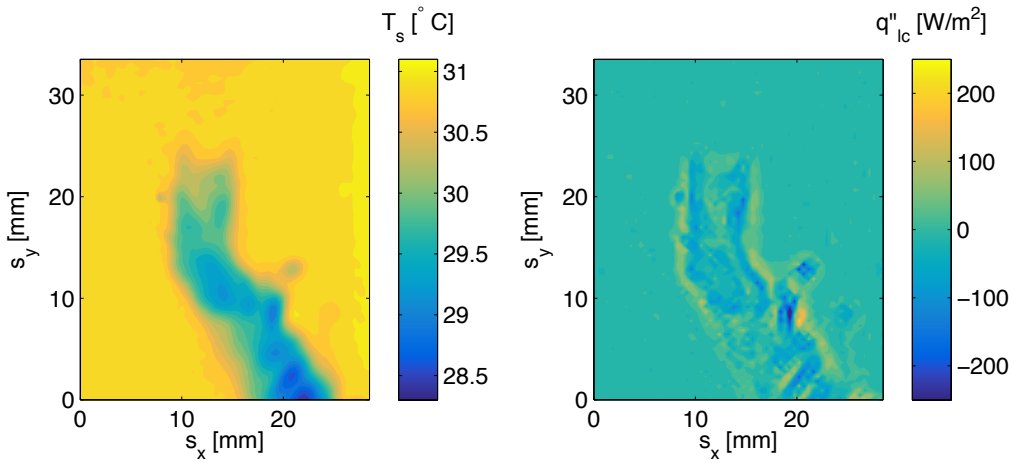

Figure 5.9: (a) Instantaneous surface temperature and (b) instantaneous heat transfer due to lateral conduction, q''_{lc}. Positive values indicate heat flow into a foil element.

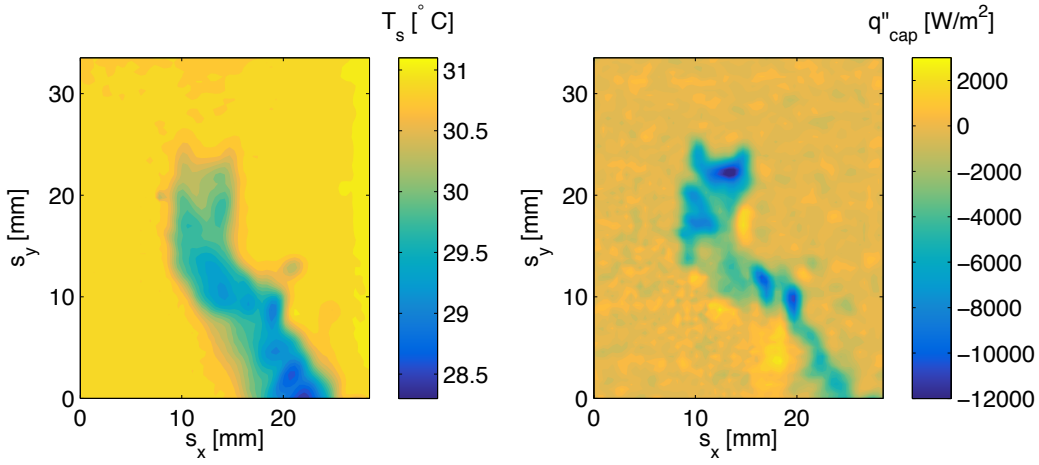

Figure 5.10: (a) Instantaneous surface temperature and (b) energy storage term, q''_{cap}.

where ρ and Cp are the density and the specific heat, respectively, of an element, and $\frac{\partial T}{\partial t}$ is the change in temperature with respect to time. This term is extremely sensitive to noise from the infra-red camera sensor. To reduce noise, the surface temperature at each instant in time, T_s, is weighted over 5 images, from T_{t-2} to T_{t+2}, with the temperature data filtered using Pascal's Triangle. Furthermore, the temporal derivative is calculated as the gradient of 5 instances of T_s. As the cooling phenomenon under investigation is rapid and transient, a large value of $\frac{\partial T}{\partial t}$is observed. This contributes to a storage term that dominates the energy balance, with maximum flux values in excess of 60 times that of the next largest term (lateral conduction). This means that the experimental results are strongly dependent on the properties of the

foil and paint and on the temporal resolution of the camera. The impact of this term on the uncertainty of measurement will be discussed further in section 5.4.

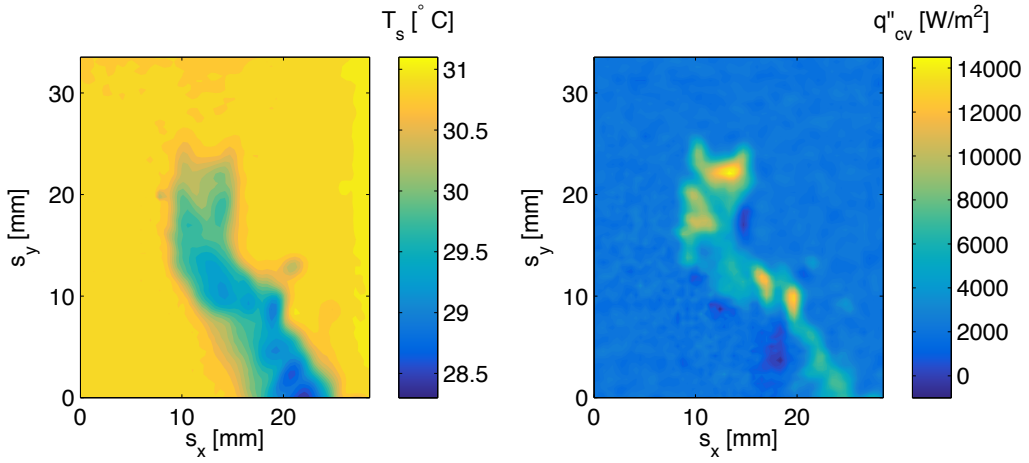

Figure 5.11: (a) Instantaneous surface temperature and (b) instantaneous convective heat flux from the foil to the bulk fluid, q''_{conv}.

Figure 5.11 shows the resultant convective heat flux, q''_{conv} ,where positive heat transfer indicates heat flow from the surface to the bulk fluid. It is also observed that although the bubble significantly enhances the convective heat transfer, it also creates some small local regions of negative heat flux. This is in agreement with the findings of Donoghue et al. [80] and will be discussed in greater detail in chapter 9.

5.3.2 Natural Convection

When the foil is heated, there exists a relative motion between the cooler fluid in the liquid bulk and the warmer fluid adjacent to the surface. The heated fluid is less dense than the surrounding fluid and rises, but is impeded slightly by the inclined surface, meaning the heat transfer due to natural convection is not as effective as transferring heat to the fluid as if it were upwards-facing and horizontal. Thus, the thermal boundary layer that exists at the surface changes with the distance s_y, and consequently so too does the surface temperature. A number of Nusselt number correlations exist for heated inclined surfaces, although these typically relate to constant surface temperature boundary conditions rather than the constant flux boundary condition in the current study. Rich [113] suggested that natural convection coefficients could be determined for vertical plate correlations by replacing g with $g\sin\alpha$

when computing the Grashof number, and to use this modified Grashof number to solve the problem as if it were a vertical plate. A Nusselt number correlation valid for the entire range of Ra_L is that of Churchill and Chu [114]:

$$Nu = \left(0.825 + \frac{0.387 Ra^{\frac{1}{6}}}{\left[1 + (0.492/Pr)^{\frac{9}{16}} \right]^{\frac{8}{27}}} \right)^2 \tag{5.27}$$

Alternatively, an empirical correlation for Nusselt number at a uniform surface temperature was developed by Fujii & Imura [115]. Taking the temperature at $L/2$ to be the mean surface temperature, the Nusselt number is:

$$Nu = 0.56(GrPr\cos\alpha)^{\frac{1}{4}} \tag{5.28}$$

where α is measured from the vertical and the characteristic length scale is the length of the surface, L. For this relation, the fluid properties are calculated at a modified film temperature, $T_f = T_s - 0.25(T_s - T_\infty)$ and the volumetric expansion coefficient, β, at the film temperature.

The correlations thus far have assumed an infinite bulk fluid. In reality, the glass tank forms an enclosure that inhibits free convective fluid flow. There exists a number of correlations for the Nusselt number in an inclined enclosure which may be more applicable to the current study than those in an infinite fluid. For laminar natural convection in a rectangular enclosure heated from the side with an aspect ratio (H/L), where H is the s_y dimension of the heated foil and L is the distance from the foil to the base of the tank, Berkovsky & Petrov [116] suggested the following correlations:

$$\overline{Nu_H}(90^\circ) = 0.22 \left(\frac{Pr}{0.2 + Pr} Ra_H \right)^{0.28} \left(\frac{L}{H} \right)^{0.09} \tag{5.29}$$

which is valid for $2 < H/L < 10$, $Pr < 10^5$, $Ra_H < 10^{13}$, and:

$$\overline{Nu_H}(90^\circ) = 0.18 \left(\frac{Pr}{0.2 + Pr} Ra_H \right)^{0.29} \left(\frac{L}{H} \right)^{-0.13} \tag{5.30}$$

which is valid for $1 < H/L < 2$, $10^{-3} < Pr < 10^5$, $Ra_H Pr/(0.2 + Pr) > 10^3$. In the current study, $\frac{H}{L} \approx 2$, meaning both equations for Nu can be used. For an inclined enclosure with

the heated surface on top, the Nusselt number is lower than this, since the surface restricts the motion of the fluid. For an inclination angle, α, between 0° and 90°, the Nusselt number obtained by equation 5.29 or 5.30 is modified using the correlation of Caton [117]:

$$\frac{L}{H}\overline{Nu_H}(\alpha) = 1 + \left[\frac{L}{H}\overline{Nu_H}(90^\circ) - 1\right] sin\alpha \tag{5.31}$$

All of the relations thus far are for a uniform wall temperature, whereas in reality the heated foil is at a nominal uniform wall flux. In solving these equations, T_s is taken to be the temperature at $L/2$. The heat transfer coefficients obtained from these various correlations are shown in table 5.2. Note there is significant deviation between the heat transfer coefficients obtained.

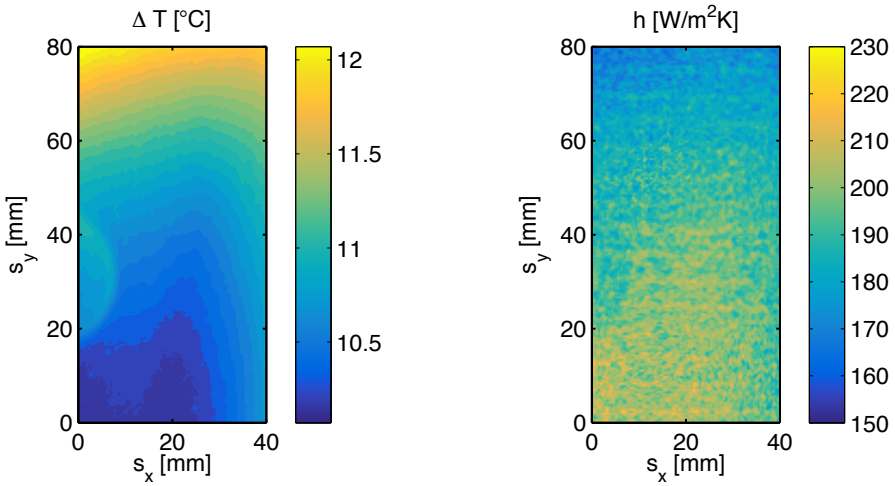

Figure 5.12: (a) surface to bulk water temperature difference $\Delta T = T_s - T_\infty$ and (b) instantaneous convective heat flux from the foil to the bulk fluid, q''_{conv}.

Figure 5.12 shows the experimental surface temperature and heat transfer coefficient due to natural convection. For the current study, the experimentally obtained heat flux due to natural convection is approximately 2100 W/m^2, while h is found using the relation $q'' = h\Delta T$. Thus, the experimental value for the heat transfer coefficient at a wall superheat of $T_e = 10^\circ C$ is $\approx 220\ W/m^2K$, although this decreases further up the foil due to the thermal boundary layer. This is within 7% of the value calculated from equation 5.29 for a cavity with $\frac{H}{L} \approx 2$. The correlations for an infinite bulk fluid provide far larger values for heat transfer coefficient, suggesting that the confinement effects of the glass tank are significant.

Table 5.2: Natural convection heat transfer for a downward facing inclined heated surface.

Equation	Ra	Nu	h $[W/m^2K]$
5.27	1.44×10^{10}	351	946
5.28	1.44×10^{10}	194	524
5.29 and 5.31	2.88×10^{10}	87.9	237
5.30 and 5.31	2.88×10^{10}	106	287

5.4 Uncertainty Analysis

This section will detail the methods employed to determine the uncertainty in the calculations for the three experimental configurations. Errors or uncertainties can generally be classified into two categories, namely precision and bias errors. Precision errors, also known as random errors, can come from a variety of sources, most often the "least count" of an analog scale. Precision errors cause scatter in experimental data, which can be quantified by means of statistical analysis. Bias errors, also known as systemic errors, are due to deviations that are not due to chance alone. For instance, an improperly calibrated device will consistently over or under-predict a measurement.

5.4.1 Precision Uncertainties

In the case of determining single point measurements, such the paint thickness measurement, the standard error is required. The mean of N samples x_i is:

$$\bar{x} = \frac{1}{N} \sum_{i=1}^{N} x_i \tag{5.32}$$

If the measured values scatter about this mean, it allows for a calculation of the standard deviation, S_x, as:

$$S_x = \sqrt{\frac{1}{N-1} \sum_{i=1}^{N} (x_i - \bar{x})^2} \tag{5.33}$$

The standard error of the mean is the standard deviation of the sample-mean's estimate of a population mean, $S_{\bar{x}}$, which is:

$$S_{\bar{x}} \cong \frac{S_x}{\sqrt{N}} \tag{5.34}$$

This analysis is used where the output of the system does not depend on the input. For situations where this is not the case (i.e. fitted curves), an analogous approach is taken. For a least-squares curve fit of a data set (x_i, y_i), a linear fit of the data set is replaced by (x_i, Y_i). Analogous to the standard deviation of a sample, the standard error for a curve-fit is as follows:

$$S_Y = \sqrt{\frac{1}{N-2}\sum D_i^2} \tag{5.35}$$

where $D_i = Y_i - \hat{Y}$ and $\hat{Y}$ is the result from the least squares fit $\hat{Y} = mx + c$. Given a curve fit, it would be advantageous to estimate the probable error in a measurement, otherwise known as precision uncertainty. If we are a certain percentage $C\%$ confident that the true value of a measurement X_i lies in the interval $X_i \pm P_X$, P_X is therefore the precision uncertainty at a confidence level of $C\%$. Typical studies take $C = 95\%$ [118]. Thus, the precision errors for the curve fit of data (x_i, Y_i) is:

$$P_{\hat{Y}} = t_{\nu,\%}\sqrt{S_Y^2\left[\frac{1}{N} + \frac{(x-\bar{x})^2}{S_{xx}}\right]} \tag{5.36}$$

where S_Y is the standard error as defined by Equation 5.35 and the value $t_{\nu,\%}$ encloses 95% of a t-student distribution with $\nu = N-2$ degrees of freedom. Finally:

$$S_{xx} = \sum x_i^2 - \left(\frac{1}{N}\right)\left(\sum x_i\right)^2 \tag{5.37}$$

Thus, it is the precision of the curve fit that is of interest when determining uncertainty, rather than the precision of any one data point that makes up the curve. Equation 5.36 is applied to all fitted curves in the current study to evaluate their associated uncertainty.

5.4.2 Propagation of Precision Uncertainties

Consider a result r, which is determined from the values of J measured variables X_i that are statistically independent. That is:

$$r = r(X_1, X_2, \ldots, X_J) \tag{5.38}$$

This section concerns the propagations of uncertainties in X_i into the result r. The overall uncertainty in r can be solved using the Taylor series method (TSM). Coleman and Steele [119] derived the uncertainty in the result, U_r, as:

$$U_r{}^2 = \left(\frac{\partial r}{\partial X_1}\right)^2 U^2{}_{X_1} + \left(\frac{\partial r}{\partial X_2}\right)^2 U^2{}_{X_2} + \ldots + \left(\frac{\partial r}{\partial X_J}\right)^2 U^2{}_{X_J} \tag{5.39}$$

where the U_{X_i} are the uncertainties in the variables X_i. This equation can be non-dimensionalised by dividing both sides by r^2 and multiplying each term on the right-hand-side by $(X_i/X_i)^2$. This gives:

$$\frac{U_r{}^2}{r^2} = \left(\frac{X_1}{r}\frac{\partial r}{\partial X_1}\right)^2 \left(\frac{U_{X_1}}{X_1}\right)^2 + \left(\frac{X_2}{r}\frac{\partial r}{\partial X_2}\right)^2 \left(\frac{U_{X_2}}{X_2}\right)^2 + \ldots + \left(\frac{X_J}{r}\frac{\partial r}{\partial X_J}\right)^2 \left(\frac{U_{X_J}}{X_J}\right)^2 \tag{5.40}$$

where U_r/r is the relative uncertainty of the result. In this section, equation 5.40 is solved for the bubble motion and heat transfer analyses.

5.4.3 Uncertainty in Bubble Motion

In tracking the bubble motion, we will consider the base case of $\alpha = 30^\circ$ $d_e = 5.8$ *mm*. The uncertainty in bubble displacement is dependent on the precision errors of the curve fits that are applied to the displacement data in the s_x and s_y directions. For $\alpha = 30^\circ$ $d_e = 5.8$ *mm*, this is equivalent to a mean value of ± 0.02 *mm* in both directions at a confidence level of 95%. The displacement, s, between the bubble centroid $[x_1, y_1]$ at time t_1, and $[x_2, y_2]$ at time t_2 is:

$$s = \sqrt{(x_2 - x_1)^2 + (y_2 - y_1)^2} \tag{5.41}$$

Thus, by applying equation 5.39 to this expression, the uncertainty in displacement can be found:

$$U_s^2 = \left(\frac{\partial s}{\partial X_1}\right)^2 U^2{}_{X_1} + \left(\frac{\partial s}{\partial X_2}\right)^2 U^2{}_{X_2} + \frac{\partial s}{\partial Y_1}{}^2 U^2{}_{Y_1} + \left(\frac{\partial s}{\partial Y_2}\right)^2 U^2{}_{Y_2} \tag{5.42}$$

where $U^2{}_{X_1}$, $U^2{}_{X_2}$ etc. are the 95% confidence limits in each of the 6th order sum-of-sines

curves fitted to the centroid data. Finally, the value U_s is divided by its displacement s to find its relative uncertainty. Since the bubble velocity fluctuates as it traverses the surface, so too does its displacement. Thus, the quantities here are averaged over the whole test. Furthermore, the relative uncertainty in position, U_s/s is a function of the camera frame-rate. When sampling at 1000 Hz, $U_s/s = 12.8\%$. In reality, this represents a worst-case scenario. Recall from figure 5.2 that although the bubble displacement curve appears smooth, the bubble algorithm introduces low-level noise. This noise has the additional effect of increasing the size of the 95% confidence limits, thereby increasing the relative uncertainty. To reduce the relative uncertainty when calculating quantities that are a function of the bubble velocity, the frame-rate is halved. While this decreases the temporal resolution, this doubles the displacement s, meaning $U_s/s = 6.4\%$. The Phantom v311 specifications features a 500 ns inter-frame time. For a worst case scenario, this value is doubled, which gives $U_{\Delta T}/\Delta T = 0.05\%$. Due to the high timing accuracy of the camera, the velocity uncertainty, U_v/v, and acceleration uncertainty, U_a/a, are also 6.4%.

The accuracy in α, measured using a digital micrometer, is $\pm 0.05^\circ$, which results in a relative uncertainty of 0.2%. For the added mass coefficient, an error is introduced into the major and minor axes. Since the aliased image is interpolated and sensitised by a factor of 4, it is assumed that the uncertainty in calculating the major and minor axes is $\pm\frac{1}{4}\ px$, which results in a relative uncertainty in the added mass coefficient, $U_{C_{AM}}/C_{AM}$, of 5.1%. In terms of the bubble volume, a low flow rate and small syringe needle, combined with visual inspection of the raw bubble images, results in a relative uncertainty of 5%. This corresponds to an uncertainty in bubble diameter of 1.7%.

This approach can also be used to find the uncertainty in the force and and added mass terms. This is more for illustrative purposes, since the 1-d kinematics approach itself is fundamentally flawed. The uncertainty in force measurement is:

$$\left(\frac{U_F}{F}\right)^2 = \left(\frac{U_{C_{AM}}}{C_{AM}}\right)^2 + \left(\frac{U_V}{V}\right)^2 + \left(\frac{U_a}{a}\right)^2 = (5.11\%)^2 + (5\%)^2 + (6.44\%)^2 \qquad (5.43)$$

This gives a relative uncertainty of 9.6%. Finally, the uncertainty in the derived drag coefficient is a function of added mass, bubble diameter, acceleration, velocity and inclination

angle, given by:

$$\left(\frac{U_{C_D}}{C_D}\right)^2 = \left(\frac{C_{AM}a}{C_{AM}a - gsin\alpha}\right)^2 \left(\frac{U_{C_{AM}}}{C_{AM}}\right)^2 + \left(\frac{C_{AM}a}{C_{AM}a - gsin\alpha}\right)^2 \left(\frac{U_a}{a}\right)^2 + \left(\frac{g\alpha cos\alpha}{C_{AM}a - gsin\alpha}\right)^2 \left(\frac{U_\alpha}{\alpha}\right)^2 + \left(\frac{U_{d_e}}{d_e}\right)^2 + 4\left(\frac{U_v}{v}\right)^2 \quad (5.44)$$

This results in an uncertainty in calculating the drag coefficient of 12.9%. The results for the relative uncertainty in bubble motion are summarised in table 5.3 for $d_e = 5.8\ mm$ and $\alpha = 30^\circ$. The major source of the uncertainty in these calculations is the scatter in the centroid of the bubble tracking algorithm. This is an inherent limitation of basing the bubble mechanics on the centroid, as it is based on the average of the dynamically changing bubble interface. Therefore, it is likely to be the changes in bubble shape and the rebounding of the interface that are causing the scatter in centroid data, rather than the capabilities of the bubble tracking algorithm.

Table 5.3: Relative uncertainty for measured and derived parameters

Measurement	Symbol	Uncertainty [%]
Position	s	6.4
Time	t	< 0.1
Velocity	v	6.4
Acceleration	a	6.4
Diameter	d_e	1.7
Inclination angle	α	0.2
Added mass coefficient	C_{AM}	5.1
Force	F	9.6
Drag coefficient	C_D	12.9

5.4.4 Uncertainty in Fluid Motion

The last twenty years have seen a massive expansion of PIV as a flow measurement and analysis technique. However, a rigorous framework regarding the uncertainty of these methods was not in place during this expansion. As a result of this, there is no one unified theory to quantify PIV measurement uncertainty. This is a major issue facing PIV, especially since measurements involve the coupled uncertainty of the instrumentation and the algorithm.

Developing a fundamental methodology in quantifying this uncertainty is a significant challenge currently facing the PIV community [120], and different methods for estimating the local uncertainty have been studied. Wilson and Smith [121] compared PIV velocity fields to the known particle displacement for a rectangular jet flow. For a specific combination of displacement, shear, particle image density and particle image diameter, the four-dimensional uncertainty response was determined, termed the "uncertainty surface". Flow gradients, large particle images and insufficient particle image displacements resulted in elevated uncertainty in measurements of turbulence levels. Persoons et al. [122] built upon the earlier work of Persoons and O'Donovan [123], proposing the multiple pulse separation (MPS) technique to improve the dynamic range of PIV. The authors used a customised timing system to acquire double-frame images with successive different pulse separation values. To determine the optimum pulse separation, a metric was devised based on determining the local uncertainty by performing a Reynolds decomposition on the PIV displacement field.

The issue in applying these methods to the fluid motion measurements in the current study is that they require the calculation of mean and turbulent flow statistics. The temporal flow structures observed in the current study have no physical "mean" value, meaning such techniques cannot be employed. Hence, a more generalised uncertainty expression would be useful. Charonko and Vlachos [124] developed a method for measuring error bounds to within a given confidence interval for a specific, individual measurement. The authors found that a strong correlation exists between the observed error and the correlation peak ratio (i.e. the ratio of the height of the first peak to the second in the spatial correlation domain). This correlation was found to hold regardless of flow condition and image quality. Xue et al. [120] expanded this work, positing that the signal-to-noise-ratio (SNR) metrics calculated from the PIV correlation plane can be used to quantify the quality of correlation, and subsequently the uncertainty of an individual measurement. The relationship between SNR and uncertainty was explored for both the robust phase correlation (RPC) and standard cross correlation (SCC) processing for synthetic PIV images. However, the methodology in applying these methods to the particle images in the bubble wake is unclear, particularly in regions containing the moving bubble boundary.

One further aspect of the uncertainty is the loss in timing control when using a continuous wave laser as opposed to double-pulsed systems. The camera sensor observes the flow

travelling at some velocity **U** in a brief exposure time $\Delta t = 60\ \mu s$. It follows that if Δt or **U** are large, the sensor will observe a particle "streak" rather than the particle itself, resulting in a reduction in correlation strength. In the current study, the flow velocity is sufficiently small as to avoid streaking or excessive displacement. Ultimately, the transient nature of the flow observed in this case leads to difficulty in ascertaining an uncertainty metric to apply. As such, care has been taken in maximising the strength of correlation in the PIV measurements, which are performed with no interpolative filling or smoothing and are subsequently validated by the Insight 4G package. Since the main function of this measurement technique is to identify coherent structures in the sliding bubble wake, the high quality vectors obtained are considered sufficiently accurate for the current study. This comes with the caveat that future work on the correlation metrics of transient flows could provide improved insight into the uncertainty involved with such measurements.

5.4.5 Uncertainty in Heat Flux

To find the uncertainty in the measured heat flux, the Taylor series method is again used, applying equation 5.40 to each term in the foil energy balance (equation 5.19). This takes into account the uncertainties of the curves fitted to the calibration of the IR camera and the thermocouples, the precision of the current measurements and the foil and paint properties. However, errors across each pixel of the FPA are not independent of each other. The correlation between adjacent pixels in space or time can influence the experimental results and needs to be accounted for. In the case where the result r is influenced by two correlated variables X_1 and X_2, we can write:

$$b_r{}^2 = \left(\frac{\partial r}{\partial X_1}\right)^2 + \left(\frac{\partial r}{\partial X_2}\right)^2 + 2\rho_{X_1,X_2}\left(\frac{\partial r}{\partial X_1}\right)\left(\frac{\partial r}{\partial X_2}\right) b_{12} \tag{5.45}$$

where b_{12} is the product of the precision uncertainties (b_1 and b_2) of each variable (X_1 and X_2). The term ρ_{X_1,X_2} is the Pearson product-moment correlation coefficient, which measures the degree of correlation between the two variables. In the current study, the final term in equation 5.45, also known as the covariance term, is added to the lateral conduction and the heat storage terms, since these terms involve operations between adjacent pixels on the FPA in space and time, respectively. The degree of correlation is found by applying an autocorrelation analysis

on the temporal derivatives in the heat storage term and a cross-correlation analysis on the spatial derivatives in the lateral conduction term.

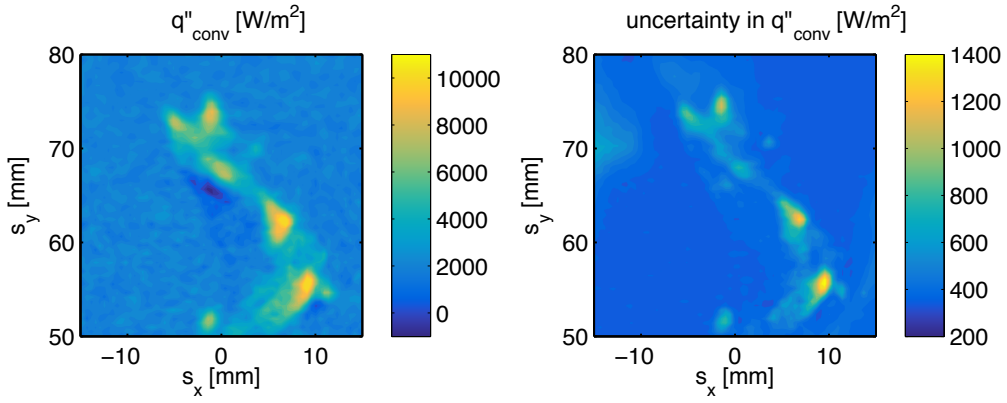

Figure 5.13: (a) instantaneous convective heat flux from the foil to the bulk fluid, q''_{conv}, (b) instantaneous uncertainty in heat flux, for $\alpha = 30°$, $d_e = 5.8\ mm$.

Figure 5.13 shows an example of the convective heat flux and its associated uncertainty at a particular instant in time. Table 5.4 shows the typical absolute and relative uncertainty values for the thermal measurements. Although the uncertainty of the curve fits applied to the thermal data is small, that of the surface temperature can propagate into the terms and have a significant effect. The uncertainty in heat flux at natural convection levels (i.e. with no bubble present) is approximately 350 W/m^2. This is in agreement with Donoghue et al. [80], who found the uncertainty in heat flux at natural convection to be approximately 300 W/m^2. An analysis of the heat generated in the foil, $\dot{q}_{gen}$, found its uncertainty to be an order of magnitude less than this value. Hence, the uncertainty in heat flux at natural convection is due to noise in the thermal camera, rather than to the calculation of the heat generated in the foil. For all tests, this results in an uncertainty of $16-18\%$, considerably larger than the 3.5% of Donoghue et al. [80]. The reason for this is that significantly less heat is passed through the foil in the current study, as tests are performed here at comparatively low wall superheats. The values of uncertainty in the bubble wake are of greater relevance here. The increased magnitude of the constituent terms results in a greater local uncertainty of ≈ 1400 W/m^2. This corresponds to an uncertainty of $\approx 10\%$ in the bubble wake, mainly due to the propagation of noise on the thermal camera into the energy balance. In the far wake, the

absolute uncertainty decreases, although the relative uncertainty can increase significantly in areas where suppressed heat transfer causes q''_{conv} to be low and hence $U''_{q\,conv}/q''_{conv}$ to become very large.

Table 5.4: Absolute and relative uncertainty for the measured thermal data

Measurement	Symbol	Absolute Uncertainty	Relative Uncertainty [%]
Surface temperature	T_s	$0.14°C$	–
Water temperature	T_∞	$0.12°C$	–
Air temperature	T_a	$0.15°C$	–
Convective heat flux: natural convection	q''_{nat}	340 - 365 W/m^2	16 – 18
Convective heat flux: near wake	q''_{conv}	800 - 1400 W/m^2	9 – 11
Convective heat flux: far wake	q''_{conv}	340 - 800 W/m^2	11 – 20

Chapter 6

Bubble Motion

When the bubble departs the injector, the difference in density between it and its surrounding medium generates a buoyancy force on the bubble, which acts in the opposite direction to gravity and is equal in magnitude to the weight of fluid displaced. A secondary force, namely drag, acts against this buoyancy. As the bubble rises, work is done on the surrounding fluid at a rate proportional to the buoyancy force times the bubble velocity. Initially, the bubble rises rectilinearly, at low velocity, with all of the work being dissipated by the viscosity of the fluid. However, as the velocity of the bubble increases further, a point will be reached at which the low viscosity water is unable to dissipate all of this work. This induces an instability in the bubble wake, which is manifested by oscillations in the bubble shape and path [13]. Thus, the fluid around the bubble is not accelerated uniformly, creating pressure differences around the bubble interface. At this point, the bubble transitions to a distorted helical rise pattern. In an open medium, the buoyancy causes the bubble to accelerate vertically until the drag force is equal and opposite, with the bubble reaching a nominal terminal rise velocity. In this current study, after rising 30 *mm* the bubble impacts the inclined surface. It now experiences the component of the buoyancy force parallel to the surface [66] . If this buoyancy force is sufficiently large (which is the case for all tests in the current study), the bubble will slide along the underside of the surface, experiencing undulating oscillations in shape and path.

As the bubble begins to slide under the surface, the buoyancy force is again opposed by a drag force that acts parallel to the surface in the direction of decreasing depth. When the buoyancy force is matched by the drag force acting in the opposite direction, the bubble

reaches its sliding terminal velocity U_T. This sliding terminal velocity is not constant due to the oscillatory path of the bubble, with the bubble accelerating and decelerating as it traverses the surface. This chapter provides measurements of the sliding bubble mechanics at a distance of 80 *mm* beyond the injection location, by which time the bubbles have reached terminal sliding velocity. The results presented in this chapter serve as a general introduction to sliding bubble behaviour, both for a single bubble and an in-line bubble pair. Chapters 7 and 8 will expand this to include information about the wake and resultant heat transfer.

6.1 Single Bubble Motion

This section investigates the motion of a single air bubble for equivalent diameters of 5.8 *mm* and 7.2 *mm* sliding under a surface inclined at 20°, 30° and 40° to the horizontal. Five tests are performed for each set of parameters, with analysis of high speed video recordings providing measurements of physical quantities based on the bubble centroid and edge data. Mean and time-fluctuating values of successive tests show some minor deviation, since the quantities are being measured over only 1-2 bubble path wavelengths and are sensitive to fluctuations. In terms of the bubble path, "spanwise" will refer to motion in the x-direction, while "length" refers to motion in the y-direction.

6.1.1 Shape and Path

Figures 6.1 and 6.2 present the centroidal path and instantaneous shape in the $x-y$ plane for single sliding bubbles of equivalent diameters of 5.7 *mm* and 7.2 *mm* respectively. The projected bubble outline is shown on these figures at spacings of 14 *ms* apart for inclination angles of 20°, 30° and 40°. The position $s_y = 0$ corresponds to the location of the first tracked bubble centroid, 80 *mm* upstream of the bubble injection site, while $s_x = 0$ corresponds to the mean spanwise position. For the 5.7 *mm* bubble (figure 6.1), the bubble shape is ellipsoidal, as predicted by the regime map of Bhaga and Weber [12]. In all cases, the bubble experiences undulating changes in path, with an amplitude and frequency dependent on the surface inclination angle. The bubble also experiences changes in shape, although these are subtle and will be discussed later in greater detail. At the lowest inclination angle of 20°, the

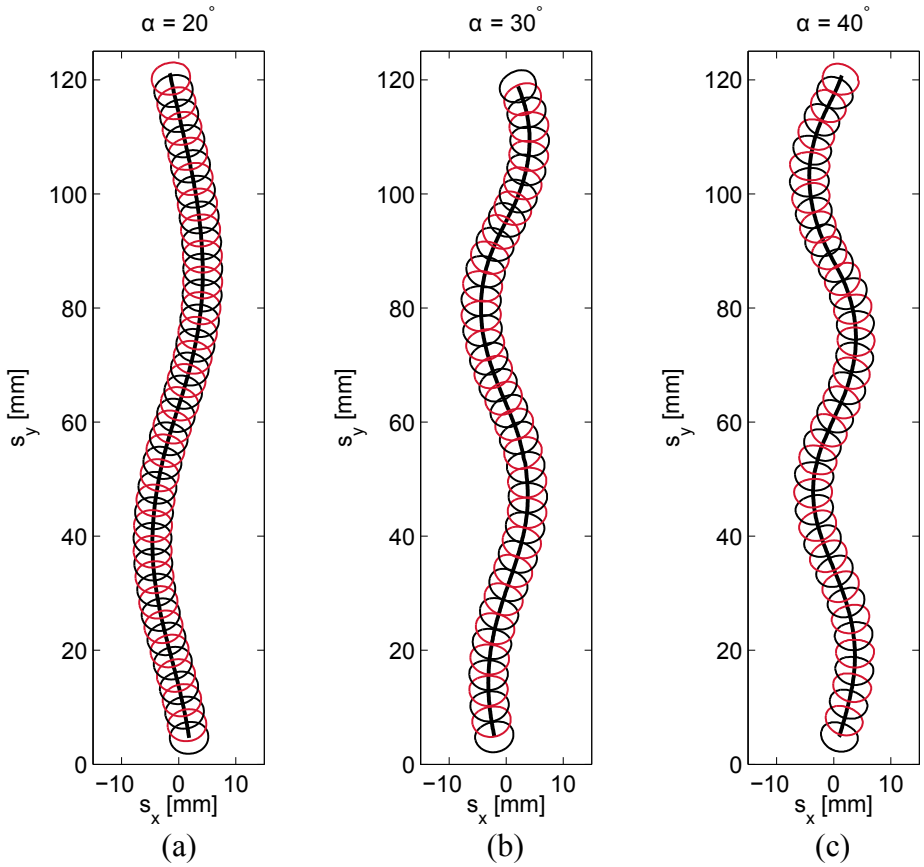

Figure 6.1: Instantaneous bubble shape and path for a bubble of $d_e = 5.7$ *mm* sliding under a surface inclined at (a) 20°, (b) 30° and (c) 40° to the horizontal. The bubble outline is provided at spacings of 14 *ms* apart.

bubble experiences low frequency, low amplitude path oscillations. As the inclination angle is increased, so too are the amplitude and frequency these undulating oscillations. Changes in bubble orientation can also be observed, with the bubbles tilting in the direction in which they are travelling. The effect of increasing the bubble diameter to 7.2 *mm* (figure 6.2) is to increase the buoyancy force and thus the bubble velocity. This results in a more elongated bubble shape, although the frequency of oscillation remains largely the same as before. Interestingly, for all tests at $\alpha = 40°$ the amplitude and frequency of the oscillations is lower than for the 5.7 *mm* bubble, which could be due to the large buoyancy force damping the path oscillations of the bubble.

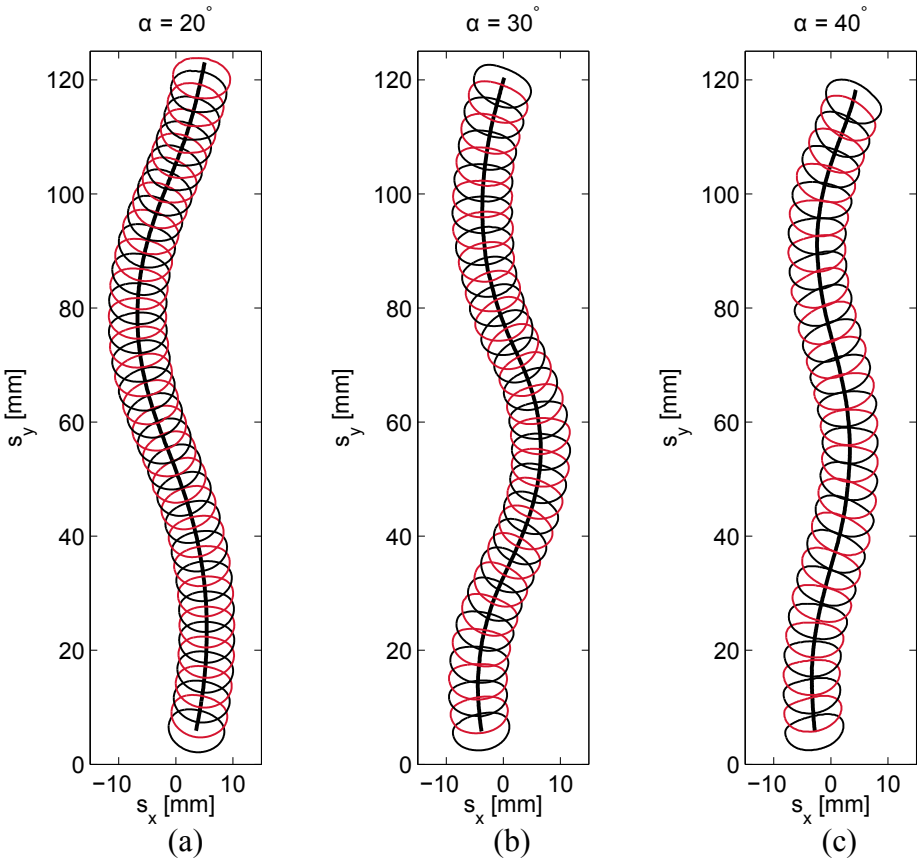

Figure 6.2: Instantaneous bubble shape and path for a bubble of $d_e = 7.2$ *mm* sliding under a surface inclined at (a) 20°, (b) 30° and (c) 40° to the horizontal. The bubble outline is provided at spacings of 14 *ms* apart.

6.1.2 Velocity and Acceleration

The bubble velocity and acceleration are calculated as the first and second derivatives of the curves fitted to the displacement data, measured both at the bubble centroid and at 360 discrete points around the bubble interface. An analysis of the edge data is presented to support the observations made from the centroid data. In this chapter, the velocity and acceleration based on the edge data are provided for $\alpha = 30°$, $d_e = 5.8$ *mm*, while data based off the centroid are detailed for all parameters tested.

Figure 6.3 (a) shows the path traced out by the endpoints of the bubble in figure 6.1, coloured by the local velocity magnitude $v = \sqrt{v_x^2 + v_y^2}$, along with the x-acceleration a_x the and y-acceleration a_y. The equivalent parameters based off the bubble centroid are provided in figure 6.3 (b) and (c) for reference. The spanwise edges of the bubble reach their maximum and minimum velocity at the local extrema of bubble path, on the outside and inside of the

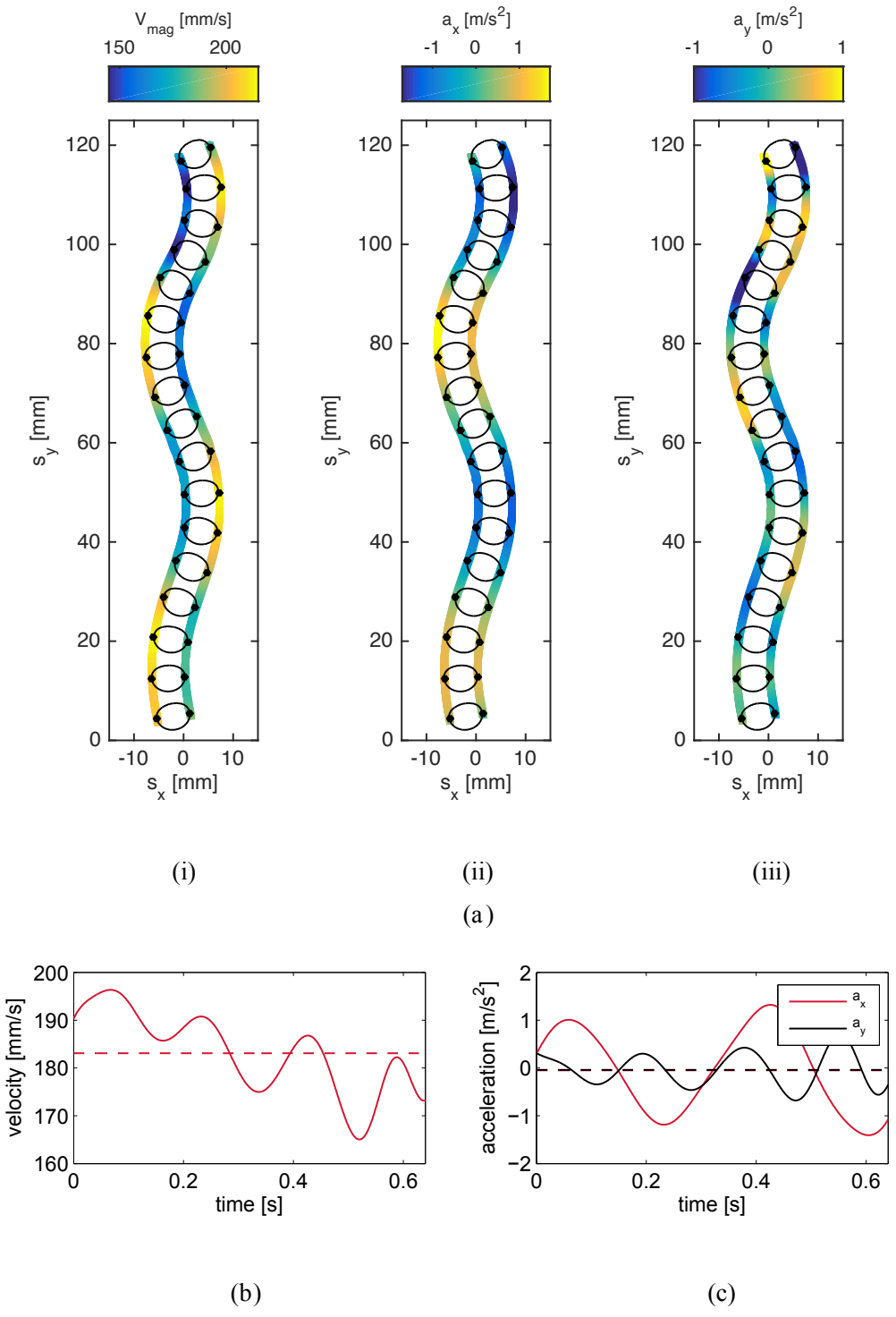

Figure 6.3: (a) Path traced out by the edge data of the bubble major axis at $\alpha = 30°$, $d_e = 5.8$ *mm*, coloured by the values at these points for (i) the velocity magnitude $v = \sqrt{v_x^2 + v_y^2}$, (ii) the acceleration in the x-direction $a_x = \frac{dv_x}{dt}$, and (iii) the acceleration in the y-direction, $a_y = \frac{dv_y}{dt}$. (b) Velocity and (c) acceleration as a function of time based off the centroid data.

path, respectively. This is due to the undulating path taken by the bubble, with the outside edge travelling a greater distance in a given time, giving rise to a larger velocity component. The centroidal velocity magnitude plot shows that the bubble velocity oscillates at twice the path oscillation frequency, with a local maximum in velocity corresponding to a local extrema in shape.

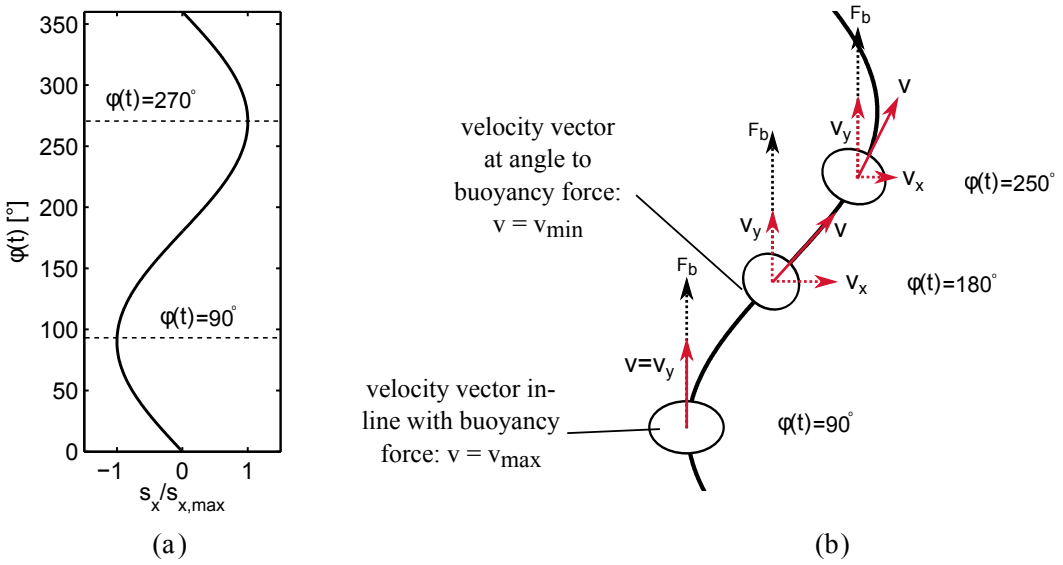

Figure 6.4: (a) The notation used when defining the phase angle, $\phi(t)$, (b) schematic showing the velocity vector, $\overrightarrow{V}$ at different phase angles. The maximum velocity occurs when the x-component is at a minimum and the velocity vector is aligned with the buoyancy force, F_b.

The velocity magnitude in figure 6.3 is the magnitude of the bubble velocity vector, $\overrightarrow{V}$, which has a magnitude and direction dependent on the location of the bubble along its path,. This location is defined by the phase angle, $\phi(t)$, shown in figure 6.4 (a). For the current study, $\phi = 0°$ corresponds to a zero spanwise position, while $\phi = 90°$ is the local minimum in spanwise position. Figure 6.4 (b) shows the direction of $\overrightarrow{V}$ at different phase angles. Recall that the bubble is experiencing a constant buoyancy force F_B, with the path undulations triggered by an instability in the bubble wake. For all surface inclination angles and bubble volumes examined, the y-component of the velocity is larger than the x-component due to this buoyancy force. Thus, it follows that the bubble reaches its maximum velocity when the direction of its velocity vector is directly in line with the buoyancy force, which maximises v_y and hence v_{mag}. This occurs at the local spanwise path extrema, namely $\phi = 90°$ and $\phi = 270°$. As the bubble travels towards its zero spanwise displacement, it experiences a

velocity component in the spanwise direction, with its major axis tilting by an orientation angle θ. At zero spanwise displacement ($s_x = 0\ mm$), the orientation ,θ, is maximum and $\overrightarrow{V}$ is at a minimum. As the bubble travels towards its next local extrema, the velocity vector aligns itself with the direction of the buoyancy force, increasing in magnitude.

The centroid plots in figure 6.3 also show that for this particular test the bubble velocity is decreasing as a function of time. This is also visible from the edge data, where the velocity magnitude of each successive inside edge is decreasing with each oscillation. Such behaviour was observed for a quarter of all tests, with the majority of cases fluctuating about a steady mean velocity. This change in motion is a result of the coupling that exists between the bubble, surrounding fluid and the surface. Occasionally, this will cause a significant amount of liquid to be shed from the near wake. This was referred to as "transitional" motion by Donnelly [68], who found this to occur in a number of different modes: steadily decreasing, sliding rectilinearly, or sliding rectilinearly before reverting to oscillatory motion. Donnelly [68] claimed that this behaviour was linked to the build-up and subsequent ejection of a significant amount of liquid from the bubble wake at the local extrema in bubble path. This large ejection of fluid causes a comparatively higher x-component of $\overrightarrow{V}$, therefore resulting in a lower velocity magnitude. This greater x-component causes the sharper turns the bubble makes nearer the top of the surface.

This is supported by figure 6.3, which presents the edge data coloured by the spanwise acceleration, a_x. A positive value of a_x indicates an acceleration in the positive spanwise direction, and vica versa. The maximum acceleration in this direction also occurs at the bubble extrema, with close to zero acceleration at zero displacement. Thus, a_x fluctuates between its maximum value and zero at twice the path displacement. A key region of interest is on the outside of the bubble path $s_y = 85\ mm$, after which the bubble velocity decreases significantly. At this location, the outside edge of the bubble experiences a large acceleration in the positive direction, which initiates a sharp turn to the right. This acceleration is a result of a force, F_x, that restores the bubble towards the zero displacement. This force is the reaction force to the fluid shed into the bubble wake, which will be discussed in greater detail in chapter 7. For now, it is sufficient to state that the significant acceleration at $s_y = 85$ mm supports this theory of transitional behaviour. The third plot in figure 6.3 (a) shows the y-component of the acceleration, a_y, where a positive a_y means the bubble is accelerating

in the direction of the buoyancy force. Analysis of the major axis edge data shows that a_y is maximum as the bubble approaches a local extremum and its velocity vector is aligned with the buoyancy force. Meanwhile, the inside of the path at maximum displacement has a_y close to 0. Conversely, the maximum deceleration occurs as the bubble approaches the zero displacement. After the ejection of material into the wake at $s_y = 85$ *mm*, the bubble experiences a large deceleration in the opposite direction of the buoyancy force, thereby decreasing the magnitude of $\overrightarrow{V}$.

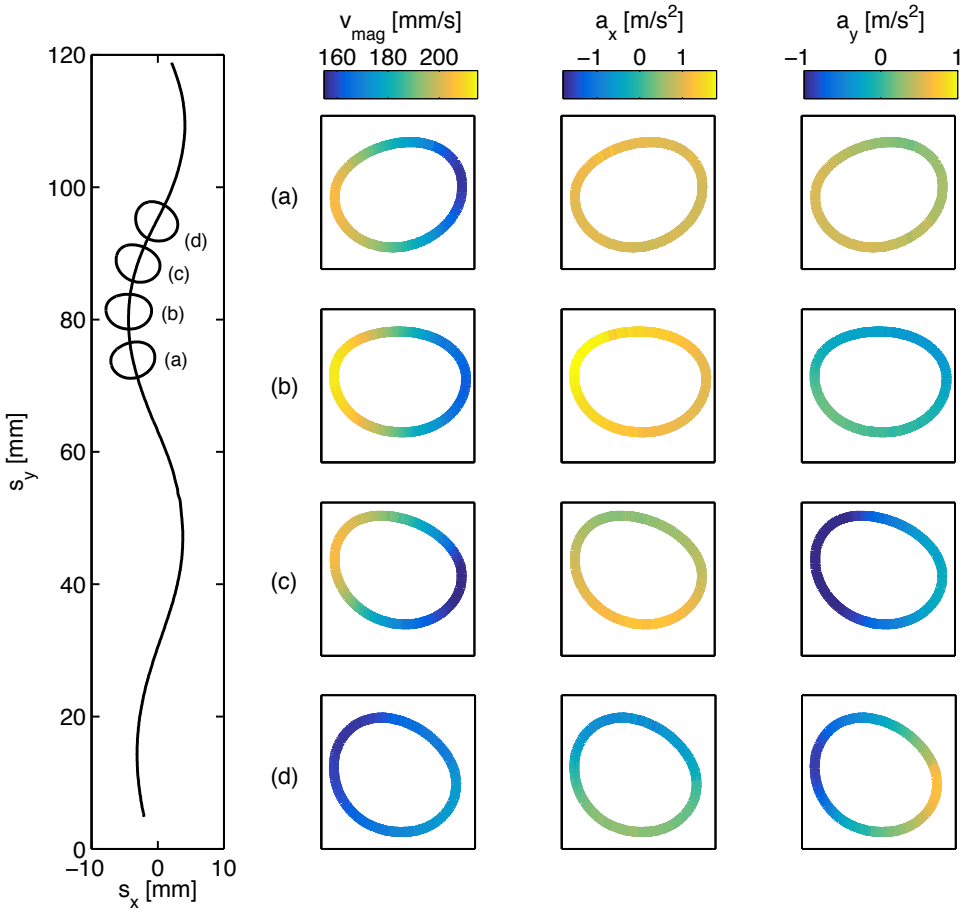

Figure 6.5: Velocity magnitude, a_x and a_y calculated at 360 points around the bubble, for $\alpha = 30°$, $d_e = 5.8$ *mm*, with each row corresponding to the locations on the bubble path identified by (a-d).

For the same test, figure 6.5 expands the edge data across the entire bubble interface, using 360 points at four instances in time, marked as (a-d) on the bubble path. This provides an insight into the circumferential distribution of velocity and acceleration around the bubble, and allows a more in-depth analysis of the key region around $s_y = 85$ *mm* that was previously

identified as significant. In the location (a) in figure 6.5, the bubble is approaching its local minimum in position, with the large velocity on the outside of the path. The velocity magnitude transitions circumferentially to the minimum velocity on the right hand side of the bubble, with its magnitude largely symmetrical about the bubble major axis. The bubble is decelerating in the spanwise direction across its entire interface, since the bubble is moving in the negative spanwise direction but its acceleration is in the positive spanwise direction. The outside of the bubble path is accelerating in the direction of the buoyancy force as the bubble approaches its local minimum in path. This local minimum occurs in figure 6.5 at the location (b). At this instant in time, the bubble velocity on the outside edge is at its local maximum. The bubble shape is also notably ellipsoidal at this point, with slightly sharper tips along its major axis. On the outside of its path, the bubble experiences a large acceleration in the positive spanwise direction, while the bubble has close to zero acceleration in the direction of the buoyancy force.

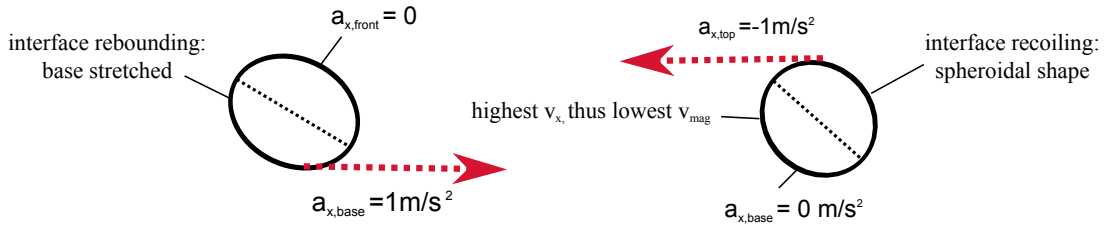

Figure 6.6: Sketch showing the interface rebounding and recoiling, corresponding to the locations (c) and (d) on figure 6.5.

At the point (c), the velocity vector of the bubble is now at an angle θ from the buoyancy force, with the major axis of the bubble tilting by θ from the horizontal. As the bubble returns towards its zero displacement, the circumferential velocity magnitude decreases, with a local minimum at the inside edge of the major axis. The distribution of spanwise acceleration is now asymmetrical about the bubble major axis, with the bottom of the bubble accelerating in the positive direction but the top having $a_x \approx 0$. This indicates a rebounding of the bubble interface, corresponding to the base of the bubble being stretched when the bubble leaves a turn and decelerates, and recoiling soon after. This significant rebounding of the bubble interface results in a large spanwise component of velocity, which in turn leads to a significant deceleration of the bubble in the vertical direction. This results in a low circumferential

velocity and the bubble experiencing a large tilt of $\theta \approx 30^\circ$ (location (d) on figure 6.5) and a more spherical shape. A sketch identifying the rebounding and recoiling process is shown in figure 6.6. Thus, it has been shown that the bubble shape fluctuates from ellipsoidal at the path extrema to more spheroidal at zero displacement. At the location (d), the top of the bubble experiences a spanwise deceleration as it approaches its next local extrema. The outside of the bubble path is also experiencing a positive acceleration in the direction of buoyancy. The superposition of these forces will subsequently act to tilt the bubble in the counter-clockwise direction, thereby repeating the cycle identified in (a-d) for the upcoming local maximum in the bubble path.

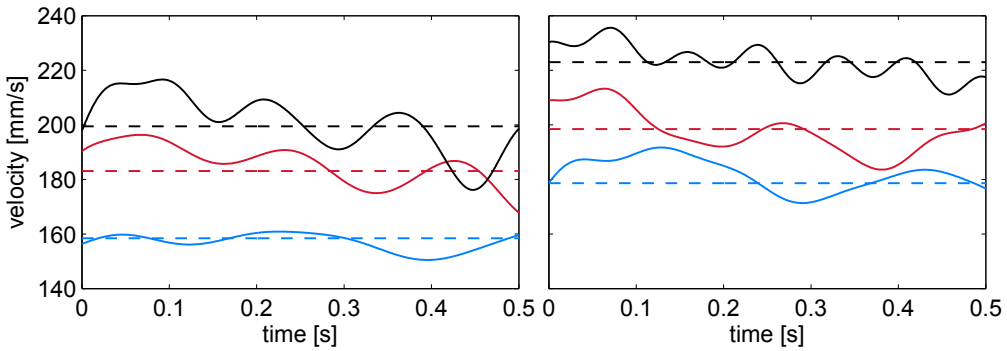

Figure 6.7: Time-varying (solid lines) and mean (dashed lines) velocity magnitude $|v| = \sqrt{(v_x)^2 + (v_y)^2}$ in mm/s for the (a) 5.8 mm and (b) 7.2 mm bubble at $\alpha = 20^\circ$ (−), 30° (−) and 40° (−).

To this point, the edge data have been used to provide an insight into the bubble mechanics. For the remainder of this section, bubble motion based on the centroid measurements will be discussed. Figure 6.7 shows the time-varying and mean bubble velocity for each surface inclination angle for $d_e = 5.8$ mm (a) and $d_e = 7.2$ mm (b). Note that the velocity scale is the same for (a) and (b). Figure 6.7 (a) shows the velocity for the 5.8 mm bubble for the three inclination angles studied. Increasing the inclination angle results in a larger buoyancy force and a larger mean velocity magnitude. As the velocity magnitude fluctuates at twice the path oscillation frequency, it is evident that the higher path frequencies previously observed at larger α result in larger frequency velocity fluctuations. The buoyancy force also scales with the bubble volume, as is evident in figure 6.7 (b). The frequency of velocity oscillation is largely independent of the bubble volumes, with the exception being the tests at $\alpha = 40^\circ$,

which have high-frequency velocity fluctuations for the 7.2 *mm* bubble, despite having a comparatively low amplitude path. These high order fluctuations are likely due to interface deformations around the bubble base that are damped out due to the large buoyancy force. The increase in mean velocity magnitude from 30° to $\alpha = 40°$ is also larger than for the equivalent 5.8 *mm* diameter bubble. This can be explained by considering the more damped path of the bubble at $\alpha = 40°$, $d_e = 7.2$ *mm*. The oscillations of the bubble are lower in amplitude, corresponding to a lower spanwise velocity component and thus a greater velocity magnitude.

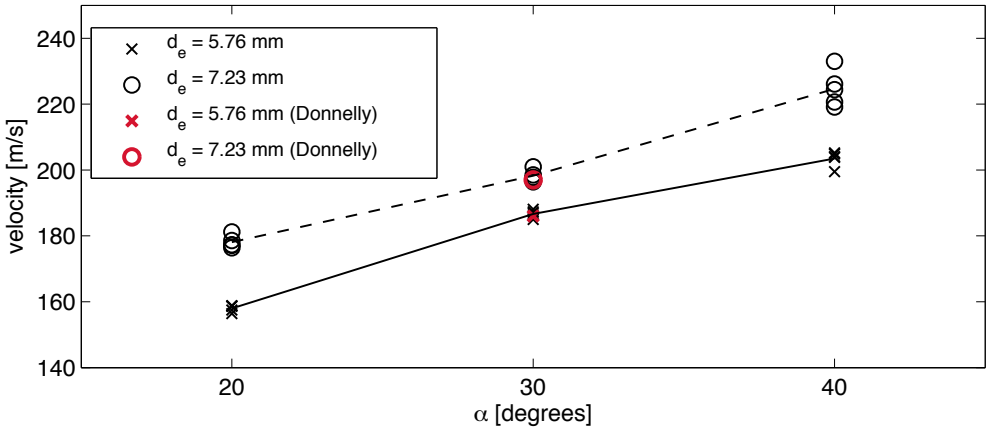

Figure 6.8: Mean velocity magnitude for all tests as a function of surface inclination angle for the 5.8 *mm* bubbles (×) and 7.2 *mm* bubbles (○). Also shown are the overall mean velocity (solid and dotted lines) for each bubble diameter and the mean of all tests obtained by Donnelly [68] at $\alpha = 30°$.

The mean velocity from each test is condensed into figure 6.8, along with the average results at 30° for an unheated surface taken from Donnelly [68]. Tests that exhibited extreme transitional behaviour (i.e. those transitioning from a rectilinear to a sinusoidal path) were not considered. Some deviation exists between tests due to slightly varying initial conditions and because the velocity is being averaged over 1-2 wavelengths only. These differences in velocity are more pronounced at higher bubble Reynolds numbers, where the bubble diameter and velocity are larger. The upper limit for terminal velocity, U_∞, can be found based on the drag on a freely rising spherical bubble of diameter d_e. This is 215.2 mm/s for $d_e = 5.8$ *mm* and 258.6 mm/s for $d_e = 7.2$ *mm*. These values, along with a variety of useful dimensionless parameters derived form the mean velocity measurements, are shown in table 6.1. The sliding bubble velocity tends towards these upper limit values with increasing inclination angle,

although this will begin to tail off at some critical angle, expected to be around 50°, with the onset of bubble bouncing.

Table 6.1: Bubble velocity and dimensionless parameters.

α [°]	d_e [mm]	U_b [mm/s]	U_∞ [mm/s]	Re	Eö	We	St	Mo
20	5.76±0.15	158.5	215.2	875	4.52	2.01	0.15	2.56×10^{-11}
	7.23±0.08	178.6	258.6	1286	7.12	3.23	0.18	2.56×10^{-11}
30	5.76±0.15	183.1	215.2	1050	4.52	2.68	0.18	2.56×10^{-11}
	7.23±0.08	198.5	258.6	1429	7.12	3.95	0.2	2.56×10^{-11}
40	5.76 ±0.15	199.5	215.2	1145	4.52	3.18	0.25	2.56×10^{-11}
	7.23 ±0.08	223	258.6	1606	7.12	4.99	0.23	2.56×10^{-11}

The range of Reynolds and Eötvös numbers in table 6.1, along with the constant Morton number, are in the oblate ellipsoidal regime of Bhaga and Weber [12]. The Weber number increases from $2-5$, where the critical value between the surface tension and inertia dominated shape regimes is $We = 3$. Thus, these ellipsoidal bubbles will be affected both by surface tension and intertia. Although the precise mechanism of vortex shedding has not been discussed thus far, the Strouhal number does not scale significantly with increasing Reynolds number.

6.1.3 Force and Drag Coefficient

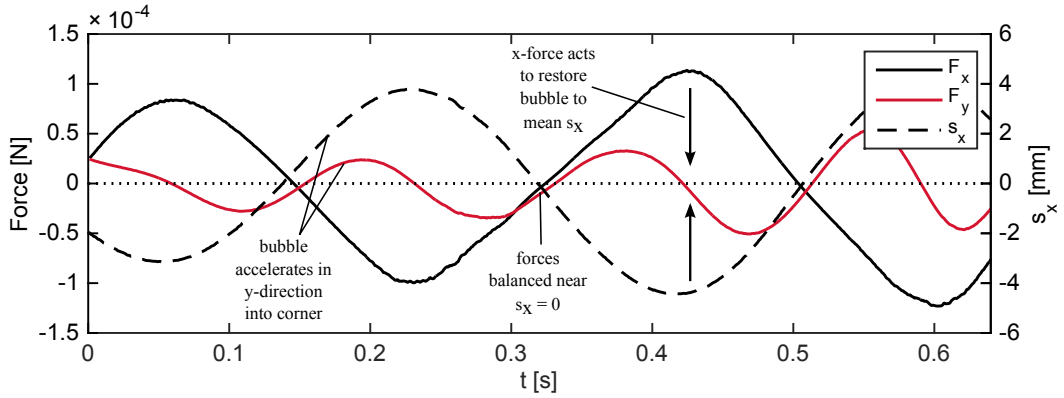

Figure 6.9: Net force in the x-direction (−) and y-direction (–) as a function of time for $d_e = 5.8$ mm, $\alpha = 30°$ (left axis), x-displacement as a function of time (right axis)

This section presents the forces calculated by the 1-d kinematics approach. The net forces ΣF_x and ΣF_y take a similar shape to the acceleration and fluctuate about a mean of zero. The net forces in the spanwise direction fluctuate at the path frequency, with the bubble

experiencing zero net x-force (or acceleration) at zero displacement and maximum force at maximum displacement. The forces along the length of the bubble path fluctuate at twice the path frequency, with the bubble experiencing zero net y-force and zero acceleration at both maximum and zero displacement. Figure 6.9 illustrates this by plotting these forces and the bubble path as a function of time for $\alpha = 30^{\circ}$, $d_e = 5.8\ mm$. The net spanwise force/acceleration at any point tries to restore the bubble towards its mean displacement $s_x = 0$. The net forces in the y-direction reflect the bubble accelerating as it approaches a turn to a local extrema of position, at which point ΣF_y is zero. As the bubble returns towards its zero displacement, it experiences a deceleration. Finally, at zero displacement, the net forces are balanced, although this configuration is not stable for ellipsoidal bubbles. The magnitude of these forces increases with surface inclination angle and volume.

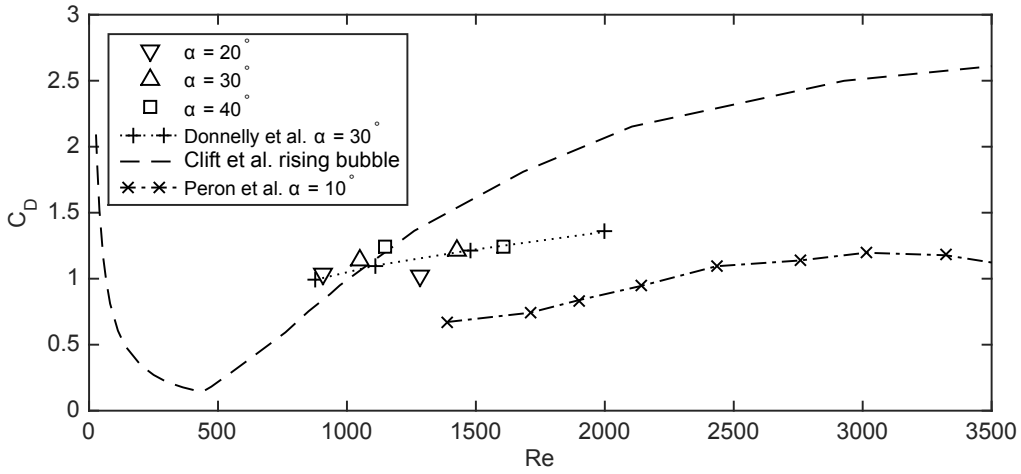

Figure 6.10: Time-averaged drag coefficient as a function of Reynolds number for all tests here, with the sliding bubble results of Donnelly [68] at $\alpha = 10^{\circ}$, Peron et al. [66] at $\alpha = 10^{\circ}$ and the rising bubble results of Clift et al. [21] provided for comparison.

Plots of average drag coefficient versus Reynolds number have been performed in the literature, meaning the 1-d force analysis can at least provide a useful means of comparison between various studies. Figure 6.10 compares the temporally averaged drag coefficients of the current study with the unheated results of Donnelly [68], the experiments of Peron et al. [66] at their maximum inclination angle tested of 10°, and the drag coefficient for a freely rising bubble taken from Clift et al. [21]. Perron et al. [66] showed that increasing the surface inclination angle increased the drag coefficient, which likely continues until the onset of bouncing $(45 - 50^{\circ})$. This means that the average results for drag coefficient show

qualitative agreement with the results of Perron et al. [66] and Donnelly [68].

6.1.4 Eccentricity and Orientation

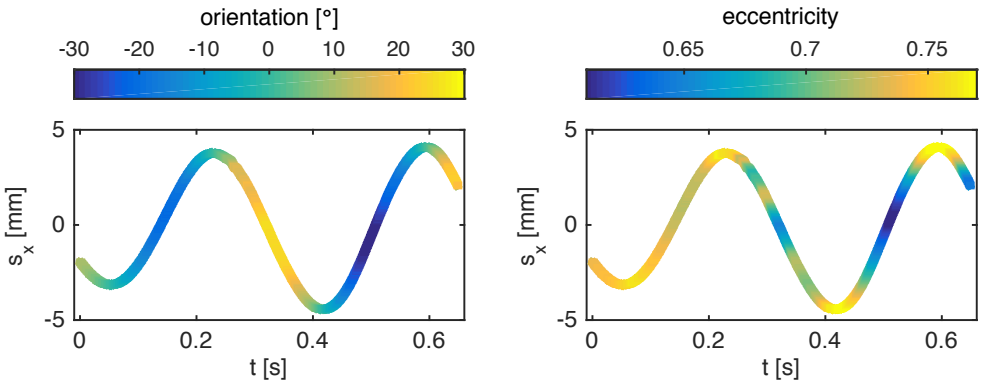

Figure 6.11: x-displacement, s_x as a function of time, coloured by (a) the orientation of the bubble, measured in degrees, and (b) the eccentricity of the bubble, for which an eccentricity of 0 indicates a perfect sphere and an eccentricity of 1 is a line segment.

The bubble tilt and shape have been referred to numerous times up to this point, and are examined more formally in this section. The shape is expressed in terms of eccentricity, which is zero for a perfect sphere and unity for a line segment. The shape regime map of Bhaga and Weber [12] shows that the bubble shape transitions from spherical to oblate ellipsoids with increasing Reynolds number. Thus, it is not surprising that the bubble shape is dependent on its velocity, with a high-eccentricity, elongated shape at the path extrema and a more rounded shape at zero displacement. The orientation angle, θ, is the angle made between the bubble major axis and the positive x-axis. While it traverses the surface, the major axis of the bubble is orientated perpendicular to the direction that it travels; thus, θ is zero at the local extrema and path and is maximum at the zero displacement. Figure 6.11 shows the spanwise position, s_x, for a bubble with $\alpha = 30°$, $d_e = 5.8$ *mm* as a function of time, coloured by the orientation and eccentricity. The instant in time $t = 0.42$ *s* on figure 6.11 corresponds to the bubble shedding a large quantity of fluid into its wake, which results in the bubble taking a spheroidal shape at $t = 0.5$ *s* due to its decreased velocity magnitude.

The bubble orientation for all parameters is shown in figure 6.12. In each test, the magnitude of the bubble tilt is dependent on the component of the bubble velocity vector in the spanwise direction, and fluctuates at the path frequency. Some higher order changes in

orientation are observed, which could be due to higher order changes in shape corresponding to the interface rebounding. For the 7.2 *mm* diameter bubbles (b), the orientation at $\alpha = 40^\circ$ is lower than expected, indicative of a low spanwise component of the bubble velocity vector at this large Reynolds number.

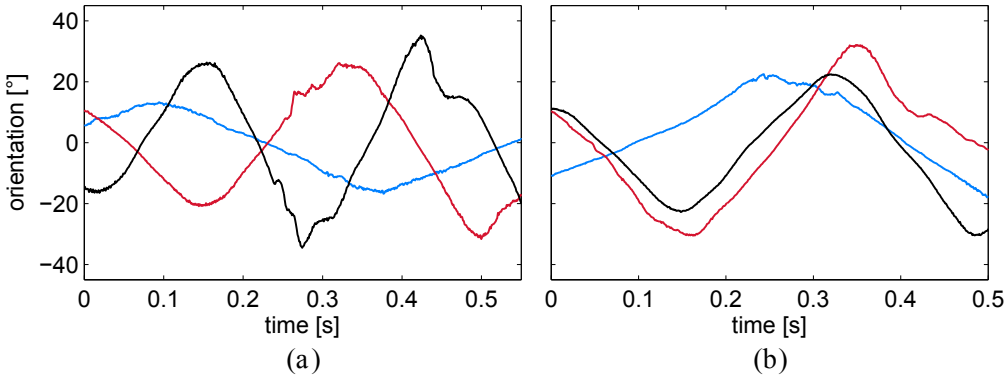

Figure 6.12: Time-varying orientation θ in degrees for the (a) 5.8 *mm* and (b) 7.2 *mm* bubble at $\alpha =$ 20° (–), 30° (–) and 40° (–).

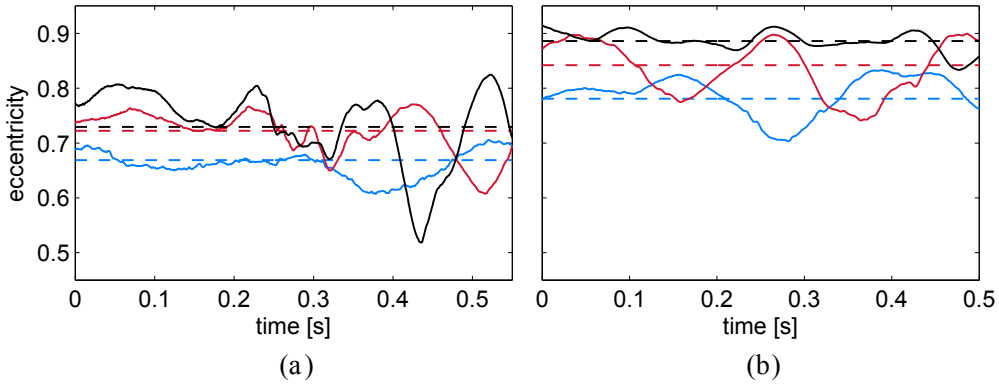

Figure 6.13: Time-varying (solid lines) and mean (dashed lines) eccentricity $|\nu| = \sqrt{1-(b/a)^2}$ for the (a) 5.8 *mm* and (b) 7.2 *mm* bubble at $\alpha = 20^\circ$ (–), 30° (–) and 40° (–). An eccentricity of 0 indicates a perfect sphere, whereas an eccentricity of 1 is a line segment.

Figure 6.13 shows the mean and time-varying eccentricity for all parameters tested. The bubble eccentricity has the same frequency and a similar shape to the velocity magnitude, although there are some higher-order fluctuations visible due to the recoiling and rebounding of the bubble boundary. The eccentricity generally increases with increasing inclination angle and bubble volume, although the mean values are influenced by rapid changes in bubble shape and have less physical meaning. Typically, the 5.8 *mm* bubbles have a larger path

amplitude and a greater spanwise component of velocity, meaning they experience more dramatic shape oscillations. Increasing the bubble diameter increases the Reynolds number and thereby the bubble's "oblateness". At the largest Reynolds number corresponding to 40°, the oblate bubble shape experiences only minor fluctuations.

6.1.5 Contaminated Systems

To this point, the bubble velocity has been used as they key parameter in determining the bubble behaviour. However, the mechanics of two-phase systems is highly dependent on the fluid properties. In section 2.1, it was explained that contaminants in the liquid phase, also called surfactants, build up on the rear face of the bubble, inducing a Marangoni stress and a partial slip boundary condition. This behaviour remains the same for sliding bubbles, although the sliding surface adds a further layer of complexity to proceedings, as impurities can adhere to the underside of the surface. It is useful to investigate the influence of surfactants on sliding bubble motion, particularly to determine if the addition of PIV seeding particles will cause a transition to contaminated motion. In order to trigger such motion, 18.75 μl of liquid soap is added to the deionised water in the tank, corresponding to 0.0075% v/v concentration, consistent with that of Tomiyama et al. [27]. Figure 6.14 shows a range of measured quantities for $\alpha = 30°$, $d_e = 5.8\ mm$.

The addition of impurities to the liquid phase dramatically changes the surface tension of the fluid and fundamentally alters the bubble motion. The amplitude of the path oscillations has decreased significantly, with the bubble instead experiencing high-frequency, large magnitude shape changes and an orientation of $\approx 0°$. The velocity magnitude plot is high-magnitude and repeating, with a mean velocity significantly larger than for a bubble sliding in deionised water. This finding is in conflict with the literature on rising bubbles, which describes the partial slip boundary conditions resulting in increased drag and a dampening of the bubble oscillations. However, in the case of a sliding bubble, by damping the path oscillations the velocity vector becomes aligned with the buoyancy force. Although the presence of the partial-slip boundary condition could be retarding the motion as for rising bubbles, the removal of the v_x component has a greater influence on the bubble velocity. These findings are in agreement with that of Donnelly [68] and DeBisshop et al. [70] for

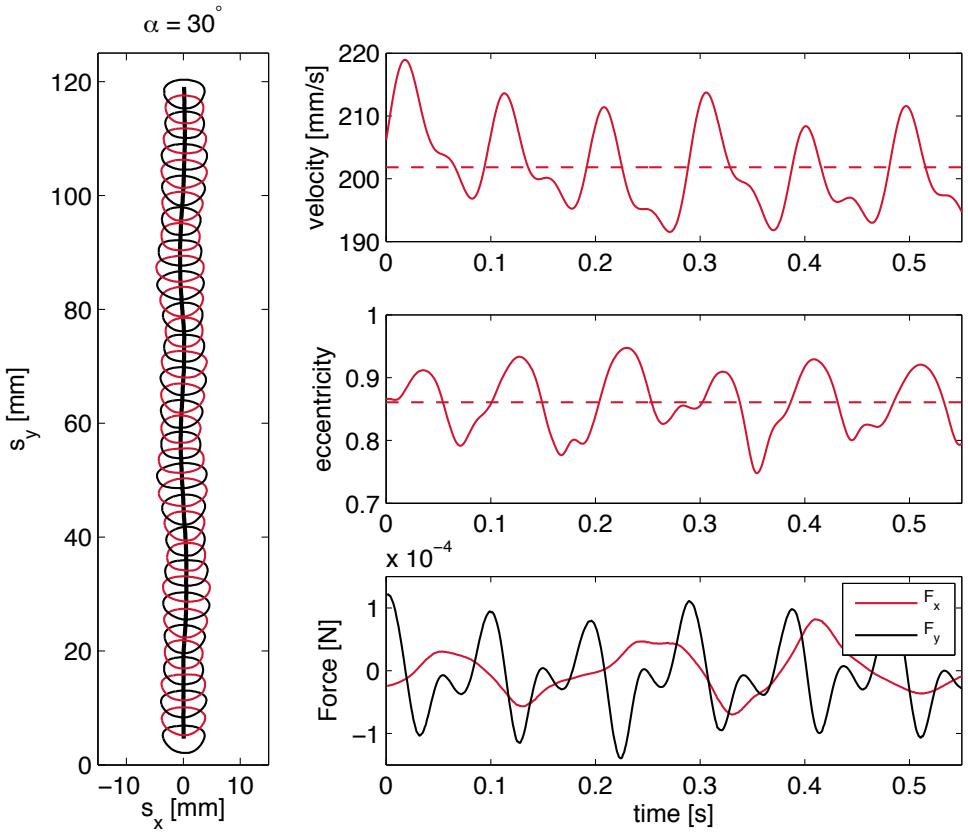

Figure 6.14: Shape and path of a bubble with $\alpha = 30°$, $d_e = 5.8$ *mm* in an impure fluid (left), temporal variation of the bubble velocity, eccentricity and force (right).

sliding bubbles.

As the path oscillations are close to zero, variations in velocity are caused only by the changing bubble shape. The bubble shape takes on a similar repeating structure to the velocity plot, with high magnitude shape changes from oblate to rounded and a greater mean eccentricity than the oscillating bubble case. Unlike the oscillating bubble, $\Sigma F_y > \Sigma F_x$ due to the low amplitude of the path oscillations. These path oscillations are visible on the ΣF_x plot on Figure 6.14, while the ΣF_y curve shows the bubble being accelerated in the direction of buoyancy as its shape becomes more stretched, decelerating after the interface recoils.

Further insight into this motion is provided by figure 6.15, which shows the velocity and acceleration of the major axis for the same test. The velocities of the bubble tips are not symmetrical about the bubble's minor axis, which would be the case if the bubble was sliding entirely rectilinearly. However, the low-amplitude path results in the velocity having a stronger component on alternating sides, generally increasing directly before and after the

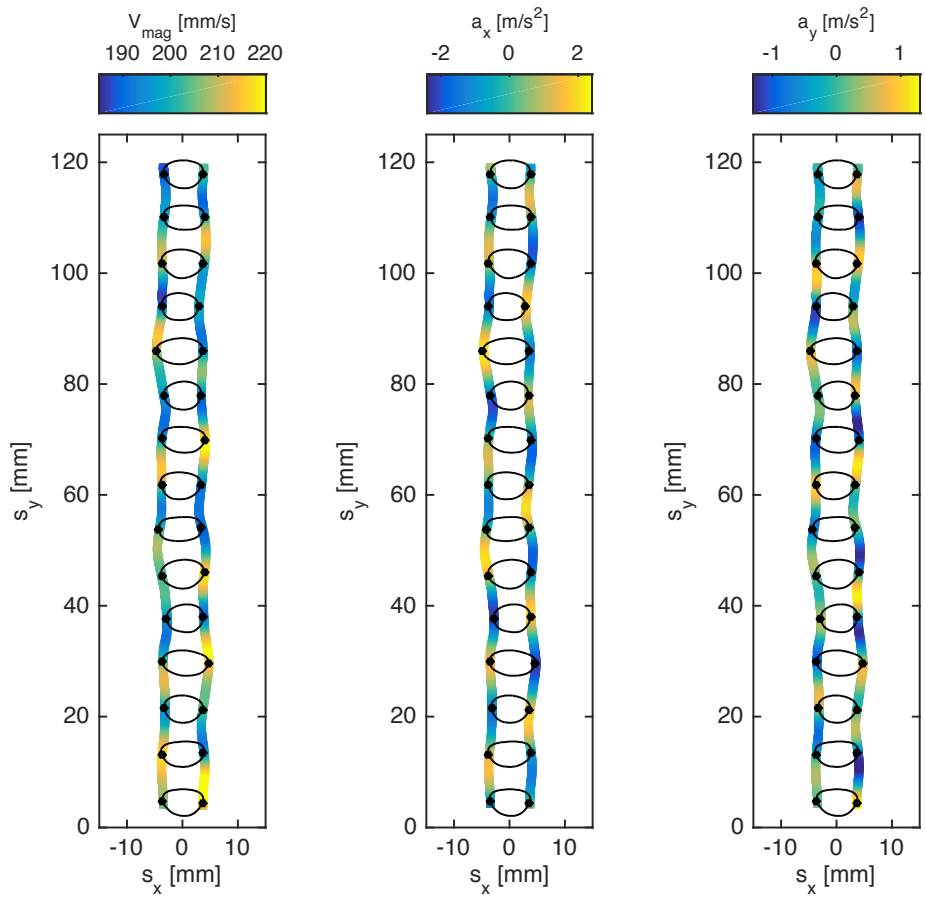

Figure 6.15: Path traced out by the edge data of the bubble major axis in an impure system at $\alpha = 30°$, $d_e = 5.8$ *mm*, coloured by the values at these points for (i) the velocity magnitude $v = \sqrt{v_x^2 + v_y^2}$, (ii) the acceleration in the x-direction $a_x = \frac{dv_x}{dt}$, and (iii) the acceleration in the y-direction, $a_y = \frac{dv_y}{dt}$.

bubble shape recoils (i.e. changes from oblate to spherical). Although the net force in the x-direction is apparently low, high-magnitude fluctuations in acceleration acting in opposite directions are observed on the a_x plot. Since the net force is calculated based off the (low amplitude) spanwise displacement of the bubble centroid, these significant fluctuations are not accounted for. This shows the usefulness of the bubble edge point tracking in determining two-phase system behaviour. The acceleration on either side of the bubble interface acts to stretch the bubble out or to compress it. The acceleration in the direction of buoyancy also reveals the edges of the major axis accelerating and decelerating as the bubble is stretched and compressed.

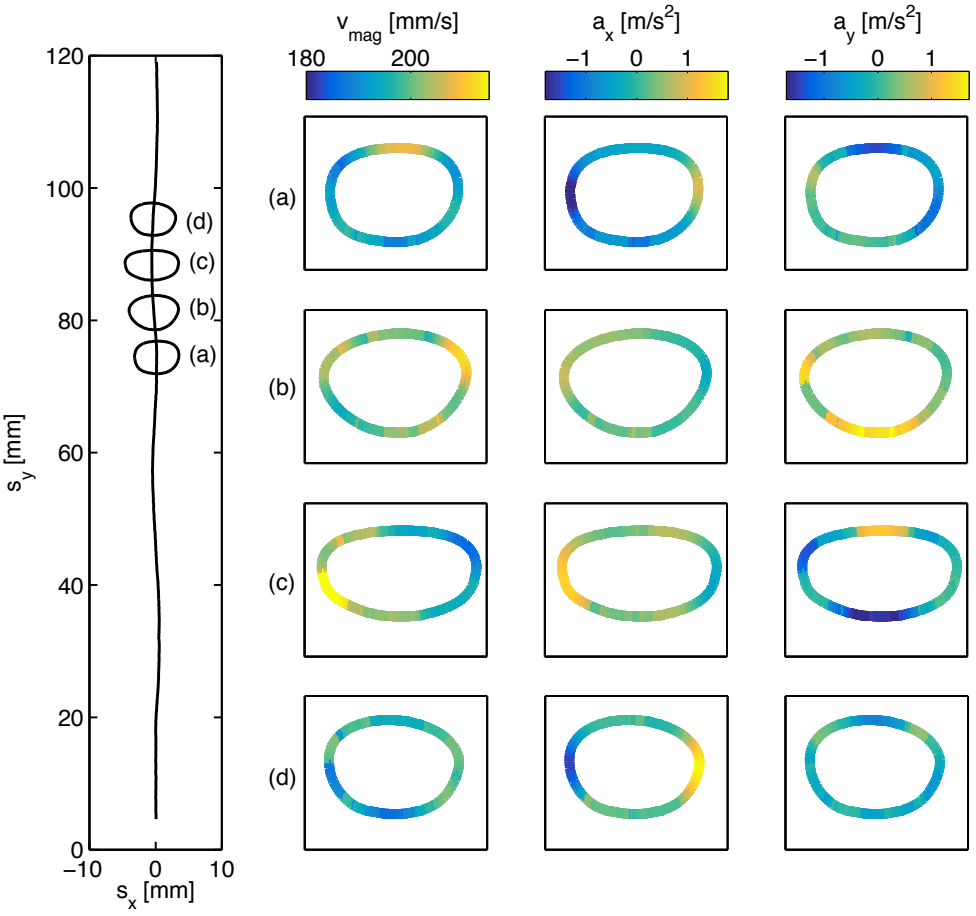

Figure 6.16: Parameters calculated at 360 points around the bubble in a contaminated system for $\alpha = 30^{\circ}$, $d_e = 5.8\ mm$, at the locations on the bubble path identified by (a-d). The first column is velocity magnitude, the second is x-acceleration, the 3rd is y-acceleration.

Finally, the circumferential velocity and acceleration are calculated at 360 points around the bubble interface at the four instances in time (a-d). At (a), the bubble is beginning to elongate across its major axis. At this point, the top of the bubble is moving with the largest velocity. An analysis of the edge data shows that the top of the bubble is in fact accelerating back towards the bubble centroid, rebounding inwards as the sides are stretched. At this point, the interfacial spanwise acceleration is close to zero except at the edges of the major axis. At these points, either side of the bubble are stretching outwards. At the point (b), the bubble has elongated and has a shape that is asymmetrical about its major axis, due to only the top of the bubble having rebounded towards the centroid. The acceleration in the y-direction at (b) shows that base of the bubble is experiencing an acceleration in the positive y direction, indicating it is about to rebound towards the centre. Thus, there is a phase lag

between the top and bottom of the bubble rebounding. At the position (c), the bubble base has just rebounded and is at maximum elongation. This results in a large circumferential velocity, particularly on the outside of the bubble interface since it is at a local minimum s_x in position. The y-acceleration is of interest here, as it now acts in the opposite direction, stretching the bubble along its minor axis and compressing the major axis of the bubble. Finally, at the position (d), the major axis of the bubble has become compressed, with a low circumferential velocity. The bubble has largely reverted to the same behaviour as seen in (a), and promptly continues this cycle.

6.2 Multiple Bubble Motion

When considering the applications of two-phase flows, it is likely that real engineering systems will involve more than one sliding bubble. The literature on interacting rising bubbles describes the bubble-bubble interactions, such as dancing, kissing and occasional coalescence of two bubbles, with these interactions heavily dependent on the fluid properties and the presence of surfactants. There are many types of bubble-bubble interactions, which are extremely sensitive to a large range of parameters. Studies on bubble swarms often negate this by taking a global, statistical approach in their analysis. However, what these interactions have in common is that they are all initiated by one bubble entering the wake of another. Therefore, studying the mechanics of a trailing bubble can provide insight into the bubble mechanics of more complex systems. The following section presents results of the same quantities previously tested for a 5.8 *mm* diameter bubble pair at all three surface inclination angles, released in a streamwise in-line configuration (that is, one after the other), with the trailing bubble $4-5$ bubble diameters downstream of the leading bubble.

6.2.1 Shape and Path

Figure 6.17 shows the leading and trailing bubbles at an instant in time when the leading bubble is 0.05 *s* from the end of its path for all surface inclination angles. The paths taken by both bubbles are shown, along with dashed lines to show the path the bubbles take after this instant in time. The mean separation in the y-direction between the two bubbles across these

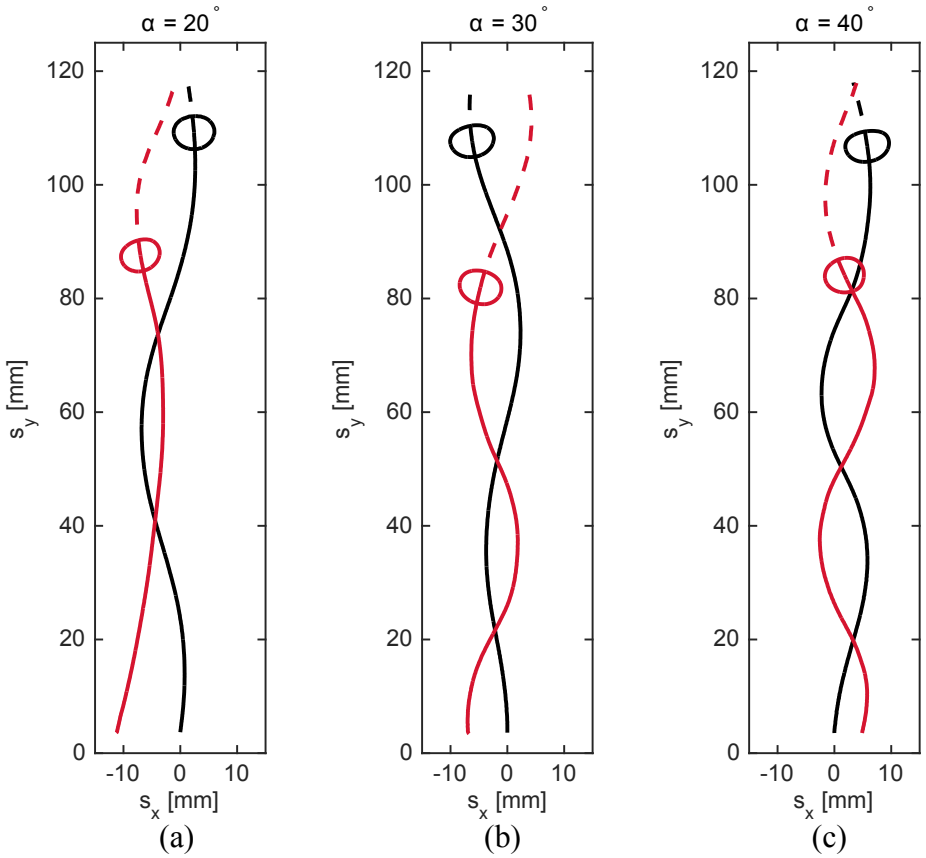

Figure 6.17: Bubble path shown for two 5.8 *mm* diameter bubbles sliding under the surface, released in an in-line formation for $\alpha = 20°$, $30°$ and $40°$. The average distance between leading bubble $(-)$ and trailing bubble $(-)$ is 24.5 ± 0.5 *mm*. The bubble shapes are shown at an instant in time where the leading bubble is 0.05 *s* from leaving the interrogation window.

tests is $d_y = 24.5 \pm 0.5$ *mm*, which changes as a function of time due to the oscillatory bubble paths. Figure 6.17 shows that although the two bubbles are at different phase angles, their paths are in phase and opposite in amplitude. Interestingly, this configuration is found to be true for all tests in the current study for $d_y < 7d_e$. This arrangement is also in agreement with the freely rising bubble experiments of Fan & Tsuchiya [13] and Brücker [39], and is also independent of the initial displacement of the bubbles. This can be observed for the $\alpha = 20°$ test, in which the trailing bubble exhibits transitional behaviour, adopting a path with a large wavelength. Both bubbles enter the measurement region travelling in the positive spanwise direction, but a short time after passing through the the leading bubble wake, the trailing bubble path becomes aligned in-phase with the leading bubble. For the leading bubble, the frequency and amplitude of motion is unaffected by the trailing bubble, but the trailing bubble experiences significantly larger path amplitudes than those of single bubbles, for all surface

inclination angles.

6.2.2 Velocity and Acceleration

The velocity and acceleration of the trailing bubble at $\alpha = 30^\circ$ is shown in figure 6.18 for the centroid and edge data. The leading bubble path is also provided. For a trailing bubble, the mechanics of the bubble interface are fundamentally altered. As was the case for a single bubble, the velocity magnitude is large on the outside of the path and low velocity on the inside of the path. However, in this case the edge data on the major axis also exhibit secondary, high frequency velocity fluctuations that act on alternating sides of the bubble. This is reflected by the centroidal velocity data, which shows a larger mean and fluctuating velocity than a single bubble. The high order changes in velocity occur at twice the frequency of the base velocity fluctuations, and correspondingly four times the path frequency. High velocity regions occur at phase angles of 0°, 90°, 180° and 270°. Two of these correspond to the trailing bubble entering the wake of the leading bubble, which it does at its zero displacement since the path are in phase. The other two phase angles are at the local extrema in spanwise path, with the bubble outside edge found to decrease slightly in velocity as it turns the path. This is conceivably due to the bubble interface rebounding after the initial change in velocity.

The spanwise acceleration of the trailing bubble centroid is not significantly different from the single bubble case, although the peaks of the curves are more flattened. For the edge data, some minor fluctuations in a_x occur where the bubble paths intersect, which will be discussed presently. Since a_x is largely similar in magnitude for single and trailing bubbles, it follows that the induced motion by the bubble wake is in the direction of buoyancy. The third plot on figure 6.18 shows the acceleration in this direction. The bubble acceleration a_y fluctuates at the same frequency as its velocity but with a phase lag, accelerating towards the previously identified high velocity regions.

The rapid fluctuations of these quantities requires a more in-depth analysis of the bubble interface. This is provided in figure 6.19 at instances in time 25 *ms* around the key location of s_y = 50 *mm*, which corresponds to the trailing bubble intersecting the path of the leading bubble. In the first row at location (a), the bubble is turning towards the zero displacement,

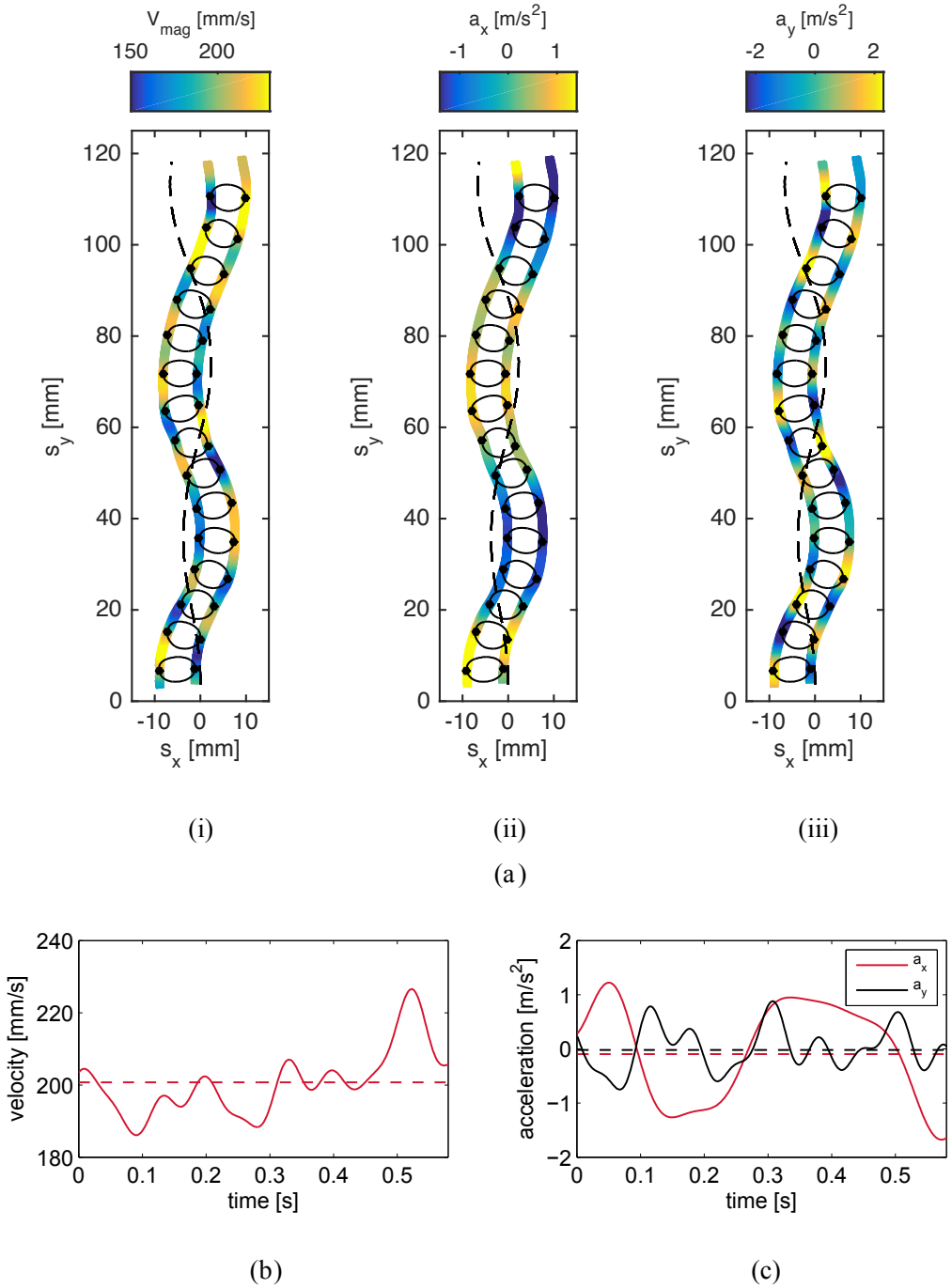

Figure 6.18: (a) Path traced out by the edge data of the trailing bubble major axis at $\alpha = 30°$, $d_e = 5.8$ *mm*, coloured by the values at these points for (i) the velocity magnitude $v = \sqrt{v_x^2 + v_y^2}$, (ii) the acceleration in the x-direction $a_x = \frac{dv_x}{dt}$, and (iii) the acceleration in the y-direction, $a_y = \frac{dv_y}{dt}$. The leading bubble path is shown as the dashed line. (b) Velocity and (c) acceleration as a function of time based off the centroid data.

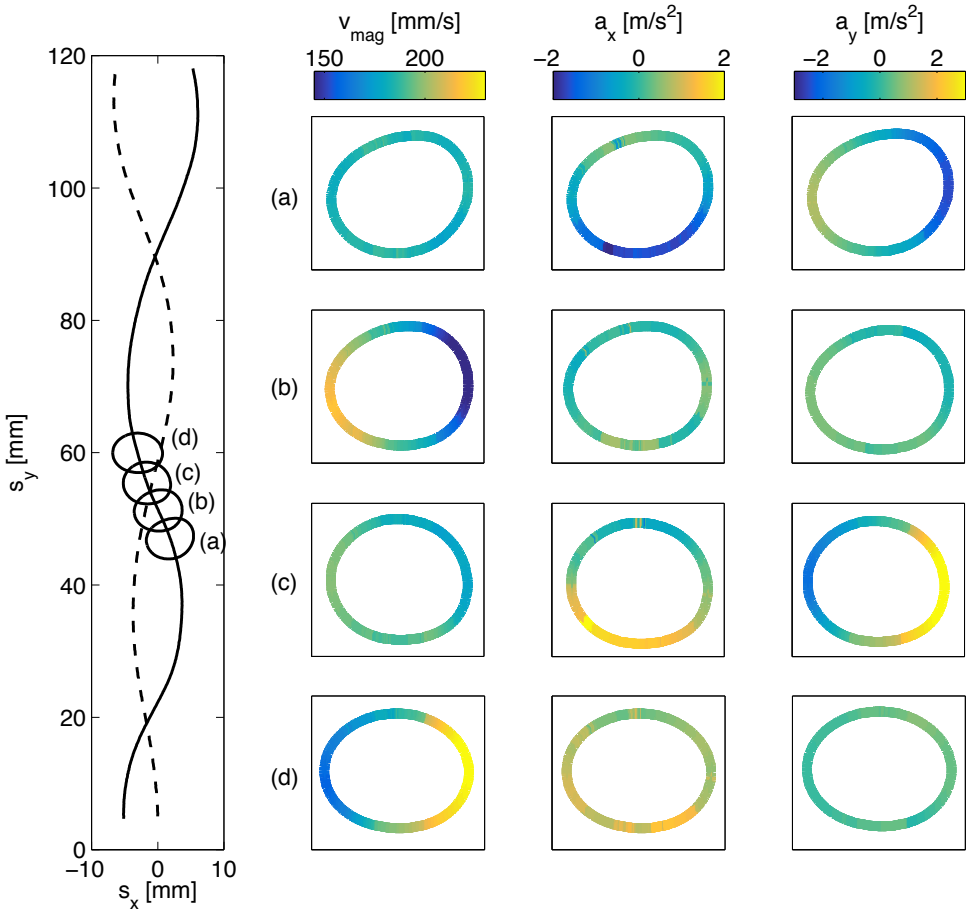

Figure 6.19: Parameters calculated at 360 points around the trailing bubble, for $\alpha = 30°$, $d_e = 5.8$ *mm*, at the locations on the bubble path identified by (a-d). The first column is velocity magnitude, the second is x-acceleration, the 3rd is y-acceleration.

with a behaviour consistent with the single bubble shown in figure 6.5 (c), with the one exception to this being the acceleration in the y-direction. At this phase angle, a_y was found to decrease at all locations around the bubble interface for a single bubble, while in this case there is an acceleration on the inside edge of the bubble. This is likely due to the trailing bubble passing through the non-stationary fluid in the wake of the leading bubble, which moves in the direction of buoyancy. This acceleration results in a subsequent increase in velocity on this inside edge, which can be observed 25 *ms* later at the location (b). The portion of the trailing bubble that has intersected the leading bubble's path experiences an increase in velocity. The superposition of the bubble velocity vector and this wake-induced acceleration causes the bubble to experience a clockwise rotation, which is opposite to the counter-clockwise rotation expected at this phase angle. Depending on the strength of the

fluid in the wake of the leading bubble and the initial velocity vector of the trailing bubble, this motion can result in a momentary "rocking" of the bubble interface, with the orientation of the bubble remaining the same sign. However, in this case, the induced tilt change is sufficiently strong to change the orientation completely, as can be observed in figure 6.19 at location (c). The bubble takes on a rounded shape, even though the velocity of the edge data is not low in magnitude. This is again in contrast to the single bubble case, wherein a spherical shape occured at regions of minimum circumferential velocity. At this instant, the right hand side of the bubble has entered the leading bubble wake, and experiences a sharp acceleration in the direction of buoyancy. The left hand side of the bubble is longer intersecting the fluid from the leading bubble wake, and as such begins to decelerate. The x-acceleration of the bubble base is also affected, experiencing an acceleration in the positive spanwise direction.

The result of these various accelerations can be seen in row (d), where the bubble is approaching its local minimum in path displacement. The inside edge of the bubble path has increased significantly in velocity, while the bubble has become elongated in shape. After this point, the bubble interface will rebound again such that when it reaches its local minimum in path displacement, the maximum velocity will be at the outside edge of the bubble. This interaction between the two bubbles is very complex, with the moving fluid to the rear of the leading bubble having a profound effect on the mechanics of the trailing bubble. The key influence of the leading bubble wake is to induce high-frequency changes in the circumferential velocity of the trailing bubble, with each side of the bubble being accelerated when it passes through the leading bubble wake and decelerated when it leaves the wake. This asymmetrical circumferential acceleration causes intricate changes in the trailing bubble shape and orientation, which will be discussed presently.

Figure 6.20 shows the mean and fluctuating centroidal velocity of the leading (a) and trailing (b) bubbles for all three inclination angles. The mean velocity does not always increase as in figure 6.18, as the fluctuations are being averaged over 1-2 wavelengths only, which is a small sample size. The amplitude and frequency of the trailing bubble velocity fluctuations are larger than the leading bubble for all tests. For $\alpha = 20°$, recall that the trailing bubble initially experiences somewhat transitional behaviour, with the bubble sweeping a long arc at $t = 0.22$ s, after which its velocity increases substantially. The trailing bubble

velocity for $\alpha = 30^\circ$ has been discussed in detail, and that at $\alpha = 40^\circ$ is largely similar, with a repeating structure of high magnitude peaks corresponding to the bubble being at its maximum s_x and the secondary peaks corresponding to induced velocity by the leading bubble.

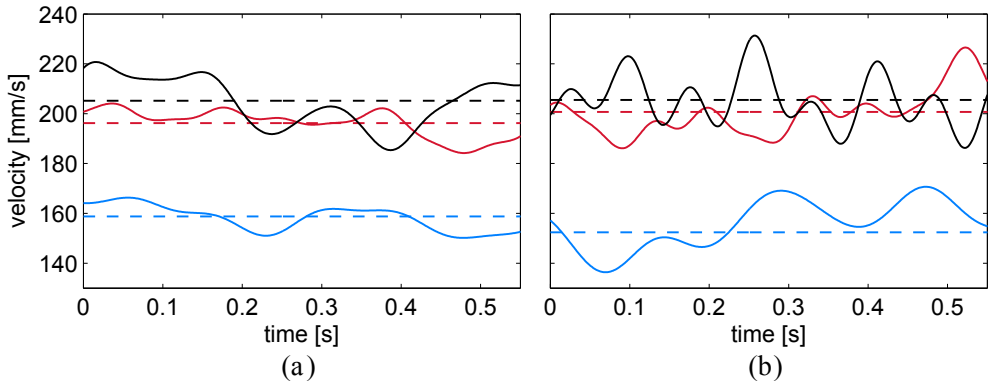

Figure 6.20: Time-varying (solid lines) and mean (dashed lines) velocity magnitude $|v| = \sqrt{(v_x)^2 + (v_y)^2}$ in mm/s for the (a) leading and (b) trailing bubbles at $\alpha = 20^\circ$ (–), 30° (–) and 40° (–).

6.2.3 Eccentricity and Orientation

The leading bubble wake induces significant changes in shape and orientation of the trailing bubble. Figure 6.21 shows the path of the leading (a,c,e) and trailing bubbles (b,d,f) coloured by the eccentricity for all three inclination angles. The leading bubble paths are shown on the trailing bubble plots as dashed lines. For $\alpha = 20^\circ$, the trailing bubble experiences little changes in shape until it intersects the leading bubble path, with the shape oscillating after this point. For $\alpha = 30^\circ$, the trailing bubble experiences dramatic shape oscillations between oblate and approximately spherical, with the bubble shape again at its most spherical at the mean path displacement and most oblate at the path extrema. Some secondary shape oscillations also occur due to the wake-induced motion in the process described in figure 6.18. A key point is that the bubble shape no longer matches its velocity, as was the case for the single bubble case. The same is true for $\alpha = 40^\circ$, although the fluctuations in shape are larger.

Finally, the orientation, θ, is shown in figure 6.22. As was explored in figure 6.19, passing through the leading bubble wake induces changes in orientation in the trailing bubble.

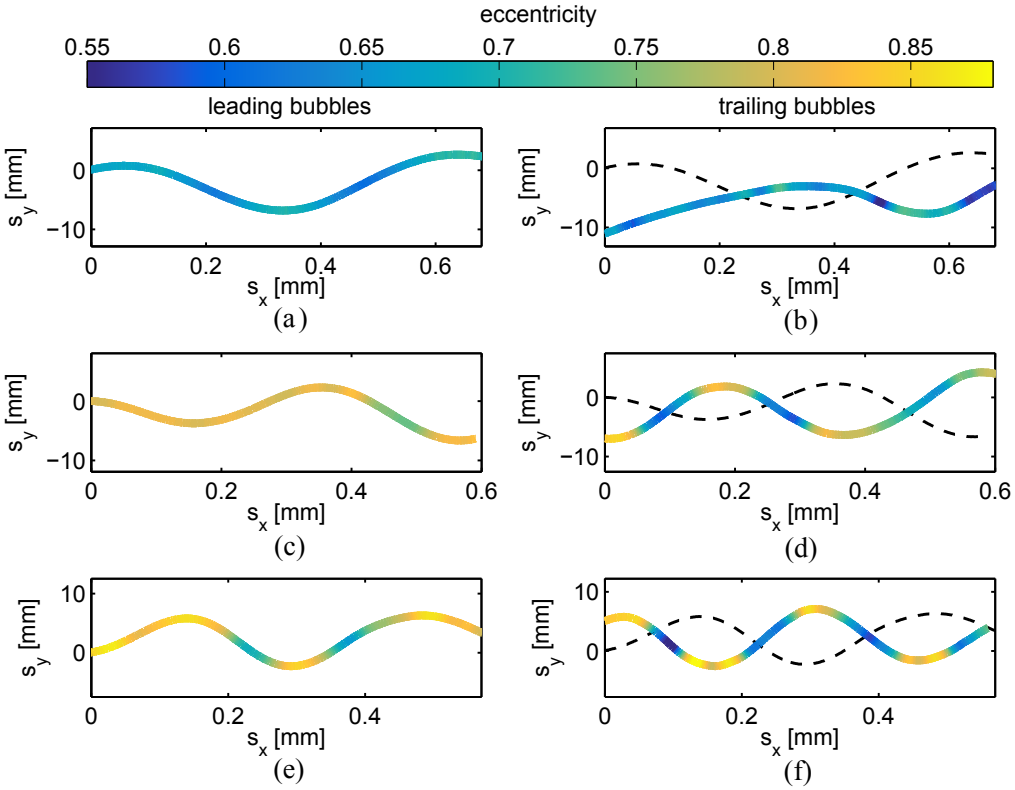

Figure 6.21: x-displacement, s_x as a function of time, coloured by the eccentricity for the leading (left) and trailing (right) bubbles, at $\alpha = 20°$ (a,b), 30° (c,d) and 40° (c,d) .

However, the magnitude of induced orientation change is complex and difficult to predict, as it depends on the velocity of the fluid in the wake of the leading bubble and the velocity vector of the trailing bubble. At $\alpha = 20°$, the bubble travels with relatively little tilt until the bubble moves into the wake of the leading bubble, adopting the in-phase bubble path, at which point it increases rapidly. At $\alpha = 30°$, the induced motion on the trailing bubble is sufficient to change the sign of the orientation angle, with these mechanics having been discussed in detail around figure 6.19. At $\alpha = 40°$, the leading bubble causes secondary fluctuations in the leading bubble orientation, although these are not sufficient to change the sign of θ.

6.3 Summary

This chapter has investigated the motion of both a single bubble and an an-line bubble pair sliding under an inclined surface for a range of bubble diameters and surface inclination angles, for clean and contaminated water. Quantities describing the mechanics of these

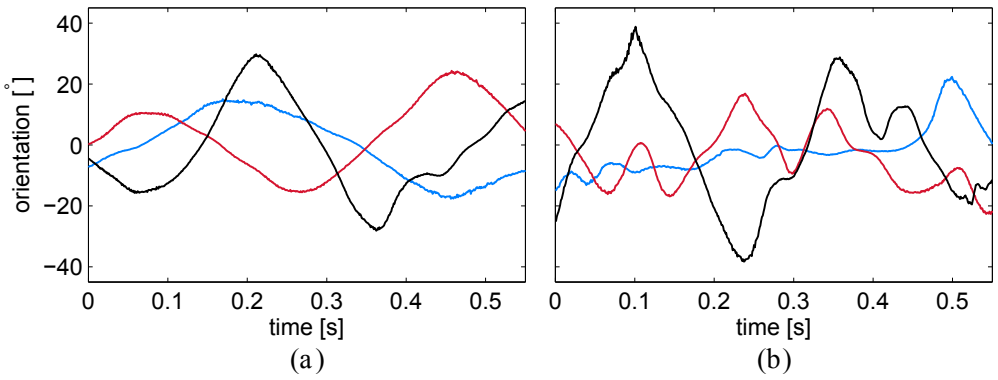

Figure 6.22: Orientation, θ, for the (a) leading and (b) trailing bubbles at $\alpha = 20^\circ$ (−), 30° (−) and 40° (−).

sliding bubbles, such as shape, velocity and orientation, have been investigated, with a key focus on the changes that occur in these during a bubble-wake interaction. Basing the mechanics of a sliding bubble solely on the motion of its centroid results in many of the dynamic aspects of the flow being ignored. The tracking algorithm introduced in section 5.1 has allowed for the mechanics of the bubbles to be expressed in terms of its centroid and interface, providing a more complete description of sliding bubbles. All bubbles in the current study are in the ellipsoidal regime defined by the Reynolds, Weber and Morton numbers, and thus experience undulating path and shape oscillations as they traverse the surface, with a velocity that fluctuates about a mean at twice the path frequency. In some cases, the mean velocity was found to decrease in time. An analysis of the bubble edge data revealed this is due to the bubble taking sharper turns due to the ejection of a large quantity of liquid into the wake, resulting in a reaction force that slows the bubble in the vertical direction. A force balance was performed on the sliding bubble, showing that the forces do not remain in equilibrium, with the bubbles experiencing net forces in the spanwise and length directions due to this wake instability. The mean of net forces acting on the bubble was zero, and a fluctuating drag coefficient was observed.

Two-phase flows are heavily dependent on the purity of the system. It was found that the addition of a minute amount of surfactant fundamentally altered the mechanics of the bubble. In a contaminated system, bubbles were found to rise almost rectilinearly, experiencing large, repeating shape oscillations due to the partial slip condition that exists at the rear of the bubble. Unlike rising bubbles, this has the effect of increasing the bubble velocity, as this

damping of the shape oscillations results in the velocity vector remaining aligned with the buoyancy force. For multiple bubbles, it was found that the bubble paths adopt an in-phase, opposite amplitude path that appears to be the most stable configuration for an in-line bubble pair. The trailing bubbles experienced high frequency circumferential changes in velocity and acceleration, accompanied by variations in shape and orientation. These mechanics have been attributed to the trailing bubble entering and exiting the leading bubble wake, with all subsequent bubble-bubble interactions triggered by this initial bubble-wake interaction. For a more complete discussion, an understanding of the fluid motion in the leading bubble wake is necessary. As such, this analysis of bubble mechanics will continue in chapter 7 when the wake structures of sliding bubbles have been presented.

Chapter 7

Fluid Motion

This chapter presents velocity and vorticity measurements for single and paired sliding bubbles in three measurement planes, using the PIV processing techniques outlined in section 5.2. An analysis of these results will be combined with the findings in the literature on rising bubbles and bluff bodies, together with the bubble mechanics from chapter 6, to characterise the wake motion associated with sliding bubbles.

Section 6.2 showed how the addition of minute amounts of surfactant completely altered the bubble behaviour. Through experimentation, it has been found that contaminated system behaviour is not caused by the introduction of the PIV tracer particles: rather, the effect can be triggered either by the lack of fluid purity or by sedimentation gradients within the tank. The system purity is maintained as high as possible during testing by using deionised water. However, even if ideal, perfectly neutrally buoyant particles are used, the motion of the bubble can create sedimentation gradients by carrying tracer particles to the surface. To avoid this, tests are performed soon after the introduction of the deionised water and particles, with the water changed every 8 hours of testing to prevent transition to impure behaviour. Velocity and vorticity measurements are performed for the same range of parameters discussed in chapter 6, although these are predominately discussed for the base case of $\alpha = 30^{\circ}$.

7.1 Parallel Plane

In the parallel plane, two measurement planes are used at heights (distanaces from the inclined surface) corresponding to $s_z = 3$ *mm* and $s_z = 9$ *mm*, as illustrated in figure 4.2. The

discussion will centre around single and multiple bubbles of 5.8 *mm* and 7.2 *mm* diameter in each of these planes for α = 30°, although the influence of changing the inclination angle on the strength of the wake structures will also be examined. On these instantaneous velocity and vorticity plots, the bubble shape calculated from the raw PIV images is overlaid, along with the pathline of the bubble over its traverse of the measurement area. The surface is again unheated for these tests.

7.1.1 Single Bubble: $s_z = 3$ *mm*

Figure 7.1 shows the instantaneous velocity magnitude and vorticity for $\alpha = 30°$, $d_e = 5.8$ *mm*, $s_z = 3$ *mm*. This provides instantaneous measurements of the flow field at three instances in time: $t = t_0$, and $t = t_0 + 0.2$ *s* and $t = t_0 + 0.4$ *s*. For the vorticity plot, positive vorticity is counter-clockwise rotation (gold), while negative vorticity is clockwise (blue). The bubble, tracked from the raw PIV image, is shown in white.

The first instant in time in the sequence, figure 7.1 (a) and (d), corresponds to the bubble centroid at the position $s_y = 60$ *mm*. In both velocity and vorticity plots, the significant motion induced by the bubble in the surrounding fluid is immediately apparent. The difference in location between the bubble's traverse pathline and the regions of non-zero velocity and vorticity show the advection of the flow during the time scale of the bubble's transit. These occur both along the length and spanwise directions, resulting in a wake structure that "overshoots" the bubble path. The bubble, which in figure 7.1 (a) and (d) is at a local minimum in spanwise position, accelerates the quiescent fluid directly in front of it. On either side of the bubble, counter-rotating regions of circumferential vorticity are observed at the tips of the bubble major axis, which are the locations of maximum interface curvature. For a region extending to $1-2$ bubble diameters downstream of the bubble base, the near wake is observed, which is defined as that moving in direct association with the bubble (the near wake is occasionally referred to as the attached wake for this reason). As was observed by Brücker [39] for freely rising bubbles, vortex shedding is found to occur at each local extrema of the bubble path. This occurs because at these locations, the bubble and its previous near wake have opposite spanwise components of velocity, thereby separating. At the equatorial edges of the bubble, the vorticity on the inside of the bubble path is larger in magnitude than that

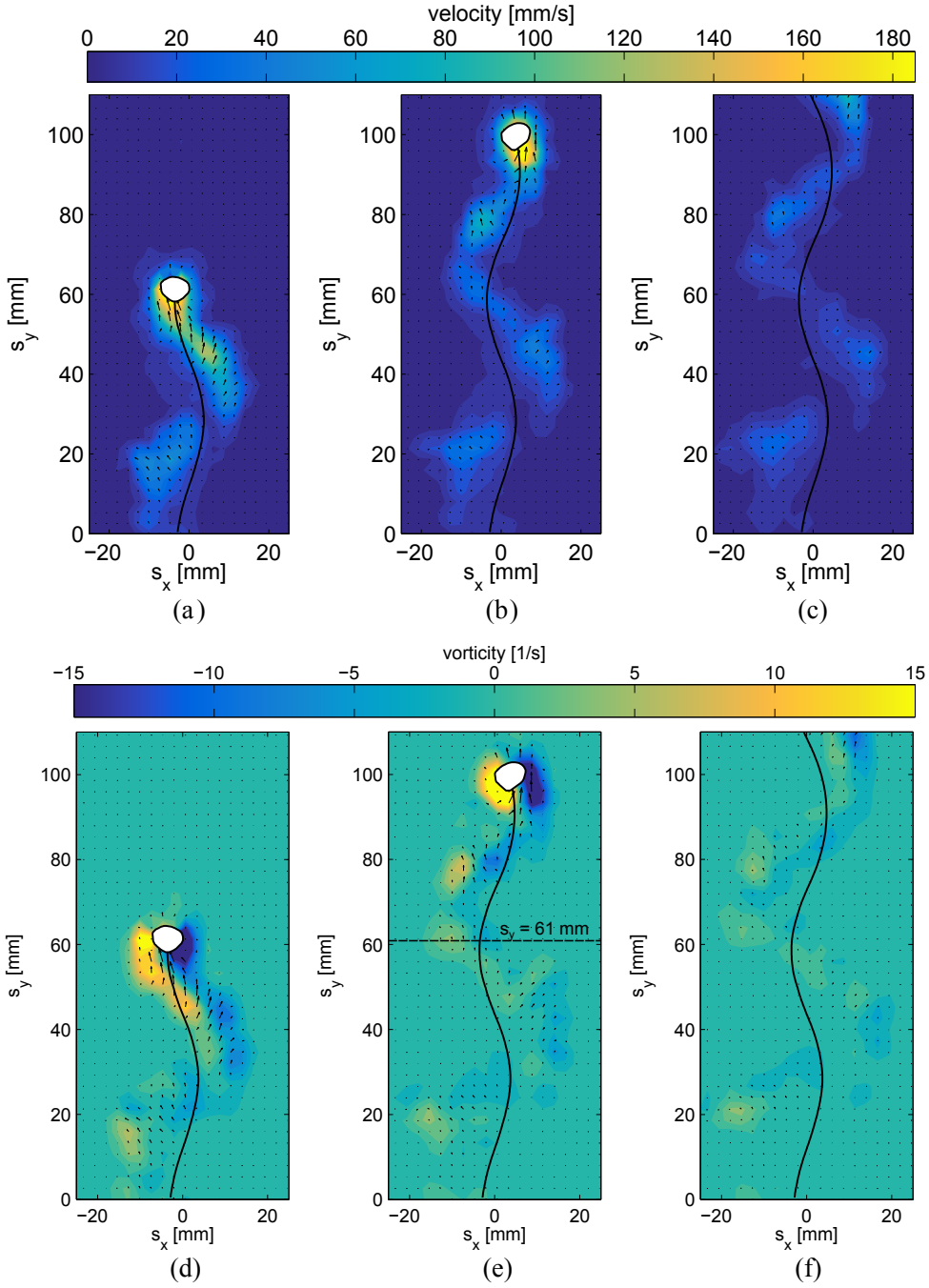

Figure 7.1: Fluid velocity magnitude $V_{mag} = \sqrt{U^2 + V^2}$ $[mm/s]$ (top) and vorticity Ω =curl(**U**) $[1/s]$ in a parallel plane at $s_z = 3$ *mm* for $\alpha = 30°$, $d_e = 5.8$ *mm*, with the approximate bubble shape and path overlaid. Each image in this sequence is $\Delta t = 0.2$ *s* apart.

on the outside, causing the bubble to rotate towards the inside of its path. This dominant vorticity component results in the replenishment of the near wake with the fluid from the inside of the bubble path. Approximately 1-2 bubble diameters downstream, the opposite direction of vorticity is stronger in magnitude, extending downstream to form the “tongue”

shaped regions of vorticity also identified by Brücker [39].

The second image in each sequence, figure 7.1 (b) and (e), shows both the near and far wake of the bubble, which is now at a local maximum in spanwise position at the location $s_y = 100\ mm$. In the far wake, the affected regions of fluid have increased in size but decreased in magnitude, by this time having significantly overshot the bubble path. Thus, the far wake takes the general form of comparatively high velocity regions at the path extrema and comparatively low fluid velocity separating these areas. Finally, for the last image pair 0.2 seconds later, the strength of velocity and vorticity in the wake have decreased in magnitude substantially. The shed structures continue to spread into the bulk fluid, albeit doing so at a lower velocity. This is due to a combination of viscous dissipation in the fluid and out-of-plane motion normal to the surface.

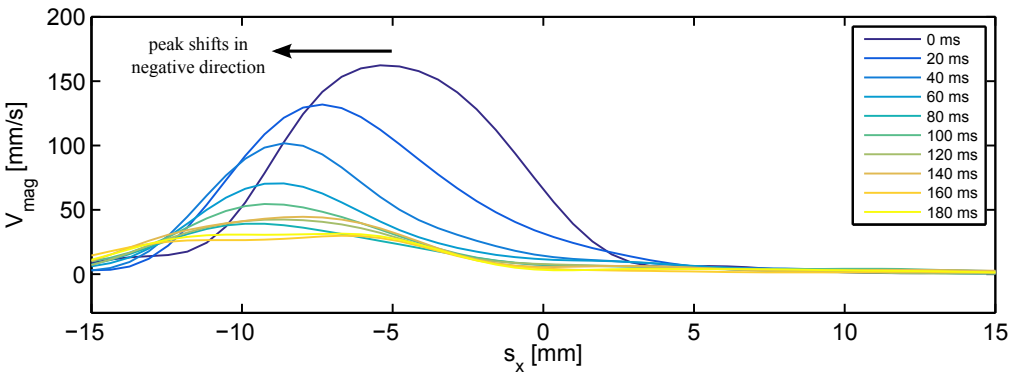

Figure 7.2: Velocity magnitude along a defined slice of the surface at $s_y = 61\ mm$ for $d_e = 5.8\ mm$, $\alpha = 30°$, with successive lines corresponding to 20 *ms* intervals.

The temporal evolution of the local velocity is provided in figure 7.2 along the horizontal line in figure 7.1 (e) corresponding to $s_y = 61\ mm$. This plot starts at a time t_0, directly after the base of the bubble has passed through $s_y = 61\ mm$. At this location the bubble is at a local minimum of spanwise position. As was found in figure 7.1, the near wake occurs directly after the bubble passage and moves at close to the bubble velocity, acting over an area two bubble diameters in size. At this local minimum, the bubble changes direction due to the wake instability, travelling in the positive spanwise direction. The now detached near wake continues on its original course in the negative spanwise direction. This results in the peak of the velocity profiles shifting to the left. The local maxima of the velocity distribution here also decrease dramatically, as do their gradients. By $t = 0.2\ s$ after the bubble passage, the

local peak in velocity has reduced to 10% of the maximum value observed in the near wake.

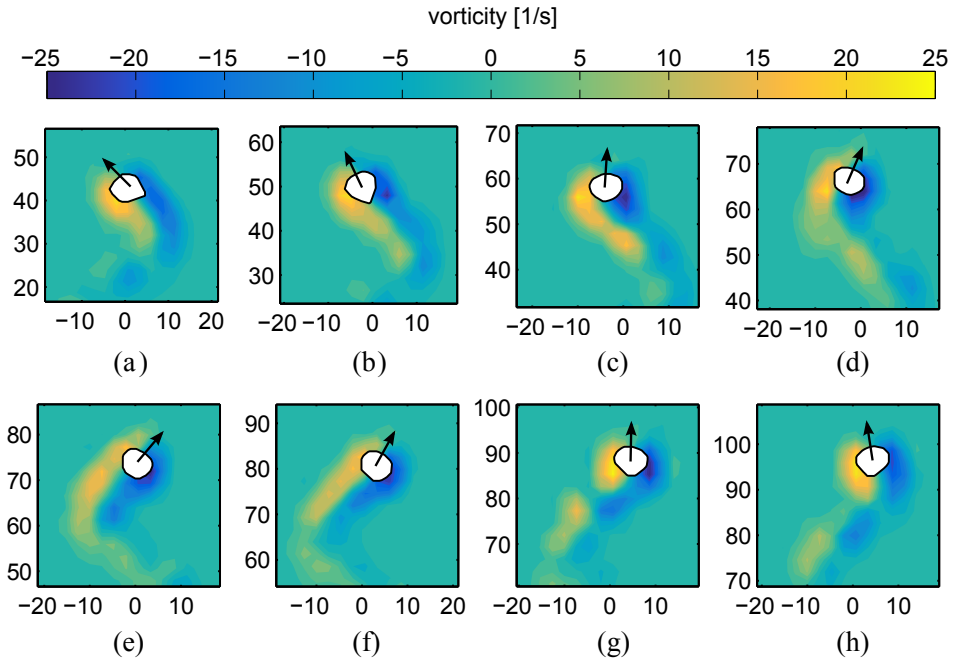

Figure 7.3: Vorticity distribution in the near wake of the d_e = 5.8 *mm* bubble at instances in time 20 *ms* apart, with velocity vectors omitted.

Figure 7.3 shows the temporal vorticity distribution in the near wake at instances in time 20 *ms* apart, as the bubble completes one wavelength of motion. The relative strength of the vorticity components on either side of the major axis is linked to the phase angle of the bubble's path. The fluid motion is observed to begin some small distance upstream of the bubble, where the bubble accelerates the fluid directly in front of it. This leads into a pair of counter-rotating regions of vorticity around the bubble circumference, approximately 2 bubble diameters in size in the spanwise direction. These form the near wake, travelling at approximately the bubble velocity. At the inversion points of the bubble path, fluid is separated from the near wake, shedding a vortical structure that also moves normal to the surface. At this point of separation, the vorticity of the fluid on the inside of the bubble path is of greater magnitude, drawing fluid into the near wake from this side. This repeating process is clearly visible in figure 7.3, which results in the variations in bubble mechanics reported by chapter 6.

The effect of increasing the bubble diameter to 7.2 *mm* is shown in figure 7.4. Although the general nature of the wake structures changes very little, the magnitudes of velocity and vorticity increase somewhat, as too does the size of the affected region. Again, the

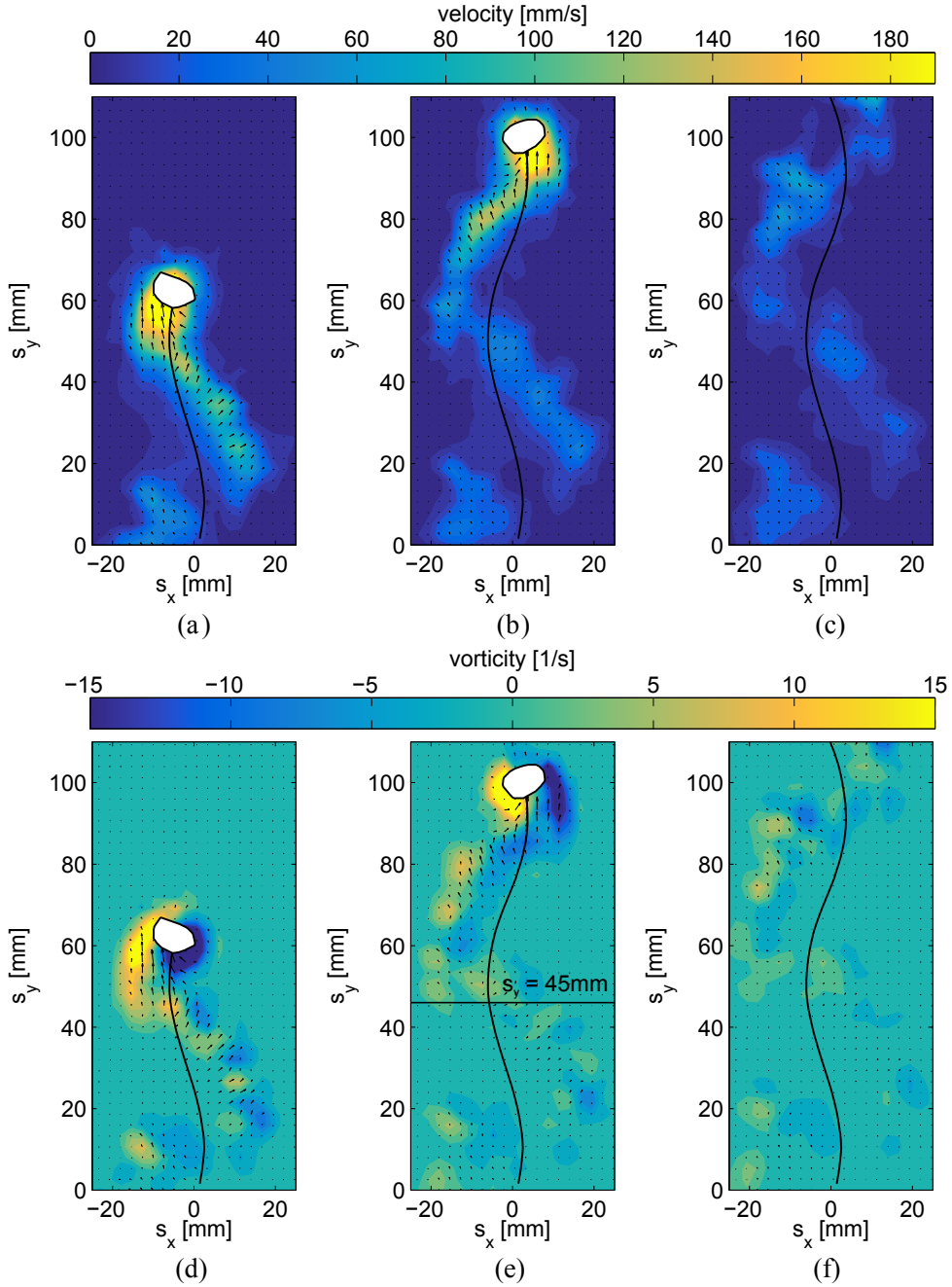

Figure 7.4: Fluid velocity magnitude $V_{mag} = \sqrt{U^2 + V^2}$ $[mm/s]$ (top) and vorticity Ω =curl(**U**) $[1/s]$ in a parallel plane at s_z = 3 *mm* for $\alpha = 30°$, $d_e = 7.2$ *mm*, with the approximate bubble shape and path overlaid. Each image is $\Delta t = 0.2$ *s* apart.

overall wake structure consists of a near wake that stretches up to 1.5 bubble diameters downstream of the bubble base, and a far wake downstream of the bubble. The wake evolves in a similar manner to the 5.8 *mm* case, but is slightly more chaotic, with some secondary, "tailed" structures at the base of each discrete shed region. These tail-shaped regions will

be discussed shortly. The advection effects in the far wake are also noticeable, lasting for a significantly longer time and overshooting the bubble path to a greater extent. The temporal evolution of the local velocity for $d_e = 7.2$ *mm* is provided in figure 7.5 along the horizontal line corresponding to $s_y = 45$ *mm* on figure 7.4 (e). In this case, both the velocity magnitude and the affected region are larger than the equivalent $d_e = 5.8$ *mm* plot. A secondary peak is also observed in the positive spanwise direction as the bubble wake is advected into the measurement region. The larger advection effects are also visible here, as the local velocity after 0.2 *s* is now approximately 20% the peak value in the near wake, as opposed to 10% for the $d_e = 5.8$ *mm* bubble.

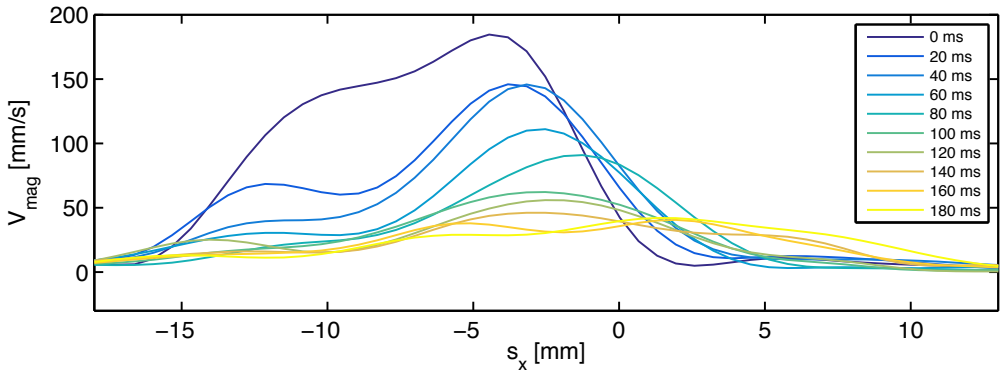

Figure 7.5: Velocity magnitude along a defined slice of the surface at $s_y = 45$ *mm* for $d_e = 7.2$ *mm*, $\alpha = 30°$, with each line corresponding to a 20 *ms* interval.

Figure 8.12 shows the temporal vorticity distribution in the near wake for $d_e = 7.2$ *mm*. Although the magnitude and size of the affected region are larger than for the $d_e = 5.8$ *mm* bubble, the separation of fluid from the near wake occurs in a similar manner. Also highlighted on figure 8.12 are zones of interaction between regions of opposite fluid rotation that occur following the separation from the near wake. These measurements are indicative of a complex 3-dimensional wake structure that sheds from the near wake at each path extrema.

To show these key flow features better, supporting sketches for both bubble diameters are provided in figure 7.7. The regions of highest vorticity, direction of fluid entrainment and the "tongued" regions where the vortex separates from the near wake are all identified.

The flow structures observed thus far are in a plane that bisects the near wake of the bubble, revealing an attached near wake extending to $1-2$ bubble diameters downstream of the bubble that travels in close association with the bubble, with opposite directions of

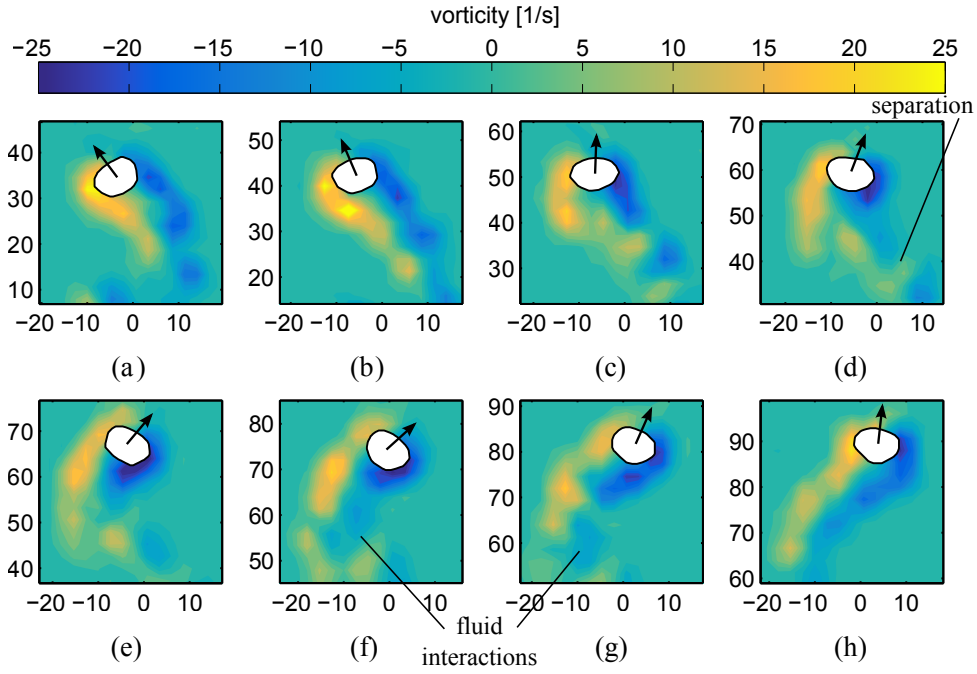

Figure 7.6: Vorticity distribution in the near wake of the d_e = 7.2 *mm* bubble at instances in time 20 *ms* apart.

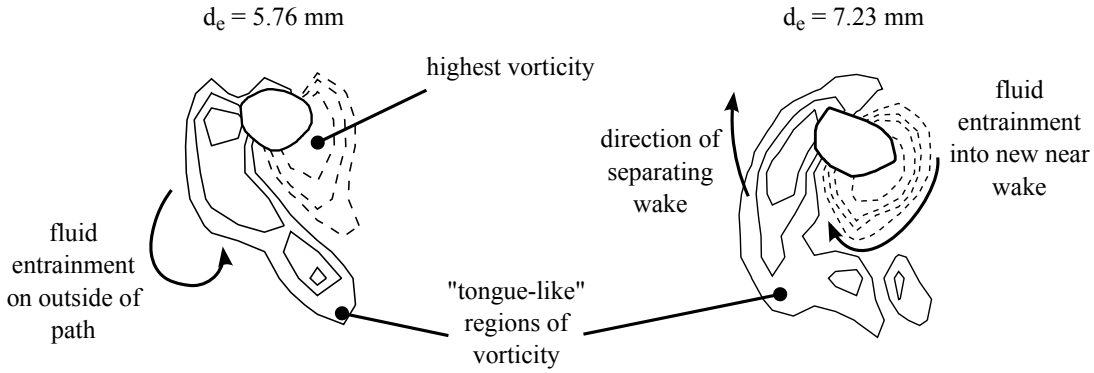

Figure 7.7: Sketch showing the near-wake circumferential vorticity distribution for both bubble diameters, with the flow features identified in the PIV data identified.

vorticity on either side of this zone. It will be observed shortly using additional measurement planes that these structures move away from the surface in the normal direction. Thus, the fluid velocity in the far wake reduces due to both viscous dissipation and out-of-plane fluid motion. As such, measurements of the fluid motion in the far can provide a useful means of quantifying the bubble-induced fluid motion, as well as comparing the strength of structures at different surface inclination angles and diameters. This was performed by Roig et al. [125], who found an exponential decay in the mean vorticity in the wake of a bubble rising within a

thin gap. In the current study, fluid motion experiments for $s_z = 3$ *mm* have been performed for both volumes at $\alpha = 20°$, $30°$, and $40°$. It is found that the strength of the wake structures shed by the bubble scales with bubble volume due to advection effects. Increasing the surface inclination angle results in a greater energy in the wake due to the higher bubble velocity, as well as a higher path frequency. These plots are largely similar to the $\alpha = 30°$ case and for brevity are not shown here.

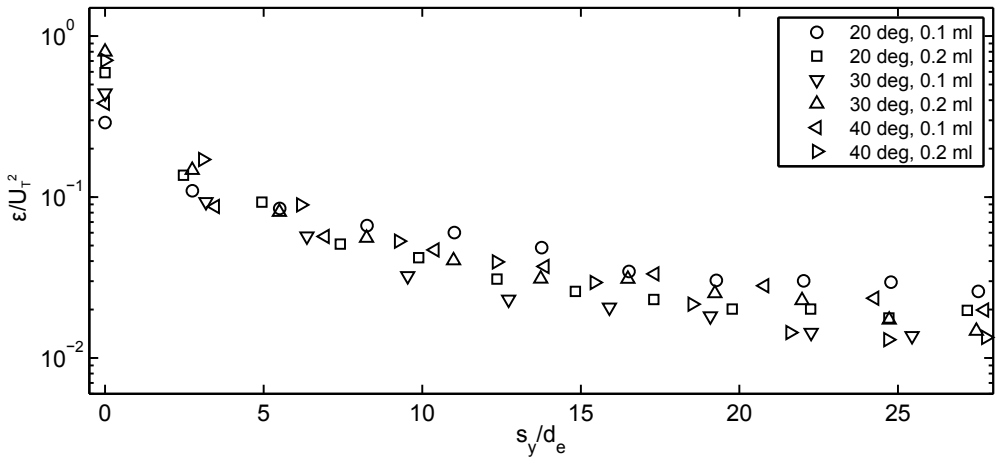

Figure 7.8: Flow enstrophy, normalised by ${U_T}^2$, versus the dimensionless distance from the bubble to the interrogation window, s_y/d_e, for the range of surface inclination angles and bubble volumes tested in the current study.

However, perhaps a better way of quantifying the energy of the flow rather than the mean vorticity is the flow enstrophy. The enstrophy can be thought of as the quantity directly related to the kinetic energy of a fluid model; specifically, that due to dissipation effects in the fluid. Under certain conditions, this quantity is proportional to the rate of decay of the flow's energy. The enstrophy of a two-dimensional flow field can be expressed as:

$$\varepsilon = \frac{1}{2}\int_s (\nabla \times \mathbf{u})^2 \, ds \tag{7.1}$$

Therefore, to quantify the global effect of the sliding bubble on the surrounding fluid, it is necessary to solve for the surface integral of the square of the vorticity field. Chapter 5 showed that the PIV algorithm erroneously detects velocity vectors within the bubble boundary. As such, the enstrophy calculation concerns the flow field after the bubble has left the interrogation window. Figure 7.8 shows a logarithmic plot of enstrophy in the flow

field with respect to the dimensionless distance from the bubble to the top of interrogation window, $\Delta s_y/d_e$, for all values of α and d_e. To collapse this data, the in-plane enstrophy is normalised by the square of the terminal bubble velocity measured for each test in chapter 6: i.e. $\varepsilon^* = \varepsilon/U_T^2$. Essentially, this graph shows the behaviour of the liquid phase as a ratio of the kinetic energies of the bubble and the vortices generated. The decay rate of enstrophy in the flow is exponential, and is largely consistent for the range of parameters studied. This is due to both viscous dissipation and out-of-plane motion. Since convective heat transfer is dependent on the fluid motion, it is expected that the surface cooling should experience a similar decay.

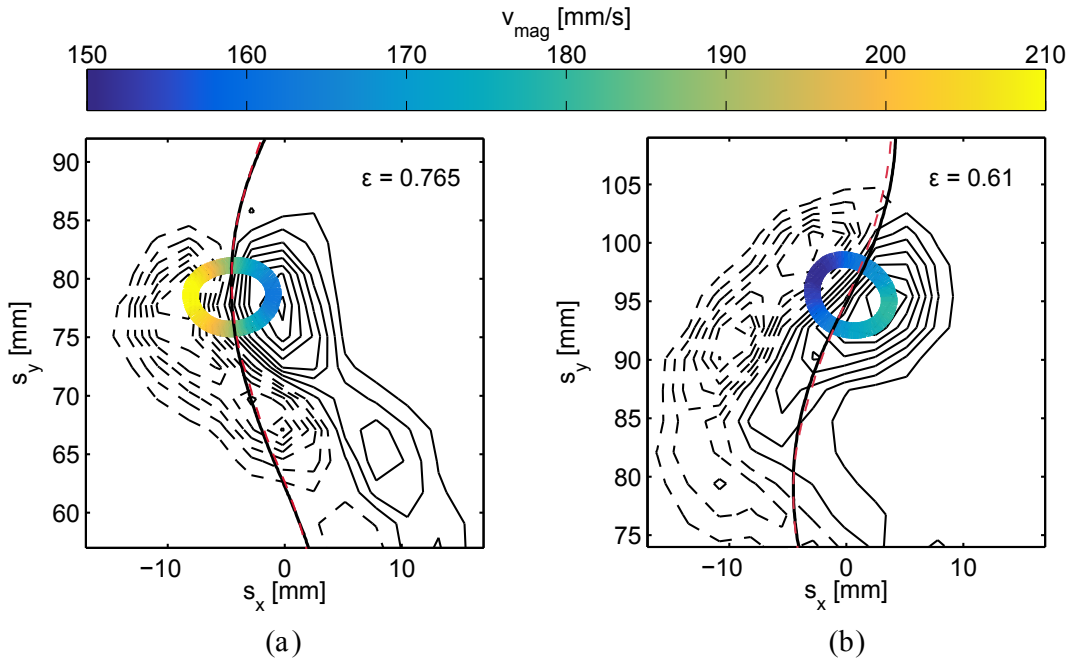

Figure 7.9: Contours representing positive (− −) and negative (−) isocontours of vorticity in the $s_z = 3$ *mm*, mapped to the equivalent bubble location on the corresponding bubble motion path at two pathwise locations. The bubble paths for the fluid motion test (−) and the bubble motion test (− −) and the bubble eccentricity at each location are also provided

Figure 7.9 links the bubble mechanics to the vortex shedding by spatially mapping the bubble motion from chapter 6 for $\alpha = 30^\circ$, $d_e = 5.8$ *mm* to isocontours of vorticity in the $s_z = 3$ *mm* plane at two instances in time corresponding to the bubble being at its local minimum and local mean in path. The changes in circumferential velocity around the bubble interface occur due to the oscillatory bubble path, which itself is caused by the wake instability due to the large size of the bubble. This results in a two-way coupling between the fluid in

the bubble wake and the deformation of the bubble interface. At the local minimum in path, fluid from the near wake separates and is replenished from the inside of the bubble path. At this location, the bubble's velocity vector is aligned with the buoyancy force and its shape is comparatively ellipsoidal ($\varepsilon = 0.76$), while the outside edge of the bubble traces a larger path and has a larger velocity. As the instability returns the bubble to its mean displacement, its near wake continues to be replenished by fluid on the inside of its path. Meanwhile, the velocity vector of the bubble is no longer aligned with the buoyancy force and experiences a lower velocity magnitude around its interface. This lower velocity corresponds to a shift downwards in the regime map in figure 2.1, resulting in a more spheroidal shape of $\varepsilon = 0.61$. This means that the major axis of the ellipse, and correspondingly the affected region of fluid, are smaller at this point. This behaviour repeats as the bubble traverses the surface.

7.1.2 Single Bubble: $s_z = 9\ mm$

The velocity and vorticity in the $s_z = 9\ mm$ plane for $\alpha = 30°$, $d_e = 5.8\ mm$ are provided in figure 7.10. This measurement plane is sufficiently far from the surface as to be unaffected by the immediate passage of the bubble. Instead, this plane captures a cross section of the fluid motion normal to the surface in the far wake. One issue with PIV in this plane is that the bubble is still visible and is detected by the algorithm as a collection of particles with a velocity U_T, despite there being no motion in-plane. This is addressed by masking the velocity vectors in the vicinity of the tracked bubble. Note also that the scales of velocity and vorticity in this case are lower than those in the $s_z = 3\ mm$ plane, indicating the majority of high-velocity fluid motion remains close to the surface. In figure 7.10, instantaneous snapshots of the flow field are provided at the locations $t = t_0$, and $t = t_0 + 0.2\ s$ and $t = t_0 + 0.4\ s$. In this plane, the far field velocity is of greater interest, and thus t_0 corresponds to $s_y = 100\ mm$ rather than $s_y = 60\ mm$.

The PIV results in this plane reveal the three-dimensional nature of the wake, as the measurement plane is beneath the base of the bubble yet detects significant fluid motion. Additionally, the divergence of the velocity field, $\nabla \cdot \mathbf{U}$, is non-zero and shows the direction of normal velocity W is away from the surface. A short time after the bubble passage, fluid enters the plane approximately 3 bubble diameters upstream of the previous spanwise

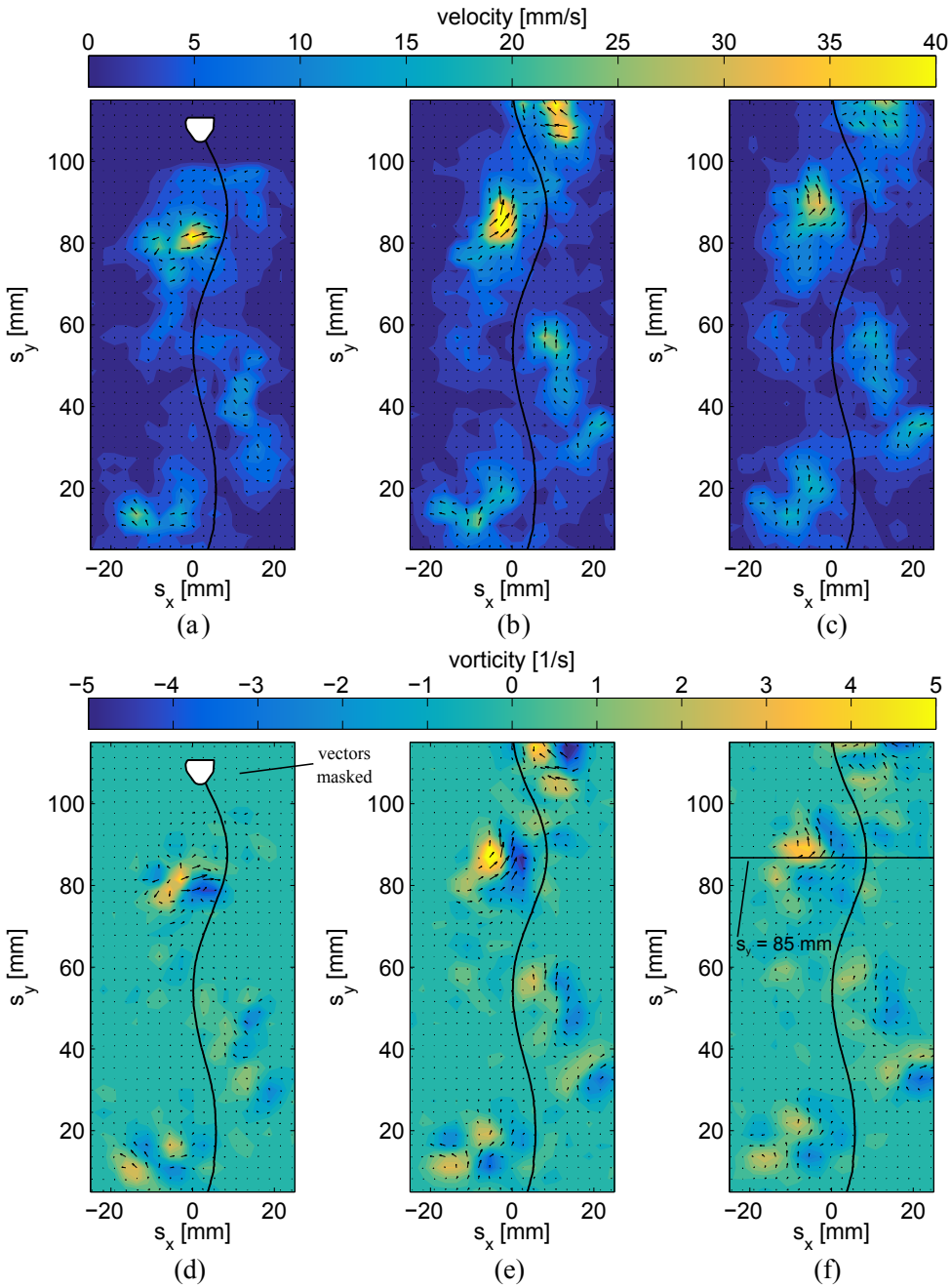

Figure 7.10: Fluid velocity magnitude $V_{mag} = \sqrt{U^2+V^2}$ $[mm/s]$ (top) and vorticity Ω =curl(**U**) $[1/s]$ in a parallel plane at $s_z = 9$ *mm* for $\alpha = 30°$, $d_e = 5.8$ *mm*, with the approximate bubble shape and path overlaid. Each image is $\Delta t = 0.2$ *s* apart.

path extrema. This indicates that the wake structures initially shed at the local extrema in path are advected along the length of the bubble's pathline before they enter the $s_z = 9$ *mm* plane. In this plane, the lower velocity magnitude results in slightly decreased coherency. Nonetheless, approximately ellipsoidal-shaped regions of enhanced velocity are visible, again with secondary "tailed" regions stretching to the rear of these regions. However, it is the

vorticity that is of most interest in figure 7.10. The high velocity regions correspond to coherent, counter-rotating regions of vorticity, which are believed to be the two-dimensional cross section of the legs of a hairpin vortex passing through the plane, shed in the near wake at the previous inversion points of the bubble path. This is most noticeable in the region $[s_x, s_y] = [-10, 80]$ *mm*, which indicates that the bubble has shed a large amount of fluid into its wake at this location. The resultant changes in bubble mechanics due to this shedding have been discussed in chapter 6.

An analysis of this time-resolved PIV reveals that large temporal velocity gradients exist within the primary shed vortices, where the high-velocity fluid region corresponds to the hairpin vortex legs appearing in plane suddenly but persisting for a significant time. At the second instant in time (figure 7.10 (b) and (e)), the vortex cores have become stretched and elliptical in shape, while the fluid in these regions has increased in velocity. The direction of vorticity causes the two components of each core to separate laterally, spreading into the initially quiescent fluid on either side of the vortex pair. Low-magnitude vortex pairs are also visible in the far wake, which is consistent with a complex 3-dimensional wake structure in which there interactions occur between the primary vortex structures and the bulk fluid. These secondary structures in the far wake act to further mix the bulk fluid, which can be seen in the last image pair, 0.2 *s* later. The velocity magnitude in this plane has began to decrease due to viscous dissipation and further out-of-plane effects.

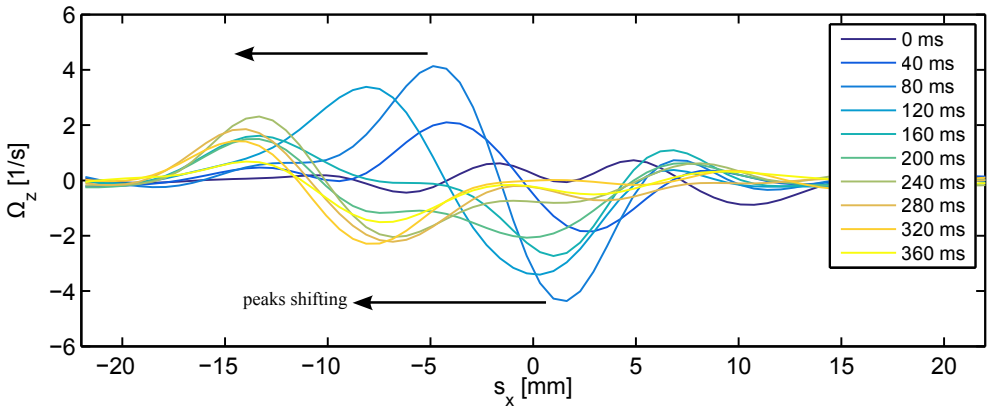

Figure 7.11: Vorticity along a defined slice of the surface at $s_y = 85$ *mm* for $d_e = 5.8$ *mm*, $\alpha = 30°$, with each line corresponding to a 40 *ms* interval.

Figure 7.11 shows the vorticity across the slice of the surface at the line $s_y = 85$ *mm* in figure 7.10 (e) plane at instances in time 40 *ms* apart. As before, $t = 0$ *s* is directly after the

passage of the bubble. The in-plane vorticity is low directly after the bubble passage, but over the next 80 *ms* a counter-rotating vortex pair enters the plane, corresponding to the vortex shed at the previous local minimum in path. This is subsequently advected in the negative spanwise direction due to the momentum of the bubble. The effects of the bubble on fluid motion in this plane also last for a significant time, with the vortex pair having reduced in magnitude to 10% of its maximum value after 0.4 *s*.

The effect of increasing the bubble diameter has a more profound effect on the wake structures in the $s_z = 9$ *mm* plane than in the $s_z = 3$ *mm* plane. An analysis of the perpendicular plane PIV that will be presented in section 7.2 reveals that the increased volume does *not* extend the bubble in the normal (s_z) direction; instead, the major axis in the parallel plane grows. However, the greater advection effects of this larger bubble volume results in a flow velocity and vorticity that are 50% larger than the 5.8 *mm* bubble, and thus more coherent wake structures. The velocity and vorticity for $s_z = 9$ *mm*, $\alpha = 30^\circ$, $d_e = 7.2$ *mm* are shown in figure 7.12. The elliptical regions of high-magnitude velocity previously discussed are instantly identifiable, as are the trailing regions of affected fluid below these. Regarding these secondary structures, a video analysis of the PIV data reveals that moments after the bubble reaches a local extremum, there is some small amount of fluid motion at this location in the $s_z = 9$ *mm* plane. Thus, these tail-shaped structures consist of fluid that rolls over the bubble base at these local extrema. Further on in time, the counter-rotating vortex pairs enter the measurement window upstream of this location, with the original structure remaining at its initial position.

As these flow structures evolve in time, the direction of vorticity is such as to draw in fluid laterally from either side of the vortex pair, resulting in bulk fluid motion normal to the surface over a region far larger than the bubble diameter. The direction of fluid motion in these vortex legs can cause can cause one component to detach and spread laterally, as shown in figure 7.12 (e) at $s_y = 50$ *mm*. The in-plane effects of the vortex structure at this height from the surface last for a significant time but eventually reduce due to further out-of-plane motion and dissipation effects. Figure 7.13 shows the vorticity across the slice of the surface at $s_y = 75$ *mm* at instances in time 40 *ms* apart. This structure was shed at the previous local maximum in spanwise position, and thus is advected in the positive spanwise direction. The magnitude of the vorticity is also larger than for the 5.8 *mm* bubble.

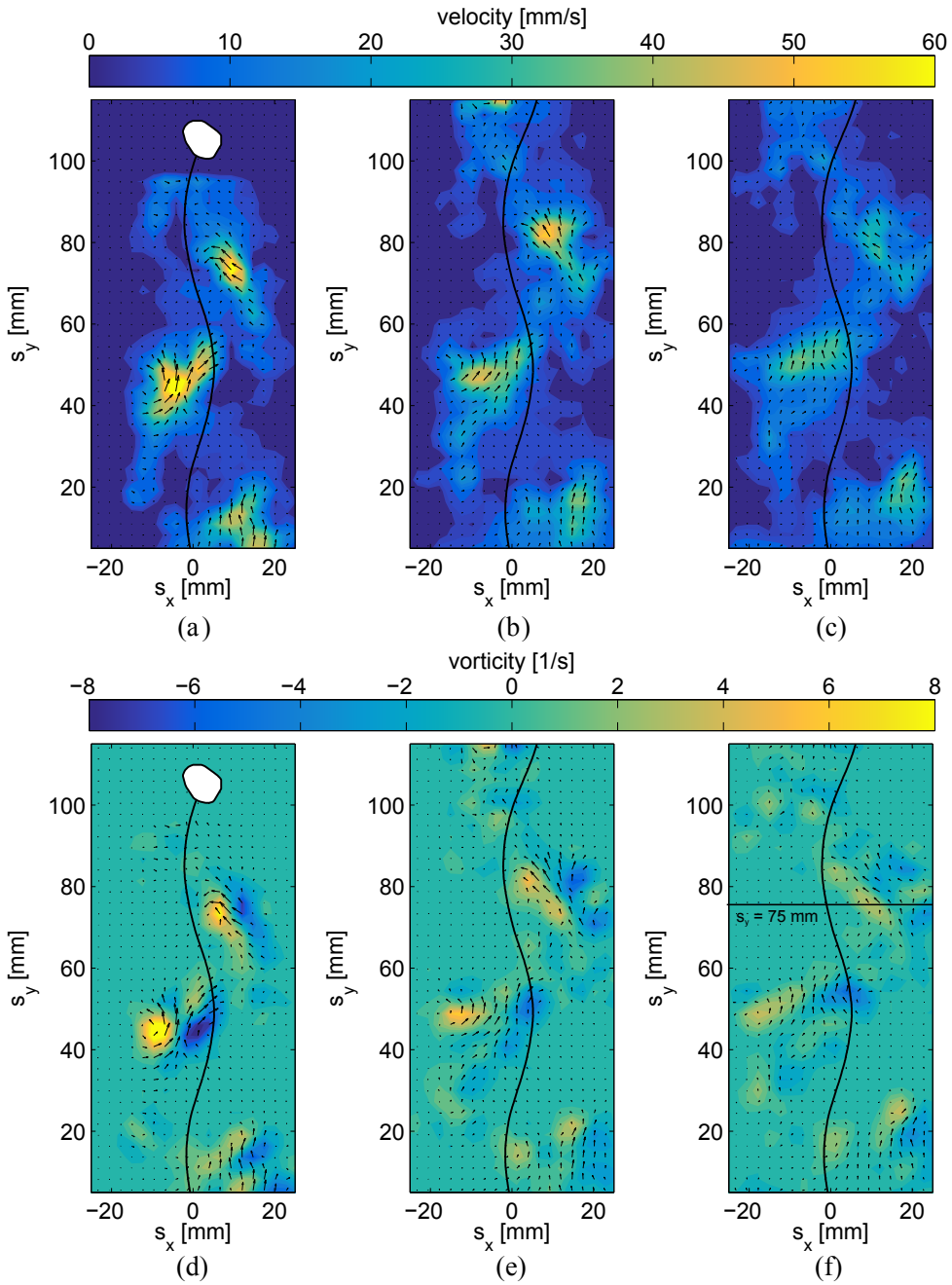

Figure 7.12: Fluid velocity magnitude $V_{mag} = \sqrt{U^2 + V^2}$ $[mm/s]$ (top) and vorticity Ω =curl(**U**) $[1/s]$ in a parallel plane at $s_z = 9$ *mm* for $\alpha = 30°$, $d_e = 7.2$ *mm*, with the approximate bubble shape and path overlaid. Each image is $\Delta t = 0.2$ *s* apart.

Supporting sketches of the fluid velocity in this plane are provided in figure 7.14 (note the $d_e = 5.8$ *mm* sketch has been flipped left to right for easier comparison). The vortex tails, direction of fluid motion and the signifcant overshoot of the structures are all identified. Recall that the attached and detached tails correspond to the fluid that rolls up over the bubble base, spreading into the $s_z = 9$ *mm* plane at the local extrema in spanwise position some time

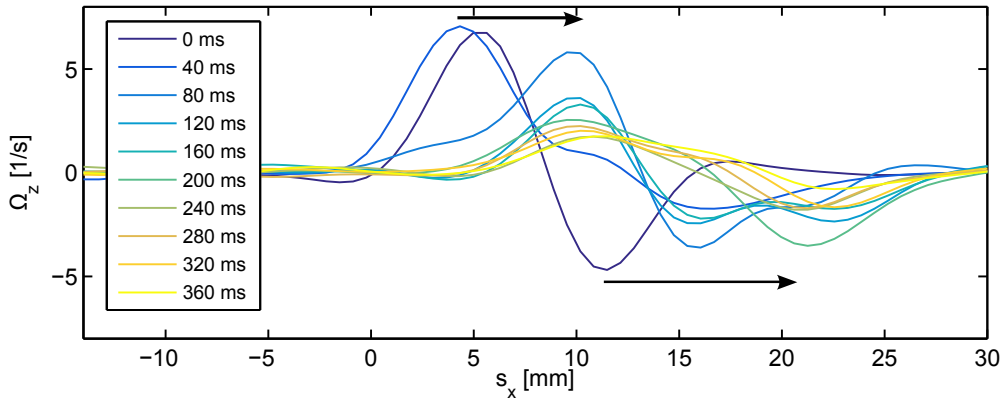

Figure 7.13: Vorticity along a defined slice of the surface at $s_y = 75$ *mm* for $d_e = 7.2$ *mm*, $\alpha = 30°$, with each line corresponding to a 40 *ms* interval.

before the primary vortex pairs enter the plane.

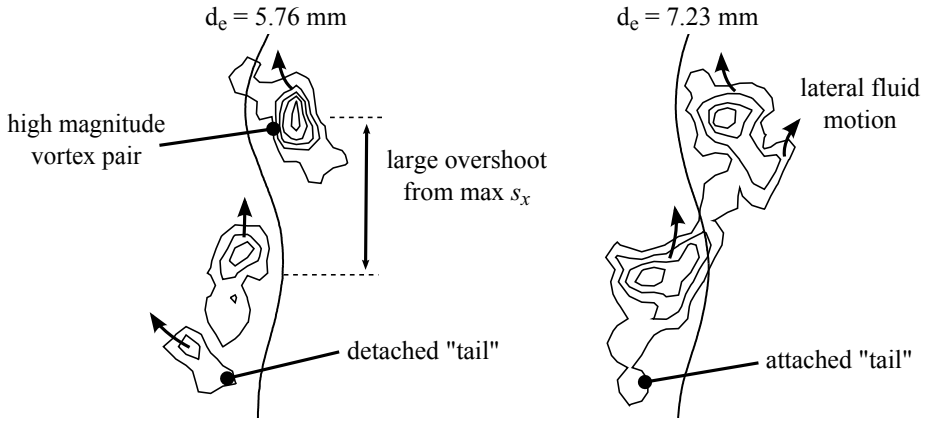

Figure 7.14: Sketches of the far wake in the $s_z = 9$ *mm* plane for both bubble diameters 0.2 *s* after bubble passage. The nature, overshoot and direction of the moving fluid are shown.

Throughout this section, hairpin vortices have been identified as the dominant mechanism of vortex shedding in the bubble wake. Figure 7.15 shows a sketch of the wake structures in both parallel planes, anticipated from the literature on rising bubbles and bluff bodies. These sketches are for a sphere in cross-flow, taken from Fan & Tsuchiya [13] and based on the experiments of Achenbach [32]. This reveals an attached near wake to the rear of the sphere and a far wake consisting of discrete hairpin vortex loops. The sketch has been modified to show the sliding surface, measurement planes and the cross-sections of the wake structure that one might expect to observe at the two heights $s_z = 3$ *mm* and $s_z = 9$ *mm*. The PIV fluid motion results obtained in these two planes are in strong agreement with this, although this image does not show the path oscillations observed behind ellipsoidal bubbles. In reality, the

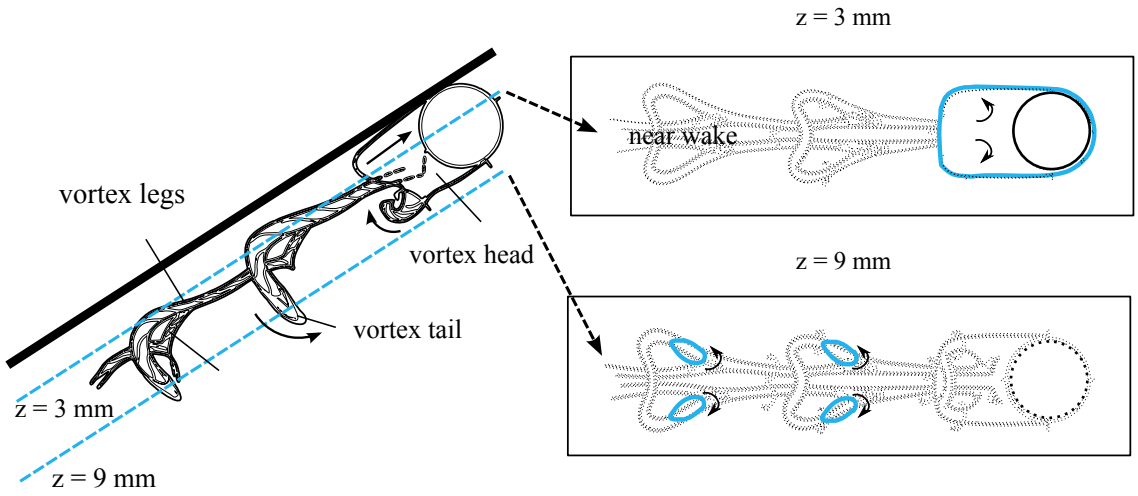

Figure 7.15: Sketch from Fan & Tsuchiya [13], based on the experiments on solid spheres of Achenbach [32], modified to show the sliding surface and the projection of the expected flow structures in each of these planes (solid blue lines).

hairpin vortex loops are more similar to those of the rising bubbles of Brücker [39] in this aspect.

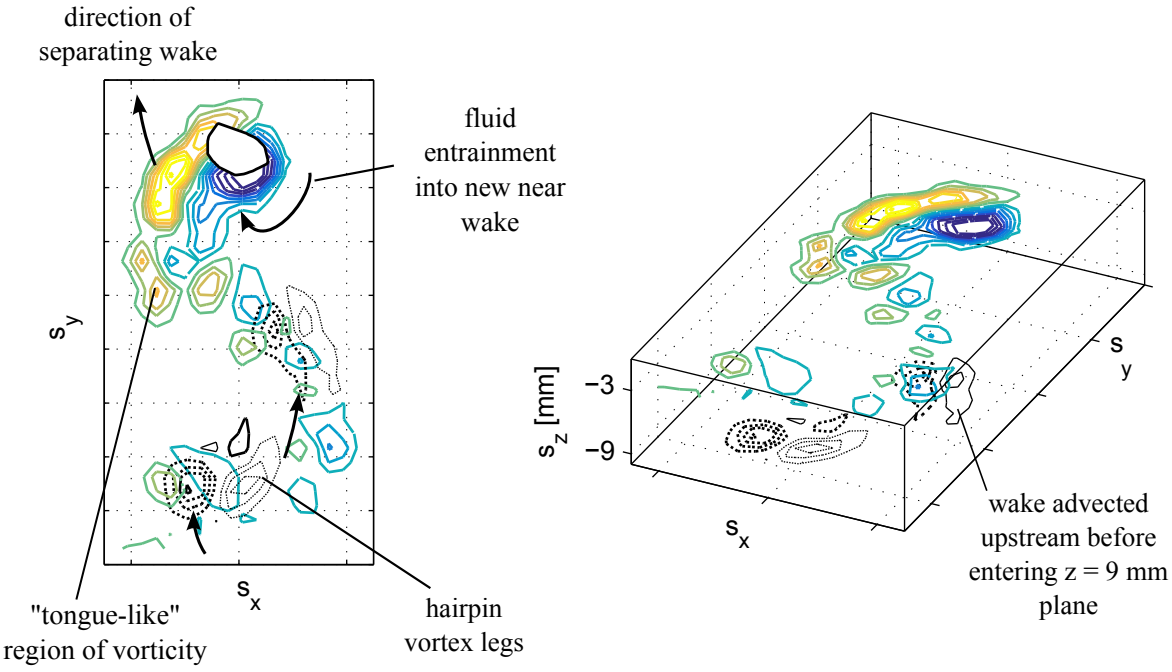

Figure 7.16: Contours representing positive and negative values of vorticity from both planes ($s_z = 3$ *mm* plane is coloured, $s_z = 9$ *mm* plane is black), spatially mapped based on the bubble path. Key components of the wake structure are also identified.

Figure 7.16 spatially maps the bubble paths in both parallel planes to show the evolution of the flow normal to the surface. The relative strength of vorticity in both planes is shown by

the contour plots, while the key aspects of the wake previously detailed are also highlighted. For clarity, the $s_z = 3$ *mm* plane is coloured and the $s_z = 9$ *mm* plane is black, and the aspect ratio in the z direction is non-unity. This spatial mapping reveals that the initial bubble-induced fluid disturbance is close to the surface, before the hairpin loops spread away, normal to the surface. The legs of these hairpin loops bisect the $s_z = 9$ *mm* plane, having been advected a significant distance along the length of the bubble path before doing so. Figure 7.16 also indicates that the bubbles appear to shed a single primary hairpin vortex at each maximum in displacement. This is in agreement with the experimental work of Brücker [39] and Lunde & Perkins [33]. Note that the numerical study of Gaudlitz et al. [47] observed many hairpin vortices shedding for each half-cycle in bubble path, a difference in behaviour that the authors attributed to the effect of surfactants in the PIV studies.

7.1.3 Multiple Bubbles

The mechanics of bubble-wake interactions were discussed in chapter 6, but a full understanding of this behaviour requires a knowledge of the wake structures. This section focuses on the velocity and vorticity of an an-line bubble pair, using the wake structures previously defined for single sliding bubbles as a starting point. In this section, the PIV data are discussed in detail for a single test with $d_e = 5.8$ *mm*, $\alpha = 30°$, as the composition of the structures does not change significantly with inclination angle.

Figure 7.17 shows the velocity and vorticity for an in-line bubble pair with an average separation d_y =25 *mm*, for $\alpha = 30°$, $d_e = 5.8$ *mm*. The bubbles take a similar in-phase path configuration to that observed in chapter 6. The opposite signs of the bubble amplitudes result in a larger affected region than for the single bubble case, and consequently a greater mixing of the fluid next to the surface. The vorticity plots reveal a complex interaction between the fluid shed from the leading bubble and the near wake of the trailing bubble, which will be discussed presently. In the first image in the sequence (figure 7.17 (a) and (d)) , the leading bubble is approaching its maximum spanwise displacement, while the trailing bubble is at its maximum. When the bubble paths intersect, the trailing bubble encounters the fluid that has separated from the leading bubble. This region of fluid acts in the direction of buoyancy, due to advection effects, while it also has a spanwise component, the direction of which depends

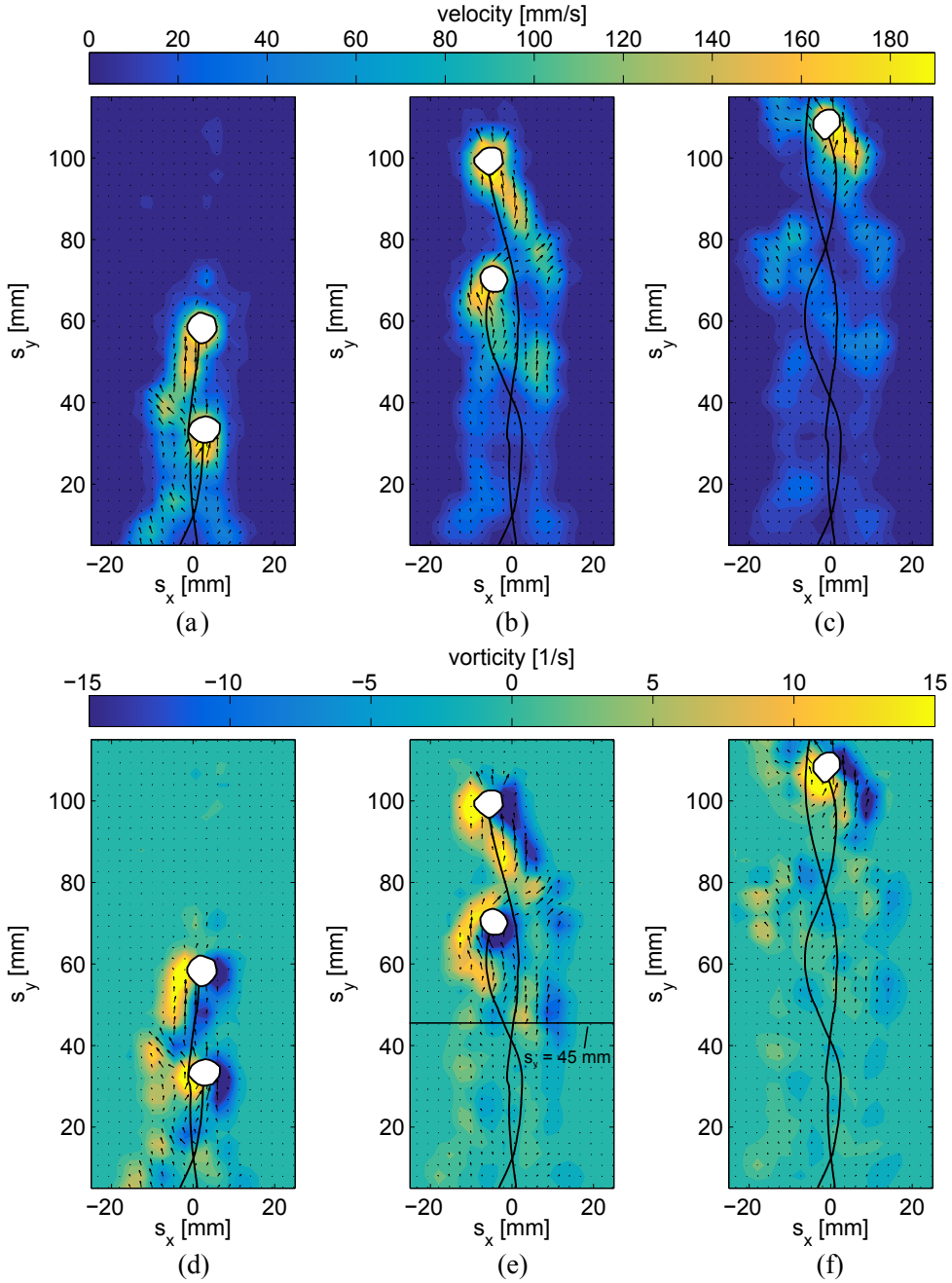

Figure 7.17: Fluid velocity magnitude $V_{mag} = \sqrt{U^2 + V^2}$ $[mm/s]$ (top) and vorticity Ω =curl(**U**) $[1/s]$ in a parallel plane at s_z =3 *mm* for an in-line bubble pair 25 *mm* apart in the *y*-direction with $\alpha = 30°$, $d_e = 5.8$ *mm*, with the approximate bubble shapes and paths overlaid. Each image is $\Delta t = 0.2$ *s* apart.

on whether it was shed at a local maximum or minimum in path. Therefore, as the trailing bubble enters this region of fluid, it is accelerated both in the direction of buoyancy and in the direction determined by the path of the leading bubble. For instance, at the first image sequence, the trailing bubble is about to pass through fluid shed from the leading bubble at its previous local minimum in path, which will subsequently accelerate the trailing bubble in

the negative spanwise direction. This means that as the trailing bubble returns to its mean position, it is accelerated in the direction in which it was originally travelling.

In figure 7.17 (b) and (e), 0.2 *s* later, the bubble paths are about to intersect again, this time with the trailing bubble now moving in the positive spanwise direction. Passing through the fluid shed by the leading bubble from its previous local maximum will again accelerate the bubble in its current direction. This coupling of the leading bubble wake and the trailing bubble accentuates the trailing bubble path oscillations, as well as inducing changes in shape as discussed in chapter 6. A further 0.2 *s* later, the fluid velocity in the far wake is significantly larger than for the single bubble case, forming a double-threaded far wake structure that appears to be a superposition of the two bubble wakes. This is not strictly the case, in fact, due to the interactions between the fluid from each bubble wake that occurs at the path intersection points.

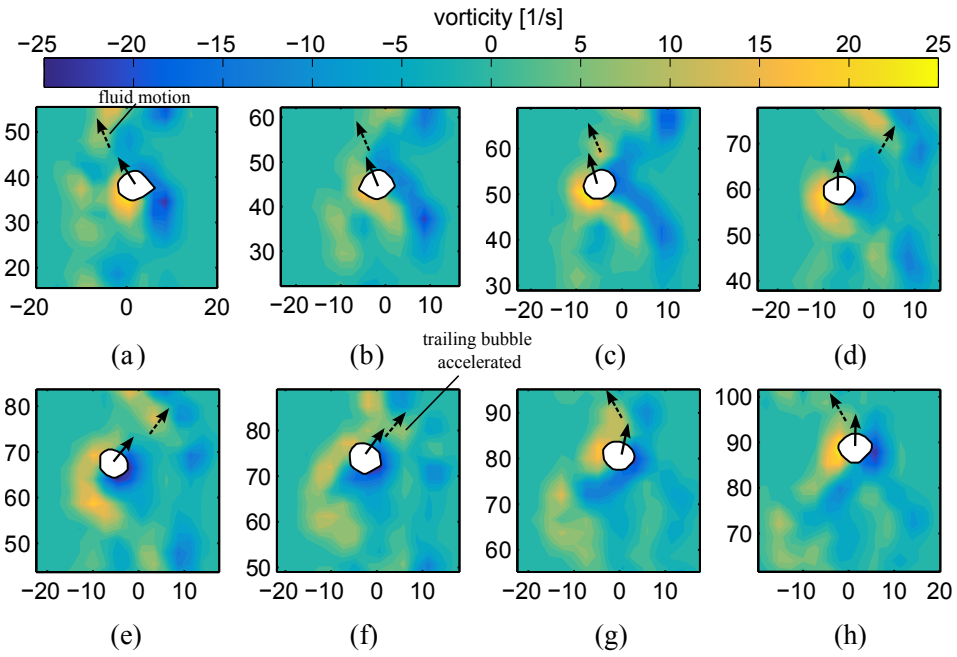

Figure 7.18: Vorticity distribution in the near wake of the trailing bubble (d_e = 5.8 *mm*), with the bubble at instances in time 20 *ms* apart. The bubble velocity vector (−) and leading bubble near-wake motion (− −) are also shown.

Figure 7.18 examines the flow field around the trailing bubble at intervals of 20 *ms*, to better show these interactions. The images (a) - (d) correspond to the bubble travelling towards its local minimum, being accelerated by the fluid shed at the previous local minimum of the leading bubble wake. The direction of fluid motion in the near wake of the leading

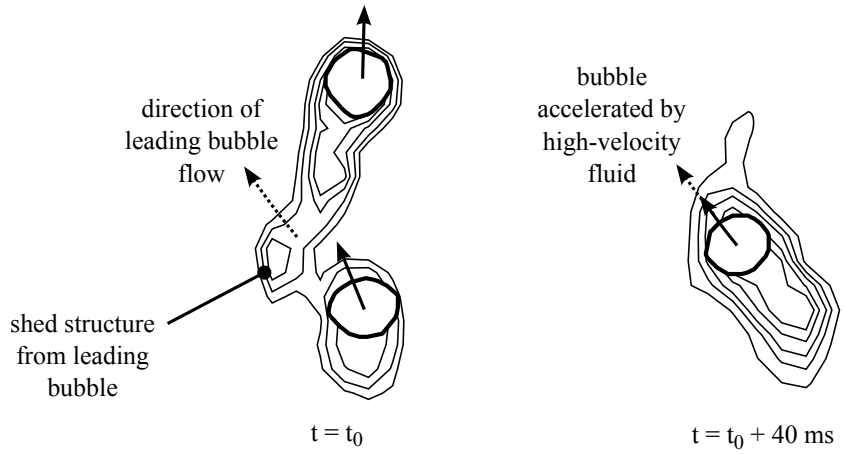

Figure 7.19: Sketch supporting figures 7.17 and 7.18, showing the direction of the bubble and fluid motion.

bubble is indicated on the figure. The next four images (e) - (h) show the motion towards a local maximum in spanwise position. This shows that the direction of the near wake that has separated from the leading bubble is such as to encourage spanwise motion in the original direction of the trailing bubble. A supporting sketch in figure 7.19 shows the bubble wake interactions for the first image sequence at t_0 and an instance in time 40 *ms* later, revealing the repeating nature of the trailing bubble velocity enhancement.

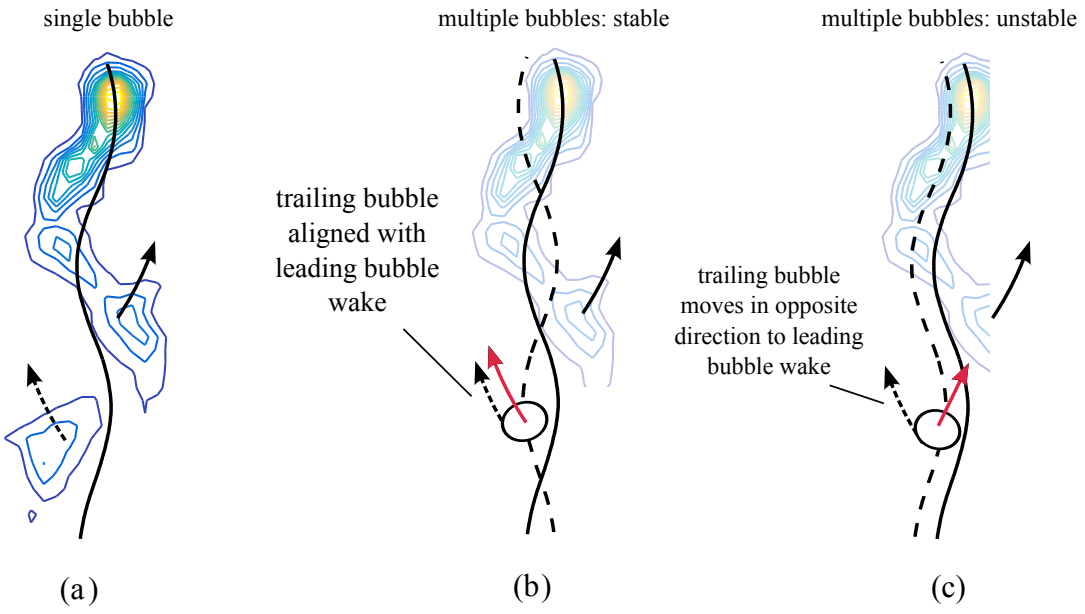

Figure 7.20: Sketch showing (a) the motion in the bubble wake, (b) the motion of an in-line bubble pair observed in the current study and (c) the unstable configuration that occurs if the two paths are identical.

The motion induced by the leading bubble wake on the trailing bubble explains why the amplitude of the trailing bubble path is larger, and can also provide an explanation for the in-line, opposite amplitude configuration adopted by the bubbles both in figure 7.17 and in the bubble motion experiments in chapter 6. To show why this is the case, figure 7.20 considers what would occur if the bubble paths were *not* in this configuration, i.e. if they were identical in amplitude and phase with a separation of $d_y = 25\ mm$. In this case, as the trailing bubble intersects the leading bubble wake, its spanwise velocity component will be opposite to that of the fluid it is passing through (figure 7.20 (c)). The induced motion of the leading bubble wake, therefore, would tend to reverse the spanwise motion of the trailing bubble. Thereby, the opposite amplitude, in-phase path configuration that the bubbles adopt appears the most stable configuration in terms of the induced wake motion.

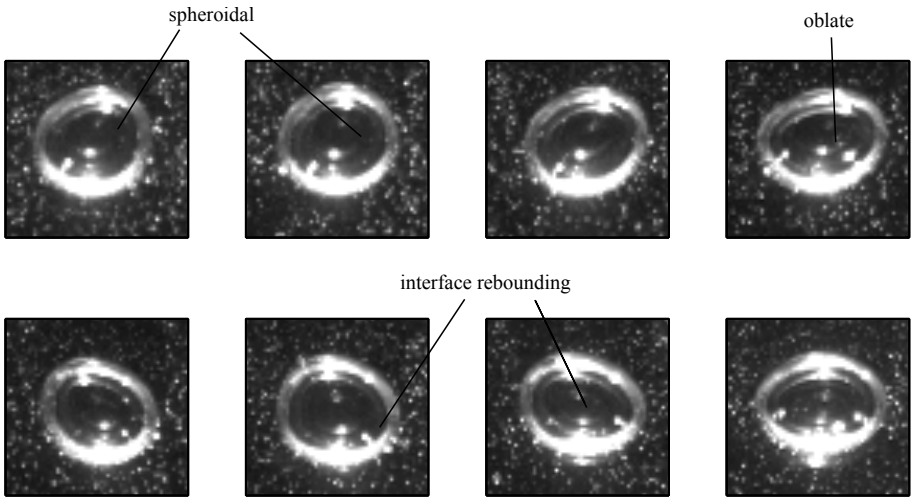

Figure 7.21: Subtle changes in trailing bubble shape from raw PIV images at the instances in time 20 *ms* apart identified in figure 7.18.

Figure 7.21 shows the raw images of the trailing bubble for the same instances in time as presented in figure 7.18. These remain consistent with the single bubble case discussed in chapter 6, transitioning from approximately spheroidal at the mean of the bubble path to oblate at the local path extrema. There are some deviations from single bubble behaviour that occur when the trailing bubble passes through the leading bubble wake, such as the base of the bubble interface rebounding at the location highlighted on figure 7.21. However, since these changes are subtle, it is necessary to combine the data from the fluid motion and bubble

motion tests to make further insights.

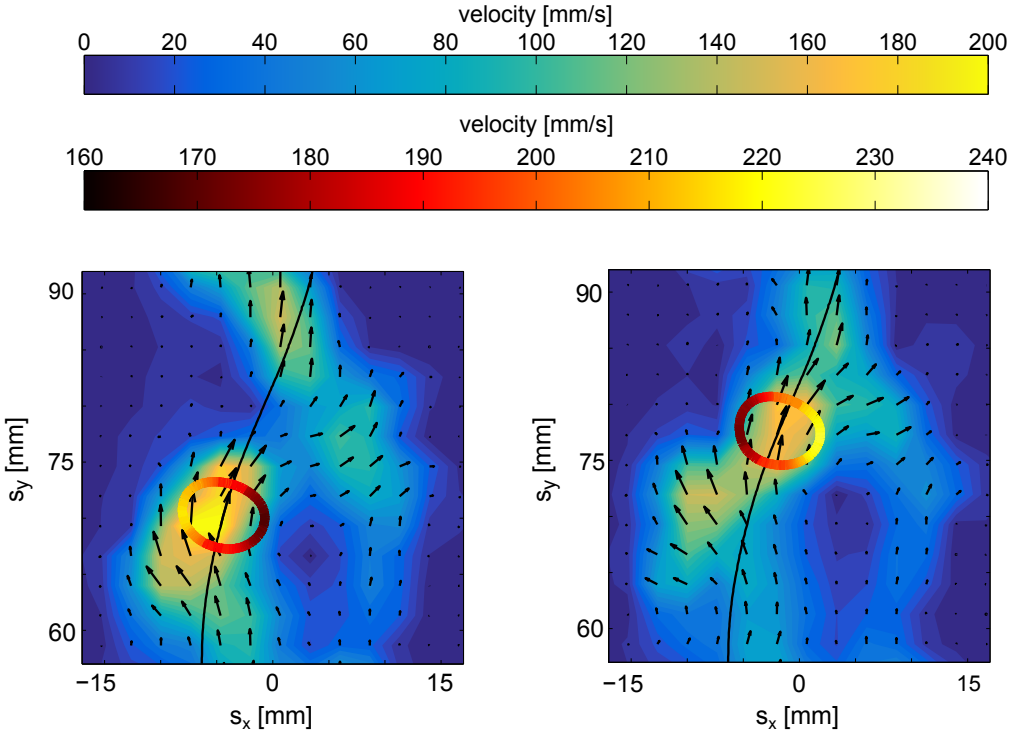

Figure 7.22: Spatial alignment of the bubble and fluid motion at two instances in time. The fluid velocity field is indicated by the arrows, while the top colour bar (green) refers to the vorticity field and the bottom colour bar (red) is the velocity about the bubble interface.

Figure 7.22 spatially aligns the bubble and fluid motion for the trailing bubble, zooming in on a small section of the wake where the trailing bubble intersects the leading bubble wake. Note the use of a second colour map is necessary to show the interfacial velocity of the bubble. It is now possible to confirm the assertions made in chapter 6 about the increase in velocity experienced by the trailing bubble. In the first image, the trailing bubble is at returning towards its local mean position and is not intersecting the leading bubble wake. At this location, its velocity is consistent with the single bubble test. However, in the second image, the right hand side of the trailing bubble has intersected the wake of the leading bubble, which has a positive spanwise component. This causes a rapid increase in the velocity of the bubble interface at this location and a subsequent rebounding of the bubble interface. This results in high order velocity fluctuations around the trailing bubble interface as different parts of the bubble enter the high-speed fluid in the leading bubble wake. As was discussed in chapter 6, this motion can result in a momentary “rocking” of the bubble interface, resulting

in rapid changes in orientation. This is dependent on both the trailing bubble velocity vector and the velocity of fluid shed by the leading bubble wake.

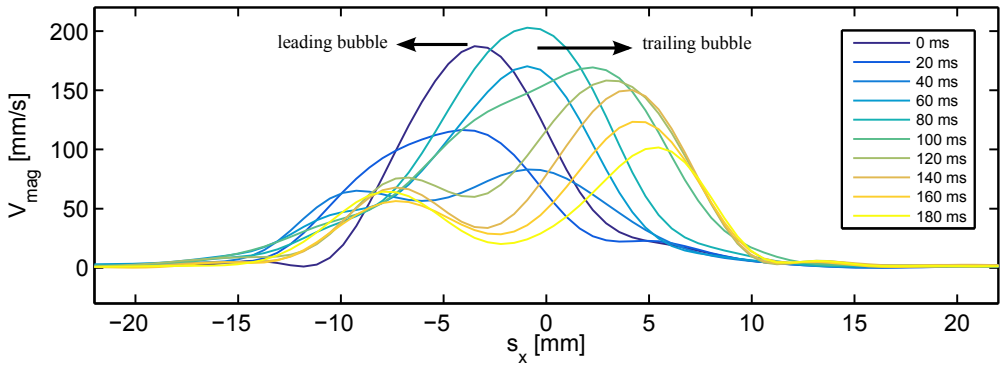

Figure 7.23: Velocity along a defined slice of the surface at $s_y = 45$ *mm* for the bubble pair, with each line corresponding to a 20 *ms* interval.

The influence of a sliding bubble pair on the local fluid velocity can be inferred from figure 7.23 at the location s_y = 45 *mm*. Note that the peak at t = 100 *ms* corresponds to the trailing bubble entering the slice: this value should be taken with caution since the PIV measurements within the bubble interface are not accurate. The near wake of each bubble is advected in different directions, resulting in an affected region of fluid four times the bubble equivalent diameter. Thus, the two bubbles and their associated wake motion lead to considerable mixing over a spanwise area 4 bubble diameters in size.

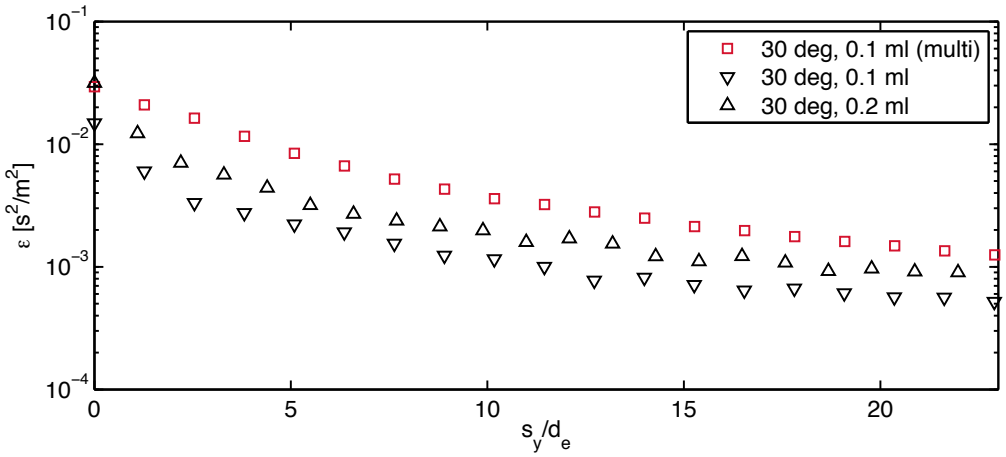

Figure 7.24: Non-normalised flow enstrophy, versus the distance from the bubble to the interrogation window, s_y/d_e, for an in-line bubble pair, with the values for two single bubbles of $d_e = 5.8$ *mm* and 7.2 *mm* provided for reference.

Solving for the enstrophy of the flow field can show the effect of a second bubble on the

kinetic energy of the fluid. Figure 7.24 shows the non-normalised enstrophy for the bubble pair, in addition to single bubbles of diameter 5.8 *mm* and 7.2 *mm* at $\alpha = 30°$. It is apparent that the induced motion in the flow field is significantly larger than that for the corresponding single bubble tests, promoting further mixing. Chapter 8 will look at these bubble-wake interactions from a heat transfer perspective, exploring whether this greater fluid mixing is linked to improved heat transfer rates.

7.2 Perpendicular plane

Up to this point, the wake structures have been noted to spread away from the surface in the normal direction, although the nature of this motion has not yet been quantified. The experiments in this section will study the fluid motion in a single perpendicular plane fixed in space, through which the bubble and its wake enter at different times. The objective of this section is to quantify the fluid motion normal to the surface offered by a single sliding bubble, particularly in terms of the extent of far wake mixing involved.

When performing PIV in this plane, the laser and camera are maintained in a fixed position at $s_y = 60$ *mm*. It follows that since the bubbles follow an undulating path, each bubble will enter the plane at a specific phase angle, while PIV provides a series of snapshots of the cross-section of its wake at different instances in time. This means that the far wake structures undergo interactions and dissipation before entering the measurement plane. It transpires that the key parameter in understanding these streamwise structures is the phase angle, since the nature and strength of the structures observed depends on the bubble entry point. Thus, tests in this section are presented at a constant bubble diameter of $d_e = 5.8$ *mm* and surface inclination angle of $\alpha = 30°$ but for three different phase angles corresponding to a local maximum, local minimum and mean in path. Figure 7.25 shows the location of these phase angles on the bubble path, along with an illustration of the bubble wake to explain how the choice of phase angle influences the fluid motion observed. Section 7.1. showed that as the near wake separates from the bubble at the extrema, it overshoots the wake. Thus, when measuring the streamwise flow structures, it is expected that when ϕ is at a local extrema, the near wake fluid motion will be rapidly advected out of plane. Additionally, as was discussed in chapter 5, the out-of-plane motion in the near wake does not allow for

effective PIV processing; at these locations, the raw images are used to infer the fluid motion.

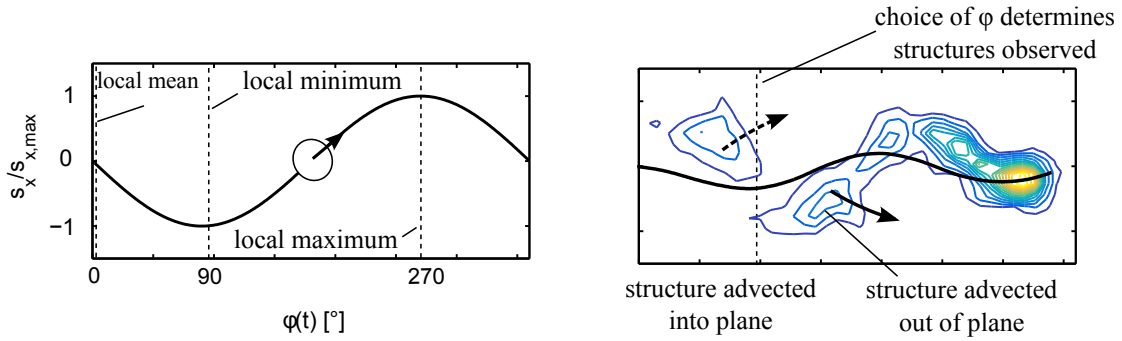

Figure 7.25: Recalling the definition of the phase angle, ϕ (a), and demonstrating its relevance to the streamwise wake structures (b) in terms of the magnitude and direction of structures observed.

7.2.1 Local Minimum s_x: $\phi \approx 90°$

In this section, results are presented for an entry point at $\phi \approx 90°$ on figure 7.25. To resolve the near wake motion, it is necessary to use the raw images to visualise the fluid motion. Figure 7.26 shows the raw PIV images at two instances in time, corresponding to 0 and 100 *ms*, respectively, after the bubble passage, where the position $s_z = 0$ denotes the surface and $s_x = 0$ is the bubble entry point. Note that this entry point $s_x = 0$ is at the local minimum in streamwise position. To show the motion of the particles, they are averaged over a time interval of 10 *ms* and 20 *ms* respectively, and an analysis of the raw image sequence is performed to infer the direction of this motion. As the bubble enters the plane, fluid is observed to roll up over the bubble base, consistent with the $s_z = 9$ *mm* PIV measurements. After the bubble passage in figure 7.26 (a), the streamwise fluid in the near wake forms a high velocity, counter-clockwise rotating region that overshoots the bubble path in the negative spanwise direction, again consistent with the parallel plane tests. At the same time, a region of fluid beneath the surface is advected towards the surface, conceivably due to the recirculation region that exists in the near wake. Further in time (b), the eddy initially shed at the local minimum has continued to overshoot the bubble path, while the region of fluid beneath the entry point has reduced in strength.

Figures 7.27 and 7.28 present plots of the velocity and vorticity fields for $\phi = 90°$. Measurements are first provided at the time t_0, 0.2 *s* after the bubble passage, with five further instances in time $\Delta t = 0.5$ *s* apart provided. The surface is denoted by the white line at

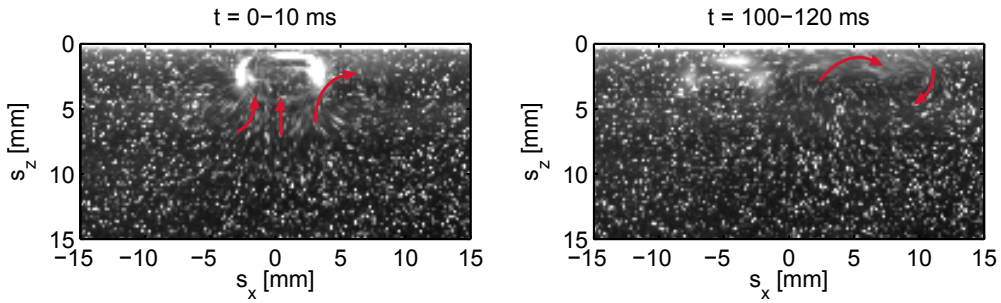

(a) (b)

Figure 7.26: Raw images of the near wake averaged over time intervals 10 *ms* and 20 *ms* respectively, starting at two instants in time 0 and 100 *ms* after the bubble passage for $\alpha = 30°$, $d_e = 5.8$ *mm*, $\phi = 90°$.

$s_z = 0$ and the entry point indicated by the white circle (this does not move with the bubble). Note the velocity and vorticity magnitudes are significantly lower than in the parallel plane measurements.

Focusing first on the bubble velocity, figure 7.27 (a) shows a high velocity, counter-clockwise rotating region of fluid moving in the negative spanwise direction, in agreement with the second image in figure 7.26. This initial fluid disturbance due to the near wake remains close to the surface, i.e. within 2 bubble diameters at 0.2 *s*. Note that the velocity vectors below $s_z = 15$ *mm* are as a result of bias errors due to the relatively low flow velocity at this location. In figure 7.27 (b), 0.5 seconds later, this eddy has diminished rapidly in strength. Rather than viscous dissipation, this reduction in velocity is due to out-of-plane motion. At this instant, a small quantity of fluid that was shed at the previous downstream local maximum begins to enter the plane to the right of the entry point.

One second after the bubble passage (figure 7.27 (c)), a significant volume of fluid has entered the measurement plane from this local maximum in path. This region is large in size and in magnitude, and acts to draw fluid away from the surface. An analysis of the raw image sequence reveals that this region is the cross section of a large, discrete structure that begins to enter the measurement plane 0.7 seconds after the bubble passage. This region is large in size since it has spread during this time before entering the plane. A low-magnitude secondary structure has also entered the plane at the location of the previous primary vortex, remaining close to the surface and spreading in a negative streamwise direction. In figure 7.27 (d), there has been further in-plane mixing, spreading up to 4 bubble diameters away in the

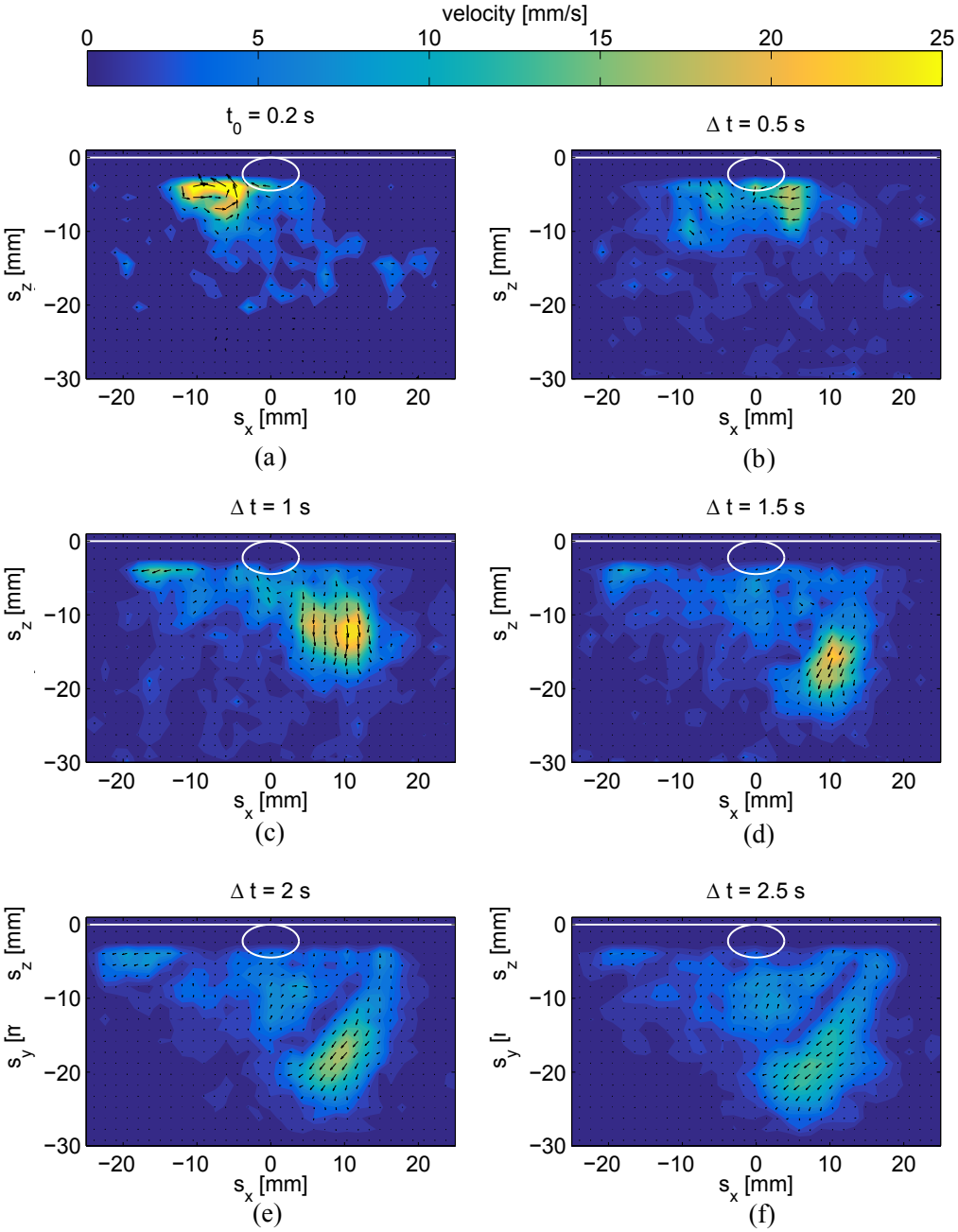

Figure 7.27: Fluid velocity magnitude $V_{mag} = \sqrt{U^2 + V^2}$ $[mm/s]$ in a perpendicular plane at $s_y = 60$ mm for $\alpha = 30°$, $d_e = 5.8$ mm, $\phi = 90°$, with the bubble having travelled through the plane, away from the viewer. The surface is denoted by the white line at $s_z = 0$ mm, and the in-plane entry plane of the bubble shown by the white circle. Each image is $\Delta t = 0.5$ s apart, while the first image t_0 is 0.2 seconds after the bubble passage.

direction normal to the surface. The magnitude of the velocity in the interrogation window has also decreased, which is attributed mainly to viscous dissipation as the structure remains in-plane. At the final two instances in time (figure 7.27 (e) and (f)), the velocity magnitude

continues to decrease, while the primary and secondary structures begin to join, forming a low velocity, large-scale structure that spreads out to the fluid bulk and persists for many seconds after the bubble passage.

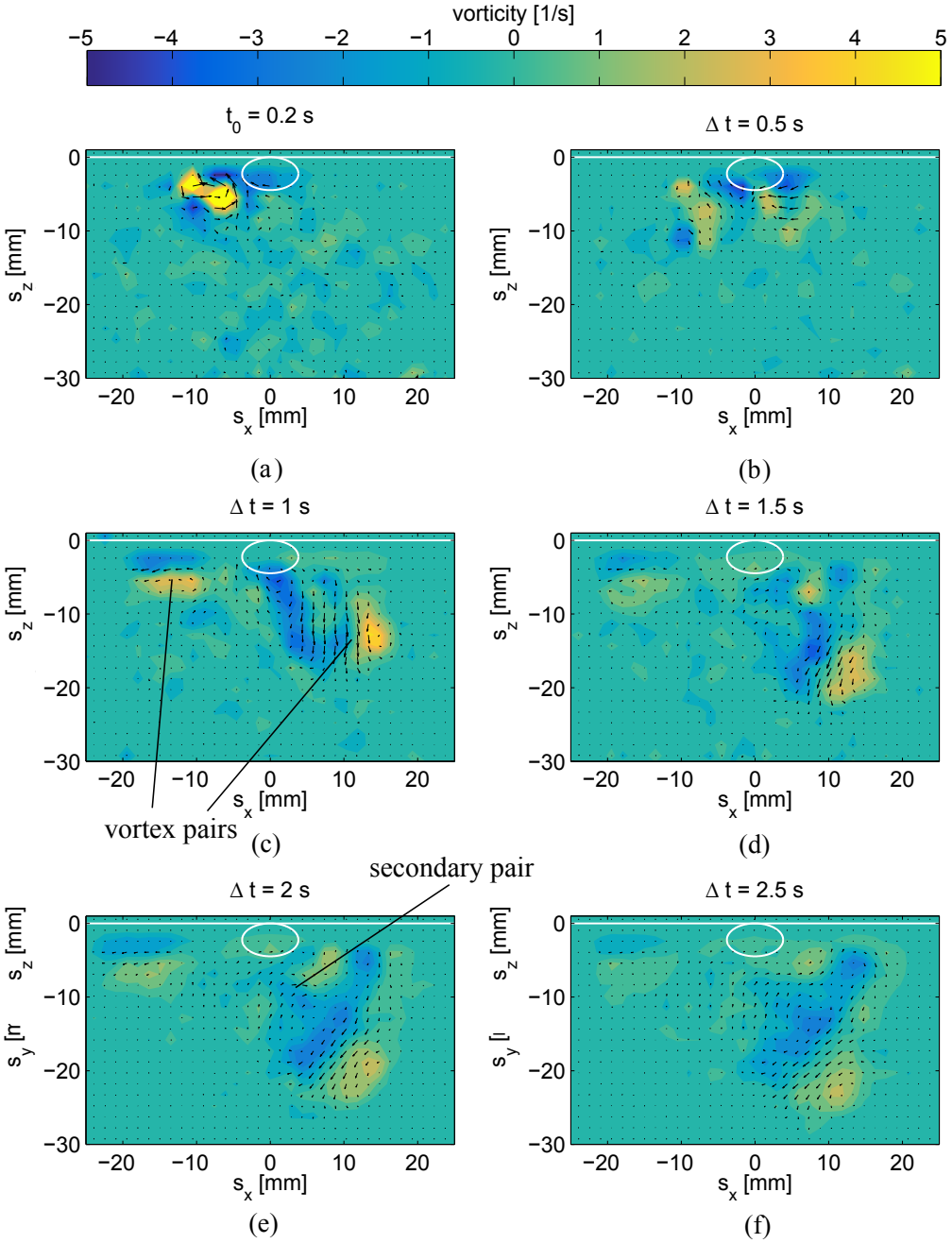

Figure 7.28: Fluid vorticity Ω_y =curl(**U**) $[1/s]$ in a perpendicular plane at $s_y = 60\ mm$ for $\alpha = 30°$, $d_e = 5.8\ mm$, $\phi = 90°$, with each image $\Delta t = 0.5\ s$ apart, with the first image t_0 0.2 seconds after the bubble passage.

The vorticity in the perpendicular plane at the same instances in time is provided in

figure 7.28. The high velocity regions identified in figure 7.27 correspond to counter-rotating pairs of vorticity. This corresponds to the legs of the hairpin vortices that were shed downstream of the measurement plane entering the measurement plane at different times. In the far wake, the direction of counter-rotating vorticity is such as to draw fluid away from the surface in the normal direction, advecting fluid up to 4 bubble diameters from the surface. There also exists some secondary vortical structures, which can temporally evolve, dissipate or move out of plane. These structures can also interact with the primary vortex pairs and the fluid bulk, leading to complex fluid motion.

In these experiments, a three-dimensional wake is being observed at various instances in time. Figure 7.29 reconstructs the in-plane mixing as isosurfaces of vorticity at $\Omega_y = \pm 1.3$ s^{-1}, allowing for the temporal evolution of vorticity to be examined in greater detail for three different views. Recall from chapter 5 that the dimension along the length of the bubble path, Δs_y, is a measure of the distance between the bubble and the measurement plane at that instant in time. Since this value is large, the axes are normalised by the bubble diameter. The z-axis is also flipped to better show the fluid motion. The PMMA surface is represented by the white rectangle, and the bubble outline and velocity vector are shown at the origin.

The extent of fluid mixing offered by the sliding bubble is evident in figure 7.29. The fluid motion in the streamwise plane persists for longer than 5 seconds after the bubble passage and spreads up to 5 bubble diameters both laterally and normal to the surface. Various features of the three dimensional wake structure are also visible, which exist in-plane as counter-rotating regions of vorticity. This is consistent with the cross-section of the legs of a hairpin vortex structure shed at the local path extrema. The first of these regions is denoted as A and is shed at the local minimum of the bubble path as it enters the measurement plane at $\phi = 90°$. At this location, the fluid in the wake is at high velocity, and is advected through the plane rapidly. This fast-moving region remains within 2 bubble diameters of the surface. One second after the bubble passage, a second structure B enters the plane on the opposite side of the bubble path. This corresponds to the hairpin vortex shed at the previous local maximum in bubble path being advected into the plane. This region is high in velocity and spreads away from the surface, causing significant mixing. The secondary fluid structures observed are consistent with the findings of Acarlar and Smith for a near-wall bluff body flow [98]. One example of this is the secondary vortex pair B', which could be due to the interactions

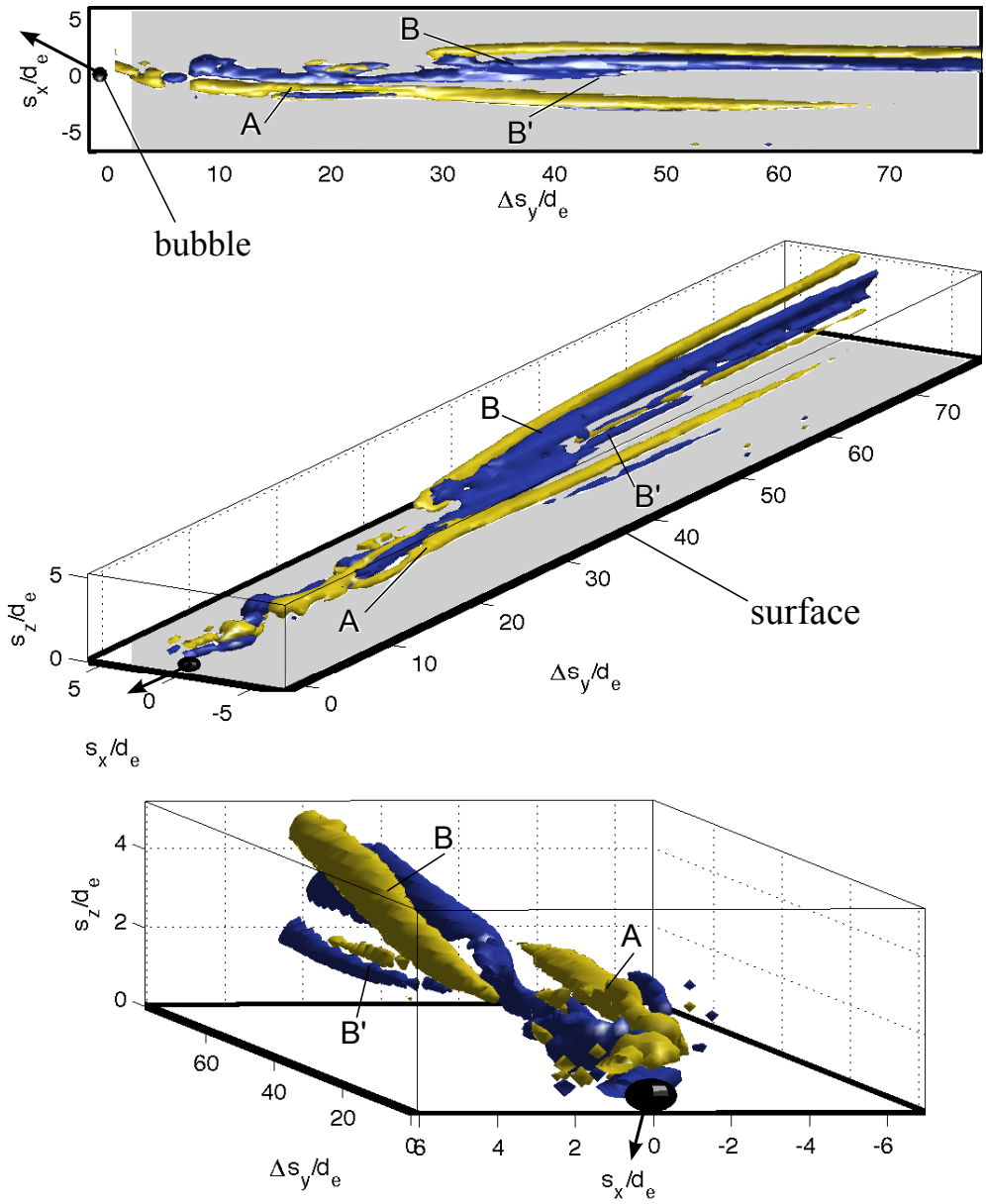

Figure 7.29: Three views of the streamwise reconstruction of vorticity for isosurfaces of $\Omega_y = \pm 1.3$ at $s_y = 60$ *mm* for $\alpha = 30°$, $d_e = 5.8$ *mm*, $\phi = 95°$. The surface is shown in white, while the z-axis is flipped for clarity. A 3-D representation of the bubble is shown on the origin, while Δs_y is the distance between each slice of vorticity and the bubble at that point. The key structures A, B and $B*$ are also highlighted.

between the hairpin vortex loops at B and the quiescent bulk fluid before the structure entered the plane.

7.2.2 Local Maximum s_x: $\phi \approx 270^\circ$

Next, the wake structures are studied for a test where the bubble enters the measurement plane at $\phi = 270^\circ$. In this case, the position $s_x = 0$ is the local streamwise maximum of the bubble. Ideally, this should be a mirror image of that at $\phi = 90^\circ$ but it will become apparent that this is not the case, although the structures are broadly similar to those at $\phi = 90^\circ$. This section will focus on why these differences in behaviour occur.

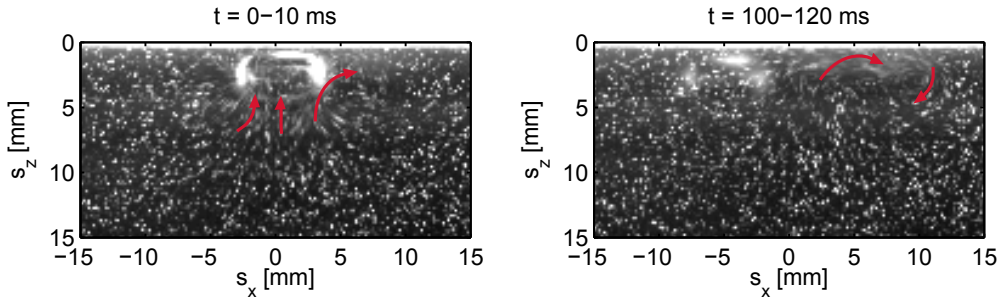

(a) (b)

Figure 7.30: Raw images of the near wake averaged over time intervals 10 *ms* and 20 *ms* respectively, starting at two instants in time 0 and 100 *ms* after the bubble passage for $\alpha = 30^\circ$, $d_e = 5.8$ *mm*, $\phi = 270^\circ$.

Figure 7.30 shows the flow visualisation results directly after the bubble has passed through the plane. This is very similar to the $\phi = 90^\circ$ case, except with fluid now being shed in the positive streamwise direction corresponding to the local maximum of the bubble's path. Again, the near wake of the bubble draws fluid towards the surface in the normal direction. An analysis of the raw PIV video sequence again shows the vortex to the right of the bubble to be advected upstream quickly.

Figure 7.31 provides the velocity at the same instances in time as for the $\phi = 90^\circ$ case. In figure 7.31 (a), 0.2 *s* after the bubble passage, fluid in the near wake is advected in the positive spanwise direction, but has decreased rapidly in magnitude by 0.5 seconds later in figure 7.31 (b). At the instant in time (b), a large region of fluid has entered the plane at $s_x < 0$, moving away from the surface in the normal direction. More fluid has entered the plane at $\Delta T = 0.5$ *s* than was the case for the $\phi = 90^\circ$ test, which could be due to the bubble taking sharper turns after shedding a large quantity of fluid from its wake, as in the "transitional behaviour" regime discussed in chapter 6. Additionally, there is a $\approx 5^\circ$ uncertainty in determining the

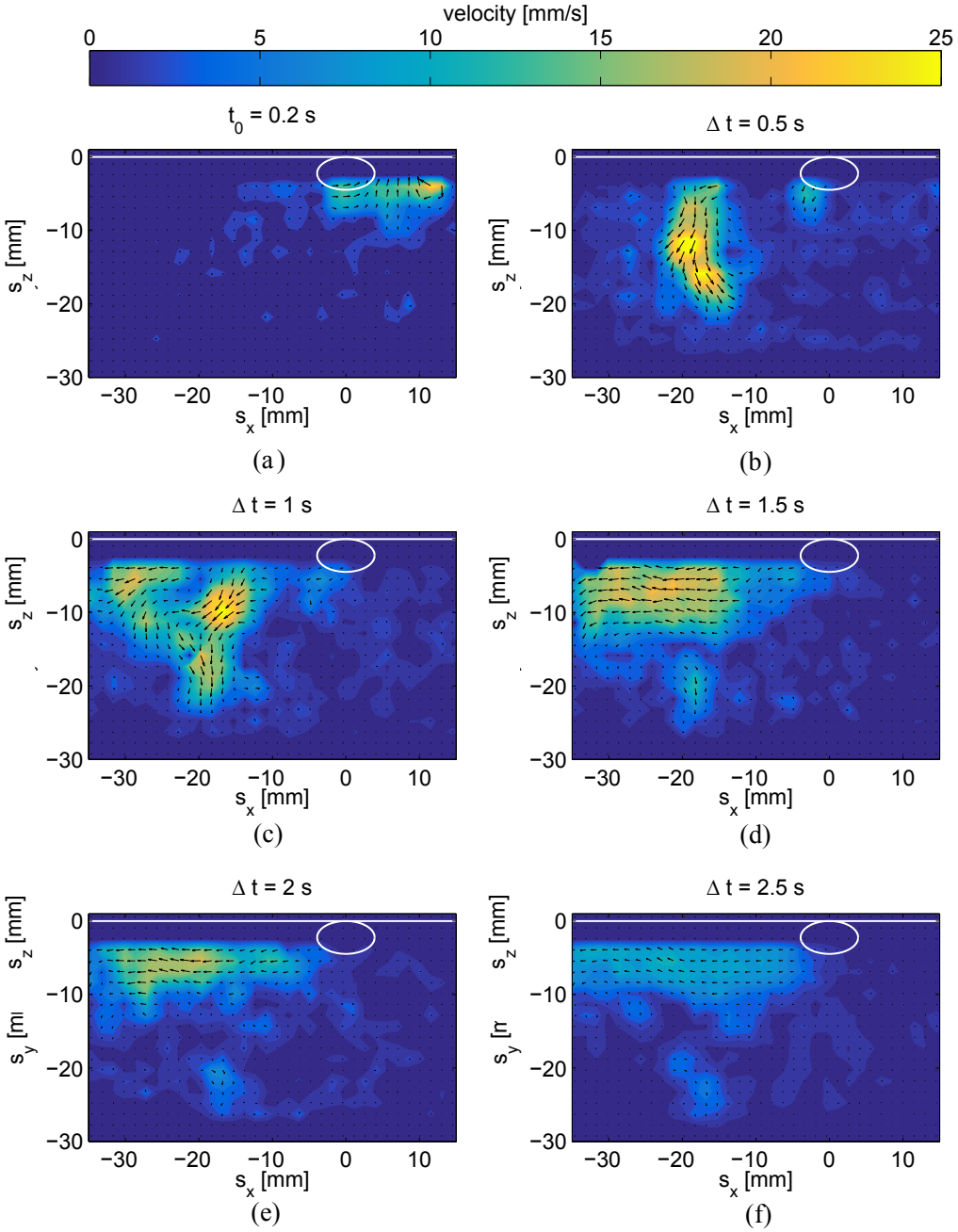

Figure 7.31: Fluid velocity magnitude $V_{mag} = \sqrt{U^2 + V^2}$ $[mm/s]$ in a perpendicular plane at $s_y = 60$ mm for $\alpha = 30°$, $d_e = 5.8$ mm, $\phi = 270°$, with each image $\Delta t = 0.5$ s apart and the first image t_0 0.2 seconds after the bubble passage.

phase angle; this could also be a factor due to the dependence of the observed structures on the phase angle. After 1 second (figure 7.31 (c)), the structure has split into discrete regions: one acting close to the surface and one moving away from the surface in the normal direction. Of the two, the former is greater in magnitude, meaning that as this structure evolves, it does so predominately in the spanwise direction, meaning there is less motion normal to

the surface than for $\phi = 90°$. This behaviour is consistent with the bubble taking a shorter wavelength path, shedding more fluid in the spanwise direction at each sharp path extremum. This causes an affected region in the spanwise plane of up to 6 bubble diameters from where the bubble entered the plane. At Δt = 1.5 s after the bubble passage in figure 7.31 (d), the structure has evolved to a single region moving solely in the negative spanwise direction, with little fluid motion in the normal direction, aside from a secondary structure that has detached from beneath the primary region. Further in time (figure 7.31 (e) and (f)), these regions dissipate in strength.

The vorticity in the perpendicular plane reveals that as the high velocity region enters the plane in figure 7.32 (b), its cross section is initially a combination of two counter-rotating vortex pairs. At $\Delta t = 0.5$ s and $\Delta t = 1$ s, the primary vortex pair moves away from the surface in the normal direction and the secondary pair remains in relatively close proximity to the surface. Further in time, the vortex pairs dissipate rapidly. It has previously been ascertained that each vortex pair corresponds to the legs of a hairpin vortex. In this case the second vortex pair could be as a result of the bubble shedding a large quantity of fluid as it undergoes transitional behaviour. Thus, although the fluid motion induced by the bubbles at $\phi = 90°$ and $\phi = 270°$ is broadly consistent, some deviations exist. This is likely due to the wake being a complex, three-dimensional structure which varies in velocity with ϕ, while previous work indicated the amount of liquid shed by the bubble at each path extrema can vary [68].

The reconstruction of the vortical structures at $\Omega_y = \pm 1.3\ s^{-1}$ in the streamwise direction for $\phi = 270°$ is provided in figure 7.33. Initially, clockwise vorticity emanates from the right of the bubble. This mixing continues several diameters downstream, and is visible at the location A. The in-plane mixing of this structure does not last for a significant time, as this fluid is advected rapidly out of plane. At 25 bubble diameters downstream, the large-scale structure B enters the plane. This structure can be split into 3 vortex pairs, starting with the pair B, which appears in the measurement window comparatively far from the surface and continues to spread into the bulk fluid normal to the surface. Next is the high speed fluid, B', which starts close to the surface under the pair B. Several bubble diameters downstream, a second pair B'' enters the plane in the negative spanwise direction. These two secondary structures join together in time.

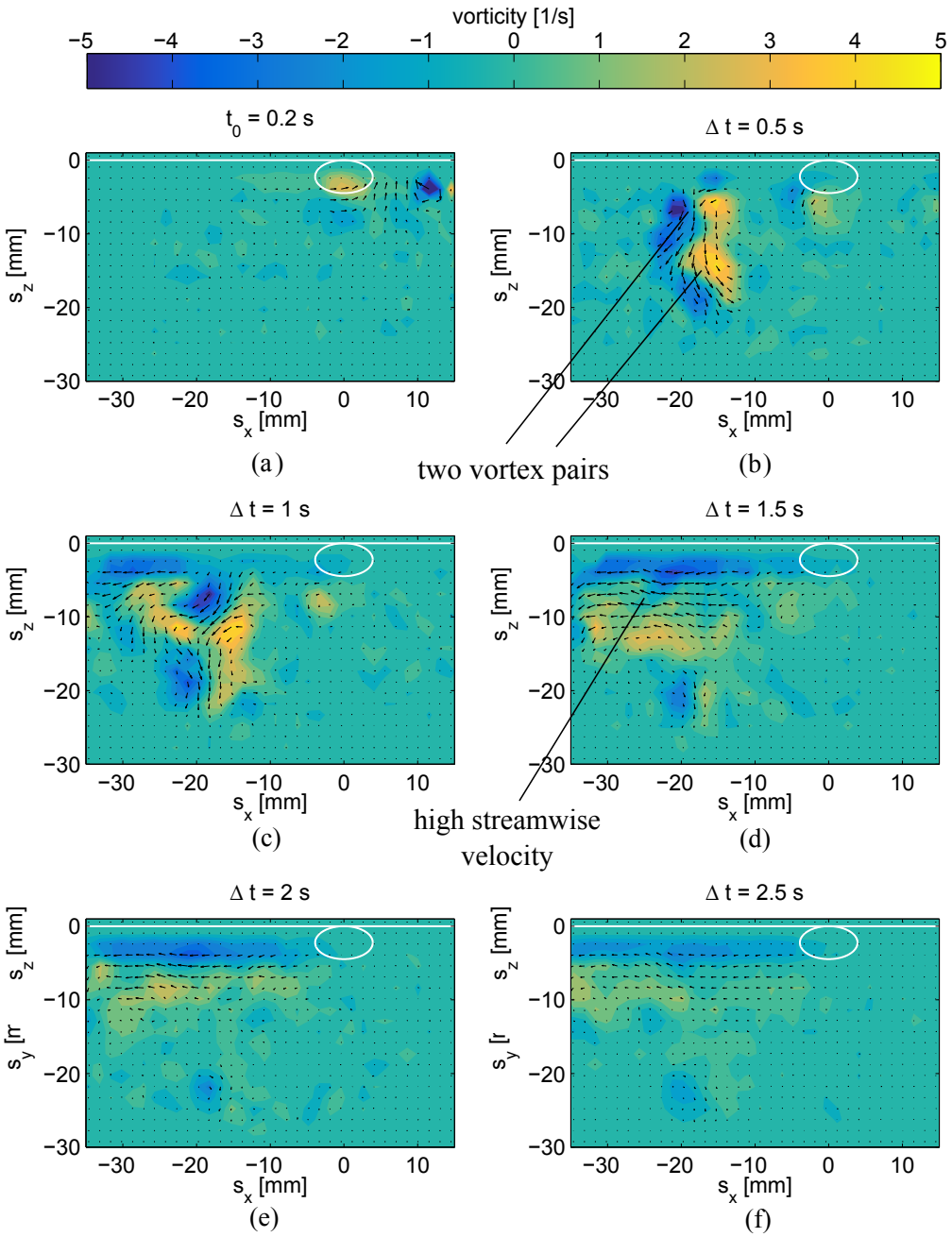

Figure 7.32: Fluid vorticity Ω_y =curl(**U**) $[1/s]$ in a perpendicular plane at $s_y = 60$ *mm* for $\alpha = 30°$, $d_e = 5.8$ *mm*, $\phi = 270°$, with each image $\Delta t = 0.5$ *s* apart, with the first image t_0 0.2 seconds after the bubble passage.

7.2.3 Local Mean s_x: $\phi \approx 0°$

The final test examined in the perpendicular plane is $\phi \approx 0°$, or the mean spanwise displacement. The near-wake visualisation in figure 7.34 reveals a clockwise rotating region that overshoots the bubble path in the positive spanwise direction, corresponding to the vortex

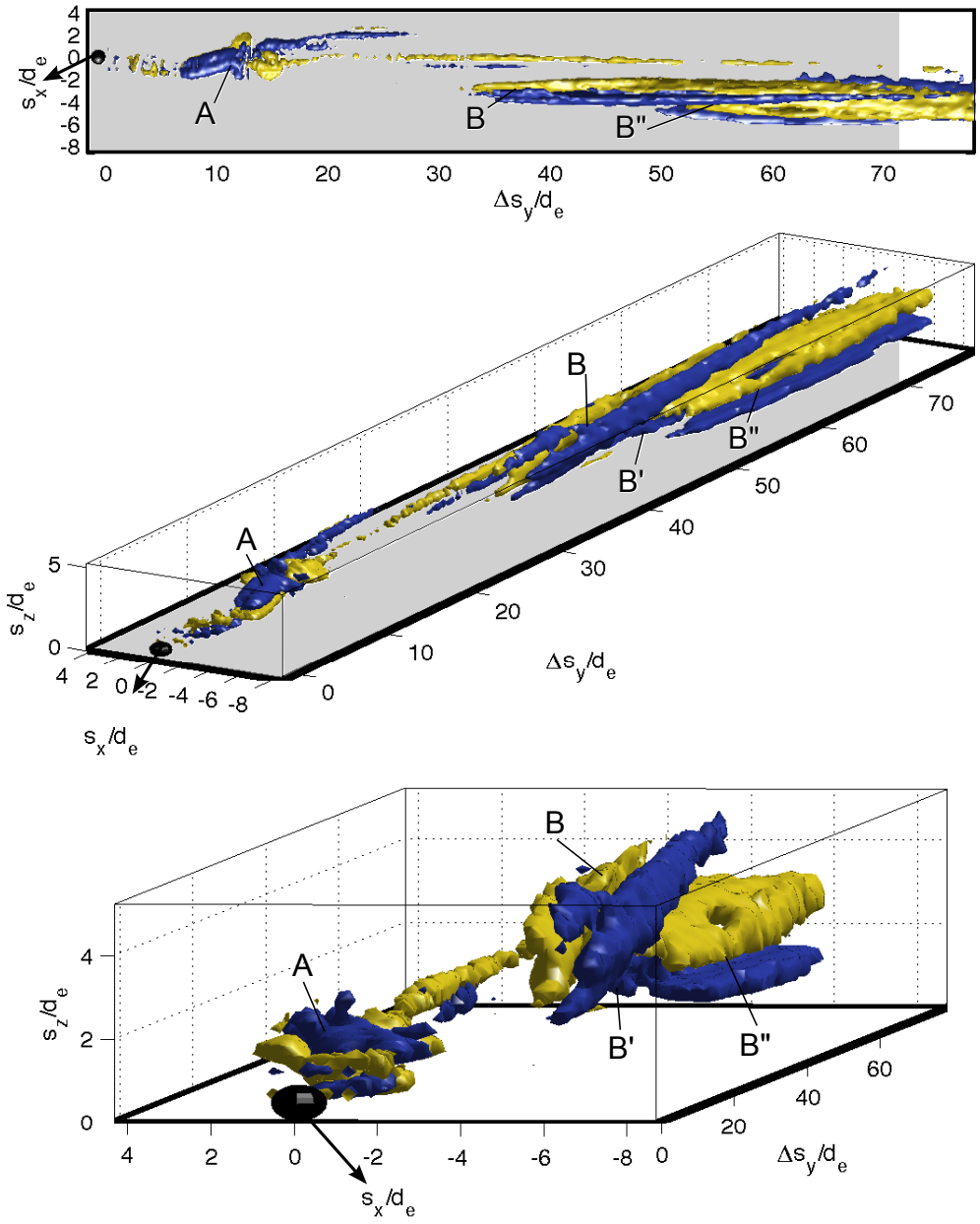

Figure 7.33: Three views of the streamwise reconstruction of vorticity for isosurfaces of $\Omega_y = \pm 1.3$ at $s_y = 60\ mm$ for $\alpha = 30°$, $d_e = 5.8\ mm$, $\phi = 270°$. The key structures A, B, B' and B'' are highlighted.

shed at the previous local maximum. This initial region is greater in magnitude than either of those observed when the phase angle was at the local extrema in path. This can be explained by considering that the near wake shed at the previous local maximum is initially advected *into* the plane, in contrast to the tests at the local extrema, wherein the near wake is rapidly advected out of plane.

Figure 7.35 shows the velocity for $\phi \approx 0^\circ$. Note that the flow structures in this plane are provided at later instances in time than for the previous two tests, as more interesting far wake behaviour is observed. Furthermore, the high velocity in the near wake means that it is not possible in this case to perform effective PIV until 0.3 *s* after the bubble passage, as opposed to the 0.2 *s* previously chosen. The scale of the colour bar for this test has also been reduced slightly in order to show the far wake structures better, while the large range in spanwise motion means the *x*-axis limits change between figures. At the time t_0 in figure 7.35 (a), the clockwise rotating region acting in the positive spanwise direction is visible, introducing a large quantity of fluid to the surface in this plane. One second later (figure 7.35 (b)), the clockwise motion continues in the positive spanwise direction. The fluid velocity magnitude has reduced significantly at the location of the primary vortex since it has been advected out of plane. At $\Delta t = 2$ *s* (figure 7.35 (c)), this structure has decreased further in strength, dying out completely by $\Delta t = 3$ *s* in figure 7.35 (d). At this point, the wake shed at the previous local minimum in path (i.e. with a phase angle delay of 270°) enters the plane. The fluid in this region is low in velocity due to viscous dissipation, but can still be observed to move away from the surface, forming a coherent structure that exists up to five seconds after the passage of the bubble (figure 7.35 (e) and (f)). Fluid motion in this plane acts over a significant area, spanning 8 bubble diameters in the spanwise direction.

The vorticity for this test in figure 7.36 can be seen to have a high magnitude in the near wake but a low magnitude in the far wake, hence the colour bar axis limits are reduced to better show the latter. The complex vortex pairs that exist in the near wake are the cross-

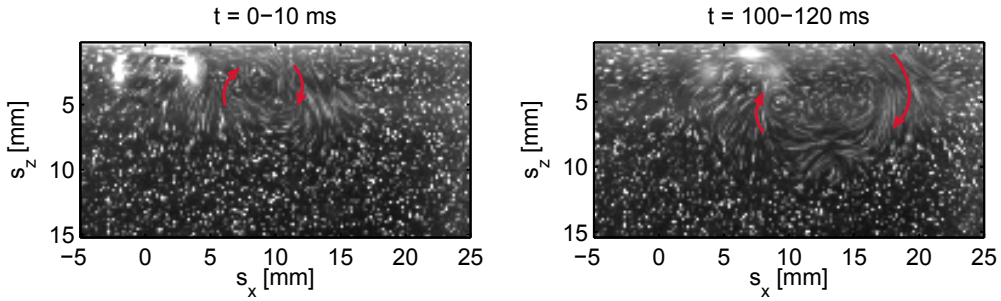

Figure 7.34: Raw images of the near wake averaged over time intervals 10 *ms* and 20 *ms* respectively, starting at two instants in time 0 and 100 *ms* after the bubble passage for $\alpha = 30^\circ$, $d_e = 5.8$ *mm*, $\phi = 0^\circ$.

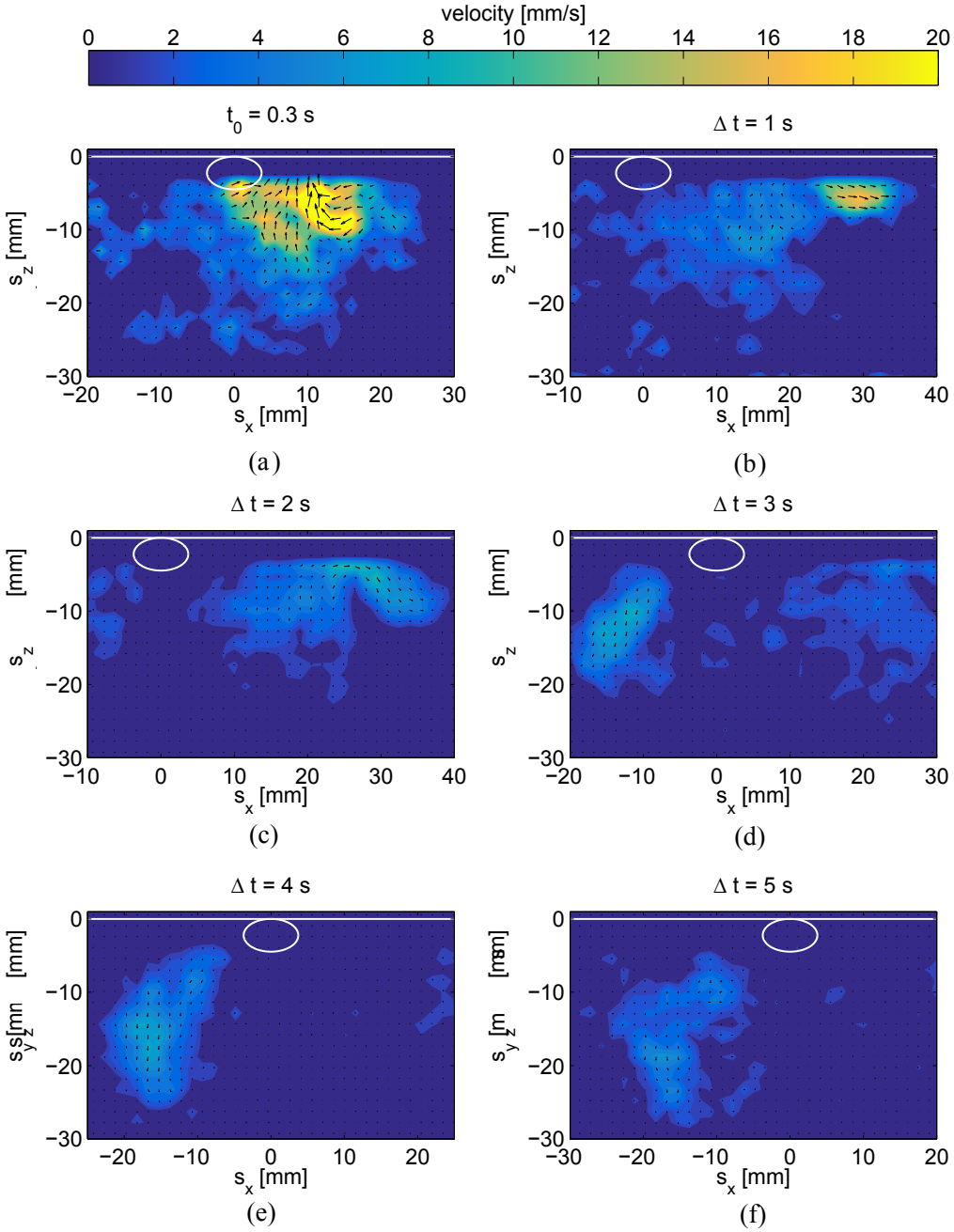

Figure 7.35: Fluid velocity magnitude $V_{mag} = \sqrt{U^2 + V^2}$ $[mm/s]$ in a perpendicular plane at $s_y = 60$ mm for $\alpha = 30°$, $d_e = 5.8$ mm, $\phi = 0°$, with each image $\Delta t = 1$ s apart and the first image t_0 0.3 seconds after the bubble passage.

section of intricate mixing structures and have been observed previously for the other phase angles. The subsequent structures that enter the plane take the form of counter-rotating pairs that temporally increase in size but decrease in strength.

The reconstructed isosurfaces of vorticity are shown for this test in figure 7.37. To identify the low-strength, far-wake structures, a lower magnitude isosurface is chosen in the bottom

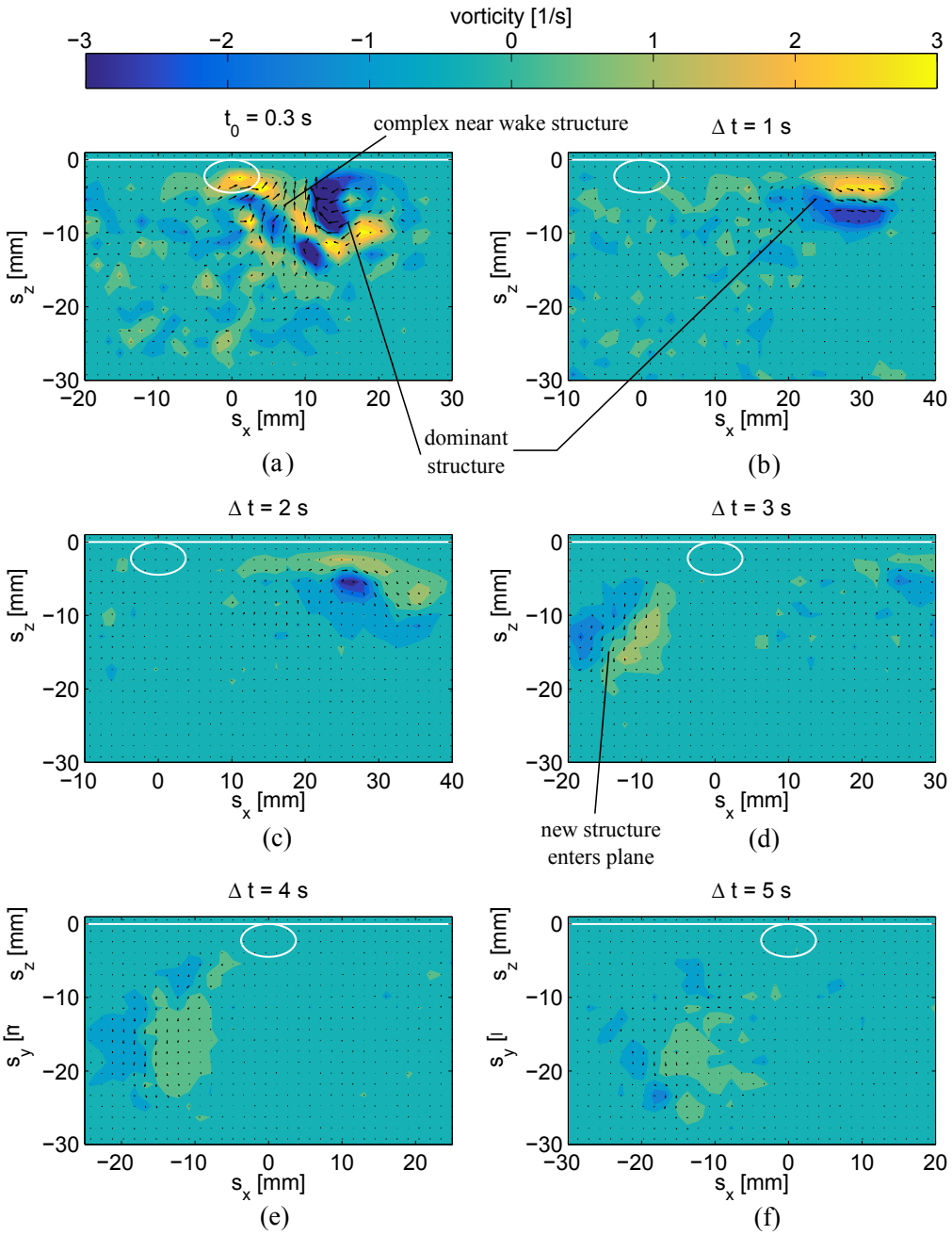

Figure 7.36: Fluid vorticity Ω_y =curl(**U**) $[1/s]$ in a perpendicular plane at $s_y = 60$ *mm* for $\alpha = 30°$, $d_e = 5.8$ *mm*, $\phi = 0°$, with each image $\Delta t = 1$ *s* apart and the first image t_0 0.3 seconds after the bubble passage.

image, of $\Omega_y = \pm 0.8\ s^{-1}$, while the top two images are $\Omega_y = \pm 1.3\ s^{-1}$ as before. The far wake structure is only shown in the bottom image, as the reduced scale of the image results in lower resolution. The fluid disturbance caused by the near wake of the bubble, A, is greater in velocity and persists for a longer time than the corresponding region A for $\phi = 90°$ and 270°, forming the coherent pair A'. This leads in to the second primary region that enters the

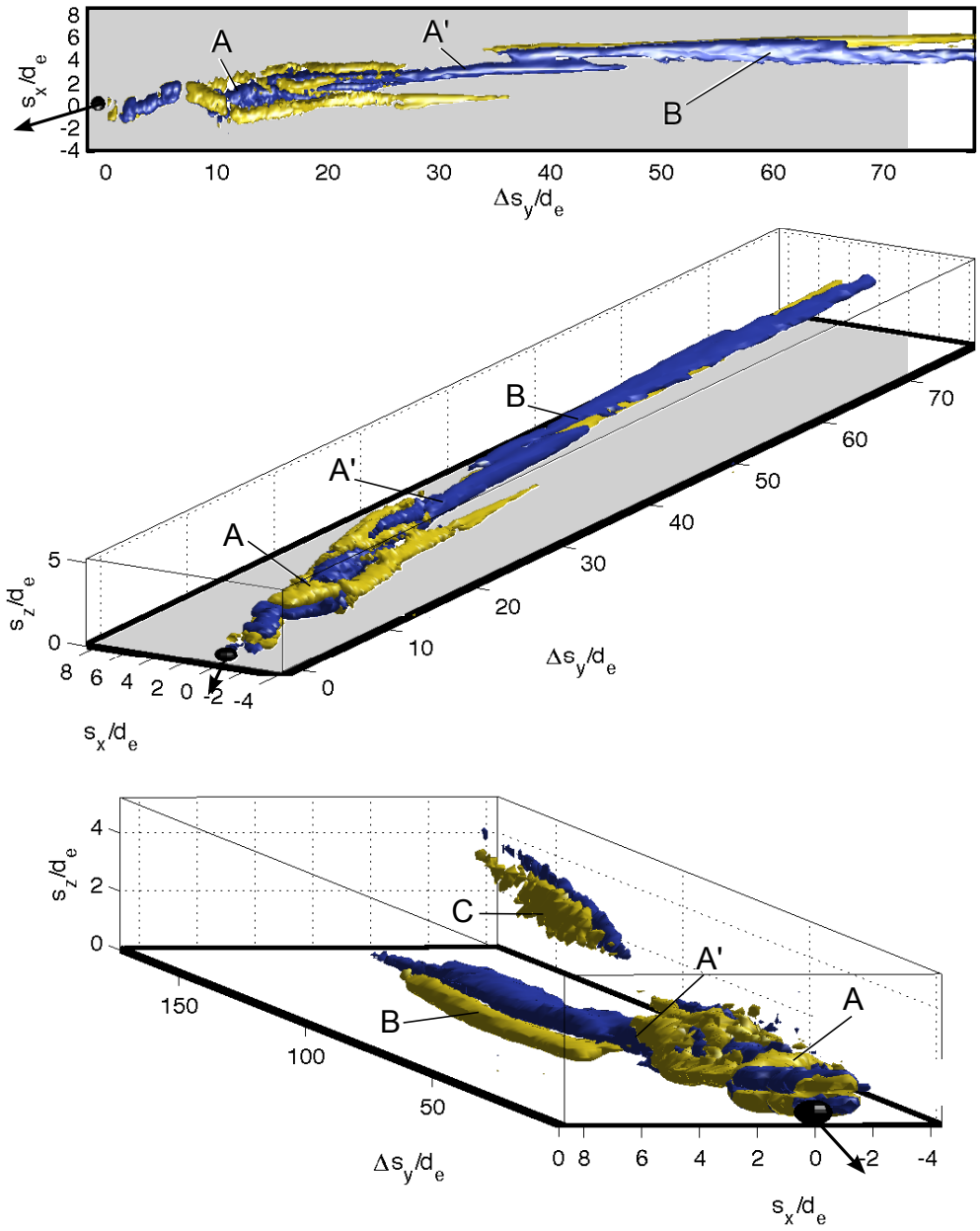

Figure 7.37: Top two views are of the streamwise reconstruction of vorticity for isosurfaces of $\Omega_y = \pm 1.3$, bottom $\Omega_y = \pm 0.8$ at $s_y = 60$ *mm* for $\alpha = 30°$, $d_e = 5.8$ *mm*, $\phi = 0°$. The key structures A, A', B and C are also highlighted.

plane at B, which corresponds to fluid shed from the previous local maximum in path. This fluid enters the plane earlier than for the $\phi = 90°$ or $270°$ cases, and its motion remains close to the surface. Finally, a greater distance downstream of the bubble, a third structure C enters the plane, which is the fluid shed at the previous local minimum of the bubble path. This far wake structure is consistent with those seen in the previous tests in that it is a greater distance

from the surface, extending up to four bubble diameters away.

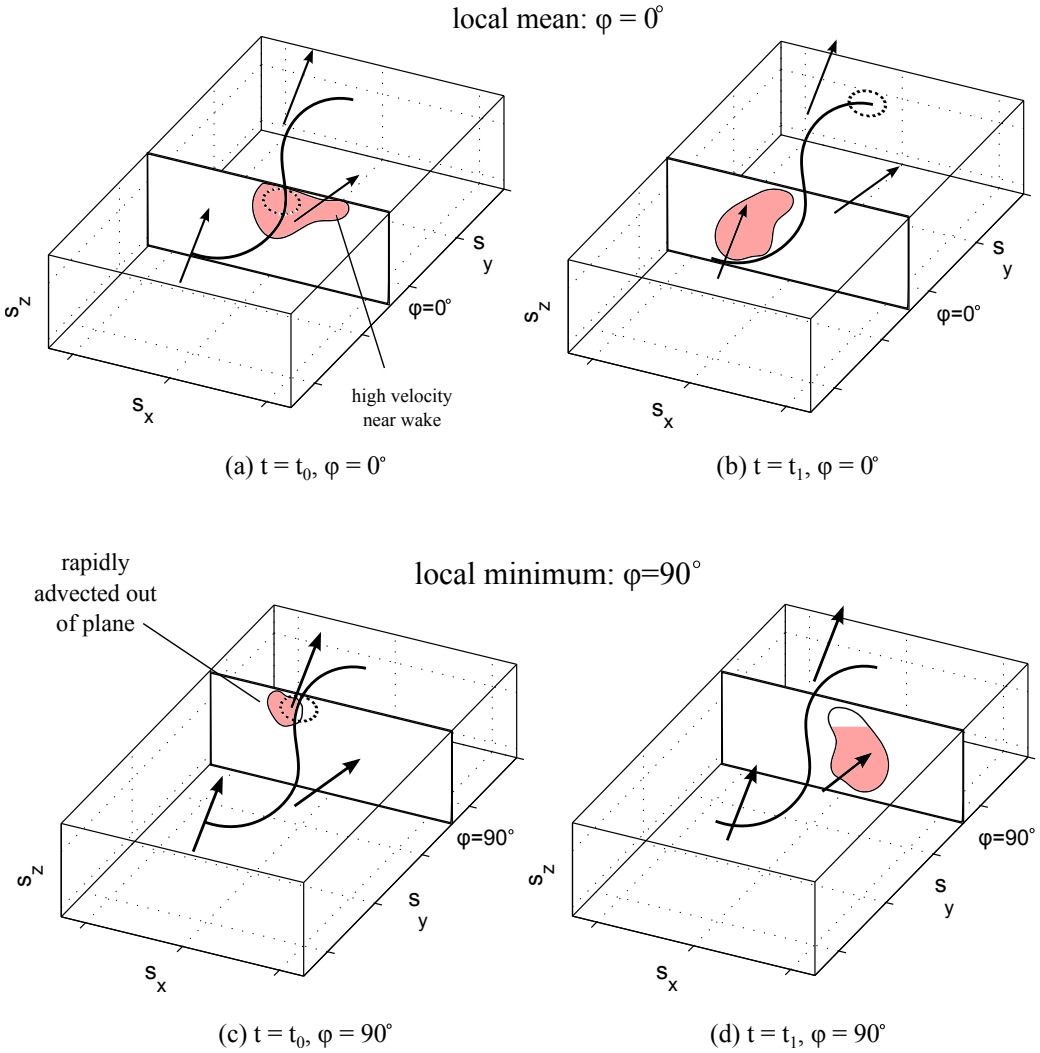

Figure 7.38: Sketch explaining the variation in the flow structures observed in the perpendicular PIV measurement planes at $\phi = 0^\circ$ and $\phi = 90^\circ$ at two times t_0 and t_1 approximately 0.5 s apart. The bubble location and path are provided, and the arrows indicate the motion of the shed fluid in the bubble wake.

A sketch showing the dependence of the wake structures observed on the phase angle is provided in figure 7.38. The bubble and its path are shown for both phase angles at two instants in time, t_0 and t_1. The direction of the bubble wake is indicated on the figure by means of arrows; this is shed from the bubble at the local path extremum and continues to overshoot the path in the spanwise and length directions. When the bubble enters the plane at $\phi = 0^\circ$, high velocity fluid from the near wake shed at the previous local maximum

($\phi = 270^\circ$) follows soon after, and is advected through the plane and in the positive spanwise direction. This results in a high magnitude region of vorticity in the near wake for the $\phi = 0^\circ$ case. At some time t_1 later, the wake shed at the previous local minimum of path ($\phi = 90^\circ$) enters the plane, with low velocity. For the bubble at $\phi = 90^\circ$, the wake separates from the bubble as it enters the plane; however, the momentum of the bubble means that this structure is advected through the plane rapidly and appears lower in magnitude than the $\phi = 0^\circ$ test. At a time t_1 later, the wake structure shed at the previous local maximum ($\phi = 270^\circ$) enters the plane. Although the structures observed at different phase angles vary slightly, the isosurfaces of vorticity presented in the current section are indicative of a wake structure that separates from the bubble at the extrema of bubble path and spreads normal from the surface. This initially causes a significant disturbance of the bulk fluid in the near wake, which acts close to the surface. Later in time, the wake structure decreases in strength but spreads away normal to the surface, causing a large affected region of fluid.

7.3 Summary

This chapter has investigated the flow structures in the wake of both single sliding bubbles and in-line bubble pairs. Measurements have been performed in 3 planes for a range of bubble diameters and surface inclination angles, although the majority of the findings presented relate to $\alpha = 30^\circ$. Two separate parallel measurement planes have been used to understand the motion of the bubble wake in the direction of the bubble's momentum. The overall wake structure deduced from PIV velocity and vorticity fields consists of a near wake that moves in close association with the bubble, which forms a recirculation region to the rear of the bubble. Fluid separates from this near wake at twice the path frequency at each extremum of path displacement. In the normal direction, fluid rolls up over the bubble base, moving away from the surface in a similar fashion to the flow over near-wall bluff bodies discussed in chapter 2. The far wake takes the form of asymmetrical, oppositely-oriented hairpin vortices that spread into the bulk fluid. This vortical structure bears some similarity to the hairpin vortices shed by near-wall bluff bodies and freely rising bubbles. However, the flow structures differ from rising bubbles as they are constricted by the presence of the surface, while they differ from near-wall bluff bodies in that they shed at alternating sides of the bubble due to the bubble

path oscillations.

In a plane perpendicular to the bubble, streamwise PIV measurements have revealed periodically shed vortices that develop in coherent pairs. In the recirculation region to the rear of the bubble, fluid is also drawn towards the surface. These vortices spread outwards into the bulk fluid, increasing in size but decreasing in strength rapidly due to viscous dissipation and out-of-plane motion. The data in this plane show the extent of the mixing offered by a single sliding bubble, creating an affected region normal to the surface many bubble diameters in size, and fluid motion persisting for several seconds after the bubble passage. The point on its oscillating path through which the bubble enters the measurement plane, represented by a phase angle, affects the nature and strength of the wake structures observed.

Additionally, the effect of introducing a bubble pair to the surface was to promote fluid mixing. However, whether this enhanced fluid mixing has a positive effect on convective heat transfer rates from the surface remains to be seen, since the interactions between the bubble and the thermal boundary layer will lead to further complexity. This will be addressed in the following chapter.

Chapter 8

Heat Transfer

This chapter presents surface temperature and convective heat flux measurements for single and multiple sliding bubbles by solving the energy balance presented in section 5.3. This is of relevance for the current study since many of the applications of sliding bubbles concern convective heat transfer. The review of the literature in chapter 2 revealed the effectiveness of sliding air bubbles at enhancing heat transfer at relatively small superheats. This chapter will explore this heat transfer enhancement for air bubbles, with a plate inclined at $\alpha = 30^{\circ}$ and $d_e = 5.8 - 7.2$ *mm*; the spatial and temporal evolution of the surface temperature will be presented and compared to those of the literature. Section 7.2 revealed that introducing a pair of bubbles in an in-line formation to the surface caused improved mixing of the bulk fluid, although it has been noted that this may not necessarily result in enhanced heat transfer. Thus, the key objective of this chapter is to understand the role that bubble-wake interactions play in convective cooling. This will provide a basis for future optimisation of two-phase air-water convective heat transfer.

As the temperatures of the fluid body and the heated surface differ, a thermal boundary layer develops at the surface. With increasing distance from the leading edge (in this case the base of the foil section), the effects of heat transfer spread further into the fluid and the thermal boundary layer grows. For vapour bubbles, contributions to the overall heat transfer have been found to come from the evaporation of the liquid micro-layer present between the bubble and heated surface and from disturbances to the thermal boundary layer caused by the motion of the bubble. For the gas bubbles considered in the current study, all convective heat

transfer is due to the bubble-induced bulk fluid motion. One key parameter in this case is the surface-to-fluid temperature difference, T_e. In the current study, T_e is kept intentionally low at $\approx 10°C$ to understand the convective effects of the air bubbles and prevent any alternate modes of heat transfer known to occur at larger T_e, such as nucleate boiling. Note that this value changes somewhat due to the developing thermal boundary layer on the underside of the surface, as was observed in section 5.3.2.

8.1 Single Bubbles

In this section, the surface temperature and convective heat flux are presented for single bubbles of diameter $d_e = 5.8$ and 7.2 *mm* sliding under a heated surface inclined at $\alpha = 30°$ to the horizontal, with a mean $T_e \approx 10°C$. To account for the developing thermal boundary layer and allow for easy comparison between tests, the temperature plots are expressed in terms of the non-dimensional surface temperature ΔT^*. This is given by:

$$\Delta T^* = \frac{T_s - T_\infty}{T_0 - T_\infty} \tag{8.1}$$

where T_s is the local instantaneous surface temperature, which was shown on figure 5.12. T_0 is the surface temperature with no bubble present and T_∞ is the bulk fluid temperature. Therefore, ΔT^* is equal to 0 when the surface is at the bulk fluid temperature and 1 when it is at its original temperature. The convective heat flux is similarly non-dimensionalised and can be considered as an enhancement ratio of forced to natural convection, q^*:

$$q^* = \frac{q''_{conv}}{q''_{nat}} \tag{8.2}$$

where q''_{conv} is the local, instantaneous convective heat flux and q''_{nat} is the convective heat flux with no bubble present.

8.1.1 Convective Heat Flux: d_e = 5.8 *mm*

Figure 8.1 shows the dimensionless surface temperature and enhancement ratio at three instances in time 0.2 *s* apart, consistent with the timeframe of the $s_z = 3$ *mm* plane PIV results

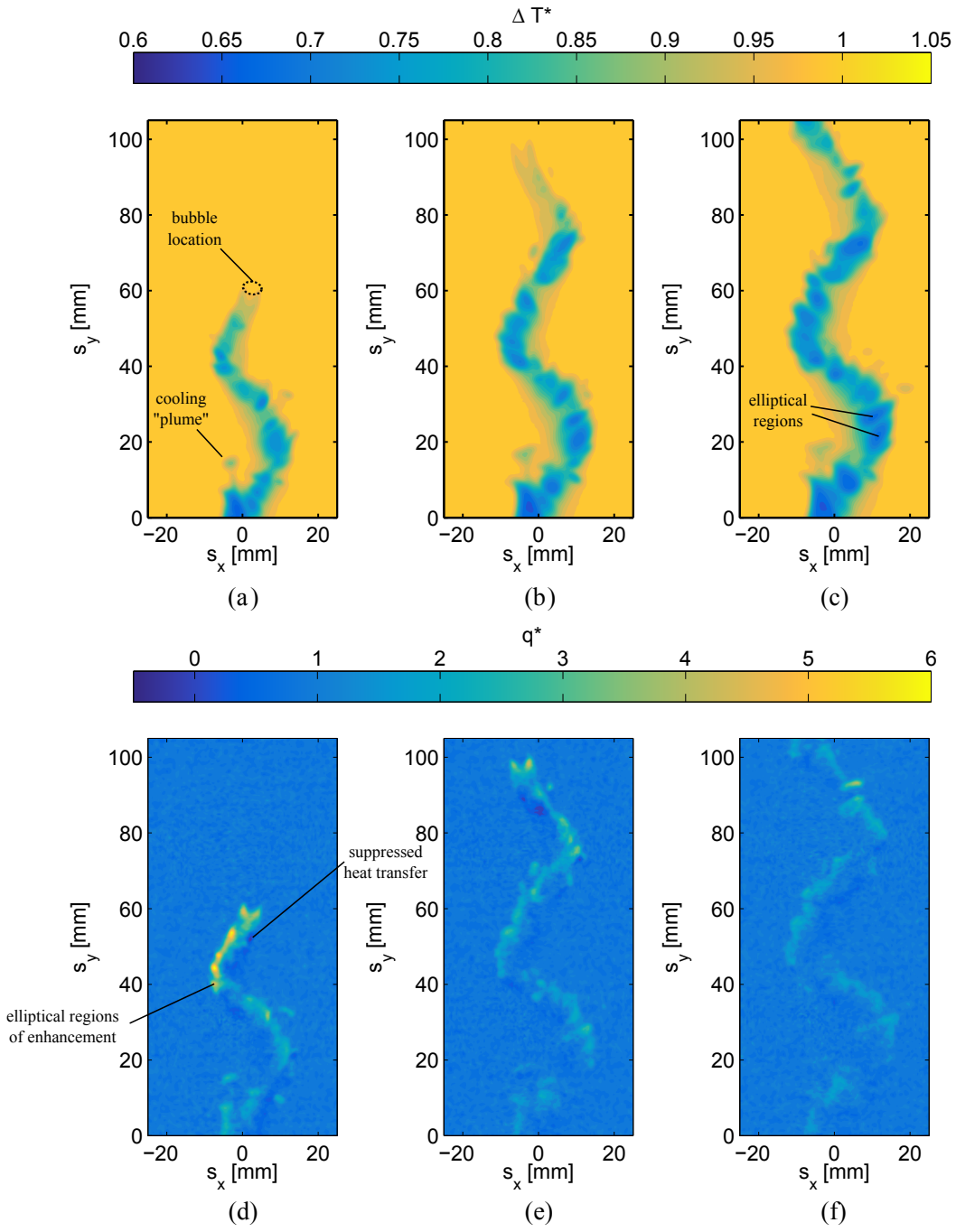

Figure 8.1: Dimensionless temperature ΔT^* (top) and convective flux enhancement $q*$ (bottom) for $d_e = 5.8\ mm$, $\alpha = 30^\circ$ and a mean superheat $T_e = 10^\circ C$, taken at instances in time corresponding to $t = 0\ s$ (a,d), $t = 0.2\ s$ (b,e) and $t = 0.4\ s$ (c,f).

of section 7.1. Immediately apparent is the excellent agreement between the surface cooling patterns and the wake structures previously observed. The bubble forms a “snake”-like cooled region that is advected along the length and spanwise directions, overshooting the bubble path. In figure 8.1 (a), the bubble is at the position $s_y = 60\ mm$. In the wake of the bubble is

an extended region of reduced surface temperature, which is approximately the width of the bubble base immediately to the rear of the bubble and widens to approximately 1.5 bubble diameters at the base of the interrogation window. The lowest surface temperature is observed at the base of the interrogation window. In this far wake, the surface temperature distrubtion takes the form of a series of small elliptical regions within the wake. The near wake of the bubble introduces fresh fluid from the bulk to the surface; this can result in complex far-wake surface cooling patterns due to interactions between this fluid and the thermal boundary layer. Thus, a secondary region of surface cooling can be observed emanating from the wake at the region highlighted on figure 8.1 (a). This "plume" shaped structure is not visible in the fluid motion tests, and is likely the result of a secondary hairpin vortex interacting with the fluid at the boundary layer.

The bubble passage results in regions of significant local convective heat flux enhancement relative to natural convection levels. These regions start directly to the rear of the bubble and can extend further downstream than the near wake (4-5 bubble diameters rather than 1-2). Typically, large convective heat transfer corresponds to regions with a high fluid velocity, although some enhancement can be observed in the slow-moving far wake. At the rear of the bubble, the convective heat transfer forms a triangular-shaped region that starts at the major axes of the bubble. This enhancement is consistent with a recirculation region at the rear of the bubble, as observed by Qiu & Dhir [89]. Downstream of the bubble, local heat flux enhancements of up to 6 times natural convection levels are visible, corresponding to the outside of the wake structure shed at the previous local minimum in path. These take the form of small, elliptical-shaped regions of cooling within the wake. On the inside of the bubble path is a small region of *suppressed* heat flux, where the local temperature is increased. These regions will be examined in greater detail later. Further downstream in the far wake, the heat flux has reduced to ≈ 2.5 times that of natural convection levels at the base of the interrogation window.

Figure 8.1 (b) and (e) show the results 0.2 s later, at which time the bubble is at $s_y \approx 100$ mm. The surface temperature in the far wake has reduced further, although the convective heat transfer enhancement has dropped to under twice that of natural convection levels. Note that the local convective flux at the bubble, shown in figure 8.1 (e), is lower than that in the first image (d). This is most likely due to the increased thickness of the thermal boundary

layer at the top of the foil, which means that the fluid being drawn in towards the surface is at a higher temperature, thereby reducing the relative enhancement effect. Another region of suppressed heat flux is visible on the inside of the bubble path. Finally, a further 0.2 seconds later in figure 8.1 (f), the convective heat flux in the far wake has reduced to 1.5 times that of natural convection and the minimum surface temperature in figure 8.1 (c) remains at $\Delta T^* = 0.6$, which corresponds to a decrease of $4°C$. As the cooled region evolves temporally, it is advected up the foil at a more significant rate than the fluid motion tests; this is due to the motion of the thermal boundary layer at the surface. In the far wake, some smaller regions of low surface temperature begin to join together into larger elliptical regions.

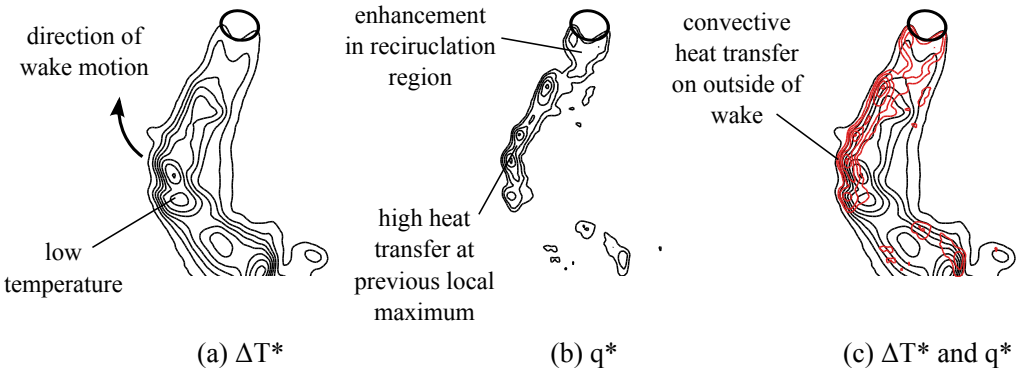

Figure 8.2: Sketch of (a) ΔT^* and (b) $q*$ in support of figure 8.1, revealing the features of interest for heat transfer enhancement. These two are spatially mapped in (c).

Figure 8.2 provides supporting sketches of ΔT^* and q^* distributions corresponding to the first instant in time in figure 8.1. Note that the surface temperature in (a) does not decrease significantly until some time after the bubble passage: the minimum surface temperature in this region is observed at the previous local minimum in bubble path. This minimum surface temperature corresponds to a local maximum in convective heat transfer in figure 8.2 (b), which exists as a series of smaller enhanced areas which are conceivably linked to different parts of the complex hairpin vortex structure impacting the surface. Although the temperature observed at the bubble is not as low as in the far wake, the thermal gradients are large at this location. This results in significant convective heat transfer in the near wake as the comparatively cool bubble and its recirculation region remove heat from the surface. Finally, when ΔT^* and q^* are spatially aligned, as shown in figure 8.2 (c), we can observe that the convective heat transfer enhancement takes place on the outside edge of the bubble wake.

This implies that the maximum convective heat transfer corresponds to the "tongue" shaped regions on the outside of the bubble path, which were described by Brücker and observed from the fluid vorticity data in chapter 7. These similarities will be discussed further in section 8.1.2.

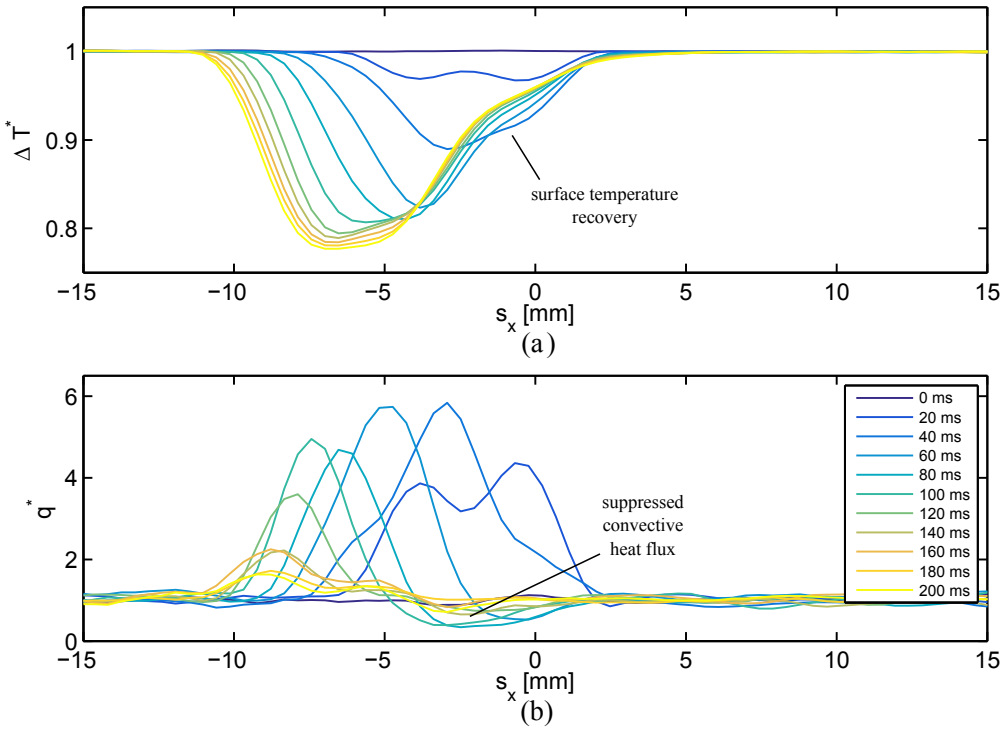

Figure 8.3: Dimensionless temperature ΔT^* (a) and convective flux enhancement $q*$ (b) for $d_e = 5.8$ *mm*, $\alpha = 30°$, $T_e = 10°C$ along a slice of the surface at $s_y = 45$ *mm*, with data shown at 20 *ms* intervals, where 0 *ms* corresponds to the bubble about to enter the slice.

Figure 8.3 shows the time-resolved dimensionless temperature difference and the dimensionless heat flux enhancement for this test along a horizontal line at $s_y = 45$ *mm*, taken at intervals 20 *ms* apart. For $t = 0$ *s*, which is just before the bubble crosses the line, ΔT^* and $q*$ are both equal to unity. 20 *ms* later, by which time the bubble has entered the line, there is relatively little change in surface temperature, although there is considerable convective heat transfer enhancement that occurs across a distance approximately that of the bubble diameter. As time elapses (up to 60 *ms*), this convective heat transfer initially increases in the near wake up to 6 times natural convection , with a corresponding decrease in surface temperature to a minimum of $\Delta T^* = 0.84$. As the position $s_y = 45$ *mm* denotes an approximate local minimum in spanwise position, it follows that this cooled fluid is advected in the negative spanwise

direction. Also observable are the regions of suppressed heat flux, where in this case q^* drops to below natural convection levels. These regions of suppressed heat transfer are found at the same locations where the initial heat transfer enhancement occurs, and correspond to a recovery in surface temperature. Later in time, the local convective flux levels steadily reduce from $q^* = 4$ down to under $q^* = 2$, while the temperature slowly continues to drop to under $\Delta T^* = 0.8$. The local evolution of convective heat transfer is similar to that observed in chapter 7 for fluid motion, although the cooling effects persist for a longer time.

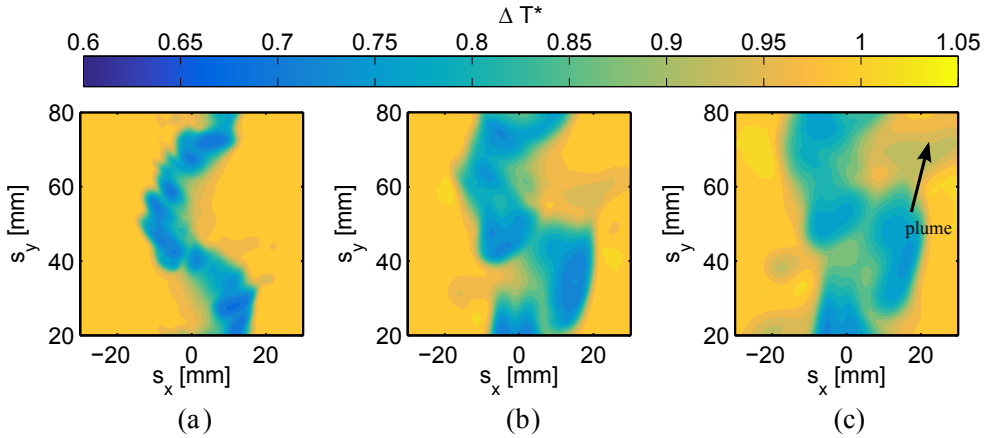

Figure 8.4: Dimensionless temperature ΔT^* for $d_e = 5.8$ *mm* over a 60×60 section of the far wake at three instances in time 1.875 *s* apart.

In the far field, the convective heat transfer enhancement factor returns to unity but the gradual increase in surface temperature continues, since it takes time for the surface to recover from the thermal depression. As the foil begins to recover, the cooled regions experience an advection more significant and complex than was evident from the fluid motion tests in chapter 7; this is due to the natural convection boundary layer on the underside of the foil moving the cooling structures up the foil. Figure 8.4 shows the surface temperature distribution of the surface over three instants in time 1.875 *s* apart, where the instant in time in figure 8.4 (a) corresponds to that of figure 8.1 (c). Over time, the local minimum in temperature observed increases, as too does the size of the affected areas. The smaller elliptical areas of low surface temperature have now joined together fully at each local extremum of the wake and are advected significantly upstream. Upstream of these local extrema, the secondary "plume" shaped cooling regions are visible, which are likely the further interaction of the hairpin vortices with the thermal boundary layer.

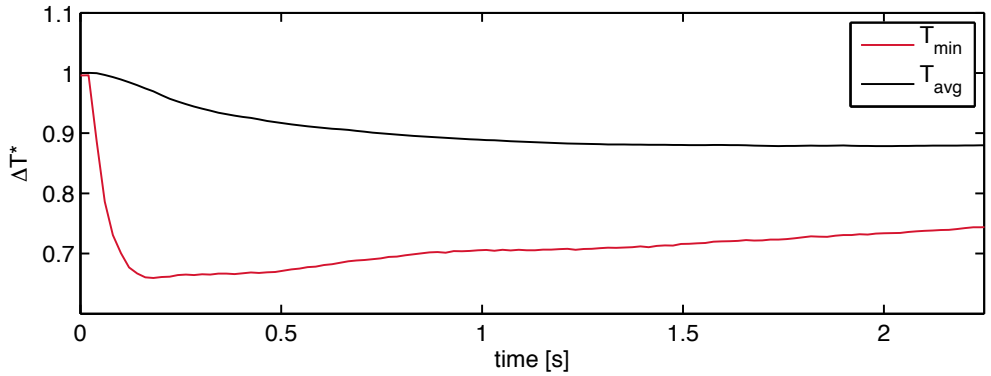

Figure 8.5: The mean (−) and minimum (−) dimensionless surface temperature ΔT^* as a function of time for $\alpha = 30°$, $d_e = 5.8$ *mm*.

Figure 8.5 shows the spatially averaged and minimum dimensionless surface temperatures for this test. Before the introduction of the bubble, the minimum and averaged normalised surface temperatures are approximately unity. As the bubble enters the interrogation window, the average temperature slowly decreases, while the minimum temperature sharply decreases. This minimum temperature is observed a significant distance downstream of the bubble in the far wake. At 0.2 *s* after the recording started, the minimum temperature begins to slowly recover, although the mean temperature continues to fall due to the cooled region spreading laterally and affecting a larger area. The surface temperature recovers slowly from this thermal depression, taking between 8-15 seconds to recover fully back to its initial values.

In order to explore further the complex process of heat flow associated with a bubble sliding under the heated surface, the instantaneous convective heat flux for the 5.8 *mm* bubble and its near wake is shown at 10 ms intervals in figure 8.6. In general, as the bubble travels further up the surface, the local maximum heat transfer decreases in magnitude due to the increasing thermal boundary layer thickness. As the bubble traverses the surface, distinct variations occur in the convective heat flux, which are linked to the phase angle of the bubble. As was discussed for figure 8.1, convective heat transfer starts at the bubble major axes and extends back in a v-shaped region, resulting in comparatively little convective heat transfer at the base of the bubble minor axis. Downstream of the bubble, the convective heat transfer enhancement takes the form of small elliptical regions within the near wake, which are conceivably linked to the different components of a hairpin vortex structure impacting the surface. This occurs on the outside of the wake. On the inside of the wake, small regions

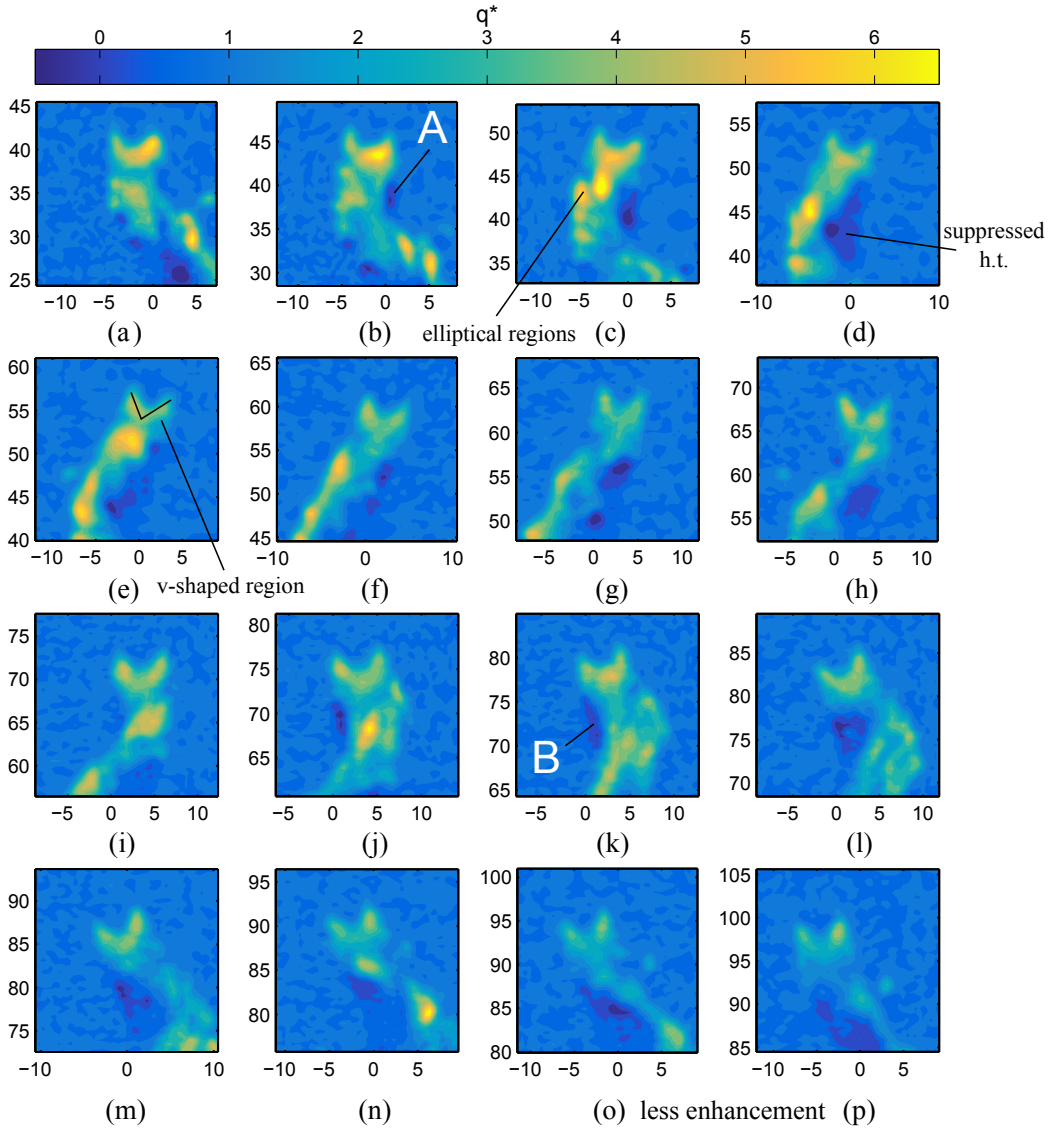

Figure 8.6: Convective flux enhancement, q^*, in the near wake for $\alpha = 30°$, $d_e = 5.8$ *mm* provided at instances in time 10 *ms* apart. The regions of interest *A* and *B* are also shown.

of suppressed heat transfer are visible. At some instances, this value is sufficiently low as to be negative. Why does this occur? Consider the region of negative convective flux, *A*, identified in figure 8.6. Prior to this image sequence, the bubble passed over the point *A* as it approached its local minimum in path, resulting in high convective flux levels and a decrease in surface temperature. However, upon reaching its local minimum, the bubble changes direction and its near wake separates, continuing to move in the negative spanwise direction. Thus, although the bubble passes over *A*, its near wake *does not*. Since there is now no cool fluid being brought to the surface at the location *A*, its surface temperature recovers, resulting

in suppressed or even negative convective heat flux.

Continuing the image sequence, a second suppressed region appears at the inside of the next local extremum, denoted as B. This behaviour thereby repeats as the bubble traverses the surface; namely the development of regions of negative heat flux at regions where the bubble passed through but its wake does not. Note that this suppressed convective heat transfer only occurs at regions in the wake where the surface temperature has already been reduced (i.e. following a period of enhancement). This can be observed on the surface temperature line plot in figure 8.3, and means that the overall effect of the sliding bubble is to increase convective heat transfer and decrease the mean surface temperature. Despite this, the instantaneous local heat flux levels are nuanced.

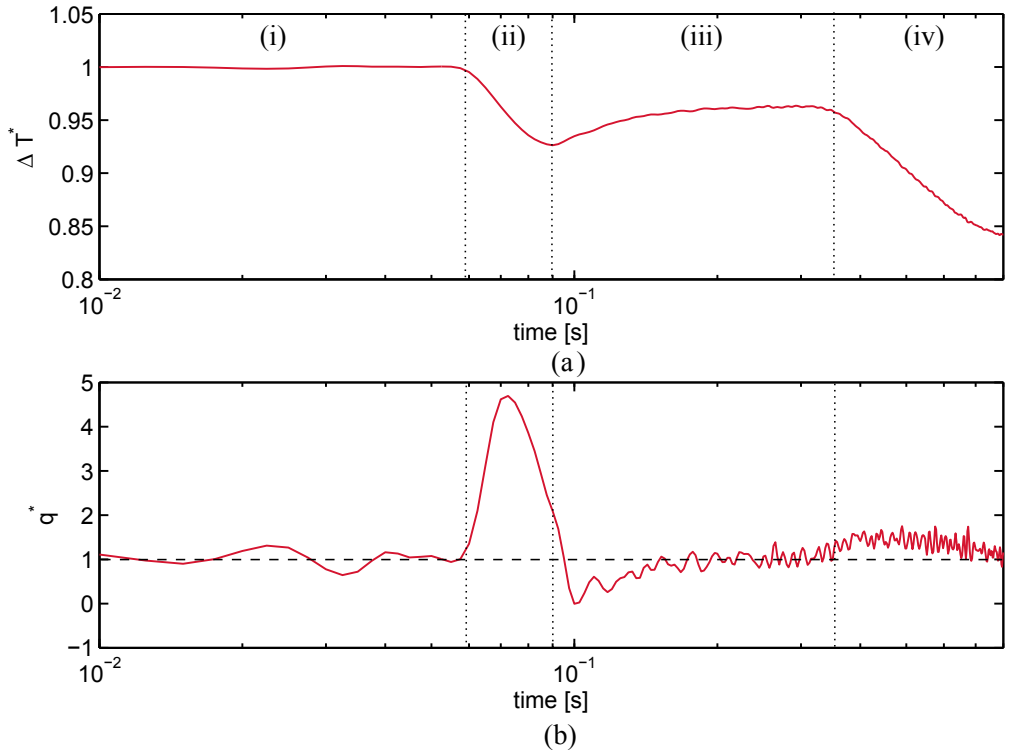

Figure 8.7: Logarithmic plot of the dimensionless temperature ΔT^* (top) and convective flux enhancement $q*$ (bottom) for $d_e = 5.8\ mm$, $\alpha = 30^\circ$ as a function of time for the key location A on figure 8.6.

Figure 8.7 shows the evolution in ΔT^* and $q*$ at the point A on figure 8.6 as a function of logarithmic time. This can be split into four zones. First, in the zone (i), there is no bubble at A, with ΔT^* and $q^* \approx 1$. As the bubble passes over point A (ii), there is a decrease in surface temperature and a corresponding enhancement in convective flux. After the bubble passage,

the near wake does not pass through A, which results in the surface recovering its temperature and a decrease in the instantaneous heat flux to below natural convection levels (*iii*), which is observed in figure 8.6 (b). Further in time (iv), the far wake downstream has been advected into A, resulting in a decrease in surface temperature and an increase in convective flux to 1.5 times natural convection levels. Eventually, ΔT^* and $q*$ tend back towards unity, although the former takes longer to achieve.

It is now possible to make a comparison between the values obtained for ΔT^* and $q*$ with those of the literature. Donnelly et al. [4] found a normalised surface temperature $\Delta T^* = 0.3$ in the far wake for $d_e = 5.8\ mm$, which is lower than the 0.6 observed in the current study. However, this was for a case with the surface at a that was closer to the water temperature ($T_e \approx 6°C$). The cooling effect of ellipsoidal bubble was $\approx 4°C$, the same as the current study. The authors found a corresponding heat transfer coefficient of 6 times natural convection levels, which is largely consistent with that observed here. Finally, the characteristic time scale of heat transfer coefficient was found by Donnelly et al. to be approximately 8-10 seconds. This is in agreement with the work of Zun et al. [49]. The current study indicates that this is dictated by the temperature difference ΔT, since the convective heat flux decreases more rapidly than this (see figure 8.7). It is worth noting that although there is good agreement between these three studies, the rate of surface temperature recovery varies depending on the heat capacity of the foil and the surrounding liquid. Thus, the temperature recovery is specific to each experimental setup. For instance, if the bubble were sliding over a heated block, this recovery in temperature would be very different. For a bouncing bubble impacting a heated surface, Donoghue et al. [80] observed a maximum enhancement of ≈ 18 times natural convection levels, significantly larger than the current study. However, this value was only observed momentarily at the bubble impact. Additionally, the large bubble velocity (U_T = 0.33 m/s) and high superheat of $T_e \approx 30°C$ contributed to this large local enhancement. Thus, the convective heat transfer measurements obtained for $d_e = 5.8\ mm$ are consistent with the literature on air bubbles.

8.1.2 Convective Heat Flux: d_e = 7.2 *mm*

The influence on ΔT^* and $q*$ of increasing the bubble diameter to 7.23 *mm* is shown in figure 8.8. As was evident from the fluid motion results, the increased bubble velocity results in greater fluid advection. This means a larger affected area of enhancement, although the surface cooling and heat flux enhancement levels are largely similar to the 5.8 *mm* test. Additionally, the greater bulk motion of the fluid leads to slightly larger values of convective flux in the far wake. Also identified on figure 8.8 is the formation of secondary shed structures at the maximum of the bubble path. Note again that the convective heat transfer plots take the form of small, elliptical regions of cooling that are visible along the outside of the bubble path up to 5 diameters downstream of the bubble. The shape of the heat transfer profiles is again in agreement with the equivalent PIV results, and evolve in the far wake to form isolated, ellipsoidal regions of cooling, joined by regions of less intense cooling. At the first instant in time, the v-shaped region of cooling in the near wake is very large, and is followed downstream by significant convective cooling up to 5 bubble diameters downstream. Over the three images, there also appear to be fewer regions of suppressed heat transfer. This will be discussed shortly. At a wall superheat of $10°C$, it appears that the effect of increasing the bubble volume on surface temperature is to provide surface cooling over a larger area, rather than a decrease in the local temperature.

Figure 8.9 shows these trends over a horizontal line at $s_y = 60$ *mm*. Although the minimum ΔT^* is only slightly lower than that of the $d_e = 5.8$ *mm* test, the affected area is larger, acting over an area two bubble diameters in size at 0.2 *s* after the bubble passage. At $s_y = 60$ *mm*, the convective heat transfer does not drop below natural convection levels. The magnitude of q^* at these instants in time is slightly lower than the previous test, although the global values of convective heat flux are not significantly different between these two bubble volumes, only the area over which it acts.

The far field temperature plots for $d_e = 7.2$ *mm* are shown in figure 8.10. The cooled structures in this case spread across the entire interrogation window, while structures from the previous local minimum and local maximum in path are advected into the measurement region. The fluid shed at the previous local minimum forms a "teardrop" shaped cool region, consistent in shape with the head of a hairpin vortex impacting the surface. At the same

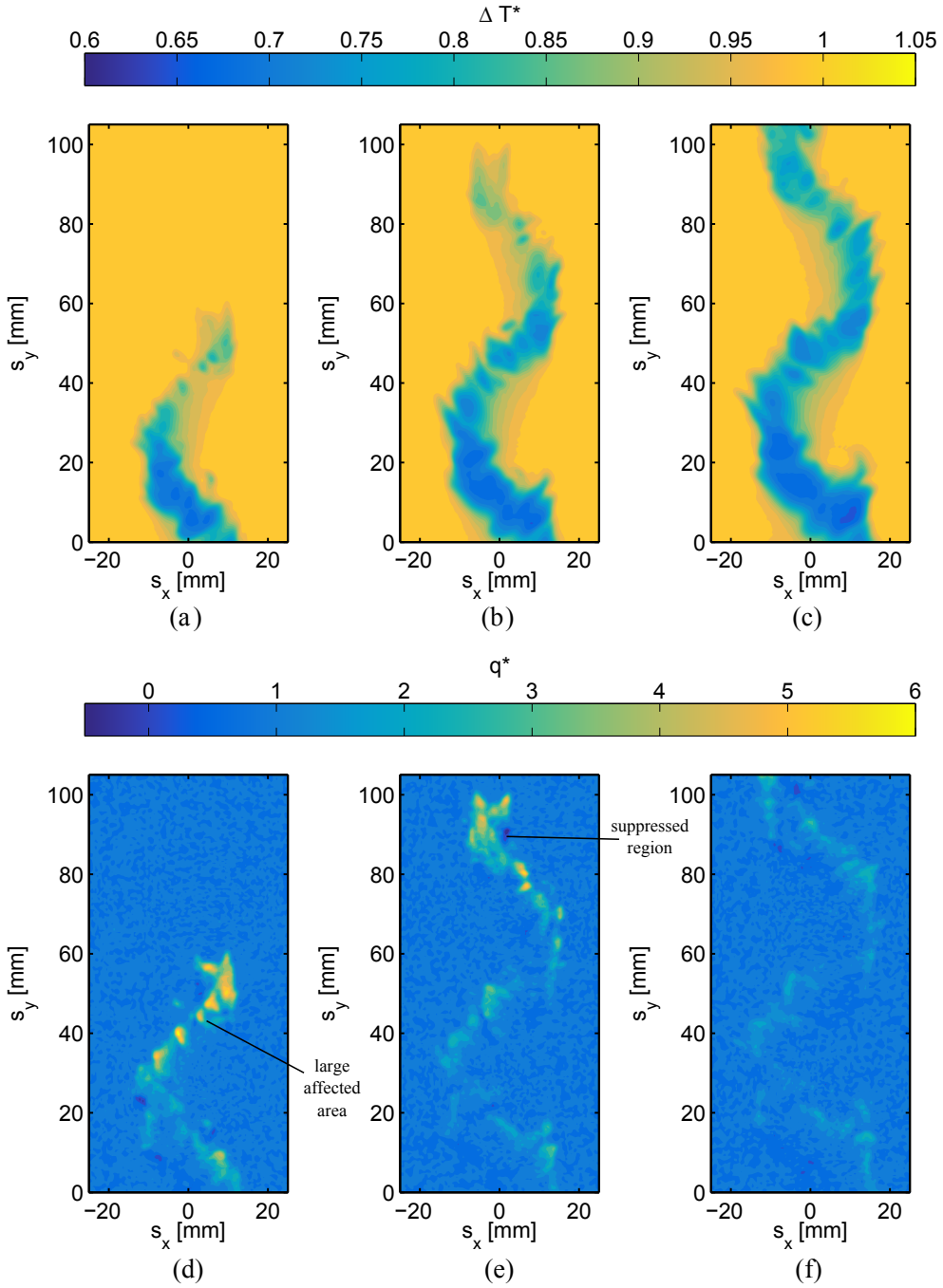

Figure 8.8: Dimensionless temperature ΔT^* (left) and convective flux enhancement $q*$ (right) for $d_e = 5.8\ mm$, $\alpha = 30°$, $\Delta T = 10°C$ along a slice of the surface at $s_y = 45\ mm$, with data shown at 20 *ms* intervals, where 0 *ms* corresponds to the bubble entering the slice.

time, the "plume" shaped cooled region shed by the previous local maximum has entered the window, having been advected by 60 *mm* up the foil. The surface-averaged and minimum temperatures for $d_e = 7.2\ mm$ are shown in figure 8.11. The minimum temperature is similar to that for the $d_e = 5.8\ mm$ bubble, while the mean temperature is only slightly larger in this

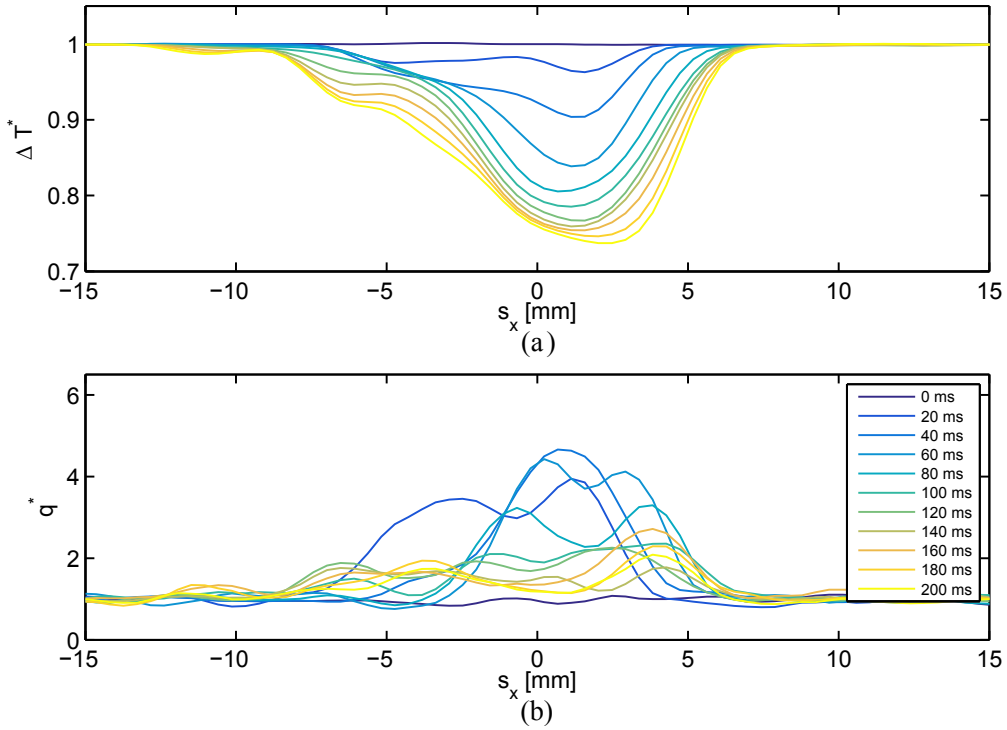

Figure 8.9: Dimensionless temperature ΔT^* (left) and convective flux enhancement q^* (right) for $d_e = 7.2$ *mm*, $\alpha = 30°$, $T_e = 10°C$ along a slice of the surface at $s_y = 60$ *mm*, with data shown at 20 *ms* intervals, where 0 *ms* corresponds to the bubble entering the slice.

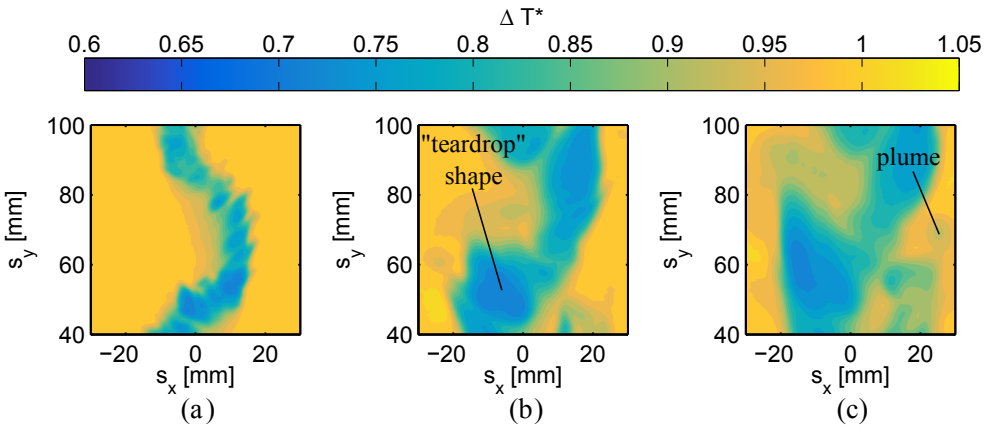

Figure 8.10: Dimensionless temperature ΔT^* in a 60×60 section of the far wake at three instances in time 1.875 *s* apart for $d_e = 7.2$ *mm*.

case, since the temperature is being averaged over a comparatively large area. Again, these temperatures are specific to this particular apparatus.

Figure 8.12 shows the convective heat flux in the near wake at 10 ms intervals for $d_e = 7.2$ *mm*. At this bubble size, there is significant convective heat flux in the far wake outside of

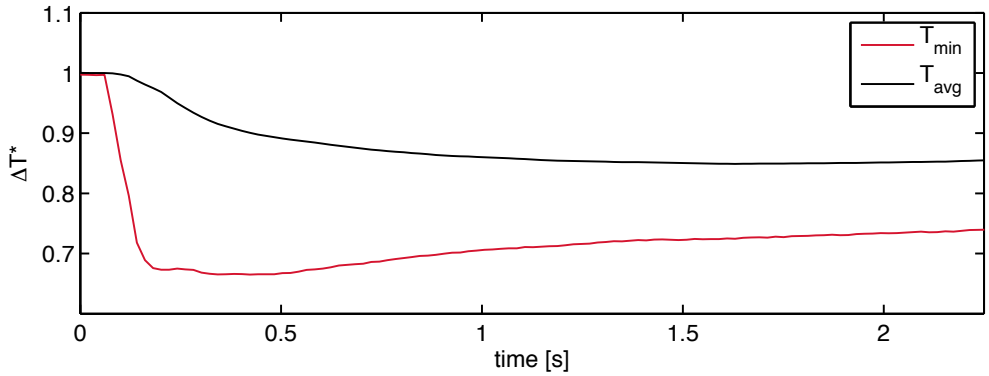

Figure 8.11: The spatially averaged mean (−) and local minimum (−) dimensionless surface temperature ΔT^* as a function of time for $\alpha = 30°$, $d_e = 7.2$ *mm*.

the viewing window. It is also clear that there is a relationship between the bubble's phase angle and the local convective heat transfer enhancement in the near wake. At the locations in the bubble path where the near wake has just separated from the bubble (i.e. directly after the extrema in path), high convective heat flux is observed in the near wake. As the bubble returns from this extremum to its mean position, there is little convective heat transfer in the near wake, although it persists at the previous local extremum. At the local extrema in path, the regions in convective heat transfer are also large in size, most noticeable at the region *A*. As the bubble traverses the surface, there are some regions of suppressed heat transfer, although these are smaller in size and magnitude than for the $d_e = 5.8$ *mm* test and dissipate rapidly. Recall that suppressed heat transfer is observed at locations on the surface where the bubble passes but its wake does not. Hence, the increased advection and affected surface area associated with the 7.2 *mm* bubble means that there are fewer locations along the bubble's path where this occurs. Finally, the cooling structure is less stable for this bubble volume; fluid often separates from the wake at the extrema in path to form cooling "plumes".

To this point, the cooling structures in the wake of a single sliding bubble have been discussed while making reference to the fluid motion experiments from chapter 7. Figure 8.13 looks at this mechanism in greater detail by spatially aligning the bubble wake with the thermal measurements. This is a somewhat qualitative comparison, since minor fluctuations in the local heat transfer are linked to a complex three-dimensional wake that features subtle differences between tests. Additionally, secondary cooling structures have been found in the case of a heated surface that do not occur under adiabatic conditions. Despite this, mapping

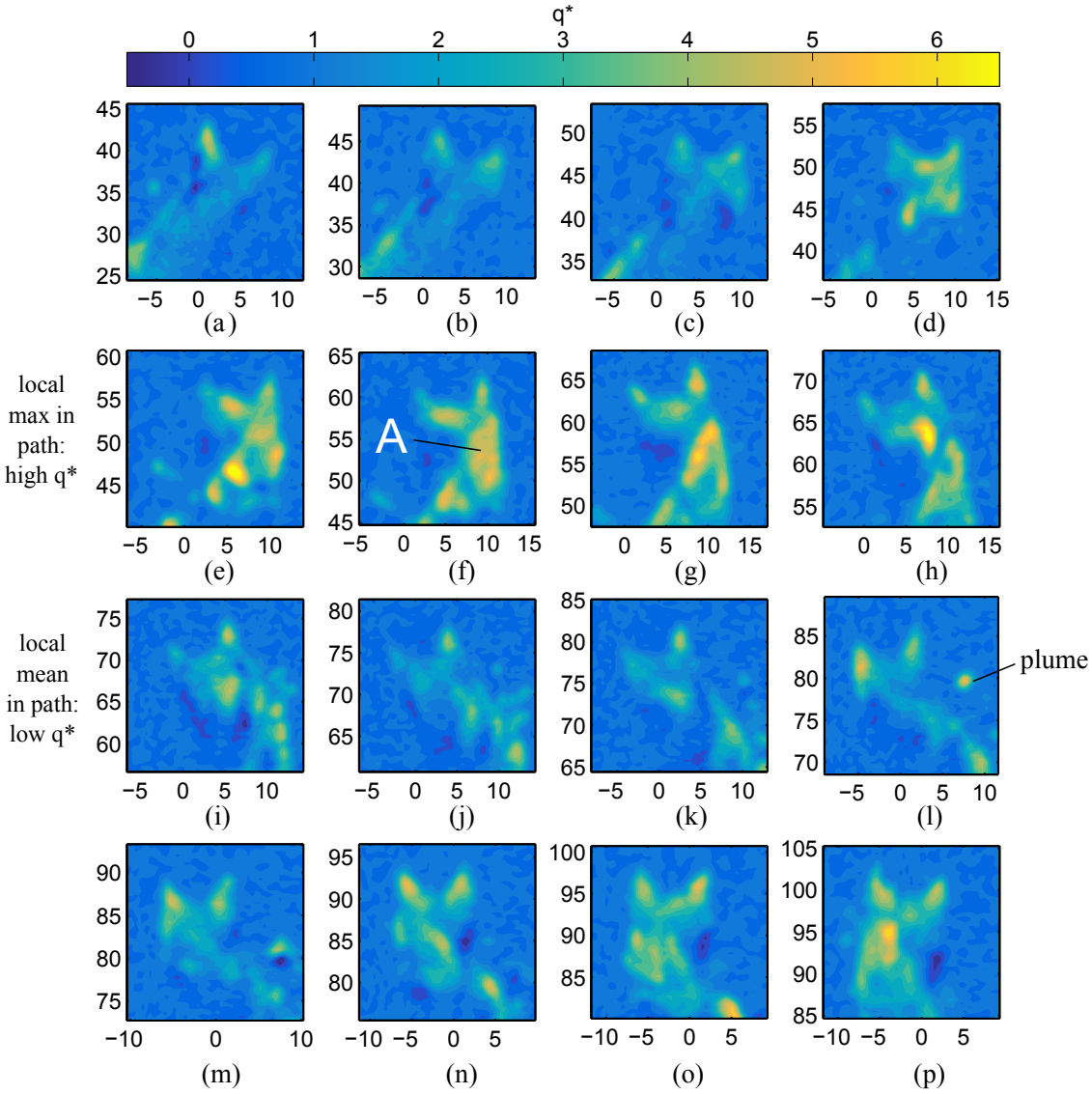

Figure 8.12: Convective flux enhancement, q^*, in the near wake for $\alpha = 30°$, $d_e = 7.2$ *mm* provided at instants in time 10 *ms* apart. The regions of interest *A* and *B* are also shown.

the two experiments remains instructive. Figure 8.13 (a) shows the local fluid velocity mapped to the surface temperature. The far wake experiences a significant thermal depression with little fluid motion or convective cooling. The reason for this is that the bubble and its near wake initially introduces cool fluid to the surface at high velocity. In the far wake, the fluid has reduced in velocity but is still below the surface temperature. The specific heat capacity of the water and the resistance of the foil mean that it takes some time to recover from this thermal depression. Also observed is the difference between the two measurement setups, wherein the secondary "plumes" due to the interaction between the wake and the

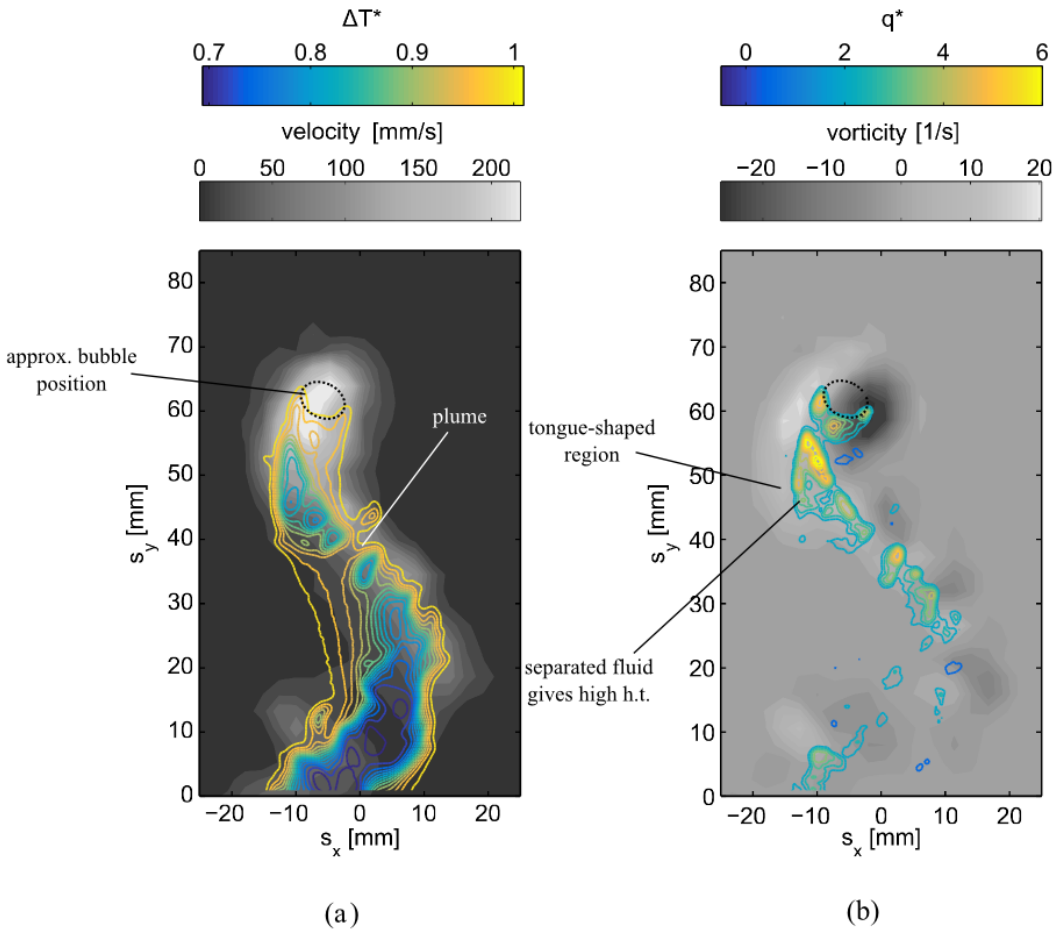

Figure 8.13: PIV velocity (a) and vorticity (b) for $\alpha = 30°$, $d_e = 7.2\ mm$. Spatially mapped onto these plots are the normalised surface temperature (a) and convective heat flux (b) from the heated tests.

thermal boundary layer are visible only for the heated tests.

Figure 8.13 (b) shows the instantaneous fluid vorticity mapped convective heat flux at the same instant in time. The highest convective flux identified at this instant is observed at the vortex that has separated from the near wake at the previous local minimum in path. This corresponds to the dominant component of vorticity at the structure that has separated from the bubble that forms a "tongue" shape. This flow region was identified as a key feature in the near wake, both by Brücker [39] and in the fluid motion study of chapter 7. The perpendicular plane PIV experiments showed a near wake structure that drags fluid towards the surface, consistent with the recirculation region to the rear of the bubble identified in the literature. The convective heat transfer experiments reveal that it takes a short time for this fluid to impact this surface. This indicates that it is the recirculation region to the rear of the bubble, rather than the bubble itself, that is contributing most significantly to convective

heat transfer. These regions of enhanced cooling do not last for an extended time due to the viscous dissipation of the fluid, meaning that the mode of heat transfer in the far wake reverts to natural convection. This natural convection is still larger than the base levels, since the fluid introduced to the surface by the bubble is cooler. In time, this fluid increases in temperature, meaning the heat transfer settles to the original natural convection levels.

8.2 Multiple Bubbles

Section 8.1 showed the convective heat flux and surface cooling associated with single bubbles at $\alpha = 30°$, revealing surface cooling that is dependent on the bubble volume and where the bubble is on its path. Thus, it is likely that the introduction of an in-line bubble pair will add further intricacy to the heat flux results due to the bubble-wake interactions discussed in section 7.1.3. The surface temperature and heat flux for an in-line bubble pair are provided in figure 8.14, first at three instances in time 0.2 *s* apart. In this case, the leading and trailing bubble major axes are highlighted on the figure for clarity. It is apparent that the cooling regions adopt a configuration consistent with the fluid motion tests, although the convection of the wake is greater. A convective heat flux pattern is observed that at first appears a superposition of two single bubble tests in an opposite configuration, although the local cooling at the trailing bubble is more complex. At the first instant in time (figure 8.14 (d)), a region of suppressed heat transfer has appeared in front of the trailing bubble just as it prepares to intersect the leading bubble wake. At the second instant in time (figure 8.14 (e)), there is a region of high convective heat flux just behind the trailing bubble, which has just intersected the leading bubble wake. Finally, after a further 0.2 *s* the convective flux levels have dropped significantly, while the surface slowly begins to recover its temperature. The surface cooling forms a double-threaded pattern wherein the secondary plumes also interact with the primary wake structure.

Figure 8.15 shows the time-resolved dimensionless temperature difference and the dimensionless heat flux enhancement at $s_y = 45$ *mm* for an in-line bubble pair. The trends here are similar to those of the equivalent local velocity plot in chapter 7, although the heat transfer enhancements do not dissipate as quickly as does the fluid velocity. The leading bubble enters the line at $s_x < 0$ *mm* and the trailing bubble enters 20 *ms* later at $s_x > 0$ *mm* .

The surface cooling and convective flux for the leading bubble are advected in the negative spanwise direction. After some time, the surface temperature begins to recover in the wake of the leading bubble, resulting in suppressed heat transfer. This does not occur in the wake of the trailing bubble. The far field temperature plots for the in-line bubble pair shown in

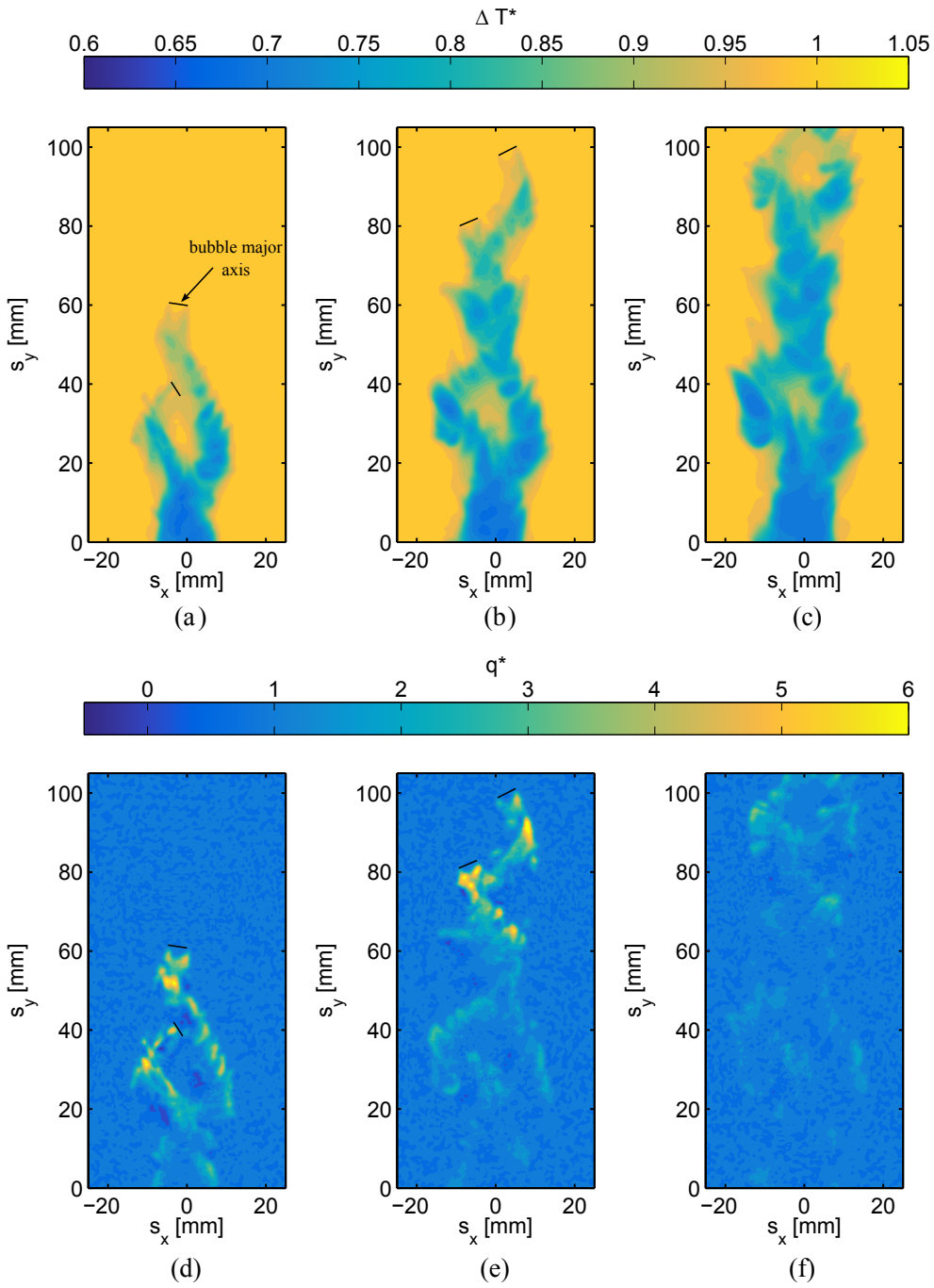

Figure 8.14: Dimensionless temperature ΔT^* (top) and convective flux enhancement $q*$ (bottom) for a bubble pair with $d_e = 5.8\ mm$, $\alpha = 30^\circ$ and a mean superheat $\Delta T = 10^\circ C$, taken at instances in time corresponding to $t = 0\ s$, $t = 0.2\ s$ and $t = 0.4\ s$.

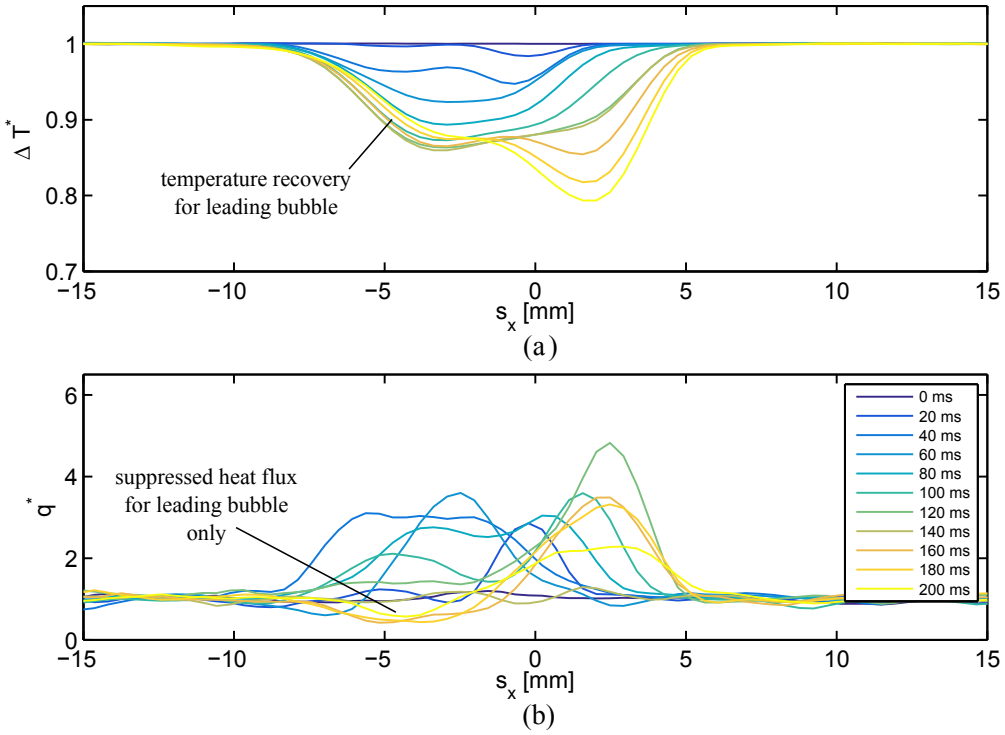

Figure 8.15: Dimensionless temperature ΔT^* (a) and convective flux enhancement $q*$ (b) for an in-line bubble pair with $d_e = 5.8\ mm$, $\alpha = 30°$, $\Delta T = 10°C$ along a slice of the surface at $s_y = 45\ mm$, with data shown at 20 ms intervals, where 0 ms corresponds to the leading bubble about to enter the slice.

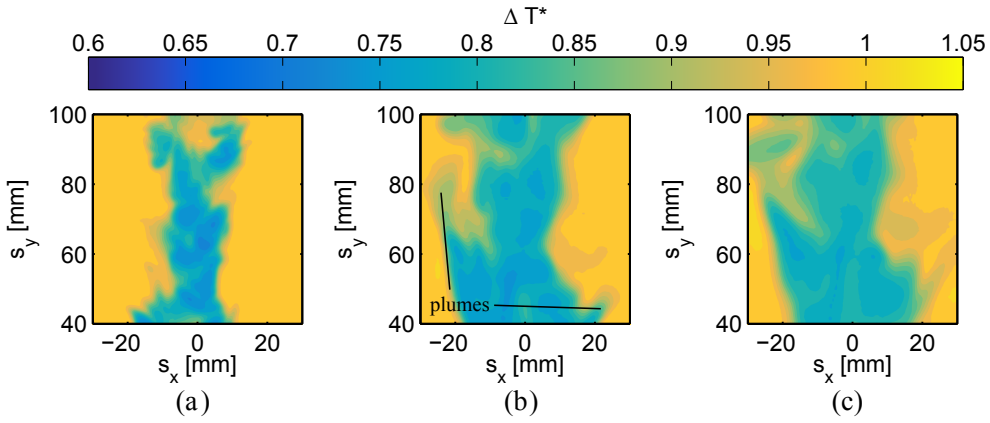

Figure 8.16: Dimensionless temperature ΔT^* for an in-line bubble pair with $d_e = 5.8\ mm$ over a $60 \times 60\ mm^2$ section of the far wake at three instances in time 1.875 s apart.

figure 8.16 are consistent with the superposition of the temperature fields for two single bubbles. Thus, structures from the previous local minimum and local maximum from each bubble are advected into the plane, affecting a large area. In particular, the secondary "plume" on the left hand side of the bubble wake is noticeable here.

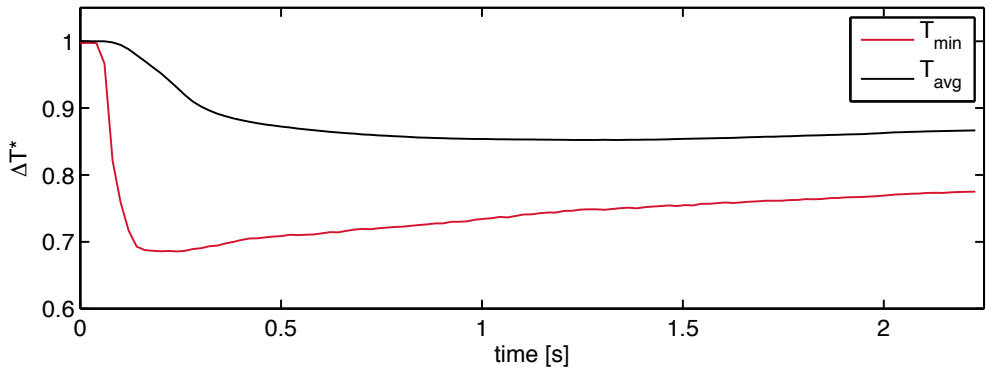

Figure 8.17: The mean (−) and minimum (−) dimensionless surface temperature ΔT^* as a function of time for an in-line bubble pair with $\alpha = 30^\circ$, $d_e = 5.8$ *mm*.

In terms of the global temperature decrease, as shown in figure 8.17, the introduction of the second bubble does not decrease the minimum surface temperature noticeably more than a single sliding bubble does. This is due to the opposite amplitudes of the bubble paths: for the majority of the time, the bubbles are cooling different parts of the foil. When the bubble paths do intersect, the complex interactions that occur can decrease the temperature, but this effect is small. The spatially averaged surface temperature does decrease from the single bubble case, although the magntiude of this effect depends strongly on the area over which the temperature is averaged.

Figure 8.18 details the convective heat transfer enhancement in the near wake of the trailing bubble at 10 ms intervals. The complex heat flux enhancement means the trailing bubble major axis is provided on the images for clarity. The cooling structure evolves dynamically due to bubble-wake interactions and to interactions between the bubbles and the thermal boundary layer. As the leading bubble traverses the surface, it forms similar regions of enhanced and suppressed convective cooling on the outside and inside of the wake, respectively, as identified in figure 8.6. Initially, the trailing bubble is travelling in the positive spanwise direction towards its mean in position. As the trailing bubble approaches the leading bubble wake, a region of suppressed heat transfer appears just in front of the trailing bubble, highlighted as A_1 on figure 8.18. This region lasts for the next ≈ 30 *ms*, until the trailing bubble has intersected the leading bubble wake. Further on in time, the trailing bubble exits the leading bubble wake and reaches its local maximum in path (figure 8.18 (d) – (f)). At this time, a region of large convective heat transfer can be observed in its near wake,

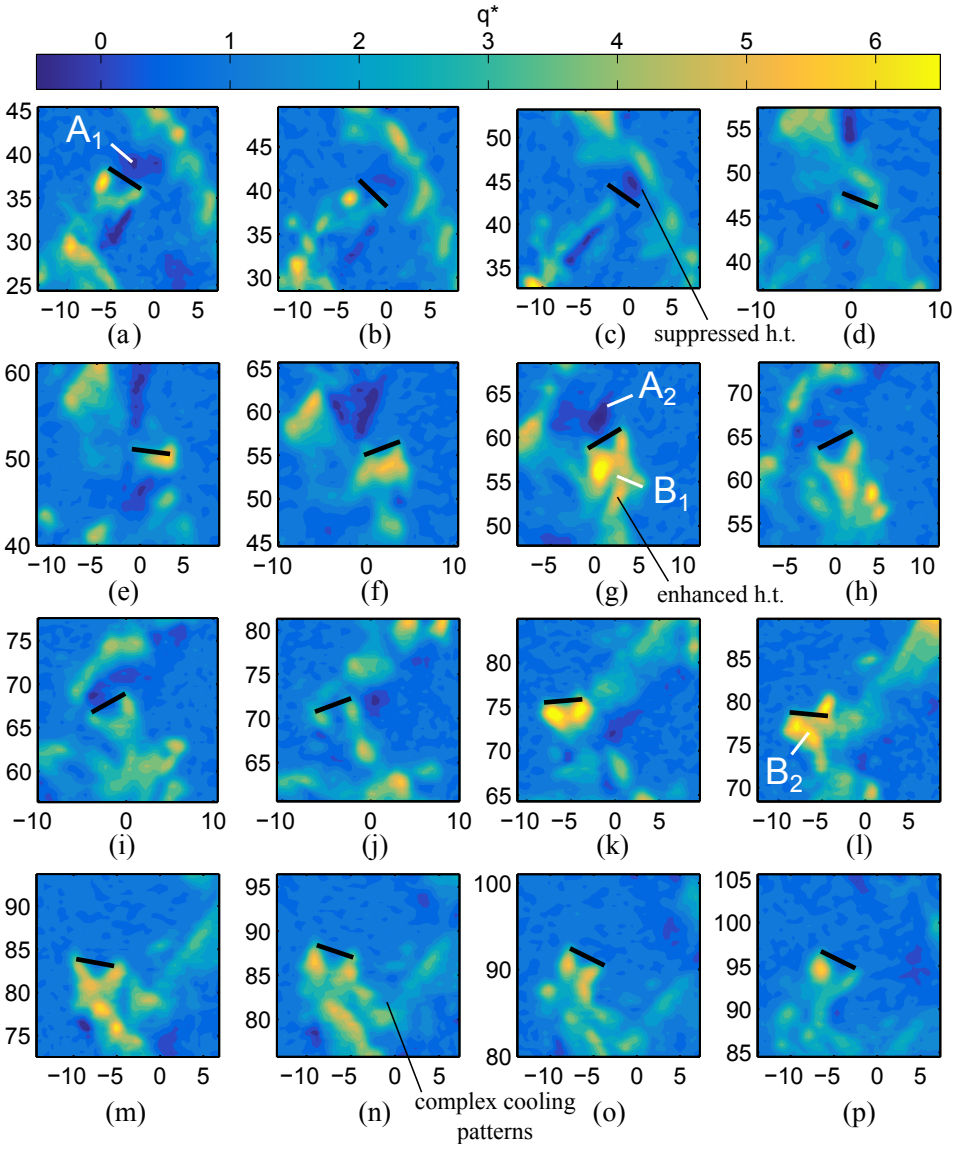

Figure 8.18: Convective flux enhancement, q^*, in the near wake of an in-line bubble pair for $\alpha = 30°$, $d_e = 5.8$ *mm* provided at instances in time 10 *ms* apart. The regions of interest *A* and *B* are also shown.

marked as B_1. This enhancement is consistent with single bubble behaviour. The next path intersection contributes to the low heat transfer at the point A_2 and later on a corresponding region of high heat transfer, B_2, appears in the near wake of the trailing bubble at the next local minimum of path. Thus, the local convective heat transfer is at a minimum as the trailing bubble approaches the leading bubble wake and is at its mean spanwise position, while it is at a maximum as the trailing bubble leaves the leading bubble wake, approaching its local maximum in path.

The key aspect to the convective heat transfer of an in-line bubble pair identified in

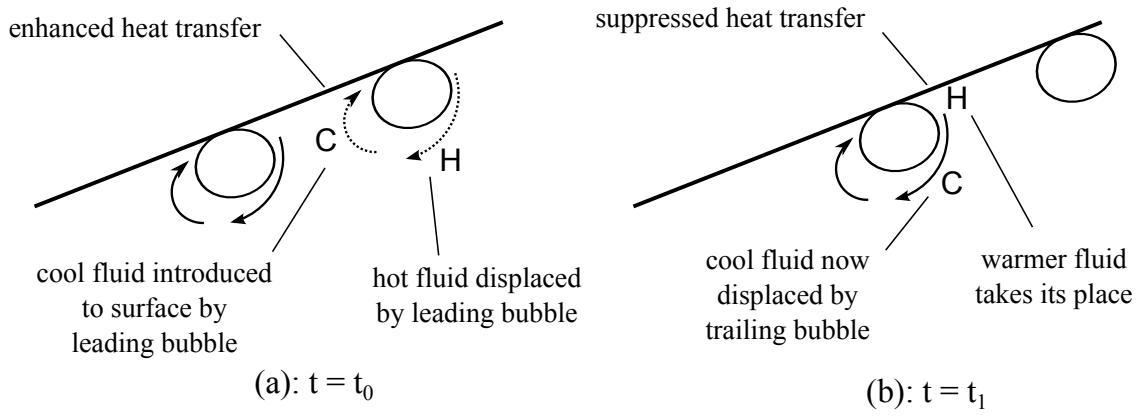

Figure 8.19: Sketch of an in-line bubble pair that provides an explanation for the regions of suppressed heat transfer identified in figure 8.18.

figure 8.18 is the suppressed convective flux that occurs where the trailing bubble intersects the leading bubble wake. Figure 8.19 provides a sketch explaining this process. At the instant in time t_0, the leading bubble displaces the hot fluid initially at the surface, while the recirculation region in its near wake draws cool fluid to the surface, thereby enhancing the convective heat transfer. Now consider what happens at the later time t_0. As the trailing bubble intersects the leading bubble wake, it now displaces the cold fluid that the leading bubble previously introduced to the surface. This leads to a small region of suppressed heat transfer just ahead the trailing bubble passage, although the is still a zone of enhanced convective heat transfer at the trailing bubble and in its near wake. As the trailing bubble exits the leading bubble wake, it is now entering a region that has not yet been cooled, thereby cooling in the same manner as a single bubble. As such, when considering the improved turbulent mixing offered by an in-line bubble pair, it is important to take into account the localised, transient regions of suppressed heat transfer, especially for two-phase applications of such flows. These regions of suppressed heat transfer, however, do not reduce the overall enhancement effect of the bubble pair.

Finally, the temporal evolution of the surface temperature and convective heat flux at the location A_1 from figure 8.18 are provided in figure 8.20. This can be split into four key regions. First, there is a decrease in temperature and increase in local convective heat flux corresponding to the first bubble entering the region A_1 (i). As the trailing bubble approaches this region, it displaces the cooler fluid at A_1, which results in the surface temperature

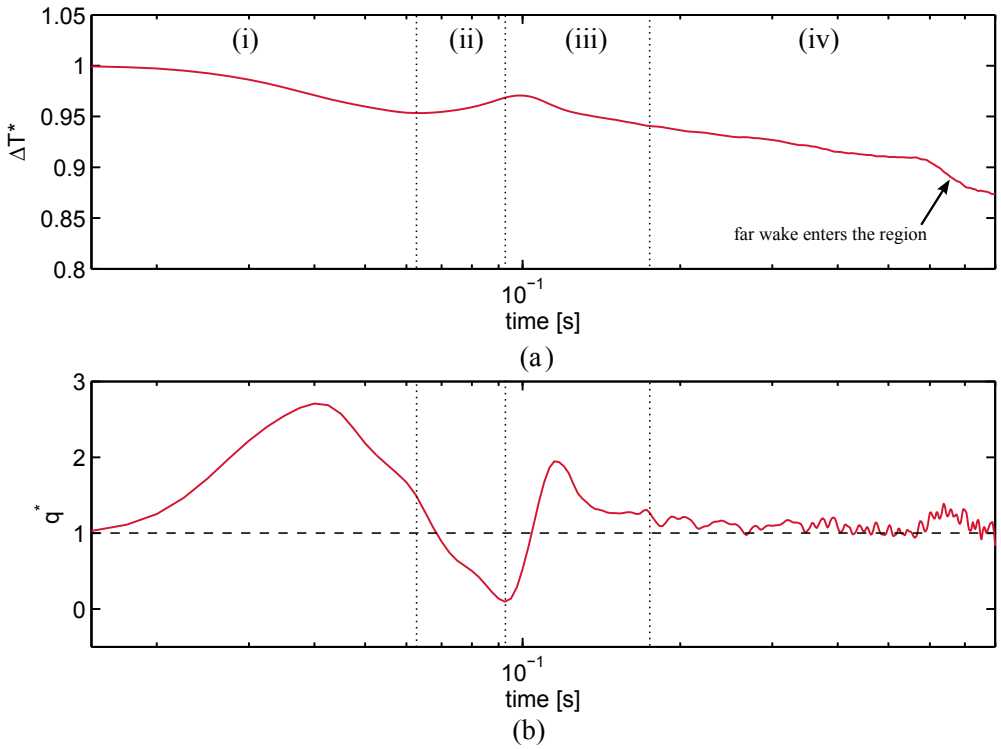

Figure 8.20: Logarithmic plot of the dimensionless temperature ΔT^* (a) and convective flux enhancement $q*$ (b) for an in-line bubble pair with $d_e = 5.8\ mm$, $\alpha = 30^\circ$ as a function of time for the key location A_1 on figure 8.18.

recovering and a decrease in the heat flux to below natural convection levels (ii). Next, the trailing bubble enters the region, corresponding to a decrease in surface temperature and a secondary increase in the local convective heat flux, although the latter is lower in magnitude than that of the first bubble (iii). Finally, as the convective heat transfer is above natural convection levels, the surface temperature continues to drop (iv).

8.3 Summary

This chapter has examined the enhancement in convective heat transfer from an inclined heated foil during the transient sliding process for single bubbles of two bubble diameters and for an in-line bubble pair for $d_e = 5.8\ mm$ at a wall superheat of $T_e = 10^\circ C$. This has been investigated in terms of both the local and global variation in surface temperature in the near and far wake. Additionally, the temporally changing convective heat transfer in the near wake of the bubble was explored at a variety of locations along the bubble's undulating path.

A substantial variation in convective heat flux was found to occur in the near wake of the bubble. Local convective heat flux levels of up to 14 kW/m^2 were observed on the outside of the bubble wake, while at the inside of the wake these flux levels could drop to below natural convection levels, even becoming negative on occasion. This behaviour is attributed to the wake structure, revealing the importance of the bubble wake in two-phase convective heat transfer applications. Downstream of the bubble, a drop in foil temperature of $\approx 4°C$ is observed for some time, although the convective heat flux has reduced. This is due to the near wake advecting cooler fluid from the liquid bulk to the surface. By spatially mapping the surface heat transfer measurements to the previously obtained PIV velocity and vorticity plots, it was possible to link regions of enhanced heat transfer to fluid features shed from the bubble at the path extrema.

A key objective of this section is to understand the role that bubble-wake interactions play in convective cooling. Introducing two bubbles to the surface in an in-line configuration results in greater spatially averaged convective heat transfer, since the opposite paths the bubbles take mean the convective cooling is spread over a larger area. However, it has been found that as the trailing bubble intersects the leading bubble wake, it can displace the cool fluid already at the surface and lead to momentarily suppressed heat transfer. Thus, although the net effect of a bubble pair is to increase convective heat transfer rates, the coupled interactions between the bubble, wake and boundary layer means that the instantaneous values can fluctuate significantly. The relationship between the bubble mechanics, fluid motion and heat transfer will be discussed further in the next chapter.

Chapter 9

Discussion

This study has sought to improve our understanding of the physics of a sliding bubble, by using a variety of experimental and analytical techniques. Chapter 6 presented a study of the dynamics of single and a pair of sliding air bubbles: namely their motion, path and shape. The bubble mechanics was explored both in terms of the centroidal and interfacial behaviour. Chapter 7 detailed the flow field measurements in the wake of a single and a pair of sliding bubbles using the particle image velocimetry technique in several measurement planes. Finally, chapter 8 reported on the convective heat flux enhancement offered by sliding bubbles.

Although these three aspects of bubble behaviour are measured separately using different experimental methods, they are inextricably linked by the bubble wake. All of the results observed in this study, be it the mechanics, bubble-bubble interactions, turbulent mixing or heat transfer, can be related back to the bubble wake. In essence, a bubble and its wake have a symbiotic relationship. This chapter will discuss the nature of this relationship with reference to “Bubble Wake Dynamics in Liquids and Liquid-Solid Suspensions" by Fan & Tsuchiya [13], an important resource on this topic.

It seems appropriate that the start point for this discussion should be the structure and nature of the wake. While multiphase systems typically consist of bubble swarms, it is possible to focus on the general case of a single bubble and its wake, and to consider subsequently the effects related to its interaction with other bubbles or wakes. Recall from chapter 2 that when the relative motion between the bubble and the fluid is small (i.e. $d_e < 1$

mm), the contour of the bubble forms part of a fluid streamline. As the Reynolds number increases, the flow will start to separate from the bubble, re-joining downstream to form the wake. The mechanics within the wake are varied and complex, but it can generally be split into two regions. First is the near wake, which travels in close association with the bubble. This region is associated with the phenomena that occur near the body base, such as the growth, formation and shedding of vortices. The remainder of the wake is downstream of this and is referred to as the far wake, the structure of which does not depend strongly on the type of body [13]. For a more rigorous description of the wake, see section 2.1.2.

The overall wake structure deduced from the PIV experiments was found to consist of a near wake that moves in close association with the bubble, with fluid separating from this near wake at twice the path frequency at each extremum of path displacement. In the near wake, fluid is also drawn towards the surface. In the far wake, fluid spreads away from the surface in the form of asymmetrical, oppositely-oriented hairpin vortices generated in the near wake. This vortical structure bears some similarity to the hairpin vortices shed by near-wall bluff bodies [98; 100; 101] and freely rising bubbles [24; 39; 41]. However, it differs from rising bubbles in that it is constricted by the presence of the surface and differs from near-wall bluff bodies since it is shed at alternating sides of the bubble due to its path oscillations. Although this structure is consistent with most of those observed in the literature, it deviates from the numerical study of Gaudlitz & Adams [47], who observed many hairpin vortices shedding for each half-cycle in bubble path for a rising bubble. The authors claimed that the deviation between their numerical data and published experimental studies was due to the influence of surfactants in PIV experiments, citing experiments using Schlieren photography in pure water to support this claim [37; 102]. This is at odds with the results observed in this study, where the introduction of surfactants was found to fundamentally alter the wake and path of the bubble, whereas the use of PIV particles did not result in a transition to this contaminated type of behaviour. An alternative explanation of the apparent discrepancy between the pure fluid Schlieren experiments and those observed by PIV is that the latter is observing a 2-D, 2 component cross section of a complex, three dimensional wake structure, in which each shed structure can contain many secondary components; these could conceivably be multiple hairpins. This is an issue inherent to inferring three-dimensional behaviour from two-dimensional data, although it is not as pressing an issue as it may at first

appear. This is because the key application of this sliding bubble flow is surface cooling, which itself is two-dimensional.

The bubble wake has been recognised as a key factor in inducing liquid mixing, for instance in gas-liquid-solid fluidised beds [13]. PIV results obtained in a perpendicular plane revealed that the fluid shed from the near wake spreads outwards into the bulk fluid, in both the spanwise and normal directions, increasing in size but decreasing in strength due to viscous dissipation. A single 5.8 *mm* diameter sliding bubble and its wake can affect a region of fluid up to 8 bubble diameters in size in the spanwise direction and 5 diameters in the normal direction. This fluid motion can persist for many seconds after the bubble passage, indicating the effectiveness of the wake as a mixing mechanism.

The interaction between the bubble interface and its surrounding fluid determines the shape and path of the bubble. In a low viscosity fluid such as water and at intermediate bubble diameters, the work done by the bubble on the surrounding fluid cannot be dissipated entirely by viscosity. Instead, some energy is released through turbulent dissipation in the wake. This generates an instability in the wake, which in turn imposes a secondary motion on the bubble, causing an undulating bubble path. The bubble shape is also controlled by the flow around the bubble, and can be described in terms of the dynamic pressures acting on the deformable bubble interface. Since the density and viscosity of the air inside the bubble is small, the pressure of the gas inside the bubble is constant. Upstream from the bubble, at its front stagnation point, the local fluid velocity is equal to zero. By Bernoulli's principle, this results in an inward push against the front of the bubble. At either side of the bubble, the fluid must accelerate around the bubble interface, which corresponds to a decreased pressure. The effect of this adverse pressure gradient is for the bubble sides to protrude outwards, forming an oblate shape. Downstream of the bubble, this negative pressure is not recovered due to the presence of the wake. The precise bubble shape is a function of the Reynolds, Morton and Eötvös numbers. In the current study, the bubbles are in the ellipsoidal regime, meaning the effects of both surface tension and inertia of the surrounding medium are important.

An analysis of the bubble centroid and interface showed the variation in bubble dynamics that occur due to the path instability. The difference in density between the bubble and the fluid means the bubble experiences a buoyancy force in the opposite direction to gravity. In this case, the inclination of the surface scales the buoyancy by the sine of the inclination

angle [66]. If the bubble were to slide rectilinearly, its buoyancy force would be opposed by a constant retarding drag force, meaning that at terminal velocity, the two will equal. However, if the bubble is of intermediate size, the dynamics become more complex. The bubble now takes on an oscillatory path, meaning that its velocity vector is only aligned with the buoyancy force at the local extrema of its path. At all other locations along the bubble path, the bubble velocity vector is not aligned with the buoyancy force, resulting in bubble dynamics that fluctuate temporally. This indicates a drag force, and therefore drag coefficient, that are not constant. The bubble shape depends heavily on its Reynolds number; thus, this fluctuating velocity results in a shape that oscillates from oblate at the high velocity path extrema to more spheroidal at the mean position.

Thus far, the wake has been shown to determine the mechanics of a single bubble. Progressing to a consideration of bubble pairs, the importance of bubble-wake interactions to multiphase applications has already been discussed, since all bubble-bubble interactions will involve this initial wake capture. Upon intersecting the wake of the leading bubble, trailing bubbles have been found to be accelerated due to the local pressure defect in the leading bubble wake region. For unsteady bubbles, the extent of the interaction causing an acceleration is limited by the critical bubble spacing, which Tsuchiya et al. [51] estimated to be 5-7 times the bubble diameter (in this study, the bubbles are at a spacing of 4 diameters apart). The trailing bubble is thereby accelerated by the leading bubble, resulting in an increased centroidal velocity and a more oblate bubble shape. Additionally, the bubbles were found to adopt paths that are in phase but opposite in amplitude. PIV experiments revealed fluid separating from the near wake of the leading bubble at the local extrema in path. Upon entering this separated fluid, the trailing bubble is accelerated not only in the direction of buoyancy but also in the spanwise direction corresponding to that of the shed fluid structure. When the bubbles adopt this in-phase, opposite amplitude path, the shed fluid accelerates the trailing bubble in the direction it is originally travelling in, implying that this is the most stable configuration for an interacting in-line bubble pair. In passing through the leading bubble wake, the trailing bubble also experiences rapid deformations around its interface. This results in complex trailing bubble dynamics, including a bubble shape that is no longer directly proportional to the bubble velocity.

Gas bubbles are known to increase heat transfer from adjacent surfaces by disturbing the

thermal boundary layer at the surface. Indeed, at low wall superheats, Houston & Cornwell [6] found that even for vapour bubbles, the disturbance effects alone accounted for a third the of heat transfer. Thus, the findings in the current study on air bubbles can also be of relevance to vapour bubble behaviour. Sliding air bubbles were found to enhance local convective heat transfer rates by up to 6-7 times that of natural convection alone, suppressing the surface temperature for a period of 20 seconds after the bubble passage. The nature of the convective heat transfer enhancement is complex, with some regions of suppressed, even negative heat transfer being observed. Chapter 8 also revealed that the maximum local convective heat transfer occurs inside the near wake, where the direction of fluid motion is towards the surface, thereby introducing cooler fluid from the bulk and enhancing convective heat transfer. Within the wake, small, elliptical regions of enhanced heat transfer were observed. This is consistent with either a single hairpin vortex with multiple secondary components or multiple hairpins being shed at each inversion of path. In any case, the wake is responsible for the majority of the convective heat transfer. The wake structures also experience significant advection effects due to the thermal boundary layer, spreading over a significant region of the surface and reducing its mean temperature further. Finally, the cooling structures for an in-line bubble pair were discussed. Surface heating creates additional complexity in these bubble-wake interactions, since the trailing bubble can momentarily decrease convective heat transfer by displacing cool fluid initially at the surface. However, since this effect is small, introducing multiple bubbles to the surface remains a more efficient mechanism of enhancing convective heat transfer.

Chapter 10

Conclusions

The characteristic behaviour of single bubbles and in-line bubble pairs sliding under an inclined surface has been experimentally investigated. This involved a study of the bubble motion, fluid motion and the associated heat transfer. To aid in the interpretation of the results and to highlight the limitations of the current research in this field of two-phase flow, a comprehensive review of the literature was performed. This included an in-depth study of the mechanics of single and interacting rising bubbles, the wake structures of rising bubbles and bluff bodies, and the heat transfer associated with sliding bubbles.

For the experimental investigation, an apparatus has been designed and built that allows for an injection of 1 or 2 bubbles of 5.8 *mm* and 7.2 *mm* equivalent diameter to a surface inclined at 20°, 30° and 40° to the horizontal, in adiabatic or heated surface conditions. Three different measurement configurations allow for measurement of the bubble motion, fluid motion and surface heat transfer. Extensive analysis has been performed on the data obtained from each experimental setup, using advanced techniques to obtain an improved understanding of these flow phenomena. This study has found the overall wake structure for a sliding bubble to consist of a near wake that moves in close association with the bubble and a far wake in which fluid moves normal to the surface in the form of asymmetrical, oppositely-oriented hairpin vortices generated in the near wake. This wake plays an important role in the bubble motion, convective heat transfer, bulk fluid mixing and bubble-wake interactions, and thus a greater understanding of these processes has been made possible.

10.1 Outcomes

The key outcomes of this work are:

- The development of a novel object tracking algorithm, which provides new insight into the mechanics of single bubbles and how the wake influences bubble-wake interactions in terms of the bubble interfaces.
- The characterisation of the sliding bubble wake structure by use of PIV for both a single bubble and an in-line bubble pair. PIV in multiple planes has also provided information on bubble-wake interactions and the turbulent mixing of the fluid.
- The development of a continuous wave PIV system, which offers 70 times the temporal resolution of an equivalent double-pulsed system while maintaining high quality time-resolved PIV with no interpolation or recursive hole filling.
- The usage of high speed thermography to characterise the effects of this wake structure on convective heat transfer from a heated surface, which is key to optimising future two-phase systems.

10.2 Future Work

Although significant contributions have been made by the current work, the field of two-phase fluid mechanics is vast and multi-layered. This study has answered some questions, but raised others. Indeed, each of the three experimental techniques used in this work could be extended. To study the bubble dynamics, a bubble tracking algorithm has been developed that provides measurements of the bubble edge data. For a sliding bubble, the interface does not experience significant rebounds; it would thus be useful to extend this algorithm to systems with more complex mechanics, such as impacting rising bubbles or vapour bubble formation.

This study has shown significant convective heat transfer enhancements due to the introduction of air bubbles to a heated surface. As a next step, it could be advantageous to take this research closer towards industrial applications. This could be achieved either by minimising the power input for an air bubble based cooling system or by modifying the

experimental apparatus to measure the interactions between two vapour bubbles, wherein the contribution of micro-layer evaporation, bubble growth and phase change to heat transfer would make for interesting results.

The PIV technique chosen for the current study does not allow for a focus on the liquid film between the bubble interface and the solid wall. Alternative techniques could be employed to resolve this important small-scale behaviour, such as micro particle image velocimetry (μPIV) and micro particle shadow velocimetry (μPSV). Indeed, the latter has recently been demonstrated to be an affordable, effective solution in measuring common two-phase flows at small scales [126].

In recent years, 3-D PIV techniques have expanded from comparatively simple stereoscopic techniques with 1 *mm* z-resolution to fully 3-D Tomographic PIV, which uses 5+ cameras and a laser that is reflected off a series of concave mirrors to create an illuminated volume. Although this method faces challenges in calibration and analysis, it is an area that is receiving significant attention within the field of fluid mechanics. This attention is justified, since it yields stunning, CFD-like plots from actual validated flow measurements. Tomographic PIV could be combined with fluorescent particles to find the 3-D, time-fluctuating wake structures behind bubbles and bluff bodies. When one considers the advancements PIV has made in the twenty years since its inception, such future applications seem nearly inevitable!

Bibliography

[1] J. Bollen, C. Brink, H. Eerens, and A. Manders, "Co-benefits of climate policy," in *PBL Report no. 500116005*, 2009.

[2] C. Field, V. Barros, D. Dokken, K. Mach, M. Mastrandrea, T. Bilir, K. E. M. Chatterjee, Y. Estrada, R. Genova, B. Girma, E. Kissel, A. Levy, S. MacCracken, P. Mastrandrea, and L. White, "Climate change 2014: Impacts, adaptation, and vulnerability. part a: Global and sectoral aspects. contribution of working group ii to the fifth assessment report of the intergovernmental panel on climate change," in *Intergovernmental panel on climate change*, Cambridge University Press, Cambridge, United Kingdom and New York, NY, USA, 2014.

[3] A. J. Robinson, "A thermal–hydraulic comparison of liquid microchannel and impinging liquid jet array heat sinks for high-power electronics cooling," *Components and Packaging Technologies, IEEE Transactions on*, vol. 32, no. 2, pp. 347–357, 2009.

[4] B. Donnelly, R. O'Reilly Meehan, K. Nolan, and D. B. Murray, "The dynamics of sliding air bubbles and the effects on surface heat transfer," *International Journal of Heat and Mass Transfer*, vol. 91, pp. 532–542, 2015.

[5] D. Donoghue, B. Donnelly, and D. B. Murray, "The enhancement effects of a plume of rising bubbles on natural convection from a heated vertical plate," *Journal of Enhanced Heat Transfer*, vol. 19, no. 4, 2012.

[6] S. Houston and K. Cornwell, "Heat transfer to sliding bubbles on a tube under evaporating and non-evaporating conditions," *International Journal of Heat and Mass Transfer*, vol. 39, no. 1, pp. 211–214, 1996.

[7] Y. Y. Yan, D. B. R. Kenning, I. A. Grant, and K. Cornwell, "Heat transfer to sliding bubbles under plane and curved surfaces," in *Institution of Mechanical Engineers Conference Publications*, vol. 2, pp. 295–295, 1995.

[8] K. Cornwell, "The influence of bubbly flow on boiling from a tube in a bundle," *International Journal of Heat and Mass Transfer*, vol. 33, no. 12, pp. 2579–2584, 1990.

[9] S. Wan, W. Zhou, Y. Wang, and C. Zhu, "High efficiency micro-bubble generator using carbon nanocoils as heater," in *Nano/Micro Engineered and Molecular Systems (NEMS), 2010 5th IEEE International Conference on*, pp. 740–743, IEEE, 2010.

[10] R. D. Blevins, *Flow-induced vibration*. New York, NY (USA); Van Nostrand Reinhold Co., Inc., 1990.

[11] W. Haberman and R. Morton, "An experimental investigation of the drag and shape of air bubbles rising in various liquids," tech. rep., DTIC Document, 1953.

[12] D. Bhaga and M. Weber, "Bubbles in viscous liquids: shapes, wakes and velocities," *Journal of Fluid Mechanics*, vol. 105, no. 1, pp. 61–85, 1981.

[13] L. Fan and K. Tsuchiya, *Bubble wake dynamics in liquids and liquid-solid suspensions*. Butterworth-Heinemann Stoneham, 1990.

[14] P. Saffman, "On the rise of small air bubbles in water," *Journal of Fluid Mechanics*, vol. 1, no. 03, pp. 249–275, 1956.

[15] J. Hadamard, "Motion of liquid drops (viscous)," *Comptes Rendus Hebdomadiares des Seances de l'Acadmie des Sciences, Paris*, vol. 154, pp. 1735–1755, 1911.

[16] W. Rybczynski, "On the translatory motion of a fluid sphere in a viscous medium," *Bull Acad Sci Cracow Ser A*, vol. 40, pp. 40–46, 1911.

[17] A. Frumkin and V. G. Levich, "On surfactants and interfacial motion (in Russian)," *Zhurnal Fizicheskoi Khimii*, vol. 21, pp. 1183–1204, 1947.

[18] R. Griffith, "The effect of surfactants on the terminal velocity of drops and bubbles," *Chemical Engineering Science*, vol. 17, no. 12, pp. 1057–1070, 1962.

[19] S. Alves, S. Orvalho, and J. Vasconcelos, "Effect of bubble contamination on rise velocity and mass transfer," *Chemical Engineering Science*, vol. 60, no. 1, pp. 1–9, 2005.

[20] P. Savic, *Circulation and distortion of liquid drops falling through a viscous medium*. National Research Council Canada, 1953.

[21] R. Clift, J. R. Grace, and M. E. Weber, *Bubbles, drops, and particles*. Courier Corporation, 2005.

[22] P. Duineveld, *Bouncing and coalescence of two bubbles in water*. PhD thesis, Twente University, 1994.

[23] I. Žun and J. Grošelj, "The structure of bubble non-equilibrium movement in free-rise and agitated-rise conditions," *Nuclear engineering and design*, vol. 163, no. 1, pp. 99–115, 1996.

[24] K. Lunde and R. Perkins, "Shape oscillations of rising bubbles," in *In Fascination of Fluid Dynamics*, pp. 387–408, Springer, 1998.

[25] J. Magnaudet and I. Eames, "The motion of high-Reynolds-number bubbles in inhomogeneous flows," *Annual Review of Fluid Mechanics*, vol. 32, no. 1, pp. 659–708, 2000.

[26] K. Ellingsen and F. Risso, "On the rise of an ellipsoidal bubble in water: oscillatory paths and liquid-induced velocity," *Journal of Fluid Mechanics*, vol. 440, no. 1, pp. 235–268, 2001.

[27] A. Tomiyama, G. Celata, S. Hosokawa, and S. Yoshida, "Terminal velocity of single bubbles in surface tension force dominant regime," *International Journal of Multiphase Flow*, vol. 28, no. 9, pp. 1497–1519, 2002.

[28] Y. Zhang and J. Finch, "A note on single bubble motion in surfactant solutions," *Journal of Fluid Mechanics*, vol. 429, pp. 63–66, 2001.

[29] G. B. Wallis, "The terminal speed of single drops or bubbles in an infinite medium," *International Journal of Multiphase Flow*, vol. 1, no. 4, pp. 491–511, 1974.

[30] R. N. Kieft, C. Rindt, A. Van Steenhoven, and G. Van Heijst, "On the wake structure behind a heated horizontal cylinder in cross-flow," *Journal of Fluid Mechanics*, vol. 486, pp. 189–211, 2003.

[31] J. Lindt, "On the periodic nature of the drag on a rising bubble," *Chemical Engineering Science*, vol. 27, no. 10, pp. 1775–1781, 1972.

[32] E. Achenbach, "Distribution of local pressure and skin friction around a circular cylinder in cross-flow up to Re = 5×10^6," *Journal of Fluid Mechanics*, vol. 34, no. 4, pp. 625–639, 1968.

[33] K. Lunde and R. Perkins, "Observations on wakes behind spheroidal bubbles and particles," in *ASME-FED Summer Meeting, Vancouver, Canada, Paper No. FEDSM97–3530*, 1997.

[34] T. Sanada, M. Shirota, and M. Watanabe, "Bubble wake visualization by using photochromic dye," *Chemical Engineering Science*, vol. 62, no. 24, pp. 7264–7273, 2007.

[35] G. Ryskin and L. Leal, "Numerical solution of free-boundary problems in fluid mechanics. part 2. buoyancy-driven motion of a gas bubble through a quiescent liquid.," *Journal of Fluid Mechanics*, vol. 148, pp. 19–35, 1984.

[36] G. Settles, "Colour-coding schlieren techniques for the optical study of heat and fluid flow," *International Journal of Heat and Fluid Flow*, vol. 6, no. 1, pp. 3–15, 1985.

[37] A. De Vries, A. Biesheuvel, and L. Van Wijngaarden, "Notes on the path and wake of a gas bubble rising in pure water," *International Journal of Multiphase Flow*, vol. 28, no. 11, pp. 1823–1835, 2002.

[38] C. Veldhuis, A. Biesheuvel, L. van Wijngaarden, and D. Lohse, "Motion and wake structure of spherical particles," *Nonlinearity*, vol. 18, pp. 1–C8, 2005.

[39] C. Brücker, "Structure and dynamics of the wake of bubbles and its relevance for bubble interaction," *Physics of Fluids*, vol. 11, p. 1781, 1999.

[40] Y. Delauré, V. Chan, and D. Murray, "A simultaneous PIV and heat transfer study of bubble interaction with free convection flow," *Experimental Thermal and Fluid Science*, vol. 27, no. 8, pp. 911–926, 2003.

[41] R. Zenit and J. Magnaudet, "Measurements of the streamwise vorticity in the wake of an oscillating bubble," *International Journal of Multiphase Flow*, vol. 35, no. 2, pp. 195–203, 2009.

[42] C. Veldhuis, *Leonardo's paradox: path and shape instabilities of particles and bubbles*. PhD thesis, University of Twente, 2011.

[43] G. Mougin and J. Magnaudet, "Path instability of a rising bubble," *Physical Review Letters*, vol. 88, no. 1, pp. 014502–1–014502–4, 2001.

[44] G. Mougin and J. Magnaudet, "Wake-induced forces and torques on a zigzagging/spiralling bubble," *Journal of Fluid Mechanics*, vol. 567, p. 185, 2006.

[45] M. Jenny, J. Dušek, and G. Bouchet, "Instabilities and transition of a sphere falling or ascending freely in a Newtonian fluid," *Journal of Fluid Mechanics*, vol. 508, no. 1, pp. 201–239, 2004.

[46] J. Cano-Lozano, P. Bohorquez, and C. Martínez-Bazán, "Wake instability of a fixed axisymmetric bubble of realistic shape," *International Journal of Multiphase Flow*, vol. 51, pp. 11–21, 2013.

[47] D. Gaudlitz and N. A. Adams, "Numerical investigation of rising bubble wake and shape variations," *Physics of Fluids (1994-present)*, vol. 21, no. 12, p. 122102, 2009.

[48] D. Enright, R. Fedkiw, J. Ferziger, and I. Mitchell, "A hybrid particle level set method for improved interface capturing," *Journal of Computational physics*, vol. 183, no. 1, pp. 83–116, 2002.

[49] I. Zun, M. Perpar, J. Gregorc, K. Hayashi, and A. Tomiyama, "Mixing of thermally stratified water layer by a free rising wobbling air bubble," *Chemical engineering science*, vol. 72, pp. 155–171, 2012.

[50] C. Veldhuis, A. Biesheuvel, and L. Van Wijngaarden, "Shape oscillations on bubbles rising in clean and in tap water," *Physics of Fluids (1994-present)*, vol. 20, no. 4, p. 040705, 2008.

[51] K. Tsuchiya, T. Miyahara, and L. Fan, "Visualization of bubble-wake interactions for a stream of bubbles in a two-dimensional liquid-solid fluidized bed," *International Journal of Multiphase Flow*, vol. 15, no. 1, pp. 35–49, 1989.

[52] M. Hayashi, A. Sakurai, and Y. Ohya, "Wake interference of a row of normal flat plates arranged side by side in a uniform flow," *Journal of Fluid Mechanics*, vol. 164, no. 1, pp. 1–25, 1986.

[53] C. Stewart, "Bubble interaction in low-viscosity liquids," *International Journal of Multiphase Flow*, vol. 21, no. 6, pp. 1037–1046, 1995.

[54] R. G. Horn, L. A. Del Castillo, and S. Ohnishi, "Coalescence map for bubbles in surfactant-free aqueous electrolyte solutions," *Advances in Colloid and Interface Science*, vol. 168, no. 1, pp. 85–92, 2011.

[55] A. Chesters and G. Hofman, "Bubble coalescence in pure liquids," in *Mechanics and Physics of Bubbles in Liquids*, pp. 353–361, Springer, 1982.

[56] D. Bröder and M. Sommerfeld, "An advanced lif-plv system for analysing the hydrodynamics in a laboratory bubble column at higher void fractions," *Experiments in Fluids*, vol. 33, no. 6, pp. 826–837, 2002.

[57] J. Bonjour, M. Clausse, and M. Lallemand, "Experimental study of the coalescence phenomenon during nucleate pool boiling," *Experimental Thermal and Fluid Science*, vol. 20, no. 3, pp. 180–187, 2000.

[58] Y. Hallez and D. Legendre, "Interaction between two spherical bubbles rising in a viscous liquid," *Journal of Fluid Mechanics*, vol. 673, pp. 406–431, 2011.

[59] B. Bunner and G. Tryggvason, "Effect of bubble deformation on the properties of bubbly flows," *Journal of Fluid Mechanics*, vol. 495, pp. 77–118, 2003.

[60] D. Robinson and D. Katz, "Effect of vapour agitation on boiling coefficients," *Chemical Engineering Science*, vol. 47, pp. 317–325, 1951.

[61] E. Zukowski, "Influence of viscosity, surface tension and inclination angle on motion of long bubbles in closed tubes," *Journal of Fluid Mechanics*, vol. 25, pp. 821–837, 1966.

[62] C. Maneri and N. Zuber, "An experimental study of plane bubbles rising at inclination," *International Journal of Multiphase Flow*, vol. 1, no. 5, pp. 623–645, 1974.

[63] T. Maxworthy, "Bubble rise under an inclined plate," *Journal of Fluid Mechanics*, vol. 229, pp. 659–674, 1991.

[64] R. Davies and G. Taylor, "The mechanics of large bubbles rising through extended liquids and through liquids in tubes," *Proceedings of the Royal Society of London. Series A. Mathematical and Physical Sciences*, vol. 200, no. 1062, pp. 375–390, 1950.

[65] H. Tsao and D. Koch, "Observations of high Reynolds number bubbles interacting with a rigid wall," *Physics of Fluids*, vol. 9, p. 44, 1997.

[66] A. Peron, L. Kiss, and S. Poncsák, "An experimental investigation of the motion of single bubbles under a slightly inclined surface," *International Journal of Multiphase Flow*, vol. 32, no. 5, pp. 606–622, 2006.

[67] J. Chen, J. C. Zhao, and K. X. Qian, "Rise velocity of air bubble under a slightly inclined plane submerged in water," in *International Conference on Fluid Machinery*, pp. 1173–1176, 1992.

[68] B. Donnelly, *The effects of a sliding air bubble on heat transfer from an inclined surface*. PhD thesis, Trinity College Dublin, Dublin, Ireland, 2011.

[69] B. Donnelly, T. S. O'Donovan, and D. B. Murray, "Surface heat transfer due to sliding bubble motion," *Applied Thermal Engineering*, vol. 29, no. 7, pp. 1319–1326, 2009.

[70] K. M. DeBisschop, M. J. Miksis, and D. M. Eckmann, "Bubble rising in an inclined channel," *Physics of Fluids (1994-present)*, vol. 14, no. 1, pp. 93–106, 2002.

[71] D. M. Eckmann, S. Kobayashi, and M. Li, "Microvascular embolization following polidocanol microfoam sclerosant administration," *Dermatologic surgery*, vol. 31, no. 6, pp. 636–643, 2005.

[72] J. Masliyah, R. Jauhari, and M. Gray, "Drag coefficients for air bubbles rising along an inclined surface," *Chemical Engineering Science*, vol. 49, no. 12, pp. 1905–1911, 1994.

[73] L. Del Castillo, S. Ohnishi, L. White, S. Carnie, and R. Horn, "Effect of disjoining pressure on terminal velocity of a bubble sliding along an inclined wall," *Journal of Colloid and Interface Science*, vol. 364, no. 2, pp. 505–511, 2011.

[74] D. C. Grahame, "The electrical double layer and the theory of electrocapillarity.," *Chemical Reviews*, vol. 41, no. 3, pp. 441–501, 1947.

[75] L. Guldbrand, B. Jönsson, H. Wennerström, and P. Linse, "Electrical double layer forces. a monte carlo study," *The Journal of Chemical Physics*, vol. 80, p. 2221, 1984.

[76] A. Addlesee and K. Cornwell, "Liquid film thickness above a bubble rising under an inclined plate," *Chemical Engineering Research and Design*, vol. 75, no. 7, pp. 663–667, 1997.

[77] A. Addlesee and P. Kew, "Development of the liquid film above a sliding bubble," *Chemical Engineering Research and Design*, vol. 80, no. 3, pp. 272–277, 2002.

[78] D. Kenning, D. Wen, K. Das, and S. Wilson, "Confined growth of a vapour bubble in a capillary tube at initially uniform superheat: Experiments and modelling," *International Journal of Heat and Mass Transfer*, vol. 49, no. 23, pp. 4653–4671, 2006.

[79] B. Podvin, S. Khoja, F. Moraga, and D. Attinger, "Model and experimental visualizations of the interaction of a bubble with an inclined wall," *Chemical Engineering Science*, vol. 63, no. 7, pp. 1914–1928, 2008.

[80] D. Donoghue, A. Albadawi, Y. Delauré, A. Robinson, and D. B. Murray, "Bubble

impingement and the mechanisms of heat transfer," *International Journal of Heat and Mass Transfer*, vol. 71, no. 0, pp. 439 – 450, 2014.

[81] D. Legendre, C. Colin, and T. Coquard, "Lift, drag and added mass of a hemispherical bubble sliding and growing on a wall in a viscous linear shear flow," *Philosophical Transactions of the Royal Society A: Mathematical, Physical and Engineering Sciences*, vol. 366, no. 1873, pp. 2233–2248, 2008.

[82] D. Kenning and Y. Yan, "Pool boiling heat transfer on a thin plate: features revealed by liquid crystal thermography," *International Journal of Heat and Mass Transfer*, vol. 39, no. 15, pp. 3117–3137, 1996.

[83] Y. Yan, D. Kenning, and K. Cornwell, "Sliding and sticking vapour bubbles under inclined plane and curved surfaces," *International Journal of Refrigeration*, vol. 20, no. 8, pp. 583–591, 1997.

[84] B. Bayazit, D. Hollingsworth, and L. Witte, "Heat transfer enhancement caused by sliding bubbles," *Journal of Heat Transfer*, vol. 125, no. 3, pp. 503–509, 2003.

[85] D. K. Hollingsworth, L. C. Witte, and M. Figueroa, "Enhancement of heat transfer behind sliding bubbles," *Journal of Heat Transfer*, vol. 131, no. 12, p. 121005, 2009.

[86] G. Sateesh, S. Das, and A. Balakrishnan, "Analysis of pool boiling heat transfer: effect of bubbles sliding on the heating surface," *International Journal of Heat and Mass Transfer*, vol. 48, no. 8, pp. 1543–1553, 2005.

[87] C. Wang and V. Dhir, "On the gas entrapment and nucleation site density during pool boiling of saturated water," *Transactions-American Society of Mechanical Engineers Journal of Heat Transfer*, vol. 115, pp. 670–670, 1993.

[88] E. Hahne and G. Barthau, "Heat transfer and nucleation in pool-boiling," *International Journal of Thermal Sciences*, vol. 45, no. 3, pp. 209–216, 2006.

[89] D. Qiu and V. Dhir, "Experimental study of flow pattern and heat transfer associated with a bubble sliding on downward facing inclined surfaces," *Experimental Thermal and Fluid Science*, vol. 26, no. 6, pp. 605–616, 2002.

[90] D. Li, S. Manickam, and V. Dhir, "A numerical study of a single bubble sliding on a downward facing heating surface," in *ASME Summer Heat Transfer Conference, San Francisco, Paper HT2005–72541*, 2005.

[91] J. Stafford, E. Walsh, and V. Egan, "Characterizing convective heat transfer using infrared thermography and the heated-thin-foil technique," *Measurement Science and Technology*, vol. 20, no. 10, p. 105401, 2009.

[92] R. J. Adrian, "Hairpin vortex organization in wall turbulencea)," *Physics of Fluids*, vol. 19, no. 4, p. 041301, 2007.

[93] T. Theodorsen, "Mechanism of turbulence," in *Proceedings of the Second Midwestern Conference on Fluid Mechanics*, pp. 1–18, Ohio State University, 1952.

[94] J. Zhou, R. J. Adrian, S. Balachandar, and T. Kendall, "Mechanisms for generating coherent packets of hairpin vortices in channel flow," *Journal of Fluid Mechanics*, vol. 387, pp. 353–396, 1999.

[95] L. Rosenhead, "Vortex systems in wakes," *Advances in Applied Mechanics*, vol. 3, p. 185, 1953.

[96] D. Marshall and T. Stanton, "On the eddy system in the wake of flat circular plates in three dimensional flow," *Proceedings of the Royal Society of London. Series A, Containing Papers of a Mathematical and Physical Character*, pp. 295–301, 1931.

[97] S. P. Metzler, *Processes in the wall region of a turbulent boundary layer*. PhD thesis, Leigh University, Pennsylvania, USA, 1980.

[98] M. Acarlar and C. Smith, "A study of hairpin vortices in a laminar boundary," *Journal of Fluid Mechanics*, vol. 175, pp. 1–83, 1987.

[99] R. Wille, "Generation of oscillatory flows," *Flow-Induced Structural Vibrations*, vol. 1, pp. 1–16, 1974.

[100] H. M. Tufo, P. Fischer, M. E. Papka, and K. Blom, "Numerical simulation and immersive visualization of hairpin vortices," in *Proceedings of the 1999 ACM/IEEE conference on Supercomputing*, p. 62, ACM, 1999.

[101] B. Stewart, M. Thompson, T. Leweke, and K. Hourigan, "Numerical and experimental studies of the rolling sphere wake," *Journal of Fluid Mechanics*, vol. 643, no. 1, pp. 137–162, 2010.

[102] C. Veldhuis and A. Biesheuvel, "An experimental study of the regimes of motion of spheres falling or ascending freely in a Newtonian fluid," *International Journal of Multiphase Flow*, vol. 33, no. 10, pp. 1074–1087, 2007.

[103] A. S. Lau, "The narcissus effect in infrared optical scanning systems," in *1977 SPIE/SPSE Technical Symposium East*, pp. 57–62, International Society for Optics and Photonics, 1977.

[104] N. Otsu, "A threshold selection method from gray-level histograms," *Automatica*, vol. 11, no. 285-296, pp. 23–27, 1975.

[105] E. Klaseboer, J.-P. Chevaillier, A. Maté, O. Masbernat, and C. Gourdon, "Model and experiments of a drop impinging on an immersed wall," *Physics of Fluids*, vol. 13, no. 1, pp. 45–57, 2001.

[106] M. Raffel, C. Willert, and J. Kompenhans, *Particle Image Velocimetry: A Practical Guide; with 24 Tables*. Springer, 1998.

[107] J. Westerweel, "Fundamentals of digital particle image velocimetry," *Measurement Science and Technology*, vol. 8, no. 12, p. 1379, 1997.

[108] F. Scarano, "Iterative image deformation methods in PIV," *Measurement Science and Technology*, vol. 13, no. 1, p. R1, 2002.

[109] R. D. Keane and R. J. Adrian, "Theory of cross-correlation analysis of PIV images," *Applied Scientific Research*, vol. 49, no. 3, pp. 191–215, 1992.

[110] O. Raghu and J. Philip, "Thermal properties of paint coatings on different backings using a scanning photo acoustic technique," *Measurement Science and Technology*, vol. 17, no. 11, p. 2945, 2006.

[111] T. L. Bergman, F. P. Incropera, and A. S. Lavine, *Fundamentals of heat and mass transfer*. John Wiley & Sons, 2011.

[112] S. Ostrach, "Natural convection in enclosures," *Journal of Heat Transfer*, vol. 110, no. 4b, pp. 1175–1190, 1988.

[113] B. Rich, "An investigation of heat transfer from an inclined flat plate in free convection," *Trans. ASME*, vol. 75, pp. 489–499, 1953.

[114] S. W. Churchill and H. Chu, "Correlating equations for laminar and turbulent free convection from a vertical plate," *International Journal of Heat and Mass Transfer*, vol. 18, no. 11, pp. 1323–1329, 1975.

[115] T. Fujii and H. Imura, "Natural-convection heat transfer from a plate with arbitrary inclination," *International Journal of Heat and Mass Transfer*, vol. 15, no. 4, pp. 755–767, 1972.

[116] B. Berkovsky and V. Polevikov, "Numerical study of problems on high-intensive free convection," in *Proceedings of International Turbulent Buoyant Convection Seminar, Dubrovnik*, 1976.

[117] I. Catton, "Natural convection in enclosures," in *Proceedings of the 6th International Heat Transfer Conference*, pp. 13–31, Toronto, Canada, 1978.

[118] J. H. Kim, T. W. Simon, and R. Viskanta, "Journal of heat transfer policy on reporting uncertainties in experimental measurements and results," *Journal of Heat Transfer*, vol. 115, no. 1, pp. 5–6, 1993.

[119] H. W. Coleman and W. G. Steele, *Experimentation, validation, and uncertainty analysis for engineers*. John Wiley & Sons, 2009.

[120] Z. Xue, J. J. Charonko, and P. P. Vlachos, "Particle image velocimetry correlation signal-to-noise ratio metrics and measurement uncertainty quantification," *Measurement Science and Technology*, vol. 25, no. 11, p. 115301, 2014.

[121] B. M. Wilson and B. L. Smith, "Uncertainty on PIV mean and fluctuating velocity due to bias and random errors," *Measurement Science and Technology*, vol. 24, no. 3, p. 035302, 2013.

[122] T. Persoons, R. O'Reilly Meehan, and D. B. Murray, "Time resolved high dynamic range PIV using local uncertainty estimation methods," in *Proceedings of the 17th Lisbon Symposium on Applications of Laser Techniques to Fluid Mechanics*, Lisbon, Portugal, 2014.

[123] T. Persoons and T. S. O'Donovan, "High dynamic velocity range particle image velocimetry using multiple pulse separation imaging," *Sensors*, vol. 11, no. 1, pp. 1–18, 2010.

[124] J. J. Charonko and P. P. Vlachos, "Estimation of uncertainty bounds for individual particle image velocimetry measurements from cross-correlation peak ratio," *Measurement Science and Technology*, vol. 24, no. 6, p. 065301, 2013.

[125] V. Roig, M. Roudet, F. Risso, and A. M. Billet, "Dynamics of a high-Reynolds-number bubble rising within a thin gap," *Journal of Fluid Mechanics*, vol. 707, pp. 444–466, 2012.

[126] S. Khodaparast, N. Borhani, and J. Thome, "Application of micro particle shadow velocimetry μpsv to two-phase flows in microchannels," *International journal of multiphase flow*, vol. 62, pp. 123–133, 2014.